

May 2018

# Synthesis and Characterization of Transition Metal Oxide and Dichalcogenide Nanomaterials for Energy and Environmental Applications

Ren Ren

*University of Wisconsin-Milwaukee*

Follow this and additional works at: <https://dc.uwm.edu/etd>

 Part of the [Materials Science and Engineering Commons](#), and the [Mechanical Engineering Commons](#)

---

## Recommended Citation

Ren, Ren, "Synthesis and Characterization of Transition Metal Oxide and Dichalcogenide Nanomaterials for Energy and Environmental Applications" (2018). *Theses and Dissertations*. 1909.  
<https://dc.uwm.edu/etd/1909>

This Dissertation is brought to you for free and open access by UWM Digital Commons. It has been accepted for inclusion in Theses and Dissertations by an authorized administrator of UWM Digital Commons. For more information, please contact [open-access@uwm.edu](mailto:open-access@uwm.edu).

**SYNTHESIS AND CHARACTERIZATION OF TRANSITION  
METAL OXIDE AND DICHALCOGENIDE NANOMATERIALS  
FOR ENERGY AND ENVIRONMENTAL APPLICATIONS**

by

Ren Ren

A Dissertation Submitted in  
Partial Fulfillment of the  
Requirements for the Degree of

Doctor of Philosophy  
in Engineering

at

The University of Wisconsin-Milwaukee

May 2018

# ABSTRACT

## SYNTHESIS AND CHARACTERIZATION OF TRANSITION METAL OXIDE AND DICHALCOGENIDE NANOMATERIALS FOR ENERGY AND ENVIRONMENTAL APPLICATIONS

by

Ren Ren

The University of Wisconsin-Milwaukee, 2018  
Under the Supervision of Professor Junhong Chen

Transition metal oxides (TMOs) and transition metal dichalcogenides (TMDs) have gained immense interest recently for energy and environmental applications due to their exceptional structural, electronic, and optical properties. For example, titanium dioxide ( $\text{TiO}_2$ ) as one of the TMO photocatalysts has been widely studied due to its stability, non-toxicity, wide availability, and high efficiency. However, its wide bandgap significantly limits its use under visible light or solar light. Recent studies also show that semiconducting TMDs could be used as potential supercapacitor electrode materials and platinum (Pt)-free electrocatalysts for economical utilization of renewable energy, because the high cost and scarcity of Pt have impeded the large-scale commercialization of many green technologies.

In this dissertation study, various novel TMO and TMD nanomaterials are designed and synthesized, and their catalytic performance is further investigated. First, a facile route for the controllable synthesis of modified  $\text{TiO}_2$  is designed to improve its photocatalytic efficiency under the visible/solar light. The resulting  $\text{Ti}^{3+}$ -doped  $\text{TiO}_2$  with tunable photocatalytic properties using a hydrothermal method with varying amounts of reductant, i.e., sodium borohydride ( $\text{NaBH}_4$ ),

showed color changes from light yellow, light grey, to dark grey with the increasing amount of NaBH<sub>4</sub>. The present method can controllably and effectively reduce Ti<sup>4+</sup> on the surface of TiO<sub>2</sub> and induce partial transformation of anatase TiO<sub>2</sub> to rutile TiO<sub>2</sub>, with the evolution of nanoparticles into hierarchical structures attributing to the high pressure and strong alkali environment in the synthesis atmosphere; in this way, the photocatalytic activity of Ti<sup>3+</sup>-doped TiO<sub>2</sub> under visible-light can be tuned. The band gap of Ti<sup>3+</sup>-doped TiO<sub>2</sub> based on the Kubelka-Munk function is 3.1 eV, which is smaller than that of pristine TiO<sub>2</sub> (3.28 eV), confirming that adding NaBH<sub>4</sub> as a reductant causes the absorption edge of TiO<sub>2</sub> to shift to a lower energy region. After 20 min of simulated sunlight irradiation of photocatalytic reactions for the degradation of methylene blue (MB) aqueous solution, nearly 97.2% of MB was degraded by the sample TiO<sub>2</sub>-4 (reduced by 12 g of NaBH<sub>4</sub> in the hydrothermal reaction), compared with the degradation efficiency of the pristine TiO<sub>2</sub> (23.5%). The as-developed strategy may open up a new avenue for designing and functionalizing TiO<sub>2</sub> materials with enhanced visible light absorption, narrowed band gap, and improved photocatalytic activity.

Second, cobalt sulfide-based (CoS<sub>x</sub>) nanostructures as one of the TMDs are competitive candidates for fabrication of supercapacitor electrodes due to their high specific surface area, high electrical conductivity, and redox-active structures. However, CoS<sub>x</sub> materials still suffer from relatively low specific capacitances, degradation of performance over long cycling duration, and tedious synthesis and assembly methods. Hence, metallic vertically-aligned cobalt pyrite (CoS<sub>2</sub>) nanowires (NWs) are prepared directly on current collecting electrodes, e.g., carbon cloth or graphite disc, for high-performance supercapacitors. These vertically-aligned CoS<sub>2</sub> NWs have a variety of advantages for supercapacitor applications. Because the metallic CoS<sub>2</sub> NWs are

synthesized directly on the current collector, the good electrical connection enables efficient charge transfer between the active CoS<sub>2</sub> materials and the current collector. In addition, the open spaces between the vertical NWs lead to a large accessible surface area and afford rapid mass transport. Moreover, the robust CoS<sub>2</sub> NW structure results in high stability of the active materials during long-term operation. Electrochemical characterization reveals that the CoS<sub>2</sub> NWs enable a large specific capacitance (828.2 F/g at a scan rate of 0.01 V/s) and excellent long-term cycling stability (0-2.5% capacity loss after 4,250 cycles at 5 A/g) for pseudocapacitors. This example of vertically-aligned metallic CoS<sub>2</sub> NWs for supercapacitor applications expands the opportunities for transition metal sulfide-based nanostructures in emerging energy storage applications.

Third, to combine the advantages of TMOs and TMDs, an aerosol processing method is developed for the facile and green synthesis of reduced graphene oxide (rGO)/tungsten disulfide (WS<sub>2</sub>)/tungsten trioxide (WO<sub>3</sub>) ternary nanohybrids, because both TMOs and TMDs are promising candidates for platinum-free electrocatalysts in renewable energy applications. The resulting hybrid material has a spherical structure constructed of crumpled graphene and WS<sub>2</sub>/WO<sub>3</sub> nanorods. The crumpled graphene/WS<sub>2</sub>/WO<sub>3</sub> (CGTH) catalyst showed a superior electrocatalytic activity in the hydrogen evolution reaction (HER), with a Tafel slope of 37 mV/dec and an onset potential of 96 mV. Compared with reported MoS<sub>2</sub>/WS<sub>2</sub>-based electrocatalysts, this hybrid material shows one of the highest catalytic activities in HER. The environmentally-friendly synthesis and outstanding performance suggest a great potential of CGTH for noble metal-free electrocatalysts in water splitting.

Next, in order to improve the specific capacity of lithium-ion batteries (LIBs)/ potassium-ion batteries (PIBs) and relieve volume expansion of nanoparticles to fulfill the urgent need of reliable energy storage applications, TMD nanomaterials especially MoS<sub>2</sub> quantum dots (QDs) have been considered promising anode materials for LIBs owing to their higher theoretical capacity and better rate capability compared with commercial graphite anodes. An exfoliated mesoporous MoS<sub>2</sub> QDs-graphite composite anode was designed and investigated. The MoS<sub>2</sub> QDs are located in the void spaces between graphite particles, thereby preventing the graphite particles from losing electrical contact with the current collector and enhancing the cycling performance of the MoS<sub>2</sub>/graphite composite anode. The optimized MoS<sub>2</sub> QDs with graphite composites displayed good charge/discharge characteristics and the capacity maintained at 449.8 mAh g<sup>-1</sup> after 300 charge/discharge cycles for LIBs. And the MoS<sub>2</sub> QDs for PIB cells exhibited a stable capacity of approximately 409 mAh g<sup>-1</sup> for 17 cycles.

Finally, metal-organic frameworks (MOFs) have attracted substantial research attention owing to their tunable pore size, high pore volume, high specific surface area, and highly ordered crystalline porous networks. Previous studies have mostly focused on sensing, drug delivery, batteries, and selective catalysis; however, their application as photocatalysts has not been thoroughly reported. It is well known that bulk MoS<sub>2</sub> is unsuitable for photocatalytic applications due to the insufficient reduction and oxidation ability for the photocatalysis. However, exfoliated MoS<sub>2</sub> exhibits a direct band gap of 2.8 eV resulting from quantum confinement, which enables it to possess suitable band positions and to retain good visible-light absorption ability. As a result, it is considered to be a promising candidate for photocatalytic applications. Encapsulating exfoliated MoS<sub>2</sub> into MOF exhibits enhanced absorption in the visible light range compared with pure MOF and the highest

hydrogen production rate could reach  $68.4 \mu\text{mol h}^{-1}\text{g}^{-1}$ , which is much higher than that on pure MOF. With suitable band structure and improved light-harvesting ability, exfoliated  $\text{MoS}_2$ @MOF can be a potential photocatalyst for hydrogen production.

This dissertation study suggests that modified  $\text{TiO}_2$  and exfoliated  $\text{MoS}_2$ @MOF can be efficient photocatalysts with enhanced visible light absorption ability; metallic  $\text{CoS}_2$  NWs could be active materials with a large specific capacitance and excellent stability; reduced graphene oxide (rGO)/tungsten disulfide ( $\text{WS}_2$ )/tungsten trioxide ( $\text{WO}_3$ ) as a ternary nanohybrid offers advantages of TMOs and TMDs, making it an outstanding noble-metal free electrocatalyst in water splitting; and  $\text{MoS}_2$  QDs with relieved volume expansion are promising anode materials for LIBs/PIBs. The study provides a scientific foundation to design and discover low-cost, efficient and stable TMOs and TMDs candidates for suitable energy and environmental applications.

© Copyright by Ren Ren, 2018  
All Rights Reserved

# TABLE OF CONTENTS

ABSTRACT .....	ii
LIST OF FIGURES .....	xi
LIST OF ABBREVIATIONS.....	xx
ACKNOWLEDGMENTS .....	xxiii
CHAPTER 1 INTRODUCTION AND LITERATURE REVIEW .....	1
1.1 Introduction .....	1
1.2 Literature review .....	2
1.2.1 Literature review on transition metal oxides .....	2
1.2.2 Literature review on transition metal dichalcogenides.....	11
1.2.3 Literature review on photocatalysis .....	16
1.2.4 Literature review on electrocatalysis for hydrogen evolution .....	24
1.2.5 Literature review on energy storage devices .....	28
1.2.6 Summary and conclusions .....	35
1.2.7 Research objective and dissertation outline .....	36
CHAPTER 2 MODIFIED TITANIUM DIOXIDE FOR PHOTOCATALYSIS.....	38
2.1 Introduction .....	38
2.2 Experimental methods .....	38
2.2.1 Material synthesis .....	38
2.2.2 Material characterization.....	39
2.2.3 Photocatalytic reaction measurements .....	39
2.3 Results and discussion.....	40
2.4 Summary and conclusions.....	54

CHAPTER 3	METALLIC $\text{CoS}_2$ NANOWIRES FOR SUPERCAPACITORS .....	56
3.1	Introduction .....	56
3.2	Experimental methods .....	56
3.2.1	Material synthesis .....	56
3.2.2	Material characterization.....	57
3.2.3	Supercapacitor measurements .....	57
3.2.4	Capacitor performance .....	57
3.3	Results and discussion.....	58
3.4	Summary and conclusions.....	70
CHAPTER 4	CRUMPLED GRAPHENE/TUNGSTEN DISULFIDE/TUNGSTEN TRIOXIDE TERNARY NANOHYBRIDS FOR ELECTROCATALYSIS.....	71
4.1	Introduction .....	71
4.2	Experimental methods .....	71
4.2.1	Material synthesis .....	71
4.2.2	Material characterization.....	72
4.2.3	Electrochemical measurements .....	73
4.2.4	Reversible hydrogen electrode (RHE) calibration .....	73
4.3	Results and discussion.....	74
4.4	Summary and conclusions.....	93
CHAPTER 5	MOLYBDENUM DISULFIDE QUANTUM DOTS FOR LITHIUM-ION AND POTASSIUM-ION BATTERIES.....	94
5.1	Introduction .....	94
5.2	Experimental methods .....	94
5.2.1	Material synthesis .....	94
5.2.2	Material characterization.....	96

5.2.3 Preparation of electrodes and coin cells .....	96
5.2.4 Electrochemistry measurements.....	97
5.3 Results and discussion.....	97
5.4 Summary and conclusions.....	108
CHAPTER 6 EXFOLIATED MOLYBDENUM DISULFIDE WITH METAL ORGANIC FRAMEWORK FOR PHOTOCATALYTIC HYDROGEN EVOLUTION .....	109
6.1 Introduction.....	109
6.2 Experimental methods.....	109
6.2.1 Material synthesis .....	109
6.2.2 Material characterization.....	110
6.2.3 Photocatalytic hydrogen production measurements.....	111
6.3 Results and discussion.....	112
6.4 Summary and conclusions.....	118
CHAPTER 7 SUMMARY AND FUTURE WORK .....	119
7.1 Summary .....	119
7.2 Future work .....	121
7.2.1 MQDs for potassium-ion batteries .....	121
7.2.2 Photocatalytic hydrogen evolution studies.....	121
REFERENCES .....	123
CURRICULUM VITAE.....	147

## LIST OF FIGURES

Fig. 1.1 The illustration of the structural dimensionality of nanomaterials with properties. <sup>49</sup> Copyright 2012 Elsevier B.V. ....	3
Fig. 1.2 a) Various applications of TiO <sub>2</sub> photocatalyst. <sup>49</sup> Copyright 2012 Elsevier B.V.; b) The structural dimensionality of TiO <sub>2</sub> nanostructures. <sup>56</sup> Copyright 2015 The Royal Society of Chemistry. ....	4
Fig. 1.3 Schematic and the optical photo of the fiber-shaped dye-sensitized solar cells structure with the conformal TiO <sub>2</sub> film deposited with ALD. <sup>60</sup> Copyright 2015 Elsevier Ltd. ....	6
Fig. 1.4 a,b) Diffuse reflectance ultraviolet-visible spectra of rutile TiO <sub>2</sub> samples. c) Mott-Schottky plots of rutile TiO <sub>2</sub> samples. d) Valence Band XPS of rutile TiO <sub>2</sub> samples. e) Band energy diagram of reference rutile TiO <sub>2</sub> and sub-10 nm rutile TiO <sub>2</sub> . <sup>63</sup> Copyright 2015 Macmillan Publishers Ltd. ....	6
Fig. 1.5 a) Schematic illustrating the fabrication of P25 TiO <sub>2</sub> /Ag <sub>3</sub> PO <sub>4</sub> /GO composites b) The proposed mechanism for visible-light-driven photocatalytic degradation of RhB and inactivation of bacteria. <sup>65</sup> Copyright 2014 Elsevier B.V. ....	7
Fig. 1.6 a) TEM images and b) EDX mappings of hollow sphere TiO <sub>2</sub> hybrid architectures c) The <i>J-V</i> characteristics of the devices with optimized counter electrode measured under solar light illuminations. <sup>71</sup> Copyright 2014 Elsevier Ltd. ....	8
Fig. 1.7 a) Schematic illustration of the charge transfer and separation in the system under visible light irradiation. b) Band gap energies, conduction band and valence band position of WO <sub>3</sub> and CdS. <sup>75</sup> Copyright 2015 Wiley-VCH. ....	9
Fig. 1.8 a) Schematic diagram of the synthesis process. b) and c) simulated band structure and projected density of states of metallic WO <sub>2</sub> -carbon mesoporous NWs. d) Volcano plot of <i>i</i> <sub>0</sub> as a function of Gibbs free energy for WO <sub>2</sub> -carbon mesoporous NWs and typical reported electrocatalysts. <sup>76</sup> Copyright 2015 American Chemical Society. ....	10
Fig. 1.9 The transition metals and three chalcogen elements are building 40 different TMDs. <sup>4</sup> Copyright 2015 Royal Society of Chemistry. ....	11

Fig. 1.10 a) Schematic of the fabrication and b) Schematic diagram and photocatalytic activity of a single layer PtSe <sub>2</sub> film. <sup>86</sup> Copyright 2015 American Chemical Society. ....	12
Fig. 1.11 a) Schematic diagram of the formation mechanism and b) Cyclic performance of the 3D MoS <sub>2</sub> -graphene composite microsphere. <sup>20</sup> Copyright 2015 WILEY-VCH. ....	13
Fig. 1.12 a) SEM images of various Group V TMDs at a magnification of 10K. b) Histograms summarize of HER performance of various Group V TMDs. <sup>93</sup> Copyright 2016 The Royal Society of Chemistry.....	14
Fig. 1.13 a) Photographs, SEM images and XPS results of chemically exfoliated 1T MoS <sub>2</sub> electrodes. b) Ragone plot of the best volumetric power and volumetric energy densities reported from various materials. <sup>18</sup> Copyright 2015 Nature Publishing Group. ....	16
Fig. 1.14 Schematic photoexcitation in a solid followed by deexcitation events. <sup>97</sup> Copyright 2004 American Chemical Society. ....	17
Fig. 1.15 a) Photograph of unmodified white TiO <sub>2</sub> and disorder-engineered black TiO <sub>2</sub> . b) HRTEM image of modified TiO <sub>2</sub> c) Spectral absorbance of the white and black TiO <sub>2</sub> . d) Schematic illustration of the band position of disorder-engineered black TiO <sub>2</sub> and unmodified TiO <sub>2</sub> . <sup>114</sup> Copyright 2011 American Association for the Advancement of Science. ....	19
Fig. 1.16 SEM images of various TiO <sub>2</sub> -based hierarchical nanostructured photocatalysts with different building units (a) particles, <sup>126</sup> Copyright 2014 Elsevier B.V., (b) nanosheets, <sup>127</sup> Copyright 2015 Royal Society of Chemistry, (c) nanowires, <sup>127</sup> Copyright 2015 Royal Society of Chemistry, and (d) nanorods. <sup>128</sup> Copyright 2011 American Chemical Society. ....	20
Fig. 1.17 Relationship between band structures of semiconductors and redox potentials of water splitting. <sup>132</sup> Copyright 2009 Royal Society of Chemistry. ....	22
Fig. 1.18 a) The band diagram of WO <sub>3</sub> QDs. b) the relationship between the particle size and the bandgap energy. <sup>133</sup> Copyright 2016 Royal Society of Chemistry. ....	23

Fig. 1.19 Amounts of H <sub>2</sub> and CO production as a function of irradiation time for CdS@ZIF-8. <sup>136</sup> Copyright 2016 Tsinghua University Press and Springer-Verlag Berlin Heidelberg. ....	24
Fig. 1.20 Experimental and theoretical plots of the exchange current density for the HER over different transition metal surfaces plotted as a function of the calculated hydrogen chemisorption energy per atom and the simple kinetic model plotted as a function of the free energy for hydrogen adsorption ( $\Delta G_{H^*} = \Delta E_H + 0.24$ eV). <sup>6</sup> Copyright 2005 The Electrochemical Society. ....	24
Fig. 1.21 a) Semiconducting single-layered TMDs and b) Metallic single-layered TMDs basal planes. The plot of the hydrogen adsorption free energy, $\Delta G_H$ , as a function of the HX adsorption free energy, $\Delta G_{HX}$ (X=S or Se). <sup>7</sup> Copyright 2015 Elsevier B.V. ....	25
Fig. 1.22 a) Schematic diagrams of MoS <sub>2</sub> /RGO hybrid with corresponding Tafel plots recorded on glassy carbon electrodes. <sup>151</sup> Copyright 2011 American Chemical Society. b) SEM image of carbon cloth fibers modified by crumpled graphene and MoS <sub>x</sub> with HER performance. <sup>152</sup> Copyright 2014 WILEY-VCH. c) Schematic diagrams of the synthesis of N-doped graphene/MoS <sub>2</sub> nanohybrids by using aerosol processing method. <sup>158</sup> Copyright 2015 American Chemical Society. ....	27
Fig. 1.23 a) Schematic diagrams of the fabrication process and b) Optical, SEM images of WO <sub>3</sub> /WS <sub>2</sub> core/shell nanowires on a W foil with long cycling performance result. <sup>13</sup> Copyright 2016 American Chemical Society. ....	29
Fig. 1.24 Schematic depictions of CoS <sub>2</sub> NWs and MWs effectively releasing the H <sub>2</sub> bubbles and effective HER performance. <sup>216</sup> Copyright 2014 American Chemical Society. ....	30
Fig. 1.25 Cycling performance of the MoS <sub>2</sub> nanosheet at the current density of 100 mA h g <sup>-1</sup> . <sup>218</sup> Copyright 2017 WILEY-VCH. ....	32
Fig. 1.26 a) Schematic illustration of the procedure for the synthesis of lithium titanate/nitrogen and sulfur co-doped graphene quantum dots. b) The specific discharge capacities of as-prepared electrodes at different rates and the cyclic performance of as-prepared electrodes at 1C. <sup>12</sup> Copyright 2015 Elsevier Ltd. ....	33

Fig. 1.27 Capacities and Coulombic efficiencies of the MoS <sub>2</sub> electrode for PIBs. <sup>223</sup> Copyright 2017 Tsinghua University Press and Springer-Verlag Berlin Heidelberg.....	34
Fig. 2.1 Photographs of pristine TiO <sub>2</sub> (a) and doped TiO <sub>2</sub> samples, (b) TiO <sub>2</sub> -1, (c) TiO <sub>2</sub> -2, (d) TiO <sub>2</sub> -3 and (e) TiO <sub>2</sub> -4. ....	41
Fig. 2.2 (a) Representative XRD pattern and (b) Raman spectra of the pristine TiO <sub>2</sub> and as-synthesized TiO <sub>2</sub> .....	42
Fig. 2.3 SEM images of pristine TiO <sub>2</sub> (a) and as-obtained TiO <sub>2</sub> nanostructures: (b) TiO <sub>2</sub> -1, (c) TiO <sub>2</sub> -2, (d) TiO <sub>2</sub> -3 and (e) TiO <sub>2</sub> -4; (f) and (g) hierarchical structures TiO <sub>2</sub> -4. ....	44
Fig. 2.4 TEM micrographs of sample TiO <sub>2</sub> -4: (a) overview image of TiO <sub>2</sub> -4, HRTEM images of TiO <sub>2</sub> -4 nanoparticles (b) and nanotube (c). (d) SAED pattern of synthesized TiO <sub>2</sub> -4.....	46
Fig. 2.5 N <sub>2</sub> adsorption-desorption isotherms for pristine TiO <sub>2</sub> and as-obtained TiO <sub>2</sub> . ....	47
Fig. 2.6 X-ray photoelectron spectra (XPS) of (a) Ti2p and (b) O1s of pristine TiO <sub>2</sub> and TiO <sub>2</sub> -4; (c) B 1s of TiO <sub>2</sub> -4; (d) EPR spectra of the pristine TiO <sub>2</sub> and TiO <sub>2</sub> -4 at 100 K under N <sub>2</sub> atmosphere. ....	49
Fig. 2.7 (a) UV-visible diffuse reflectance spectra of pristine TiO <sub>2</sub> and TiO <sub>2</sub> -4. (b) Curve-fitting by using the Kubelka-Munk function method for the calculated absorbance against the photon energy for the pristine TiO <sub>2</sub> and TiO <sub>2</sub> -4. ....	50
Fig. 2.8 (a) Photocatalytic degradation rate of methylene blue vs. irradiation time using pristine TiO <sub>2</sub> and as-synthesized TiO <sub>2</sub> samples. (b) The evolution of photodegradation of methylene blue solution under visible-light irradiation. (O: Original methylene blue aqueous solution; D: Dark environment; 10~50: 10~50 minutes' visible light irradiation). The photocatalytic degradation rate of methylene blue vs. irradiation time using (c) recycled TiO <sub>2</sub> -4 and (d) recycled TiO <sub>2</sub> -2. ....	52
Fig. 3.1 SEM images of CoS <sub>2</sub> NWs on (a-c) carbon cloth and (d-f) graphite disc substrates.....	59

Fig. 3.2 SEM image and EDS elemental mappings of the CoS <sub>2</sub> NWs on graphite disc substrate. The cobalt and sulfur signals match well with each other and with the nanowire structure shown in the SEM image. The carbon signal results from the graphite substrate. ....	60
Fig. 3.3 Raman spectrum of the CoS <sub>2</sub> NWs on graphite disc substrate. The inset highlights the Raman spectrum in the range of 320-450 cm <sup>-1</sup> . ....	61
Fig. 3.4 Capacitive performance of the CoS <sub>2</sub> NWs on the carbon cloth substrate with an active material loading of 1.18 mg/cm <sup>2</sup> based on geometric area. (6 M KOH(aq) electrolyte.) (a) Cyclic voltammograms of the CoS <sub>2</sub> NWs on carbon cloth substrate at different scan rates from 10 to 100 mV/s. (b) Specific capacitance versus potential scan rate for the CoS <sub>2</sub> NWs on carbon cloth substrate. (c) Galvanostatic charge/discharge curves of the CoS <sub>2</sub> NWs on the carbon cloth substrate at different mass specific currents. (d) Specific capacitance versus discharge mass specific current for the CoS <sub>2</sub> NWs on the carbon cloth substrate. Mass and area-specific capacitances were calculated using the total mass of the CoS <sub>2</sub> NWs and geometric area of the carbon cloth substrate, respectively. ....	63
Fig. 3.5 CV curves at 0.01 V/s for CoS <sub>2</sub> NWs on (a) blank carbon cloth substrate and (b) blank graphite disc substrate. ....	64
Fig. 3.6 Capacitive performance of the CoS <sub>2</sub> NWs on the graphite disc substrate with an active material loading of 1.49 mg/cm <sup>2</sup> based on geometric area. (6 M KOH(aq) electrolyte.) (a) Cyclic voltammograms of the CoS <sub>2</sub> NWs on graphite disc substrate at different scan rates from 10 to 100 mV/s. (b) Specific capacitance versus potential scan rate for the CoS <sub>2</sub> NWs on graphite disc substrate. (c) Galvanostatic charge/discharge curves of the CoS <sub>2</sub> NWs on graphite disc substrate under different mass specific currents. (d) Specific capacitance versus discharge mass specific current for the CoS <sub>2</sub> NWs on graphite disc substrate. Mass and area-specific capacitances were calculated using the mass of CoS <sub>2</sub> NWs and geometric area of the graphite disc substrate, respectively. ....	66
Fig. 3.7 CV curves at 0.01 V/s for CoS <sub>2</sub> NWs on (a) blank carbon cloth substrate and (b) blank graphite disc substrate. ....	67
Fig. 3.8 Nyquist plots of the CoS <sub>2</sub> NWs (a) on carbon cloth and (b) graphite disc substrate. The inset spectra highlight the data at a high frequency. ....	68

Fig. 3.9 (a) Cycling stability of the CoS <sub>2</sub> NWs on both substrates tested at a mass-specific current of 5 A/g. (b) Ragone charts of the CoS <sub>2</sub> NWs on carbon cloth and graphite disc substrates.....	70
Fig. 4.1 Calibration of the reference electrode against the RHE. ....	74
Fig. 4.2 Experimental setup for fabricating the CGTH hybrid materials. Aerosol droplets containing GO and precursor ions were carried by Ar and passed through the heated tube furnace. GO was thermally reduced and precursor ions adsorbed on GO sheets were converted into WS <sub>2</sub> /WO <sub>3</sub> nanocrystals. ....	77
Fig. 4.3 Electron microscopy characterization of the CGTH. (A-B) SEM images of the as-produced CGTH with different magnifications. The CGTH has a 3D crumpled structure with filler materials. (C) TEM image of the CGTH confirms the rod-like shape of the encapsulated nanomaterial and indicates the internal structure. (D) SAED pattern of the CGTH shows the lattice parameters of the encapsulated nanomaterial. (E) HRTEM image shows two distinct lattice spacings of WS <sub>2</sub> and WO <sub>3</sub> . The nanorod contains WS <sub>2</sub> and WO <sub>3</sub> . (F) HAADF STEM imaging of nanorods. (G) Elemental mapping along the green arrow in (F). (H) Elemental distribution of C, O, S, and W in (F). ....	78
Fig. 4.4 (A) SEM image, (B-F) EDS elemental mappings of the CGTH and (G) EDAX spectrum of the CGTH with copper foil background. ....	80
Fig 4.5 SEM images of the control groups. (A) The suspension was aerosolized without GO (C1). (B) The suspension containing GO and precursor was dried and annealed without the aerosolization step (C2). (C) GO was nebulized with (NH <sub>4</sub> ) <sub>6</sub> H <sub>2</sub> W <sub>12</sub> O <sub>4</sub> to fabricate the crumpled graphene/WO <sub>3</sub> hybrids (C3). ....	81
Fig. 4.6 (A) Representative XRD pattern and (B) Raman spectra of the CGTH. The inset highlights the Raman spectrum in the range of 320-450 cm <sup>-1</sup> . ....	82
Fig. 4.7 Representative XRD pattern of the (A) C1, (B) C2, (C) C3. ....	83
Fig. 4.8 (A) XPS spectrum of CGTH; (B) N <sub>2</sub> adsorption-desorption isotherms and BJH pore size distribution for CGTH. ....	84

Fig. 4.9 XPS spectrum of (A) W4f, (B) S2p and (C) O1s of CGTH. The peaks in the O1s region located at 530.2, 532.1, 533.2 eV are assigned to lattice oxygen, oxygen vacancy and chemisorbed H <sub>2</sub> O, respectively.....	84
Fig. 4.10 Electrochemical measurements for the CGTH and control groups in H <sub>2</sub> SO <sub>4</sub> (0.5 M). (A) Polarization curves obtained with several catalysts as indicated and (B) corresponding Tafel plots recorded on glassy carbon electrodes. The current density is normalized to the area (mA/cm <sup>2</sup> ). .....	87
Fig. 4.11 (A) Nyquist plots of the CGTH, control group C1, C2 and C3 with the imaginary part versus the real part of the impedance. The data were collected under around HER overpotential ~500 mV. (B) The I-t test results of the CGTH kept at -120 mV versus RHE in an Ar-saturated 0.5 M H <sub>2</sub> SO <sub>4</sub> solution. ....	88
Fig. 4.12 Raman spectra of CGTH before and after 15 hours' test. ....	89
Fig. 4.13 The differences in current density ( $\Delta j = j_a - j_c$ ) at the overpotential of 0.55 V (vs. RHE) are plotted against scan rate and linearly fitted to estimate $C_{dl}$ . ....	90
Fig. 5.1 a, b) SEM images c, d) TEM images and e) SAED pattern of synthesized M-MoS <sub>2</sub> ; f, g) TEM images of synthesized MQDs and h) TEM image of hard template SBA-15.....	99
Fig. 5.2 a) Representative XRD pattern and b) Raman spectra of the M-MoS <sub>2</sub> and MQDs. c) N <sub>2</sub> adsorption-desorption isotherms d) Pore size distribution of M-MoS <sub>2</sub> . e) N <sub>2</sub> adsorption-desorption isotherms and f) Pore size distribution of SBA-15. ....	102
Fig. 5.3 a) AFM thickness measurement with height distribution for MQDs and b) excitation and emission PL spectra of MQDs. Inset images show the photographs of MQDs in room light (left) and under a UV light source (right) emitting 365 nm light. ....	104
Fig. 5.4 LIBs cyclic performance and Coulombic efficiency of a, b) M-MoS <sub>2</sub> -G electrodes. c, d) MQDs-G electrodes. e) A comparison of long-term cyclic performance between the two electrodes. ....	106
Fig. 5.5 Electrochemical performance of MQDs electrodes for PIBs. a, b) cyclic performance and Coulombic efficiency of MQDs electrodes at 20 mA g <sup>-1</sup> . c) rate capability of MQDs electrodes. ....	108

Fig. 6.1 The schematic of the photocatalytic reaction system. ....	111
Fig. 6.2 a-b) SEM images, c-d) EDS elemental mappings of the MZ with a copper foil background. ....	113
Fig. 6.3 a) Representative XRD patterns of the as-prepared samples; b) N <sub>2</sub> adsorption-desorption isotherms and c) Pore size distribution of MZ and ZIF-8; XPS spectrum of d) N1s, e) O1s and f) Zn 2p of MZ. ....	115
Fig. 6.4 UV-vis absorption spectra and Tauc's plot (inset) for band gap energy determination of (a) ZIF-8, (b) EM, and (c) MZ; d) Schematic illustration of the energy band structure of the as-prepared samples; e) Photocatalytic hydrogen production rate collected for MZ. ....	117

## LIST OF TABLES

Table 2.1 Surface properties of pristine TiO <sub>2</sub> and as-synthesized TiO <sub>2</sub> .....	47
Table 4.1 The atomic percentage of elements in the CGTH before and after the long-term cycling performance .....	89
Table 4.2 Comparison of HER catalytic activity for MoS <sub>2</sub> /WS <sub>2</sub> -based electrocatalysts. ....	92
Table 5.1 Surface properties of M-MoS <sub>2</sub> , SBA-15, and the intermediate products.....	103
Table 6.1 Surface properties of ZIF-8 and as-synthesized MZ.....	116

## LIST OF ABBREVIATIONS

aq.	aqueous solution
BET	Brunauer-Emmett-Teller
BJH	Barret-Joyner-Halenda
$C_a$	area specific capacitance
$C_{cv}$	specific capacitance from CV test
cf.	compare
$C_g$	specific capacitance from galvanostatic charge/discharge test
CGTH	crumpled rGO/WO <sub>3</sub> /WS <sub>2</sub> ternary nanohybrids
CHCH	cobalt hydroxide carbonate hydrate
CNTs	carbon nanotubes
CoS <sub>2</sub>	cobalt pyrite
CoS <sub>x</sub>	cobalt sulfides
CV	cyclic voltammetry
CVD	chemical vapor deposition
E	energy density
EDX (EDS)	energy-dispersive X-ray spectroscopy
EDLCs	electric double-layer capacitors
EIS	electrochemical impedance spectroscopy
EPR	electron paramagnetic resonance
ESR	equivalent series resistance
GO	graphene oxide

HER	hydrogen evolution reaction
HRTEM	high-resolution transmission electron microscopy
LIBs	lithium-ion batteries
PIBs	potassium-ion batteries
LSV	linear sweep voltammetry
MB	methylene blue
MOCVD	metal organic chemical vapor deposition
MOF	Metal-organic frameworks
NaBH <sub>4</sub>	sodium borohydride
(NH <sub>4</sub> ) <sub>2</sub> WS <sub>4</sub>	ammonium tetrathiotungstate
NWs	nanowires
NSs	nanosheets
P	power density
PVD	physical vapor deposition
R <sub>ct</sub>	charge transfer resistance
RDS	rate determining step
rGO	reduced graphene oxide
RHE	reversible hydrogen electrode
R <sub>s</sub>	series resistance
SAED	selected area electron diffraction
SEM	scanning electron microscopy
TEM	transmission electron microscopy
TiO <sub>2</sub>	titanium dioxide

TMDs	transition metal dichalcogenides
TMOs	transition metal oxides
WO <sub>3</sub>	tungsten trioxide
WS <sub>2</sub>	tungsten disulfide
XPS	X-ray photoelectron spectroscopy
XRD	X-ray powder diffraction
ZIF-8	Zeolitic Imidazolate Framework-8

## ACKNOWLEDGMENTS

I would like to first acknowledge my advisor, Prof. Junhong Chen, for his generous acceptance for me to join his research group starting my Ph.D. study at University of Wisconsin-Milwaukee (UWM) since January 2013. Dr. Chen was never lacking in creative ideas or suggestions, but more importantly, he graciously granted me the freedom to work on the research that I found most intriguing. Over the last five years, I've grown as a scientist in ways that I never anticipated. Furthermore, I would like to acknowledge the financial support from the U.S. Department of Energy (DE-EE0003208), U.S. National Science Foundation and the University of Wisconsin-Milwaukee Research Growth Initiative program. I must also acknowledge the many teachers and mentors I've had along my journey: Dr. Zhenhai Wen and Dr. Suqin Ci for the initial learning of materials synthesis, characterization and measurement; Dr. Shun Mao and Dr. Shumao Cui for the assistance of materials characterization and deeper learning of potential applications; Dr. Haihui Pu for better theoretical understanding of the materials and structures; Dr. Yantao Chen for preparing the crumpled tungsten oxide and tungsten sulfide; Dr. H. A. Owen for technical support with the SEM analyses; and Dr. S. E. Hardcastle for technical support with the XRD, Raman characterizations and XPS analyses. The X-band Electron Paramagnetic Resonance (EPR) experiment was supported by National Biomedical Electron Paramagnetic Resonance Center of Medical College of Wisconsin. Finally, I must credit my family for creating a warm, loving environment that promotes achievement. My parents, my wife, and my lovely daughter make me a better man.

# CHAPTER 1 INTRODUCTION AND LITERATURE REVIEW

## 1.1 Introduction

The clean energy supply is one of the major challenges for our society due to global population growth and potential climate change due to consumption of fossil fuels.<sup>1-4</sup> Hydrogen evolution production from water splitting is quite attractive because hydrogen is often considered as a clean fuel, an alternative to fossil fuels.<sup>5-7</sup> However, the high cost and scarcity of platinum (Pt) required for applications such as water splitting have impeded the large-scale commercialization of many green technologies.<sup>8</sup> Therefore, exploration of novel materials with a low cost to support green technologies is a major research trend. For example, transition metal oxides are the largest group of materials for photocatalytic applications such as environmental remediation and solar fuel generation.<sup>9</sup> However, most of these materials can only absorb limited visible light to promote photocatalytic reactions due to their relatively large band gap.<sup>10</sup> New strategies are needed to produce a smaller band gap of semiconductor materials in order to improve the efficiency of visible light absorbance.<sup>10</sup>

Storing electrical energy at scale is another urgent scientific challenge in transitioning from fossil fuels to clean and sustainable energy.<sup>11-13</sup> Electrochemical reactions could provide and store electrical energy efficiently via chemical bonds.<sup>14</sup> For example, hydrogen and oxygen are products from electrochemically splitting water, through which the energy can be stored in these gases and their recombination can provide clean electrical energy with water as the only by-product.<sup>15</sup> In addition, energy can also be stored by using metals such as lithium or sodium as the energy carrier.<sup>16</sup> The reactions involve the formation and reduction of metal oxides for the energy storage and conversion processes.<sup>17</sup> Besides TMOs, transition metal dichalcogenides (TMDs) have

attracted significant attention due to their exciting physical and chemical properties that make them suitable for potential applications in a variety of areas such as catalysis, electronics, photonics, energy storage and sensing.<sup>18-24</sup> Furthermore, two-dimensional layered TMDs exhibit unique electrical and optical properties that evolve from the quantum confinement effects, arising from the transition of an indirect bandgap to a direct bandgap when bulk materials are scaled down to monolayers.<sup>25,26</sup> Usually a strong photoluminescence (PL) and large exciton binding energy are accompanied with the bandgap adjustment in TMDs, making them highly attractive for optoelectronic and capacitive energy storage applications.<sup>27,28</sup> In this dissertation, various novel TMOs and TMDs have been explored for energy and environmental applications.

## **1.2 Literature review**

### **1.2.1 Literature review on transition metal oxides**

Transition metal oxides (TMOs) have been widely studied over the last few decades and TMOs possess great potential in magnetic, electronic, and optical applications. TMOs have been integrated into a variety of devices to achieve unprecedented excellent performance, such as improved gas sensing, solar cells, supercapacitors and photocatalysis.<sup>9,29-33</sup> Because the d-shells of positive metallic ions may not be completely filled by electrons in TMOs, TMOs exhibit various unique properties, which involve reactive electronic transitions, high dielectric constants, wide bandgaps, good electrical characteristics and so on.<sup>34-38</sup> Meanwhile, TMOs possess various states, such as ferromagnetic state and semiconductive state.<sup>39,40</sup> Hence, TMOs are considered to be one of the fascinating functional materials.

It is widely known that there are many factors which can employ significant influence on the performance of functional materials, including the size, specific surface area, pore structure, crystalline phase, and also the exposed surface facets. Thus, the development of performance improvements by adjusting these factors remains the focus of new-fashioned research. It is worth noting that structural dimensionality is also a major factor that can affect the performance and also has a significant impact on the properties of TMOs. The construction of nanostructures or microstructures for TMOs with interesting morphologies and properties has attracted considerable attention recently. In general, nanostructures can be categorized into four different morphologies: zero-dimensional (0D), one dimensional (1D), two-dimensional (2D) and three-dimensional (3D) nanostructures as shown in Fig. 1.1.<sup>41-43</sup> The electronic structures of the TMOs can be tuned with the size and dimension modification, which results in a variety of changes in both chemical and physical properties.<sup>44</sup> Choosing TMO materials with the appropriate dimensionalities enables us to take full advantage of the unique properties offered by the materials. Heretofore, the control of the size, shape, and structure of TMOs has been achieved by various synthesis methods, such as hydrothermal, template-free method, chemical vapor deposition (CVD), physical vapor deposition (PVD), metal organic chemical vapor deposition (MOCVD), etc.<sup>1,45-48</sup>

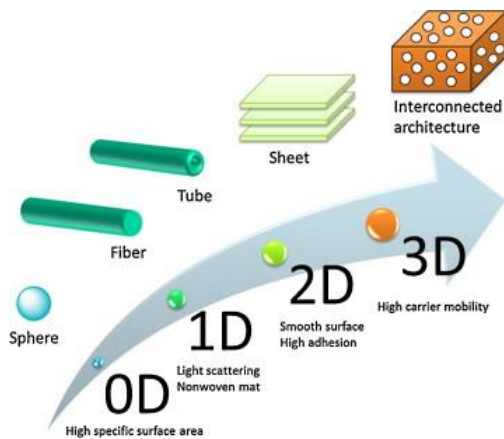


Fig. 1.1 The illustration of the structural dimensionality of nanomaterials with properties.<sup>49</sup>

Among various semiconducting catalysts,  $\text{TiO}_2$ ,  $\text{WO}_3$ , and  $\text{CeO}_2$  as inexpensive and non-photocorrosive TMOs are excellent candidates for photocatalytic degradation and photochemical water splitting.<sup>50</sup>  $\text{TiO}_2$  is one of the most investigated TMOs in materials science considering a variety of applications and thousands of papers concerning it have been published over the last decade (Fig. 1.2a). Four commonly known polymorphs of  $\text{TiO}_2$  could be found in nature: anatase (tetragonal), brookite (orthorhombic), rutile (tetragonal) and  $\text{TiO}_2$  (B) (monoclinic).<sup>51</sup> Fig. 1.2b shows that  $\text{TiO}_2$  could be engineered in different dimensions and morphologies, from 0D  $\text{TiO}_2$  nanoparticles to 1D  $\text{TiO}_2$  nanorods, nanowires and nanotubes, 2D nanosheets and 3D hierarchical structures.<sup>52-55</sup>

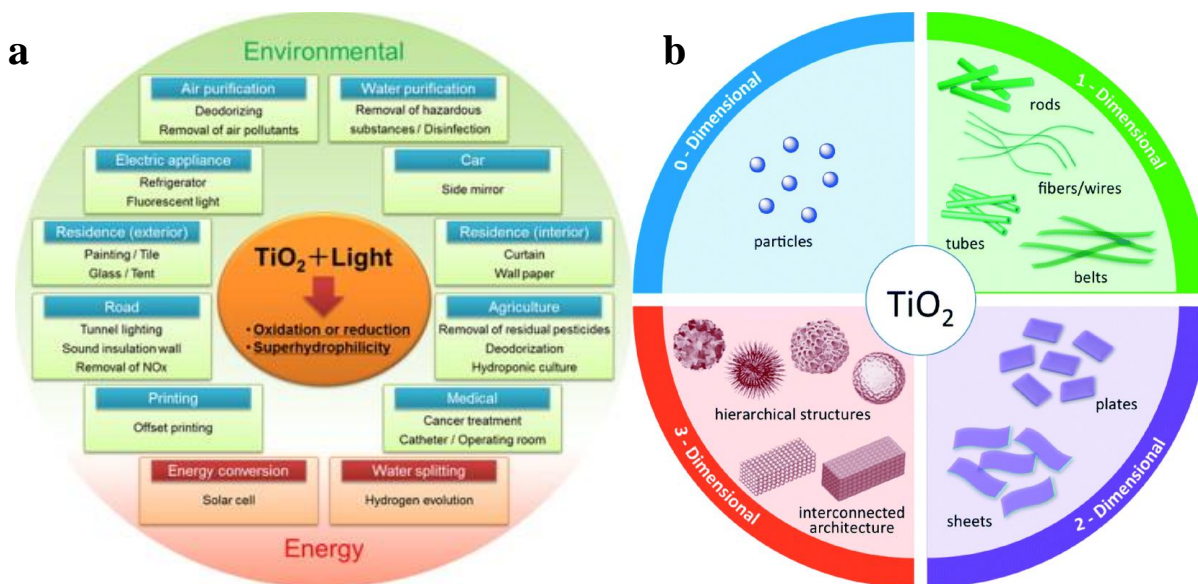


Fig. 1.2 a) Various applications of  $\text{TiO}_2$  photocatalyst.<sup>49</sup> Copyright 2012 Elsevier B.V.; b) The structural dimensionality of  $\text{TiO}_2$  nanostructures.<sup>56</sup> Copyright 2015 The Royal Society of Chemistry.

TiO<sub>2</sub> was applied in many devices exploiting solar energy due to the strong oxidizing power of photogenerated holes, low cost, and good stability.<sup>57</sup> The dye-sensitized solar cells based on TiO<sub>2</sub> can convert sunlight into electricity more efficiently.<sup>58,59</sup> Song *et al.* fabricated a TiO<sub>2</sub> thin film deposited on Ti wire with atomic layer deposition (ALD) introduced in the photoanodes which improves the performance of fiber-shaped dye-sensitized solar cells (Fig. 1.3).<sup>60</sup> It is because of the ALD treatment that enhanced the interconnection between TiO<sub>2</sub> particles and the substrate and led to the improved photocurrent. Hydrogen, which may be the fuel of the future, can be produced by splitting water under the help of photogenerated electron-hole pairs of TiO<sub>2</sub>.<sup>61,62</sup> Li *et al.* designed rutile TiO<sub>2</sub> nanoparticles below 10 nm with increased surface/sub-surface defects by a scalable hydrolysis route to achieve a state-of-the-art hydrogen evolution rate of 932  $\mu\text{mol h}^{-1}\text{g}^{-1}$  under visible light (>400 nm) and 1954  $\mu\text{mol h}^{-1}\text{g}^{-1}$  under simulated solar light.<sup>63</sup> The existence of abundant defects and Ti<sup>3+</sup> could help shift the top of the valence band of rutile titanium dioxide upwards for band-gap narrowing and also promote charge-carrier separation as shown in Fig 1.4. In addition, TiO<sub>2</sub>, as a photocatalyst, can degrade organic pollutants into environmentally friendly species, such as carbon dioxide and water.<sup>64</sup> By using electrostatically-driven assembly and ion-exchange method, Yang *et al.* fabricated P25 TiO<sub>2</sub>/silver orthophosphate/graphene oxide ternary composite materials which revealed a well-defined heterostructure where microsized Ag<sub>3</sub>PO<sub>4</sub> particles and TiO<sub>2</sub> nanoparticles decorated on high-surface-area graphene oxide (GO) nanosheets as shown in Fig. 1.5a.<sup>65</sup> The resulting composites showed improved solar light harvesting, enhanced solar photocatalytic degradation of RhB, and excellent bactericidal performance (Fig. 1.5b) because of the recombination of electron-hole pairs could be effectively suppressed by the movements of nanoparticles.

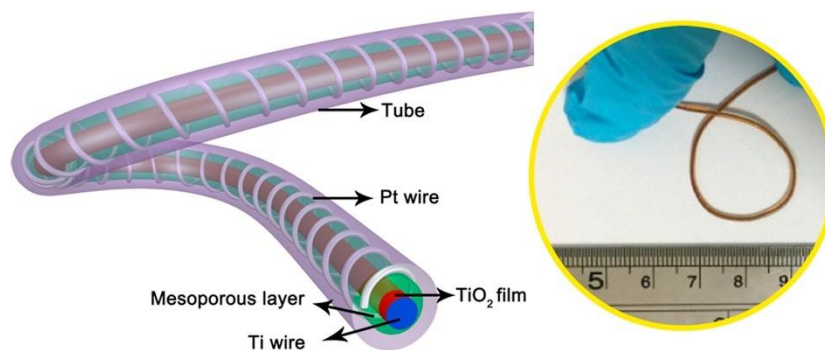


Fig. 1.3 Schematic and the optical photo of the fiber-shaped dye-sensitized solar cells structure with the conformal  $\text{TiO}_2$  film deposited with ALD.<sup>60</sup> Copyright 2015 Elsevier Ltd.

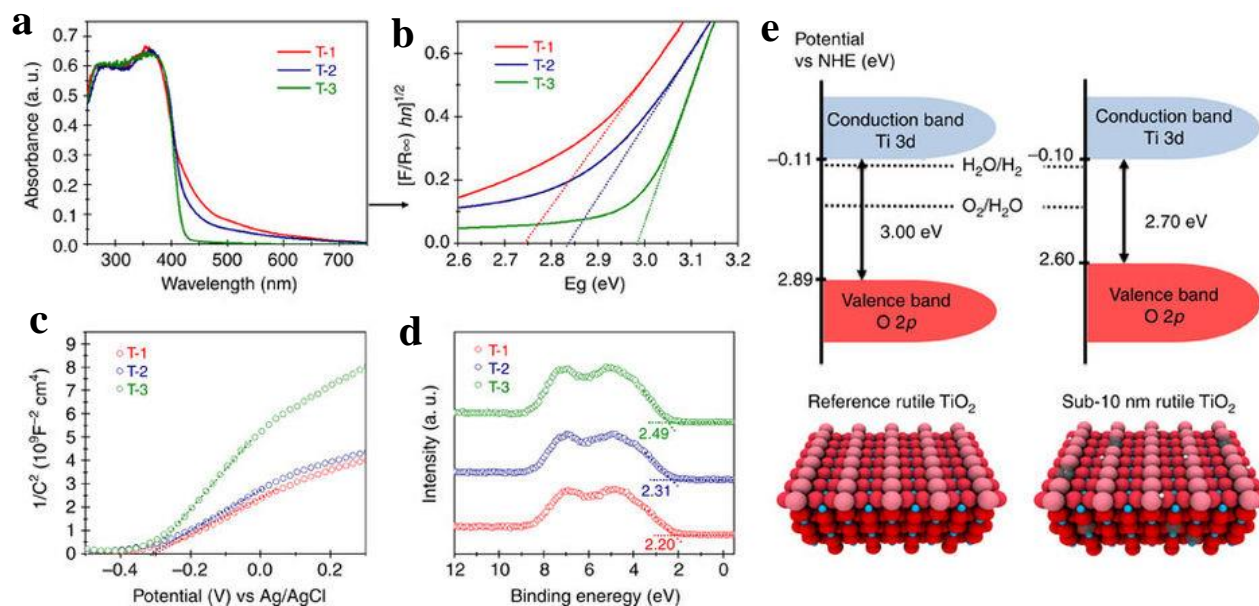


Fig. 1.4 a,b) Diffuse reflectance ultraviolet-visible spectra of rutile  $\text{TiO}_2$  samples. c) Mott-Schottky plots of rutile  $\text{TiO}_2$  samples. d) Valence Band XPS of rutile  $\text{TiO}_2$  samples. e) Band energy diagram of reference rutile  $\text{TiO}_2$  and sub-10 nm rutile  $\text{TiO}_2$ .<sup>63</sup> Copyright 2015 Macmillan Publishers Ltd.

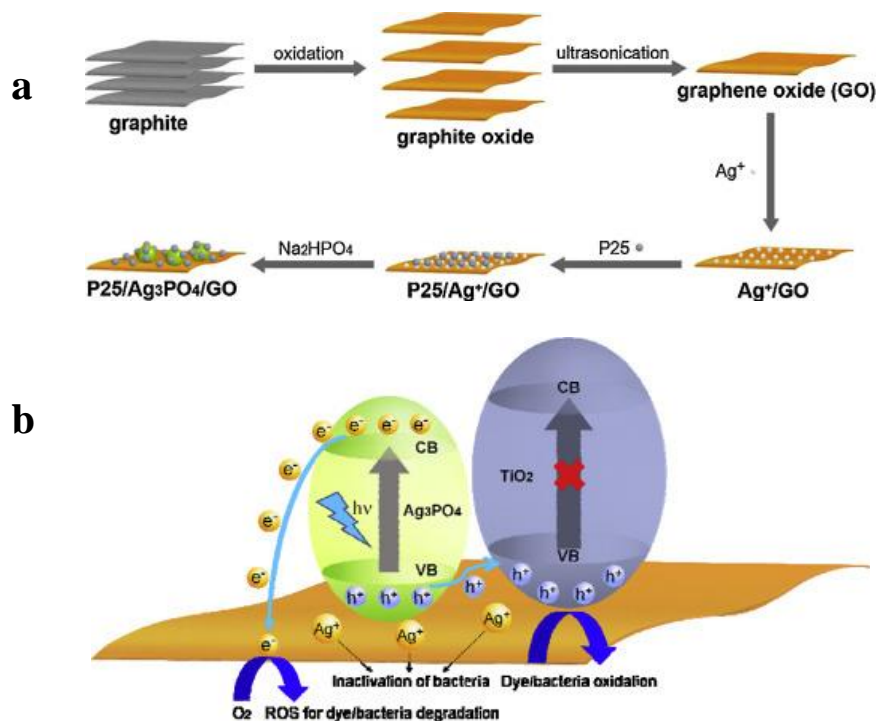


Fig. 1.5 a) Schematic illustrating the fabrication of P25  $\text{TiO}_2/\text{Ag}_3\text{PO}_4/\text{GO}$  composites b) The proposed mechanism for visible-light-driven photocatalytic degradation of RhB and inactivation of bacteria.<sup>65</sup> Copyright 2014 Elsevier B.V.

Many approaches have been applied to synthesize  $\text{TiO}_2$  and they are mainly classified as template method, electrochemical synthesis, and hydrothermal approach.<sup>66-68</sup> It is well known that nanostructures with specific exposed facets and hierarchical structures usually exhibit unique physical and chemical properties. Recently,  $\text{TiO}_2$  hierarchical structures with interesting morphologies and a high specific surface area have been synthesized by multiple methods which could be beneficial for enhancing the utilization efficiency of light.<sup>69,70</sup> Xu *et al.* developed a 3D hierarchically branched hollow sphere NWs hybrid  $\text{TiO}_2$  photoanode (Fig. 1.6a) with a considerably high specific surface area and ample porosity for efficient electrolyte infiltration, resulting in an improved light utilization efficiency and enhanced short-circuit photocurrent.<sup>71</sup> The

resulting counter electrode yields a power conversion efficiency as high as 6.01% (Fig. 1.6b) under one sun illumination (AM 1.5 G,  $100 \text{ mW cm}^{-2}$ ), which shows the talent for promising  $\text{TiO}_2$  hybrid quantum dot-sensitized solar cells (QDSSCs).

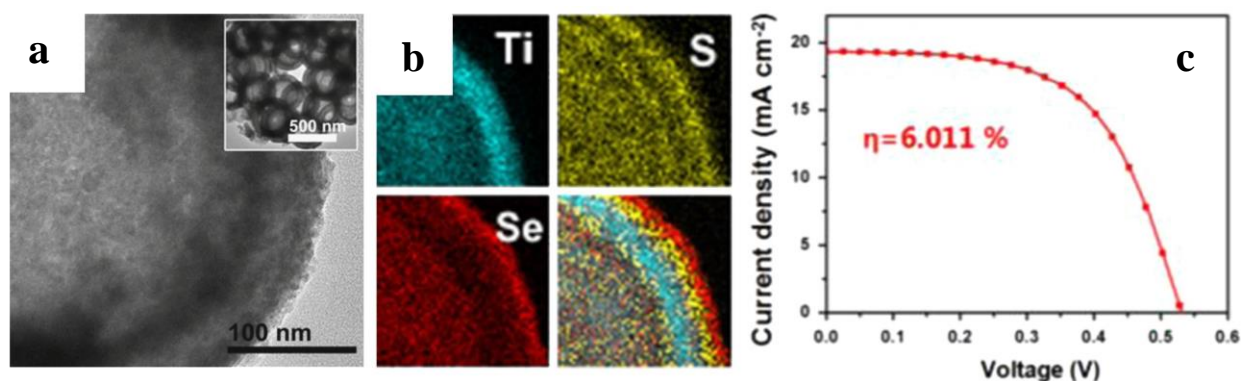


Fig. 1.6 a) TEM images and b) EDX mappings of hollow sphere  $\text{TiO}_2$  hybrid architectures c) The  $J$ - $V$  characteristics of the devices with optimized counter electrode measured under solar light illuminations.<sup>71</sup> Copyright 2014 Elsevier Ltd.

Tungsten oxides ( $\text{WO}_x$ ,  $2 \leq x \leq 3$ ) have also received considerable attention due to their earth-abundance, highly tunable composition, high chemical stability at appropriate pH value, and excellent electrical conductivity in applications such as photocatalysis, electrocatalysis, gas sensors, anode materials of Li-ion batteries, supercapacitors and so on.<sup>29,72-74</sup> Jin *et al.* fabricated CdS- $\text{WO}_3$  Z-scheme heterostructure photocatalysts which introduced CdS nanoparticles with small particle sizes covering the surface of  $\text{WO}_3$  hollow spheres by using a precipitation method.<sup>75</sup> The heterostructures show a higher photocatalytic  $\text{CO}_2$  reduction efficiency under visible light irradiation than single-phase photocatalysts due to the formation of a CdS- $\text{WO}_3$  Z-scheme system and an efficient space separation of photo-induced electron-hole pairs. In the proposed system as shown in Fig. 1.7a, holes spread to the surface of  $\text{WO}_3$  and electrons shift to the surface of CdS.

Electrons on the surface of CdS can promote photocatalytic CO<sub>2</sub> reduction to form CH<sub>4</sub>. In order to perform a highly effective photocatalytic reduction of CO<sub>2</sub>, the conduction band edge position of a photocatalyst should be more negative than the reduction potential of CH<sub>4</sub>/CO<sub>2</sub> and the valence band edge position should be more positive than the oxidation potential of O<sub>2</sub>/H<sub>2</sub>O as shown in Fig. 1.7b.

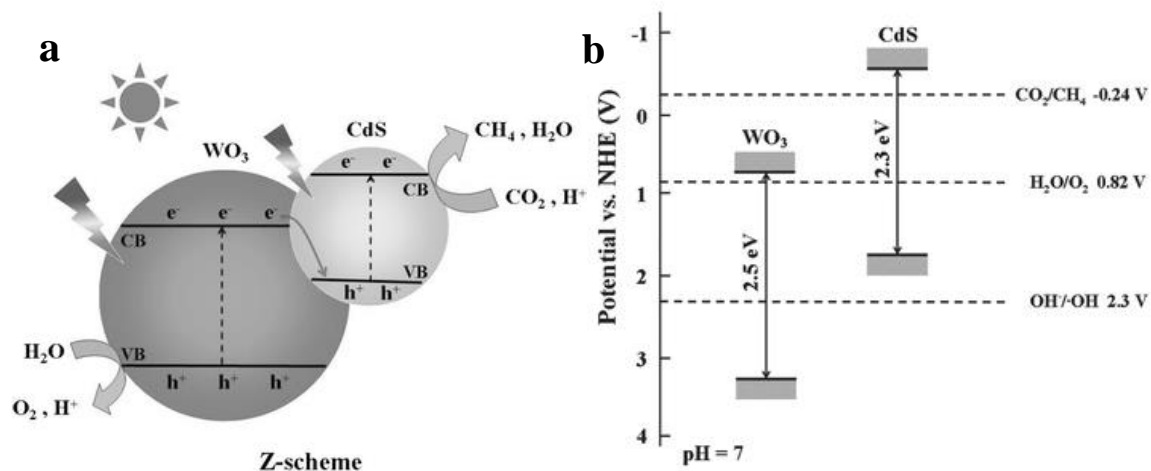


Fig. 1.7 a) Schematic illustration of the charge transfer and separation in the system under visible light irradiation. b) Band gap energies, conduction band and valence band position of WO<sub>3</sub> and CdS.<sup>75</sup> Copyright 2015 Wiley-VCH.

Many experimental and theoretical results also suggest metallic WO<sub>3</sub> could be promising candidates for energy storage and conversion applications such as effective electrocatalysts for hydrogen generation. Shang *et al.* synthesized less toxic metallic WO<sub>2</sub>-carbon mesoporous NWs with a high concentration of oxygen vacancies by using calcination of WO<sub>3</sub>-ethylenediamine hybrid precursors (Fig. 1.8a).<sup>76</sup> The as-prepared hybrids exhibit excellent performance for H<sub>2</sub> generation with an onset overpotential of only 35 mV, a Tafel slope of 46 mV/dec, and the stability of more than 10 hours. By applying density functional theory (DFT) to calculate the position of valence and conduction bands from the band structure and the projected density of states (PDOS),

the conduction band of as-prepared hybrids is crossed by the Fermi level, making them metallic and suggesting an enhanced electron mobility as shown in Fig. 1.8b. In addition, through the calculation of Gibbs free energy for HER catalysts, if the value is too large, it will be hard to adsorb  $H^*$ ; while if the value is too small, the adsorbed  $H^*$  will be difficult to desorb to generate  $H_2$ , instead of occupying the active sites and poisoning the HER process. Based on the calculation, the value of resulting materials is 0.22 eV (Fig. 1.8.d) which is close to Pt (0.09 eV). Therefore, it deserves to be called a strong theoretical proof and a direct explanation for the superior HER performance.

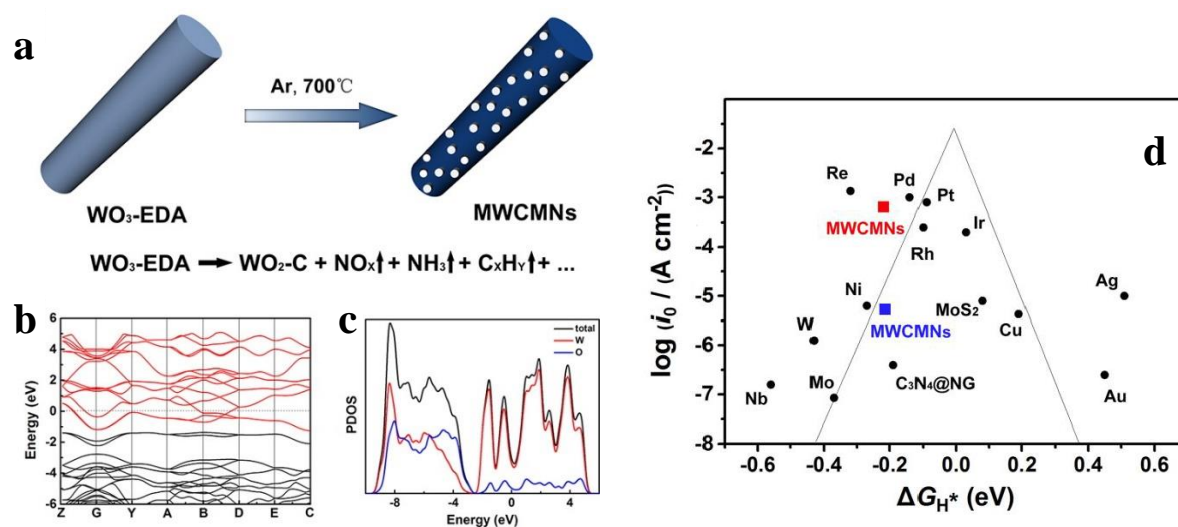


Fig. 1.8 a) Schematic diagram of the synthesis process. b) and c) simulated band structure and projected density of states of metallic  $WO_2$ -carbon mesoporous NWs. d) Volcano plot of  $i_0$  as a function of Gibbs free energy for  $WO_2$ -carbon mesoporous NWs and typical reported electrocatalysts.<sup>76</sup> Copyright 2015 American Chemical Society.

## 1.2.2 Literature review on transition metal dichalcogenides

TMD semiconductors have attracted significant attention due to their versatile and unique electrical, optical, chemical, and mechanical properties.<sup>77</sup> Among these versatile properties, TMD semiconductors provide sizable bandgaps, relatively high carrier mobility, and a high on/off current ratio in the transistor.<sup>78,79</sup> For instance, MoS<sub>2</sub>, MoSe<sub>2</sub>, WS<sub>2</sub> and WSe<sub>2</sub> exhibit tunable bandgaps that can undergo a transition from an indirect band gap in bulk crystals to a direct band gap in monolayer nanosheets.<sup>21,80</sup> These materials provide a distinct opportunity to develop high quality and atomically sharp heterostructures because of the nature of weak van der Waals interlayer interactions.<sup>19,81</sup> The variable electronic properties of TMDs supply a platform for the design of novel electronic and optoelectronic devices.<sup>24,28</sup> TMDs represent a large family of materials with the formula MX<sub>2</sub>, where M is a transition metal element from group IV to group VI (Ti, Zr, V, Nb, Mo, W, etc.) and X is a chalcogen atom (S, Se, etc.).<sup>21,82</sup> As shown in Fig. 1.9, the transition metals and three chalcogen elements possess the combinations of approximately 40 different TMDs.<sup>83</sup>

MX <sub>2</sub> M = Transition metal X = Chalcogen																	
H																	He
Li	Be											B	C	N	O	F	Ne
Na	Mg	3	4	5	6	7	8	9	10	11	12	Al	Si	P	S	Cl	Ar
K	Ca	Sc	Ti	V	Cr	Mn	Fe	Co	Ni	Cu	Zn	Ga	Ge	As	Se	Br	Kr
Rb	Sr	Y	Zr	Nb	Mo	Tc	Ru	Rh	Pd	Ag	Cd	In	Sn	Sb	Te	I	Xe
Cs	Ba	La-Lu	Hf	Ta	W	Re	Os	Ir	Pt	Au	Hg	Tl	Pb	Bi	Po	At	Rn
Fr	Ra	Ac-Lr	Rf	Db	Sg	Bh	Hs	Mt	Ds	Rg	Cn	Uut	Fl	Uup	Lv	Uus	Uuo

Fig. 1.9 The transition metals and three chalcogen elements are building 40 different TMDs.<sup>4</sup>

Copyright 2015 Royal Society of Chemistry.

As a freshly emerging class of nanomaterials, 2D TMDs own a layered structure and large surface areas and exhibit unique electrical and optical properties that evolve from the quantum confinement and surface effects that arise during the transition of an indirect bandgap to a direct bandgap when bulk materials are scaled down to monolayers.<sup>3,25,26</sup> This tunable bandgap in TMDs is accompanied by a strong photoluminescence (PL) and large exciton binding energy, which possesses great potential for applications in catalysis, sensing, supercapacitors, optics, and energy.<sup>2,84,85</sup> Wang *et al.* reported a monolayer platinum diselenide (PtSe<sub>2</sub>) with epitaxial growth of single-crystal structure as a new member of the TMDs family by applying selenization of a Pt (111) substrate (Fig. 1.10a).<sup>86</sup> The as-prepared materials show promise for application in photoelectronic and photocatalysis based on first-principle theoretic calculations and results from photodegradation experiments. Fig. 1.10b shows the visible light photodegradation portion of methylene blue (MB) molecules retained 38% after irradiation for 24 min which is four times faster than the use of PtSe<sub>2</sub> nanocrystals.

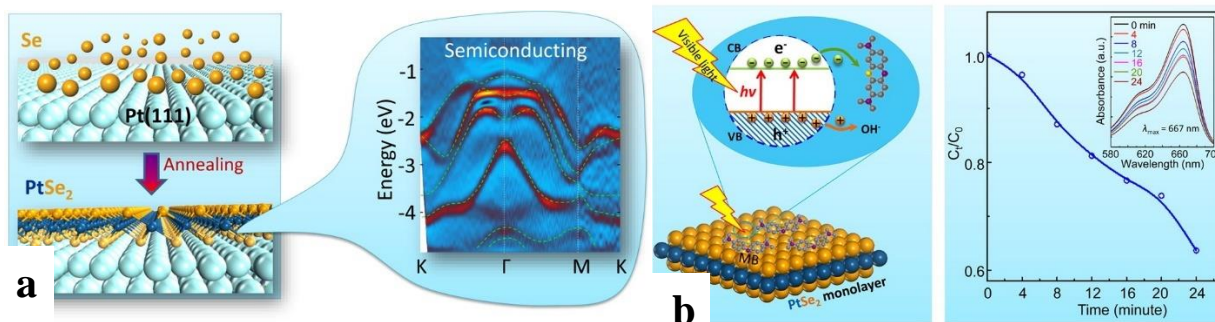


Fig. 1.10 a) Schematic of the fabrication and b) Schematic diagram and photocatalytic activity of a single layer PtSe<sub>2</sub> film.<sup>86</sup> Copyright 2015 American Chemical Society.

Up to now, various strategies have been explored for the preparation of single layer or few-layer TMD nanosheets, including mechanical peeling, chemical vapor deposition, and liquid-phase

exfoliation, chemical or electrochemical exfoliation.<sup>22,87-89</sup> With the different combination of elemental compositions, the electronic properties of TMDs can range from insulating (e.g., BN, HfS<sub>2</sub>), semiconducting (e.g., MoS<sub>2</sub>, WS<sub>2</sub>), to semi-metals (e.g., VS<sub>2</sub>, TiS<sub>2</sub>), superconductors (e.g., TaSe<sub>2</sub>, NbSe<sub>2</sub>), magnetic (e.g., CrSe<sub>2</sub>) and thermoelectric (e.g., Bi<sub>2</sub>Te<sub>3</sub>), which makes them ideal for electrochemical energy storage applications.<sup>21,82,90-92</sup> Choi *et al.* prepared an anode material with superior Na<sup>+</sup> storage properties through 3D graphene nanospheres coated with MoS<sub>2</sub> composite in spray pyrolysis process.<sup>20</sup> The Coulombic efficiency was 99.98% during the 600 cycles which may due to synergy effect of lack of stacking of the MoS<sub>2</sub> layers and the porous structure of graphene microspheres.

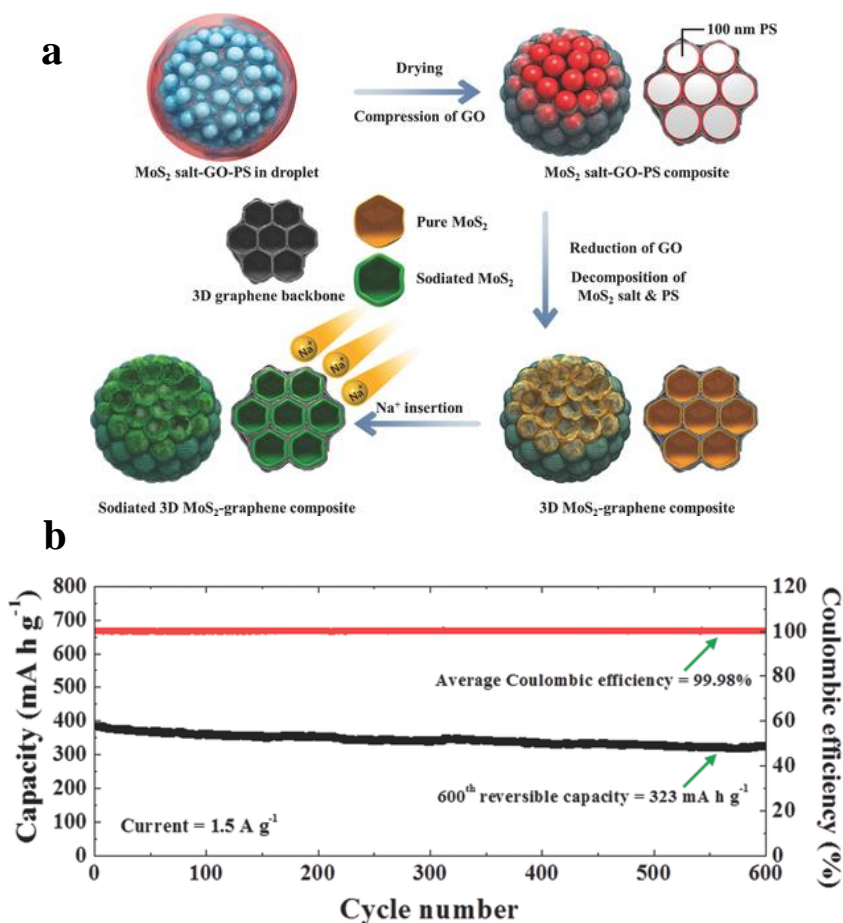


Fig. 1.11 a) Schematic diagram of the formation mechanism and b) Cyclic performance of the 3D MoS<sub>2</sub>-graphene composite microsphere.<sup>20</sup> Copyright 2015 WILEY-VCH.

In recent years, extensive studies have been focused on Group VI (Mo, W) semiconducting TMDs rather than Group V (V, Nb, Ta) metallic TMDs. From the previous calculation of Gibbs free energy of the adsorbed hydrogen, the Group V TMDs especially VS<sub>2</sub> present intriguing results. Chia *et al.* fabricated the entire set of Group V TMDs in the bulk form such as VS<sub>2</sub>, VSe<sub>2</sub>, VTe<sub>2</sub>, NbS<sub>2</sub>, NbSe<sub>2</sub>, NbTe<sub>2</sub>, TaS<sub>2</sub>, TaSe<sub>2</sub> and TaTe<sub>2</sub> (Fig. 1.12a) by using an evacuated oxygen/hydrogen welding method.<sup>93</sup> The authors discovered the TaS<sub>2</sub> possesses the fastest heterogeneous electron transfer rate which may be ideal for electrochemical sensing and VTe<sub>2</sub> carries the surprising HER activity with the lowest HER overpotential at 0.5 V vs. RHE and Tafel slope of 55 mV/dec (Fig. 1.12b).

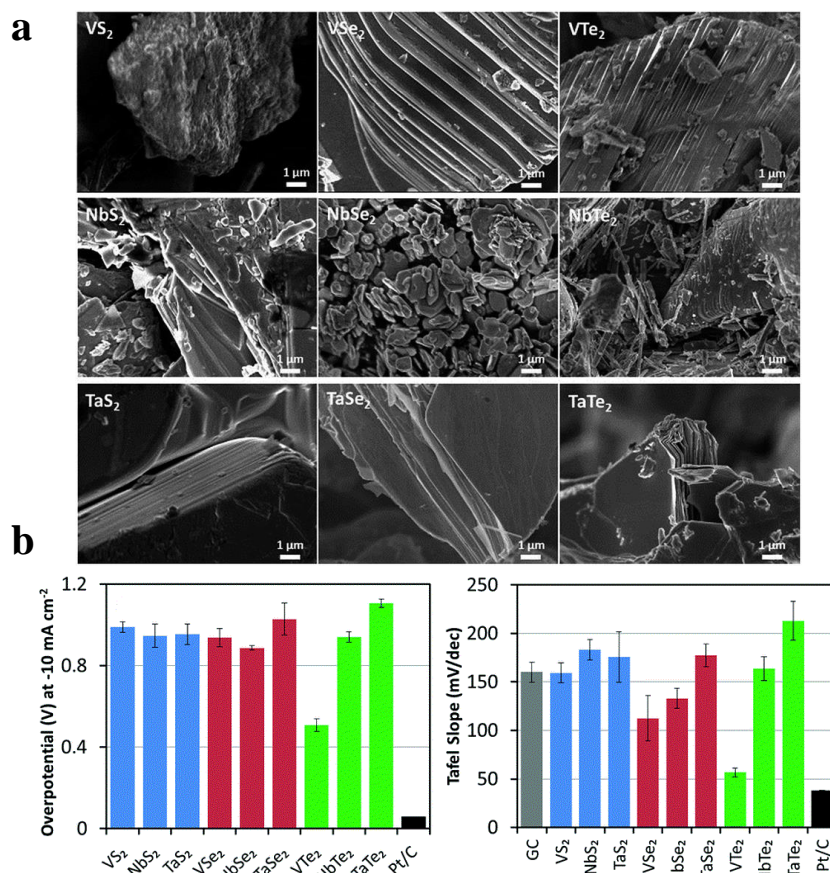


Fig. 1.12 a) SEM images of various Group V TMDs at a magnification of 10K. b) Histograms summarize of HER performance of various Group V TMDs.<sup>93</sup> Copyright 2016 The Royal Society of Chemistry.

Supercapacitors are one of the most promising energy storage technologies for the applications ranging from consumer electronics to large-scale equipment such as electric vehicles, due to their high power density, long cycle life, and relatively low cost.<sup>27</sup> 2D materials such as graphene, graphene oxide, and 2D TMDs are ideal materials to form supercapacitor electrodes due to their high specific surface area, conductivity, and redox active structures.<sup>82,84</sup> As shown in Fig. 1.13, Acerce *et al.* discovered the chemically exfoliated MoS<sub>2</sub> nanosheets (NSs) with a high concentration of the metallic 1T phase could electrochemically intercalate ions with high efficiency and power density, which is suitable as electrode materials for supercapacitor devices.<sup>18</sup> With the existence of the 1T phase confirmed by the high-resolution XPS results, the intriguing electrochemical properties of resulted materials give the credit to the intrinsic hydrophilicity and high electrical conductivity of 1T MoS<sub>2</sub> NSs. However, among the most frequently studied 2D TMDs for energy storage is the semiconducting MoS<sub>2</sub>, with several other 2D TMDs being scarcely studied, in the context of the previous literature on electrochemical energy storage.<sup>23,94,95</sup> Furthermore, considering the edges of the 2D TMDs NSs tend to provide more active sites for various processes that could improve efficiency, the potential application of TMDs for the catalysis of hydrogen evolution, hydride sulfurization, and CO<sub>2</sub> reduction has not been fully explored.

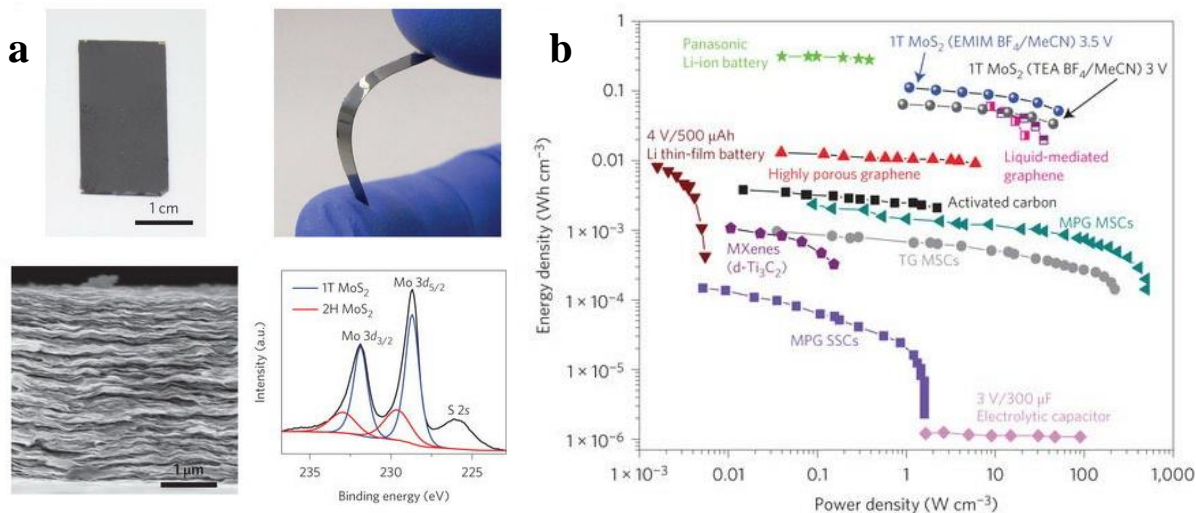


Fig. 1.13 a) Photographs, SEM images and XPS results of chemically exfoliated 1T MoS<sub>2</sub> electrodes. b) Ragone plot of the best volumetric power and volumetric energy densities reported from various materials.<sup>18</sup> Copyright 2015 Nature Publishing Group.

### 1.2.3 Literature review on photocatalysis

Photocatalysts have the ability to convert solar energy into chemical energy to degrade inorganic or organic pollutions. They are widely used for many applications including water splitting and environmental purification. The basic development for heterogeneous photocatalysis of organic or inorganic compounds by semiconductors is the formation of electron-hole pairs in the particles.<sup>96</sup> When light with energy equal to or greater than the band gap of the semiconductor is absorbed, an electron could be excited from the valence band of the semiconductor to its conduction band as shown in Fig. 1.14.<sup>97</sup> Upon excitation, the separated electrons and holes follow several pathways. The photoinduced electron transfer to adsorb organic or inorganic is caused by migration of electrons and holes to the surface of the semiconductor. While at the surface, the semiconductor could donate electrons to reduce an electron acceptor in path A; in reverse, the holes are able to migrate to the surface where an electron from a donor species can combine with the surface hole

oxidizing the donor species in path B. The probability and the rate of the charge transfer processes for electrons and holes depend upon the respective positions of the band edges for the conduction and valence bands and the redox potential levels of the adsorbate species. According to the above mechanisms, the interfacial charge transfer efficiency is limited by two important processes: (1) the confrontation between charge carrier recombination and trapping; and (2) the confrontation between trapped carrier recombination and interfacial charge transfer. Recombination of the separated electron and hole appears in the volume of the semiconductor particle (path C) or on the surface (path D) with the heat release.

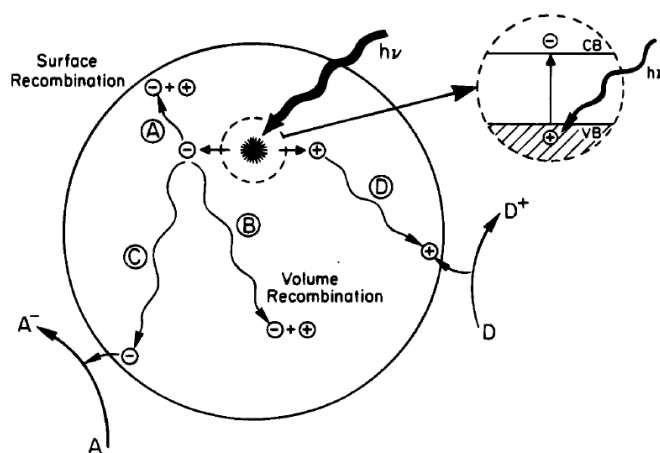


Fig. 1.14 Schematic photoexcitation in a solid followed by deexcitation events.<sup>97</sup> Copyright 2004 American Chemical Society.

Since Fujishima discovered the photocatalytic splitting of water by using titanium dioxide ( $\text{TiO}_2$ ) electrodes,  $\text{TiO}_2$  has become the most attractive photocatalyst because of its various advantages, such as structural stability, abundance, environmentally-friendliness, and low-cost.<sup>98,99</sup> However, the relatively wide band gap in  $\text{TiO}_2$  greatly hinders its efficacy for harvesting solar energy for applications in photocatalysis, solar cells, and photoelectrochemical cells. Therefore, significant

research has been committed to understanding the elemental processes and investigating methods to enhance the photocatalytic activity and efficiency of  $\text{TiO}_2$ .<sup>100,101</sup> Fortunately, continuous breakthroughs have been made in the preparation, functionalization, and modification of  $\text{TiO}_2$ -based photocatalysts to improve the absorption of visible light (~50% of solar light) for photocatalytic applications.<sup>102-104</sup> In general, modifying  $\text{TiO}_2$  with a suitable dopant not only changes the mechanism and kinetics under UV irradiation but also introduces more visible-light activity that is absent with pure  $\text{TiO}_2$ .<sup>105</sup> Three strategies have been proposed to advance properties and corresponding photocatalytic applications of  $\text{TiO}_2$ : 1) impurity-doping or dye-anchoring on  $\text{TiO}_2$  catalysts, which can extend its absorption range to visible light region;<sup>106-108</sup> 2) synthesizing  $\text{TiO}_2$  nanocrystals with specific crystal surface orientations because some specific crystalline planes, e.g., (001) plane, tend to show a higher catalytic activity than others and mixed crystallographic facets;<sup>109,110</sup> and 3) fabricating  $\text{TiO}_2$ -based nanohybrids with other functional materials, such as carbon nanotubes (CNTs) and graphene, to attain a synergistic effect between them.<sup>111-113</sup>

Recently, Chen *et al.* reported a conceptually different method to improve solar absorption ability by introducing disorders in the surface layers of nanophase  $\text{TiO}_2$ , i.e.,  $\text{Ti}^{3+}$ -doped  $\text{TiO}_2$ .<sup>114</sup> The study showed that disorder-engineered  $\text{TiO}_2$  nanocrystals (Fig. 1.15) exhibit substantially improved solar-driven photocatalytic activities for photo-oxidation of organic molecules and water splitting. Unfortunately, the preparation processes had to be conducted in a high-pressure hydrogen system for a reaction period as long as five days, which leads to disadvantages of long reaction time, low yield, and more waste residues. Therefore, it is highly desirable to develop improved methods for fabrication of such  $\text{Ti}^{3+}$ -doped  $\text{TiO}_2$ . Many investigations have demonstrated that  $\text{Ti}^{3+}$ -

containing (blue) TiO<sub>2</sub> that contains oxygen vacancies exhibit significant photocatalytic activity in the visible light region; however, the catalyst could not maintain such activity for a sufficiently long period of time.<sup>115</sup>

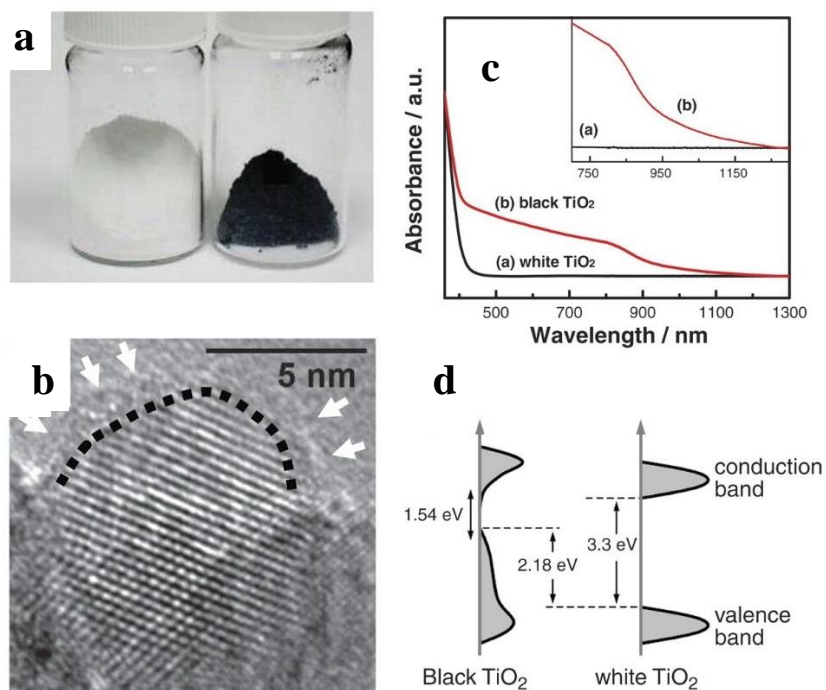


Fig. 1.15 a) Photograph of unmodified white TiO<sub>2</sub> and disorder-engineered black TiO<sub>2</sub>. b) HRTEM image of modified TiO<sub>2</sub> c) Spectral absorbance of the white and black TiO<sub>2</sub>. d) Schematic illustration of the band position of disorder-engineered black TiO<sub>2</sub> and unmodified TiO<sub>2</sub>.<sup>114</sup> Copyright 2011 American Association for the Advancement of Science.

In addition, hierarchically structured TiO<sub>2</sub>-based materials (Fig. 1.16) were reported to improve the performance of the materials because their highly porous structures were beneficial for enhancing the utilization efficiency of light.<sup>69,70</sup> However, the capability of visible light absorption still needs further improvement. TiO<sub>2</sub>-based photocatalysts synthesized by hydrothermal treatment have drawn great attention since hydrothermal methods possess advantages of convenience,

relatively low processing temperature, and high yield.<sup>116-118</sup> Although NaBH<sub>4</sub> was previously reported for reducing TiO<sub>2</sub> through a hydrothermal method,<sup>119-124</sup> the resulting photocatalytic performance was inadequate because only a small amount of NaBH<sub>4</sub> was used. Fang *et al.* added NaBH<sub>4</sub> during the synthesis process with amount no more than 0.4g, which may be insufficient to enable the formation of defective or partially reduced TiO<sub>2</sub>.<sup>125</sup> In summary, there is still lack of comprehensive and systematic investigation and discussion to study how NaBH<sub>4</sub> affects the morphology, structure, and photocatalytic activity of the reducing TiO<sub>2</sub>.

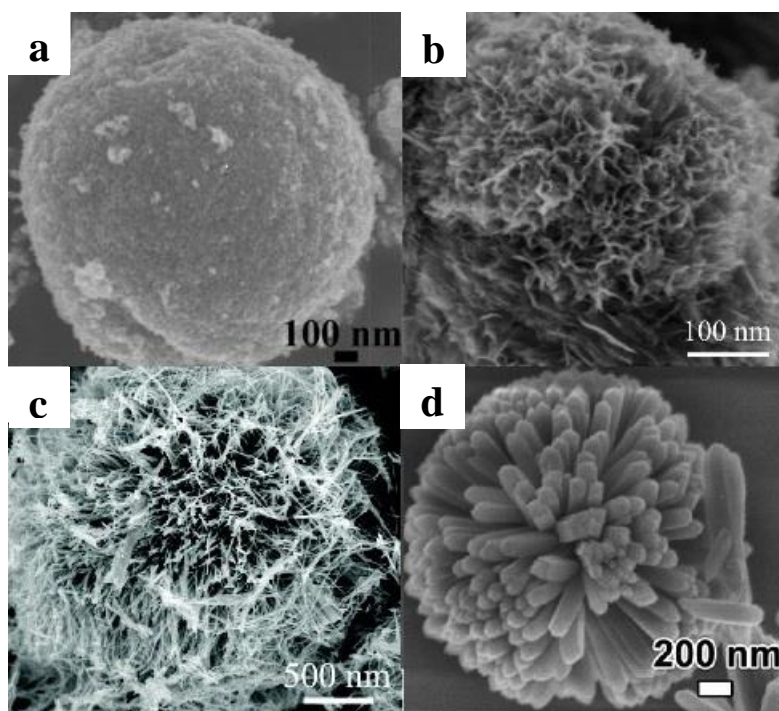


Fig. 1.16 SEM images of various TiO<sub>2</sub>-based hierarchical nanostructured photocatalysts with different building units (a) particles,<sup>126</sup> Copyright 2014 Elsevier B.V., (b) nanosheets,<sup>127</sup> Copyright 2015 Royal Society of Chemistry, (c) nanowires,<sup>127</sup> Copyright 2015 Royal Society of Chemistry, and (d) nanorods.<sup>128</sup> Copyright 2011 American Chemical Society.

The increase in demand for clean and renewable energy motivates studies on the development of novel techniques for hydrogen and oxygen production by water splitting.<sup>129</sup> Photocatalysis has been shown attractive for the generation of H<sub>2</sub> and O<sub>2</sub> using natural sunlight as an irradiation source.<sup>130</sup> Lately, TMOs and TMDs have proven to be the effective and efficient catalytic materials. In order to utilize visible light, which represents a large portion of the available solar-energy, photocatalysts should meet the following requirements for efficient conversion of solar-energy into H<sub>2</sub> by the photocatalytic water splitting: the conduction and valence band edges must be more negative than 0 V vs. NHE (pH = 0) and more positive than +1.23 V vs. NHE (pH = 0), respectively; band gap energy is smaller than 3 eV and chemical and structural properties are stable during the photocatalytic reaction.<sup>131</sup> The relationship between the band structure of a semiconductor and the redox potentials for water splitting is shown in Fig. 1.17.<sup>132</sup> For TMOs, it can be seen that WO<sub>3</sub> functions as a stable photocatalyst for O<sub>2</sub> evolution under visible light in the presence of an appropriate electron acceptor. However, the conduction band of the material is located in a more positive position over the potential of water reduction. In consequence, WO<sub>3</sub> does not have the ability to reduce H<sup>+</sup> to H<sub>2</sub> directly. For TMDs, CdSe and CdS possess suitable band structures for the water splitting under visible light irradiation, but they are not stable under the photocatalytic reaction conditions owing to their photocorrosion property (poor photoinduced stability). Therefore, the conventional TMOs and TMDs cannot effectively split water in visible light without any modifications.

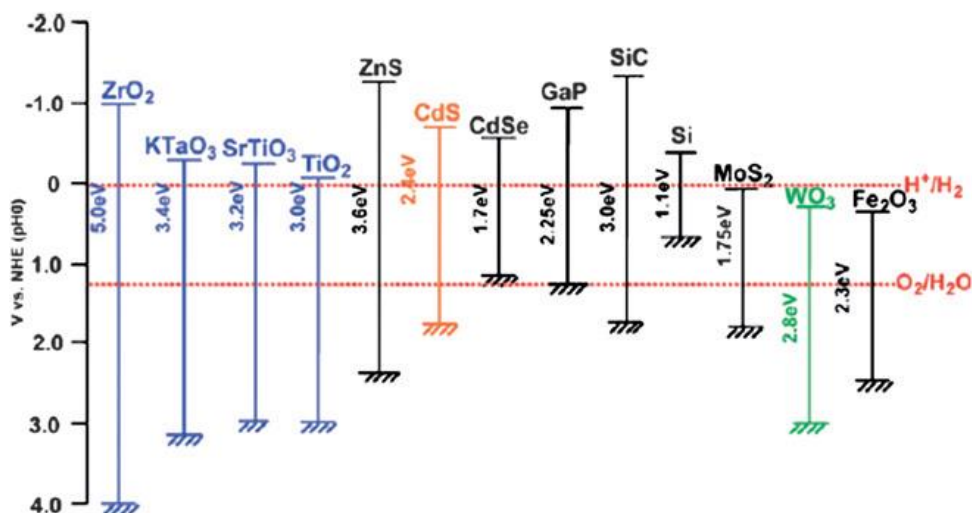


Fig. 1.17 Relationship between band structures of semiconductors and redox potentials of water splitting.<sup>132</sup> Copyright 2009 Royal Society of Chemistry.

Semiconducting QDs with intriguing quantum confinement properties, small-size effect, and composition-tunable electronic properties lead to unsaturated bonds on surfaces and edges, providing more opportunity to connect with other atoms and obtain higher activity, making them very appealing for a variety of applications and new technologies. Without modifications, the pristine TMOs/TMDs only can absorb a small portion of the full solar spectrum, resulting in inadequate utilization of visible light and infrared light ( $\sim 53\%$ ) with a lower energy in sunshine. Suzuki *et al.* reported a systematic study of the conduction band of  $\text{WO}_3$  QDs that could be tuned by size control with the quantum size effect. In Fig. 1.18a, the results showed the conduction band of engineered  $\text{WO}_3$  QDs is located at the negative side of the potential of water reduction when the size of the QDs was smaller than 1 nm.<sup>133</sup> In the meantime, the band gap expands from 2.54 eV of bulk  $\text{WO}_3$  to 3.30 eV for the 1 nm  $\text{WO}_3$  QDs (Fig. 1.18b), which is unfavorable for the photocatalytic water splitting. In this case, incorporation of another semiconductor with a smaller band gap could improve its water splitting performance.

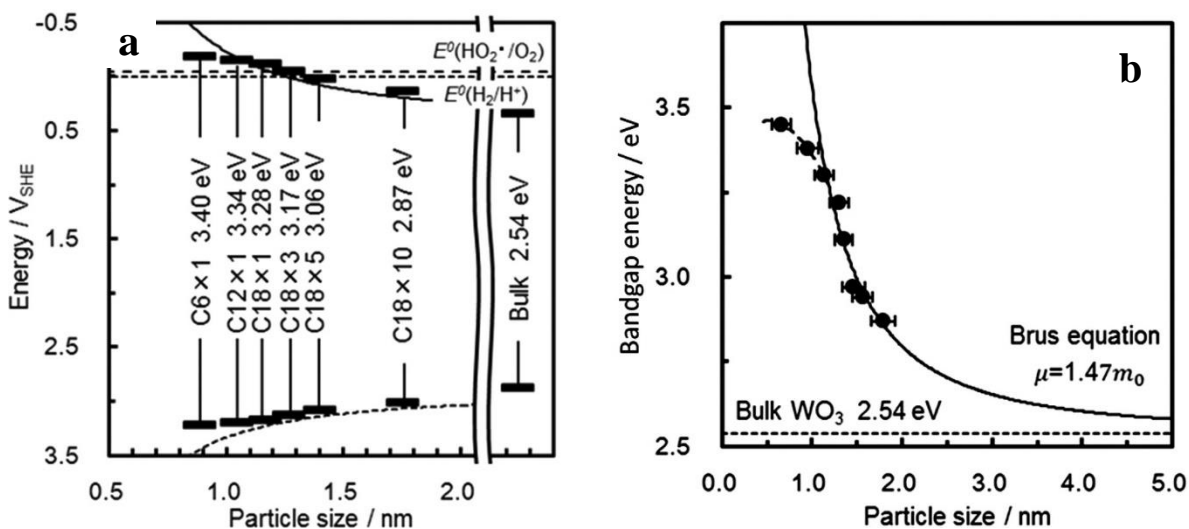


Fig. 1.18 a) The band diagram of WO<sub>3</sub> QDs. b) the relationship between the particle size and the bandgap energy.<sup>133</sup> Copyright 2016 Royal Society of Chemistry.

Zeolitic imidazolate framework-8 (ZIF-8) possesses a high specific surface area, excellent thermal and chemical stability as one of the metal-organic frameworks (MOFs).<sup>134</sup> It is constructed by Zn(II) and 2-methylimidazole ligands and widely used in adsorption, catalysis and gas separation, etc.<sup>134,135</sup> Nevertheless, the photocatalytic performance of ZIF-8 is inadequately studied. In Zeng *et al.*'s study (Fig. 1.19), CdS@ZIF-8 core-shell structures were synthesized by a two-step method, in which polyvinylpyrrolidone (PVP)-stabilized CdS NPs were first synthesized and ZIF-8 shells were grown on the surfaces of the CdS cores.<sup>136</sup> The core-shell CdS@ZIF-8 structures were applied to photocatalytic H<sub>2</sub> generation from formic acid and exhibited improved selectivity for H<sub>2</sub> generation compared with pure CdS nanoparticles. However, the H<sub>2</sub> production rate of as-prepared samples was limited.

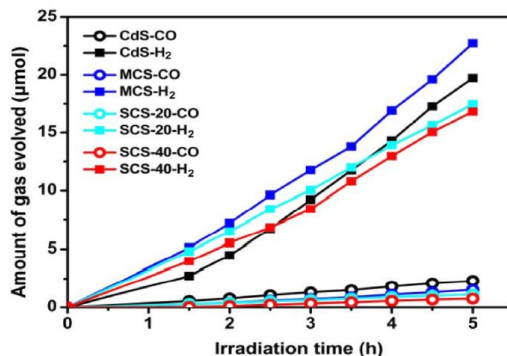


Fig. 1.19 Amounts of H<sub>2</sub> and CO production as a function of irradiation time for CdS@ZIF-8.<sup>136</sup>

Copyright 2016 Tsinghua University Press and Springer-Verlag Berlin Heidelberg.

### 1.2.4 Literature review on electrocatalysis for hydrogen evolution

Hydrogen is considered as a promising source of clean energy that could partially replace hydrocarbon fuels. There is a growing attention on hydrogen production from water splitting.<sup>132,137-</sup>

<sup>140</sup> Noble metals such as Pt-group metals are most commonly used catalysts in the hydrogen evolution reaction (HER) since they exhibit the highest activity in accordance with theoretical predictions as shown in the so-called “volcano” curve plot (Fig. 1.20).<sup>6</sup>

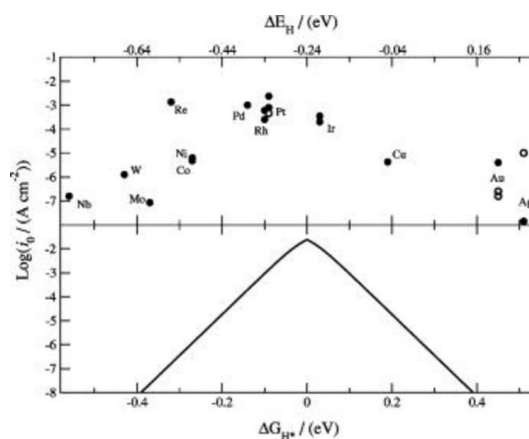


Fig. 1.20 Experimental and theoretical plots of the exchange current density for the HER over different transition metal surfaces plotted as a function of the calculated hydrogen chemisorption energy per atom and the simple kinetic model plotted as a function of the free energy for hydrogen adsorption ( $\Delta G_{H^*} = \Delta E_H + 0.24 \text{ eV}$ ).<sup>6</sup> Copyright 2005 The Electrochemical Society.

Developing novel electrocatalysts for HER with both low-cost and high-performance is a challenge. Recently, both computational and experimental studies show that TMDs, e.g., molybdenum disulfide ( $\text{MoS}_2$ ) and tungsten disulfide ( $\text{WS}_2$ ), are effective in catalyzing HER.<sup>141-</sup>  
<sup>147</sup> The exposed edges of TMDs provide active sites for HER electrocatalysis while the basal plane is catalytically inert.<sup>143</sup> Tsai *et al.* reported computationally examinations of the crystal structure (1T and 2H phase) and surface termination of several TMDs such as transition metal (Ti, V, Nb, Ta, Mo, W, Pd, Pt) with the chalcogen (S and Se) for their activity and stability.<sup>7</sup> The roles of the transition metal, chalcogen, and structure in modifying the activity and stability are established by using plane-wave density functional theory (DFT) calculation and other error estimation methods. The authors found the HER activity is strongly related to the stability of the catalyst and the metallicity is the most important parameter in determining the activity rather than structure or composition of the basal planes. Fig. 1.21 illustrates the inverse relationship for the basal planes of the semiconducting and metallic transition sulfides and selenides. Careful selection of the catalyst support can prevent TMD nanostructures from agglomeration and improve the overall performance.

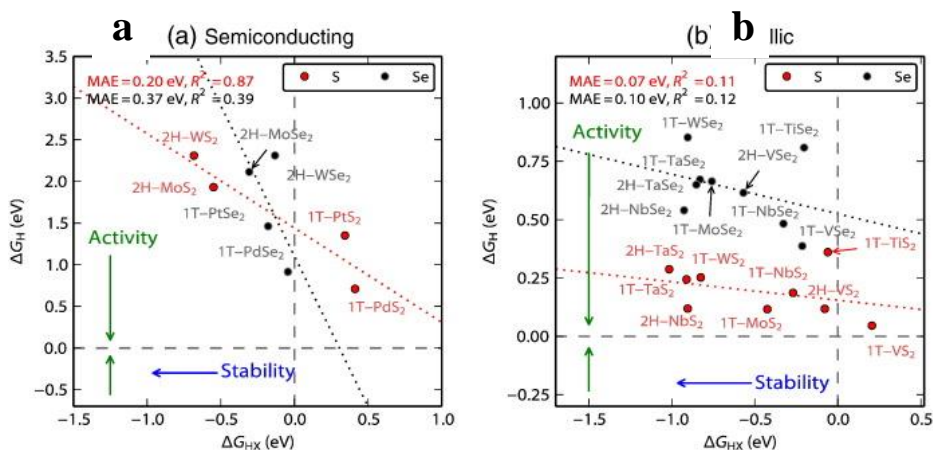


Fig. 1.21 a) Semiconducting single-layered TMDs and b) Metallic single-layered TMDs basal planes. The plot of the hydrogen adsorption free energy,  $\Delta G_{\text{H}}$ , as a function of the HX adsorption free energy,  $\Delta G_{\text{HX}}$  (X=S or Se).<sup>7</sup> Copyright 2015 Elsevier B.V.

Graphene is a two-dimensional carbon material with one atom thickness. It has a high specific surface area ( $\sim 2,600 \text{ m}^2/\text{g}$ ) and electrical conductivity ( $5\text{-}6.4 \times 10^6 \text{ S/m}$ ) that are attractive for electrocatalyst support.<sup>148-150</sup> In order to combine the benefits of TMDs and graphene, many hybrid structures of TMDs and graphene were studied to promote the HER performance. For example, MoS<sub>2</sub>/graphene hybrids have electrical coupling effects that can promote charge transfer between MoS<sub>2</sub> and graphene. In Fig. 1.22a, Dai *et al.* reported the solvothermal synthesis of MoS<sub>2</sub> nanoparticles on graphene and demonstrated excellent electrocatalytic properties of MoS<sub>2</sub>/graphene hybrid materials.<sup>151</sup> Meanwhile, graphene is also a soft material with a low bending rigidity and thus can be easily engineered with different morphologies. Huang *et al.* developed crumpled graphene particles supported MoS<sub>x</sub>, leading to aggregation-resistant hybrid materials that exhibit a small overpotential and Tafel slope (Fig. 1.22b).<sup>152</sup> Crumpled graphene with encapsulated nanomaterials can be fabricated by aerosolizing the suspension of graphene oxide (GO) and the pre-synthesized nanoparticles/precursors.<sup>153-157</sup> The crumpled morphology of graphene has abundant folds and defects, which are reported to be capable of enhancing the electrocatalytic performance. Carraro *et al.* reported a modified aerosol-based method that utilizes the precursor of MoS<sub>2</sub> and GO for the fast one-pot synthesis of crumpled MoS<sub>2</sub>/graphene hybrid materials as shown in Fig. 1.22c.<sup>158</sup> The as-produced material showed good performance in photoelectrochemical hydrogen production.

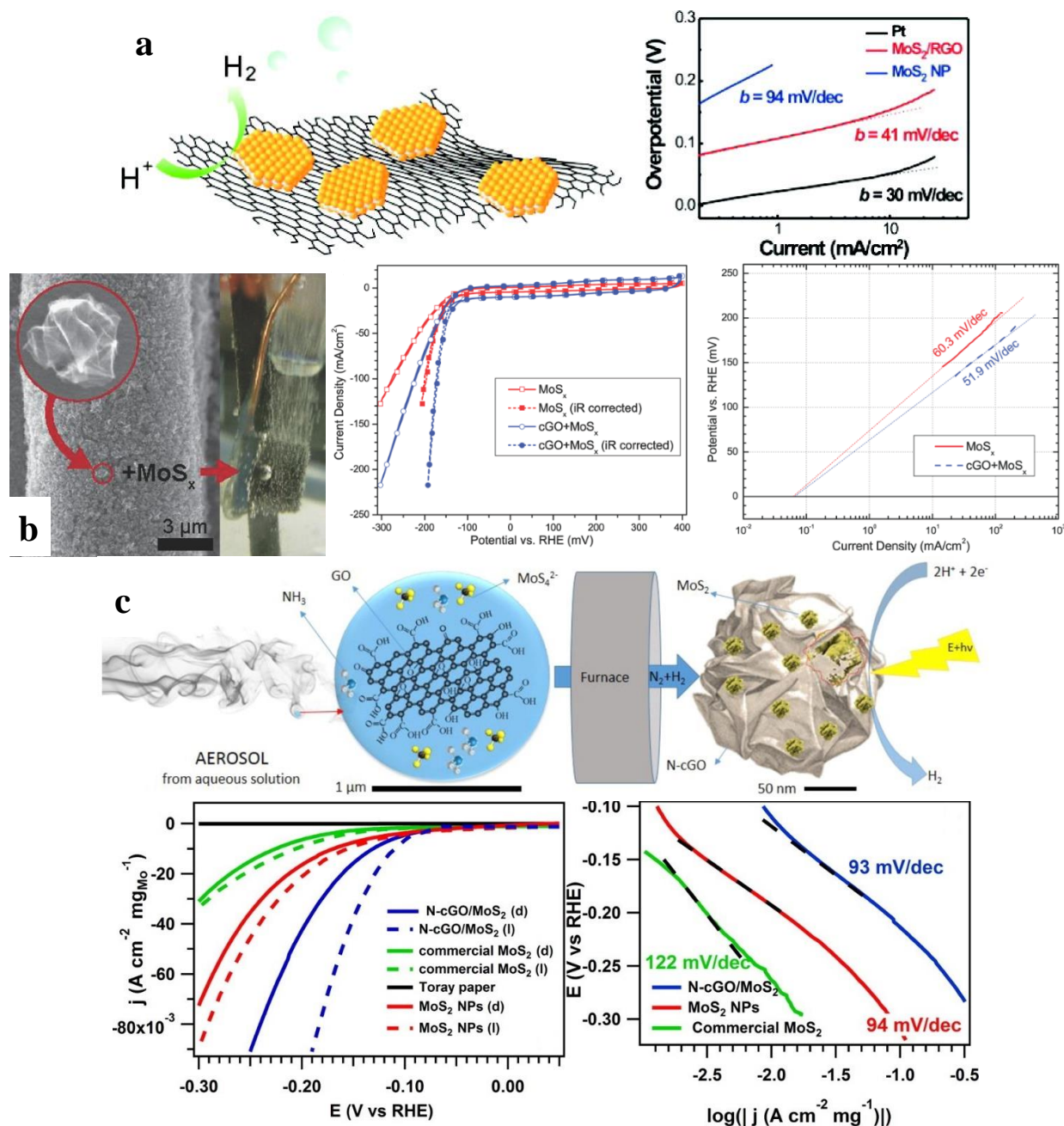


Fig. 1.22 a) Schematic diagrams of MoS<sub>2</sub>/RGO hybrid with corresponding Tafel plots recorded on glassy carbon electrodes.<sup>151</sup> Copyright 2011 American Chemical Society. b) SEM image of carbon cloth fibers modified by crumpled graphene and MoS<sub>x</sub> with HER performance.<sup>152</sup> Copyright 2014 WILEY-VCH. c) Schematic diagrams of the synthesis of N-doped graphene/MoS<sub>2</sub> nanohybrids by using aerosol processing method.<sup>158</sup> Copyright 2015 American Chemical Society.

Recent studies have shown that WS<sub>2</sub>, another important member of TMDs, is also a good candidate for HER electrocatalyst.<sup>159-161</sup> The pure phase of WS<sub>2</sub>/graphene hybrids can be fabricated by hydrothermal reaction.<sup>162,163</sup> By using graphene as the catalyst support, the WS<sub>2</sub>/graphene hybrid nanomaterials showed enhanced charge transfer and thus improved HER activity.<sup>163,164</sup> Moreover, crumpled graphene can provide extra benefits compared with conventional graphene nanosheets, e.g., preventing the aggregation of graphene sheets and improving the contact between graphene and TMDs. It was reported that the HER activity of MoS<sub>2</sub> decreases dramatically as the annealing temperature of precursor ((NH<sub>4</sub>)<sub>2</sub>MoS<sub>4</sub>) increases, while WS<sub>2</sub> has the opposite behavior.<sup>165</sup> Since crumpled graphene is commonly produced through an aerosolization method under high annealing temperature (~800 °C), WS<sub>2</sub> was selected over MoS<sub>2</sub> for the crumpled graphene/TMD electrocatalyst.

### 1.2.5 Literature review on energy storage devices

Supercapacitors are characterized by their high-power density, fast charge/discharge rate, and long lifetime. Thus, they have attracted great attention for energy storage applications, particularly in consumer electronics and transportation systems.<sup>166-169</sup> Supercapacitors can be categorized into electric double-layer capacitors (EDLCs), pseudocapacitors, and hybrid capacitors.<sup>170</sup> Pseudocapacitors leverage Faradaic electron charge transfer via redox reactions, intercalation, or electrosorption, and generally have higher specific capacitance than EDLCs but lower rate capability and stability.<sup>170-172</sup> Commonly used electrode materials in pseudocapacitors include TMOs, such as RuO<sub>2</sub><sup>173,174</sup>, MnO<sub>2</sub><sup>175-178</sup>, Ni(OH)<sub>2</sub>/NiO<sup>179-181</sup>, Co<sub>3</sub>O<sub>4</sub><sup>182-184</sup>, SnO<sub>2</sub><sup>185,186</sup>, as well as conducting polymers such as polyaniline and polypyrrole<sup>187,188</sup>. Choudhary *et al.* fabricated an array of 1D NWs seamlessly integrated with conformal 2D TMD layers (Fig. 1.23a) and the hybrids possess large surface area with atomically sharp core/shell interfaces, resulting in

supercapacitors with excellent capacitive performances.<sup>13</sup> In addition, the hybrid supercapacitor materials showed an exceptional charge-discharge retention over 30,000 cycles (Fig. 1.23b) due to their structural robustness, which holds potential for unconventional energy storage technologies.

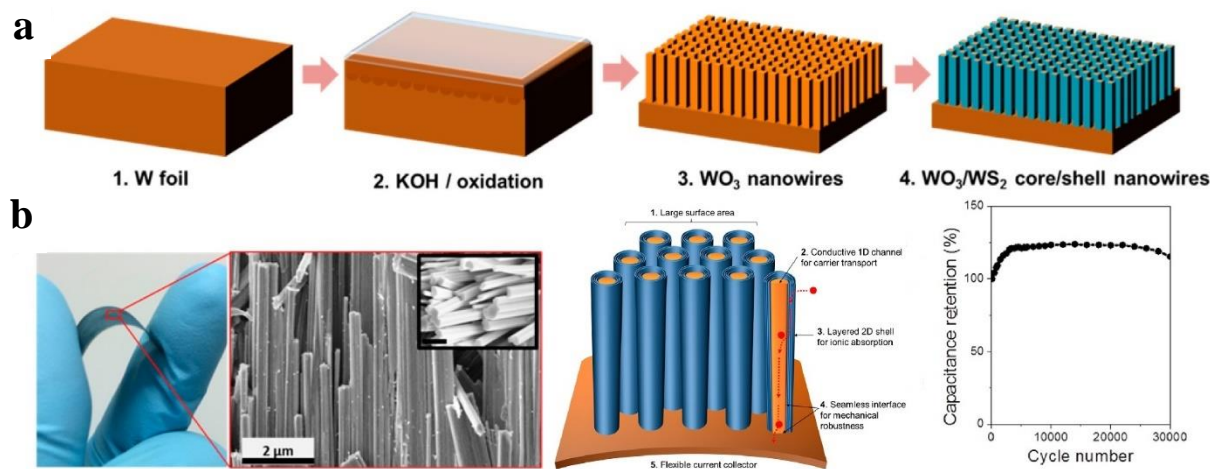


Fig. 1.23 a) Schematic diagrams of the fabrication process and b) Optical, SEM images of WO<sub>3</sub>/WS<sub>2</sub> core/shell nanowires on a W foil with long cycling performance result.<sup>13</sup> Copyright 2016 American Chemical Society.

In the past few years, TMDs based nanomaterials have been increasingly studied in supercapacitors<sup>189-194</sup>, solar cells<sup>195-197</sup>, lithium-ion batteries<sup>198,199</sup>, and catalytic<sup>200-202</sup> applications. As an important class of transition metal sulfides, cobalt sulfide-based nanostructures have been employed as electroactive materials in supercapacitors due to their high activity and low cost. Various phases of cobalt sulfides (CoS<sub>x</sub>) with different morphologies have been synthesized and studied for supercapacitors, including nanospheres/nanoparticles<sup>203-205</sup>, nanotubes<sup>206</sup>, nanowires<sup>207</sup>, nanosheets<sup>208,209</sup>, and other three-dimensional nanostructures.<sup>210,211</sup> Although some of these CoS<sub>x</sub> materials enable good performance in supercapacitors, they still suffer from

relatively low specific capacitances, degradation of performance over long cycling duration, and tedious synthesis and assembly methods. An important distinction we would like to note here is that some important transition metal sulfides have metallic polymorphs (such as the metallic 1T-MoS<sub>2</sub> or WS<sub>2</sub>) or are intrinsically metallic, such as the metallic cobalt pyrite (CoS<sub>2</sub>). They have recently found significant applications as highly active electrocatalysts for the hydrogen evolution reaction or polysulfide or triiodide reductions.<sup>212-215</sup> In Fig. 1.24, Faber *et al.* prepared a series of micro- and nano-structures of the metallic CoS<sub>2</sub> with improved HER catalytic performance due to its operational stability, cyclability, and desirable rate of hydrogen generation. The improvements enabled high current densities at low cathodic overpotentials and facilitated the releasement of H<sub>2</sub> bubbles from the electrode surface.<sup>216</sup> In particular, the high conductivity and stability of metallic CoS<sub>2</sub> could also be beneficial for good supercapacitor performance but has not yet been exploited.<sup>215,217</sup>

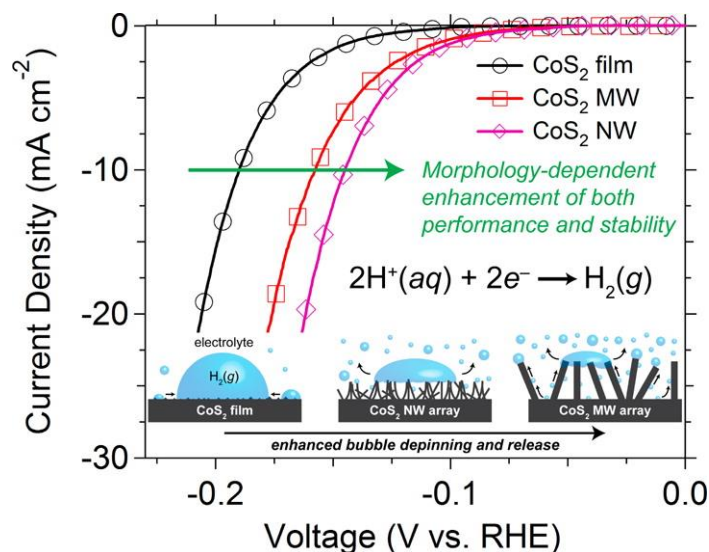


Fig. 1.24 Schematic depictions of CoS<sub>2</sub> NWs and MWs effectively releasing the H<sub>2</sub> bubbles and effective HER performance.<sup>216</sup> Copyright 2014 American Chemical Society.

LIBs have become the vital energy storage device due to the requirements of high energy density and long cycling life peculiarly for the portable equipment. However, the commercial graphite anode for LIBs could not fulfill the urgent needs of increasing energy and power densities on account of its limited theoretical capacity of  $372 \text{ mAh g}^{-1}$ . In order to improve the specific capacity of LIBs, TMD materials especially  $\text{MoS}_2$  have been considered a promising anode material for LIBs owing to their higher theoretical capacity ( $\sim 670 \text{ mAh/g}$ , based on 4 mol of  $\text{Li}^+$  insertion) and better rate capability. However, the electrical conductivity of TMDs is usually lower than graphite for their effective implementation as electrodes. Moreover, they would cause the volume expansion of nanoparticles and introduce the aggregation and restacking of NSs, which could result in the shorter cycle life and the degradation of lithium storage. Mixing  $\text{MoS}_2$  and graphite to form  $\text{MoS}_2/\text{graphite}$  composite anode can combine the advantages of  $\text{MoS}_2$  (high capacity) and graphite (good electrical conductivity); however, the large volume expansion of  $\text{MoS}_2$  could lead to graphite particles losing contact with the collector, compromising the cyclic performance. Xu *et al.* prepared a  $\text{MoS}_2$  NSs vertically on the surface of  $\text{MoO}_2$  particles by using a one-step conversion reaction using sulfur. The resulted composites showed a core-shell 3D nanoarchitecture and exhibited a high specific capacity under high loading, with significantly improved cycling stability as LIB anodes. As a comparison, the pure  $\text{MoS}_2$  NSs electrodes can only deliver 295 and 221  $\text{mAh g}^{-1}$  at the 100th and 200th cycles then continual decay occurs from the 3rd to 200th cycles as shown in Fig. 1.25.<sup>218</sup>

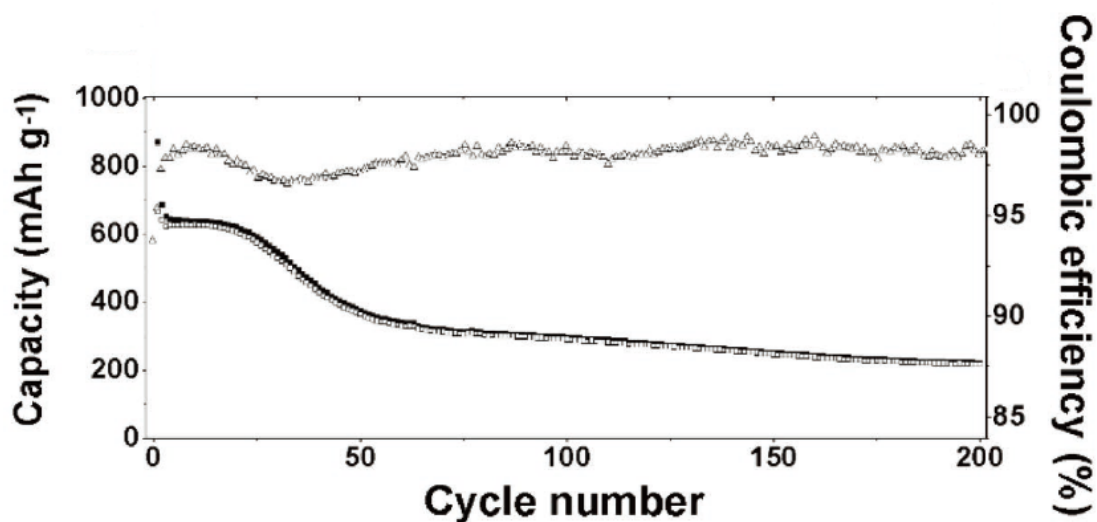


Fig. 1.25 Cycling performance of the MoS<sub>2</sub> nanosheet at the current density of 100 mAh g<sup>-1</sup>.<sup>218</sup>

Copyright 2017 WILEY-VCH.

A large number of strategies have been successfully attempted to improve the electrochemical properties of LIBs in recent years, such as fabricating multi-dimensional and multi-scale anode materials. The nanosizing effectively enhances the high-rate performance of LIBs via shortening diffusion distance of lithium ions in the electrode materials. For example, QDs with a tiny size of only several nanometers possess fascinating properties due to tunable size and surface chemistry. And QDs have shown their value-added function in the light emitting diode, supercapacitor, oxygen reduction reaction, solar cell, and sensors. Li *et al.* fabricated a lithium titanate/nitrogen and sulfur co-doped graphene QDs (Fig. 1.26a) with the fully crystalline interconnected porous framework as lithium titanate anode for LIBs.<sup>12</sup> With the assistance of the unique architecture and co-doping nitrogen and sulfur, the hybrids achieve enhanced rate performance and power density. However, the battery performance limited by the discharge capacity was only 186.2 mAh g<sup>-1</sup> in the first cycle, and charge/discharge cycles remained at 180.5 mAh g<sup>-1</sup> after 2000 cycles with the coulombic efficiency of 99.6–99.9% as shown in the Fig. 1.26b. In summary, there is still need for

more comprehensive and systematic investigation for enhancing the performance of LIBs to take the advantages of the QDs materials.

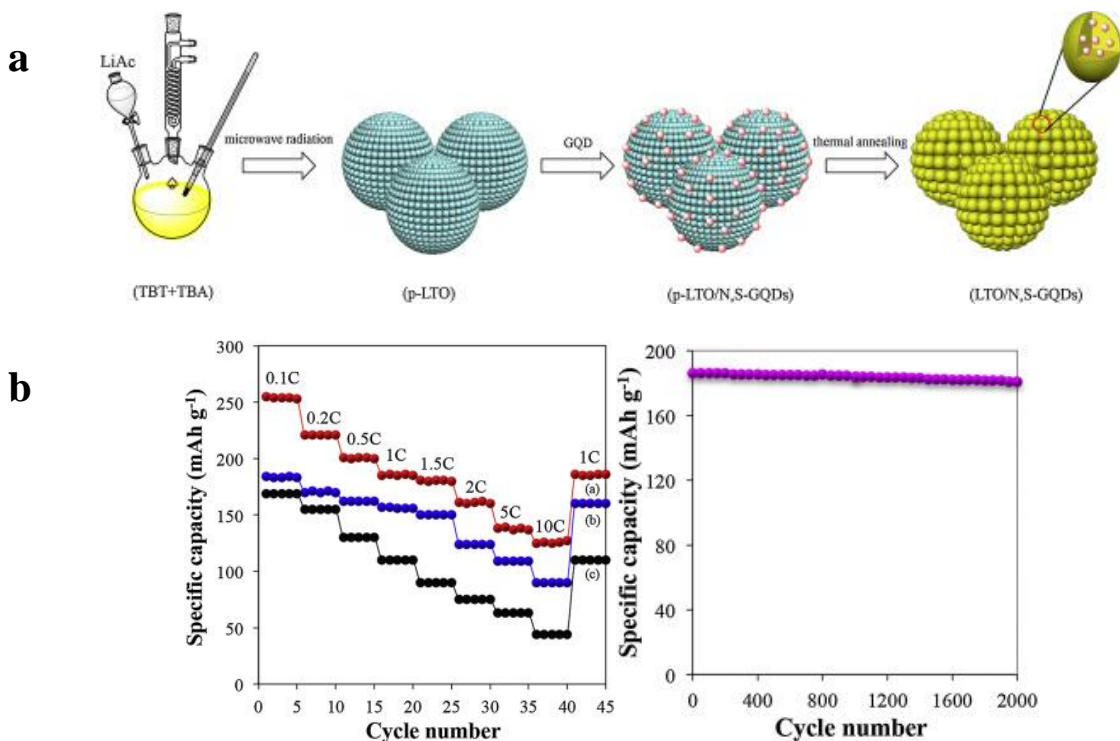


Fig. 1.26 a) Schematic illustration of the procedure for the synthesis of lithium titanate/nitrogen and sulfur co-doped graphene quantum dots. b) The specific discharge capacities of as-prepared electrodes at different rates and the cyclic performance of as-prepared electrodes at 1C.<sup>12</sup>

Copyright 2015 Elsevier Ltd.

Undoubtedly, LIBs will continue to play an important role in the field of energy storage for years to come. However, considering the limited resources of Li in the Earth's crust (0.0017 wt.%), LIBs could not fulfill the large-scale electric applications for the long-term use.<sup>219</sup> Therefore, earth-abundant elements based battery technologies are increasingly pursued recently. As a result, alkali metals with high abundance in the Earth's crust such as K (2.09 wt.%) have attracted the sight of researchers.<sup>220</sup> Unfortunately, the choice of anode materials becomes one of the major challenges

because the volume changes upon reacting with  $\text{K}^+$  ( $d = 2.76 \text{ \AA}$ ) is much larger than that for  $\text{Li}^+$  ( $d = 1.52 \text{ \AA}$ ).<sup>221</sup> In layered materials such as graphite,  $\text{K}^+$  has a reversible intercalation/de-intercalation process for forming  $\text{KC}_8$  compounds that deliver a good reversible capacity over  $200 \text{ mAh}\cdot\text{g}^{-1}$ .<sup>222</sup> In the meantime, the interlayer spacing expands from  $3.35$  to  $5.35 \text{ \AA}$  with  $\text{K}^+$  intercalation, which leads to an increase in interlayer spacing six times higher than that of Li-intercalated graphite ( $\text{LiC}_6$ ).<sup>223</sup> This huge expansion could induce the exfoliation of graphene layers that is responsible for the fast capacity decay. As a result, while significant advances have been made in the LIB industry, limited progress was attained in PIBs over recent years.

Ren *et al.* studied electrochemical potassium ion intercalation into two-dimensional layered  $\text{MoS}_2$  for potential anode material in potassium-based batteries.<sup>223</sup> The research found  $\text{K}^+$  could be electrochemically intercalated and de-intercalated reversibly in the 2D-layered  $\text{MoS}_2$ . Under this intercalation ratio, the layered structure in  $\text{MoS}_2$  was very stable during cycling. After the initial SEI layer formation during the first few cycles, 97.5% of the capacity in the 10<sup>th</sup> cycle was retained after 200 cycles. However, the charging capacity of the 10<sup>th</sup> cycle is only  $65.4 \text{ mAh}\cdot\text{g}^{-1}$ , which is limited by the theoretical capacity ( $67.0 \text{ mAh}\cdot\text{g}^{-1}$ ) with the formation of  $\text{K}_{0.4}\text{MoS}_2$ .

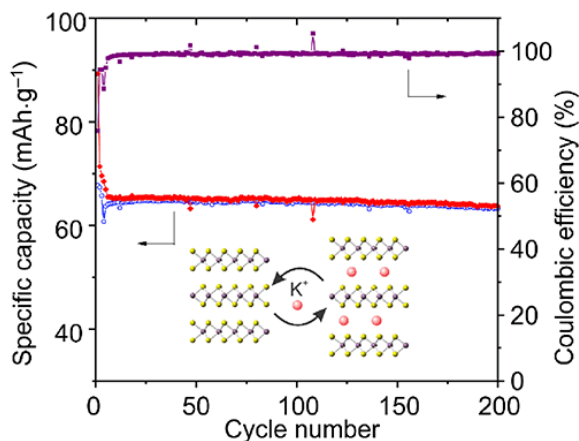


Fig. 1.27 Capacities and Coulombic efficiencies of the  $\text{MoS}_2$  electrode for PIBs.<sup>223</sup> Copyright

2017 Tsinghua University Press and Springer-Verlag Berlin Heidelberg.

### 1.2.6 Summary and conclusions

In summary, TMOs and TMDs are promising materials in various applications due to their unique structures and properties.  $\text{TiO}_2$  as one of the TMOs exhibits multiple advantages, such as structural stability, abundance, environmentally-friendliness, and low-cost in photocatalysis applications. However, the photocatalytic performance is limited as the relatively wide band gap in  $\text{TiO}_2$  is inefficient for harvesting solar energy. Modifying  $\text{TiO}_2$  by a suitable dopant will not only change the mechanism and kinetics under UV irradiation but also introduces more visible-light activity that is absent with pure  $\text{TiO}_2$ . Cobalt sulfide-based nanostructures as one of the TMDs are ideal materials to form supercapacitor electrodes due to their high specific surface area, conductivity, and redox active structures. Nevertheless,  $\text{CoS}_x$  materials still suffer from relatively low specific capacitances, degradation of performance over long cycling duration, and tedious synthesis and assembly methods. An aerosol processing method was employed to combine the advantages of TMOs and TMDs, considering they are promising candidates for platinum-free electrocatalysts in renewable energy conversion applications. In addition, TMDs QDs are promising anode material for LIBs and PIBs owing to its higher theoretical capacity and better rate capability.  $\text{MoS}_2$  QDs can be a reliable candidate for energy storage applications since they can be located in the void spaces between the graphite particles, thus improving the specific capacity of LIBs/PIBs and relieving volume expansion of nanoparticles. Last but not least, MOFs are a class of porous materials with unique properties such as tunable pore size, high specific surface area, and highly ordered crystalline porous networks but its application as photocatalysis is limited because of lack of visible light absorption ability. Thus, by combining MOFs with a visible-light-active photocatalyst such as exfoliated  $\text{MoS}_2$ , the photocatalytic hydrogen evolution can be achieved.

### **1.2.7 Research objective and dissertation outline**

The main research objective of this dissertation is to explore synthesis and characterization of novel TMO and TMD nanomaterials for various energy and environmental applications such as photocatalysis, supercapacitor, battery and hydrogen evolution. Both TMO and TMD nanomaterials have gained immense interest recently for energy and environmental applications due to their exceptional structural, electronic, and optical properties. However, these TMO and TMD nanomaterials need to be strategically modified to optimize the performance of these materials in various applications. To this end, the dissertation is organized with the following tasks.

Chapter 1 presents the background introduction and literature review of novel TMO and TMD nanomaterials for various energy and environmental applications.

Chapter 2 describes a modified  $\text{TiO}_2$  prepared by a green route with improved photocatalytic performance and broadened visible light absorption region in order to overcome the deficiency of  $\text{TiO}_2$  in visible light or solar light application.

Chapter 3 presents metallic  $\text{CoS}_2$  NWs synthesized directly on the current collector with the good electrical connection to enable efficient charge transfer between active materials and the current collector, which results in desirable energy storage performance.

In Chapter 4, an aerosol processing method is applied for facile and green synthesis of reduced graphene oxide (rGO)/tungsten disulfide ( $\text{WS}_2$ )/tungsten trioxide ( $\text{WO}_3$ ) ternary nanohybrids with

combined benefits of TMOs and TMDs. The resulting catalyst shows a superior electrocatalytic activity in the hydrogen evolution reaction.

Chapter 5 presents a series of MoS<sub>2</sub> QDs based materials that are prepared as promising anode materials for LIBs/PIBs owing to their higher theoretical capacity, better rate capability, and relieved volume expansion advantages.

Chapter 6 focuses on developing an exfoliated MoS<sub>2</sub>@MOF composite as a promising candidate for photocatalytic hydrogen evolution. The new photocatalyst exhibits enhanced absorption in visible light range with improved hydrogen production rate compared with pure MOF.

A summary of the dissertation study and future research directions are presented in Chapter 7. This study leads to low-cost, efficient and stable TMOs and TMDs candidates that can be facilely synthesized for relevant energy and environmental applications such as photocatalysis, electrocatalysis, supercapacitors, and batteries.

# CHAPTER 2 MODIFIED TITANIUM DIOXIDE FOR PHOTOCATALYSIS

## 2.1 Introduction

Modified TiO<sub>2</sub> nanomaterials are attractive TMO candidates for potential use as photocatalysts because they are stable, non-toxic, readily available, and cost-effective. As is generally known, the relatively wide band gap in TiO<sub>2</sub> greatly hinders efficient harvest of solar energy for applications in photocatalysis, solar cells, and photoelectrochemical cells. In order to overcome the deficiency of visible light or solar light absorption and enhancing the catalytic activity, this chapter presents a facile route for the controllable synthesis of Ti<sup>3+</sup>-doped TiO<sub>2</sub> with tunable photocatalytic properties using a hydrothermal method with varying amounts of reductant.

## 2.2 Experimental methods

### 2.2.1 Material synthesis

To fabricate the Ti<sup>3+</sup>-doped TiO<sub>2</sub>, a two-step hydrothermal synthesis procedure was implemented. First, 5 ml of 50 wt. % titanium (IV) bis (ammonium lactato) dihydroxide (purchased from Sigma-Aldrich) solution was dispersed in 60 ml 0.08 g/L glucose with stirring for 0.5 hours. 65 ml of the above solution was then transferred into an autoclave for hydrothermal reactions at 170 °C for 8 hours. Then the products were washed with deionized water and ethanol for 4 times each and filtered. After the calcination treatment at 500 °C for 3 hours, dried TiO<sub>2</sub> powders were obtained. Different amounts of sodium borohydride (purchased from Alfa Aesar) caplets were directly added to 60 ml water and mixed with 0.50 g TiO<sub>2</sub> powder for hydrothermal reactions in an autoclave at

180 °C for 16 hours. Finally, the  $\text{Ti}^{3+}$ -doped titanium dioxide powders were collected by filtration, washed alternately 3 times with deionized water and ethanol, and then dried at 60 °C in the air for 10 hours.

### **2.2.2 Material characterization**

The X-ray powder diffraction (XRD) analyses were conducted on a Scintag XDS 2000 diffractometer equipped with a scintillation counter and Cu k-alpha radiation (0.15418 nm) reflection mode. The microscopic morphology and structures of the samples are obtained using a Hitachi (S-4800) scanning electron microscope (SEM) and Hitachi H-9000NAR transmission electron microscope (TEM). X-ray photoelectron spectroscopy (XPS) was conducted by using VG ESCA 2000 with an Mg  $K\alpha$  as source and the C1s peak at 284.5 eV as an internal standard. The specific surface area was obtained using ASAP2020 (Micromeritics, U.S.A) Brunauer-Emmett-Teller (BET) nitrogen adsorption-desorption. The  $\text{N}_2$  adsorption-desorption measurements were carried out at 77 K using a Quantachrome Autosorb gas-sorption system. The samples were degassed at 180 °C for 2 hours before the measurements. The Raman spectra of the  $\text{Ti}^{3+}$ -doped  $\text{TiO}_2$  powders were measured using a Raman microscope (Bruker RFS 100/S spectrometer) with an excitation wavelength of 1,064 nm at an input power of 1 mW. The optical absorption spectroscopy measurements were obtained using an Ocean Optics SD2000 UV-visible spectra spectrometer with a closed quartz cell (optical path length: 1 cm).

### **2.2.3 Photocatalytic reaction measurements**

30 mg of the powder samples were ultrasonically dispersed in 50 mL deionized water followed by the addition of 0.01 g / L methylene blue (MB) aqueous solution. The mixture was then stirred

under darkness for 10 minutes to achieve adsorption-desorption equilibrium. Subsequently, the suspension with continuous stirring was exposed under a Xe lamp (AM 1.5 G and  $100 \text{ mW cm}^{-2}$ ) with an incident direction normal to the surface of the solution. At given irradiation intervals, 3 mL aliquots of the suspension were collected and separated by centrifugation. The absorption spectrum of the supernatant was measured using a UV-Vis spectrometer (Ocean Optics SD2000). The concentration of MB was determined by monitoring the changes in the absorbance maximum at 662.6 nm.

### **2.3 Results and discussion**

Reduced  $\text{TiO}_2$  samples were synthesized by adding different amounts of sodium borohydride ( $\text{NaBH}_4$ ) in the hydrothermal reaction at  $180 \text{ }^\circ\text{C}$  for 16 hours. Specifically, 0, 2, 7, 10 and 12 g  $\text{NaBH}_4$  were used in separate experiments; and the as-obtained products were denoted as pristine  $\text{TiO}_2$ ,  $\text{TiO}_2$ -1,  $\text{TiO}_2$ -2,  $\text{TiO}_2$ -3, and  $\text{TiO}_2$ -4, respectively. Figure 2.1 shows the digital photographs of the series of  $\text{TiO}_2$  samples. With the increasing amount of  $\text{NaBH}_4$ , the color of the resulting powders changes from light yellow for  $\text{TiO}_2$ -1, light grey for  $\text{TiO}_2$ -2, dark grey for  $\text{TiO}_2$ -3, to light grey for  $\text{TiO}_2$ -4, and all of these samples show a striking contrast to the white color of the pristine  $\text{TiO}_2$ . These results indicate that the hydrothermal treatment, which occurs at a mild reaction temperature, high-pressure, and a reduced atmosphere, did affect the surface properties of  $\text{TiO}_2$ .



Fig. 2.1 Photographs of pristine TiO<sub>2</sub> (a) and doped TiO<sub>2</sub> samples, (b) TiO<sub>2</sub>-1, (c) TiO<sub>2</sub>-2, (d) TiO<sub>2</sub>-3 and (e) TiO<sub>2</sub>-4.

To determine the crystal structure and possible phase changes during the hydrothermal synthesis, X-ray diffraction (XRD) was carried out to study the series of samples during the evolution process (Figure 2.2a). All of the samples show diffraction peaks matching well with the crystal structure of the anatase phase TiO<sub>2</sub> (71-1169, JCPDS). No new XRD peaks are observed for samples with 2, 7, and 10 g of NaBH<sub>4</sub>, i.e., TiO<sub>2</sub>-1, TiO<sub>2</sub>-2, and TiO<sub>2</sub>-3. However, a set of diffraction peaks appear at 27.4°, 36.1°, 44.1° and 56.6° for TiO<sub>2</sub>-4; these four peaks can be well indexed to the characteristic peaks of (110), (101), (210), and (220) crystal planes of rutile phase TiO<sub>2</sub> (75-1751, JCPDS), suggesting that TiO<sub>2</sub>-4 contained both anatase phase and rutile phase TiO<sub>2</sub>. The average crystallite size of TiO<sub>2</sub> was estimated according to the Scherrer's equation (2.1)

$$D = K \cdot \lambda / \beta \cos \theta \quad (2.1)$$

where K is the Scherrer constant,  $\lambda$  the X-ray wavelength,  $\beta$ , the peak width of half maximum, and  $\theta$  is the Bragg diffraction angle. The particle sizes for pristine TiO<sub>2</sub>, TiO<sub>2</sub>-1, TiO<sub>2</sub>-2, TiO<sub>2</sub>-3, and

TiO<sub>2</sub>-4 are 15.20 nm, 16.36 nm, 16.55 nm, 16.84 nm, and 19.76 nm, respectively. The intensities of the diffraction peaks became weaker with the increase of the amount of NaBH<sub>4</sub> from 2 g to 10 g, suggesting a decreased crystallinity for TiO<sub>2</sub> samples after the hydrothermal treatment possibly due to the formation of defects under a relatively higher pressure in a reducing environment. The crystalline degree, in turn, grew stronger with further increasing the amount of NaBH<sub>4</sub> to 14 g, which can be attributed to the increased pressure promoting the reorganization or restructuring of crystallites, thereby leading to the enhancement of the product crystallinity.<sup>224,225</sup> Raman spectroscopy was also used to characterize the series of TiO<sub>2</sub> samples (Figure 2.2b). Raman peaks appear at 147, 397, 515, and 637 cm<sup>-1</sup> corresponding to E<sub>g</sub>, B<sub>1g</sub>, A<sub>1g</sub>, and E<sub>g</sub> lattice vibration modes, respectively, which indicates that all samples are majorly dominated by anatase type titanium dioxide. The Raman bands shift toward a lower wavenumber possibly due to the increase in particle size from pristine sample to reduced sample.<sup>226,227</sup>

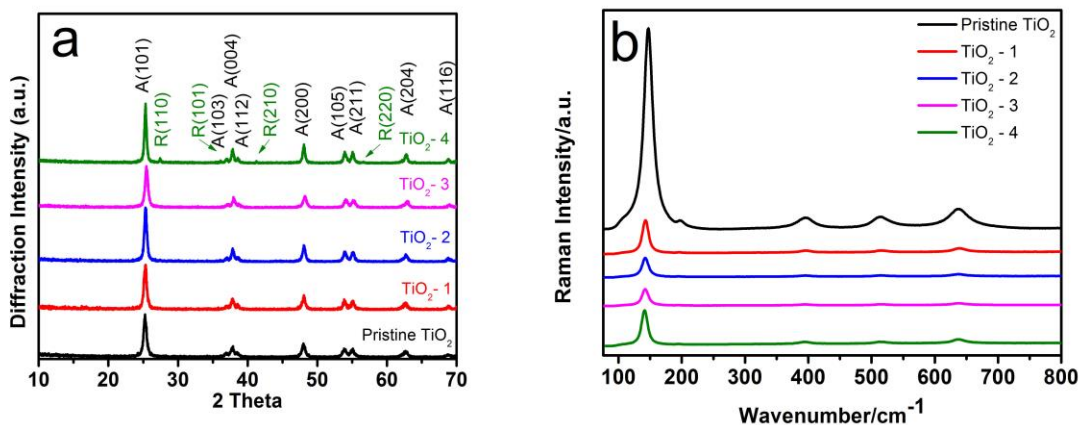


Fig. 2.2 (a) Representative XRD pattern and (b) Raman spectra of the pristine TiO<sub>2</sub> and as-synthesized TiO<sub>2</sub>.

The morphology and structure of the as-prepared TiO<sub>2</sub> were further characterized by scanning electron microscopy (SEM). Figure 2.3a-e present typical SEM images of the pristine TiO<sub>2</sub>, TiO<sub>2</sub>-1, TiO<sub>2</sub>-2, TiO<sub>2</sub>-3, and TiO<sub>2</sub>-4, respectively. The size of TiO<sub>2</sub> particles increased with increasing the amount of NaBH<sub>4</sub> in the synthesis process, which is most likely due to the agglomeration of nanoparticles induced by a higher concentration of NaBH<sub>4</sub>. The results are basically in agreement with the particle size calculation by using Scherrer's equation from XRD results. It should be noted that, for TiO<sub>2</sub>-4, there also appeared some hierarchical microstructures with an average size of 2 to 4 μm that were constructed by a large number of nanofibers about 20-30 nm in diameter, as shown in Figs. 2.3f and 2.3g. Actually, a small fraction of hierarchical microstructures was also found in the sample TiO<sub>2</sub>-3, suggesting the gradual evolution of nanostructures from nanoparticles to nanofiber upon tuning the amount of NaBH<sub>4</sub>. Hierarchical structures were previously proven to be beneficial for improving photocatalytic activity because of their special hierarchical porous structure, good permeability, and a large surface area compared with other low dimensional structures.<sup>124,228,229</sup> Furthermore, the TiO<sub>2</sub> hierarchical structure can absorb more light through multiple reflections and lead to more photogenerated electrons to participate in the photocatalytic degradation process.<sup>230,231</sup> Therefore, TiO<sub>2</sub>-4 is expected to offer enhanced light-harvesting capability and a higher specific surface area than other TiO<sub>2</sub> samples.

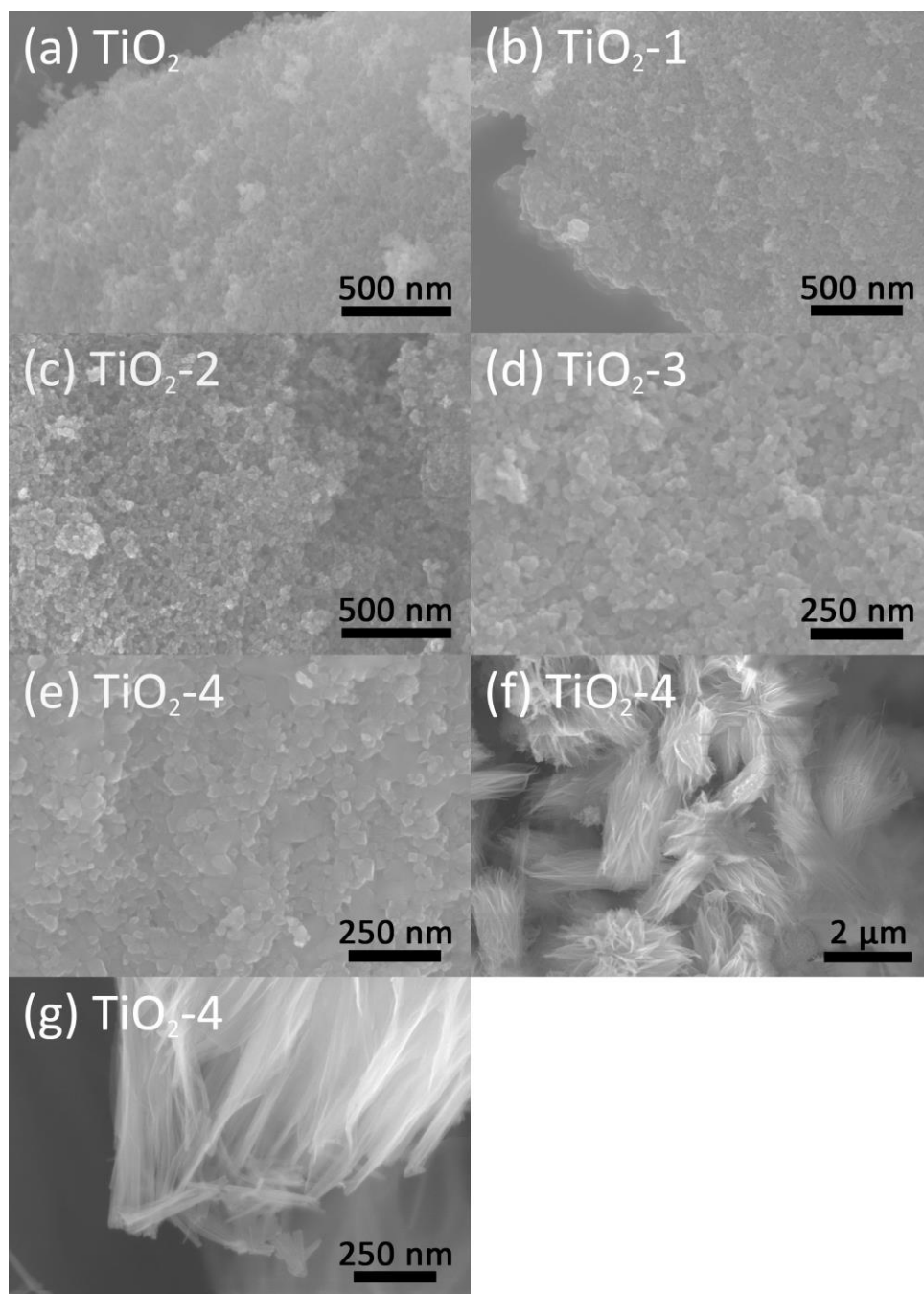


Fig. 2.3 SEM images of pristine TiO<sub>2</sub> (a) and as-obtained TiO<sub>2</sub> nanostructures: (b) TiO<sub>2</sub>-1, (c) TiO<sub>2</sub>-2, (d) TiO<sub>2</sub>-3 and (e) TiO<sub>2</sub>-4; (f) and (g) hierarchical structures TiO<sub>2</sub>-4.

The morphology and structure of as-prepared TiO<sub>2</sub> were further elucidated by transmission electron microscopy (TEM) and high-resolution TEM (HRTEM) images shown in Figure 2.4.

Figure 2.4a shows the TEM image of nanoparticles from sample TiO<sub>2</sub>-4 with discernible TiO<sub>2</sub> nanofibers, which is in agreement with the SEM observation. The TiO<sub>2</sub> nanofibers were formed possibly due to the high pressure during the phase transition process.<sup>232,233</sup> Figures 2.4b and c display the HRTEM images of an individual particle and nanofiber from sample TiO<sub>2</sub>-4, respectively. In addition, a set of well-defined diffraction rings are observed in selected area electron diffraction (SAED) patterns (Fig. 4d), which is in good agreement with the anatase phase of synthesized TiO<sub>2</sub> nanocrystals.<sup>234</sup> Pristine TiO<sub>2</sub> nanocrystals show a lattice spacing= 0.350 nm that is close to that of anatase TiO<sub>2</sub> (101) (0.351 nm). After the hydrothermal treatment by adding different amounts of NaBH<sub>4</sub>, the characteristic TiO<sub>2</sub>-3 and TiO<sub>2</sub>-4 nanocrystal lattice spacing of 0.351 nm corresponding to the (101) lattice plane of anatase TiO<sub>2</sub>, which is consistent with previous results.<sup>235</sup> There is no noticeable change in the nanocrystal lattice spacing value corresponding to the anatase (101) plane, which indicates that the Ti<sup>3+</sup> has been introduced into the lattice without modifying the dimension of the unit cell.<sup>236</sup>

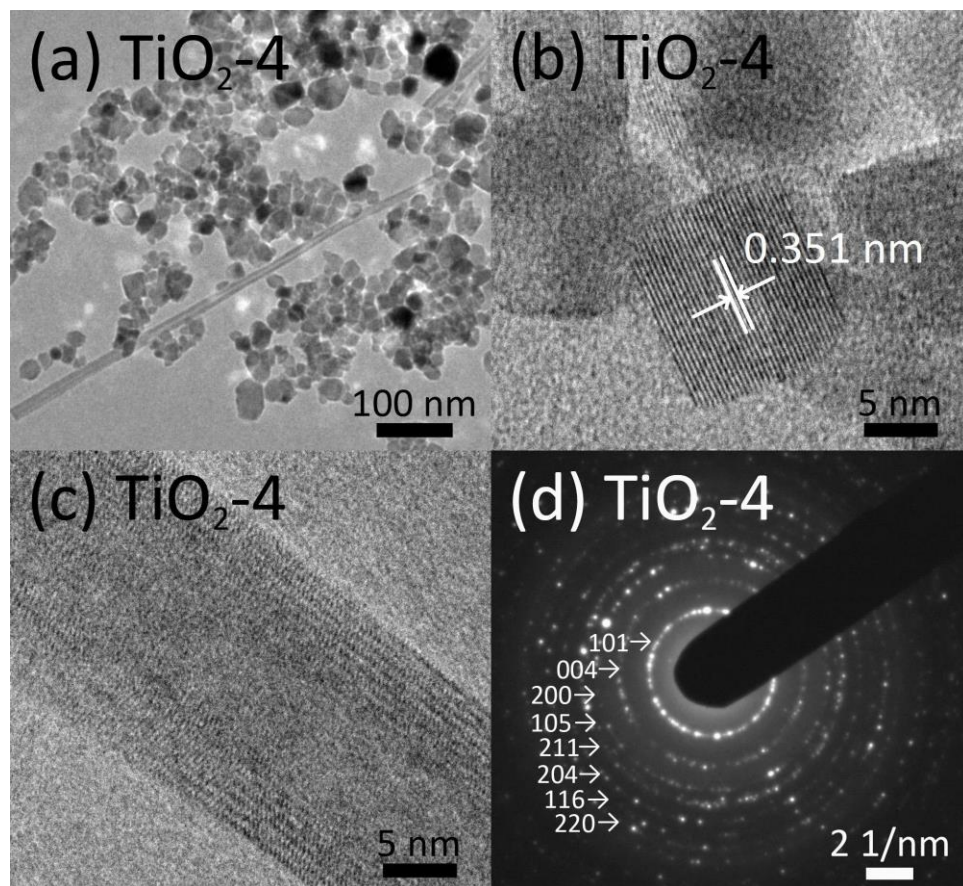


Fig. 2.4 TEM micrographs of sample  $\text{TiO}_2$ -4: (a) overview image of  $\text{TiO}_2$ -4, HRTEM images of  $\text{TiO}_2$ -4 nanoparticles (b) and nanotube (c). (d) SAED pattern of synthesized  $\text{TiO}_2$ -4.

Figure 2.5 shows the nitrogen gas adsorption and desorption isotherms of the series of  $\text{TiO}_2$  samples; all of these curves can be classified as type IV isotherm characteristic of mesoporous materials with the presence of a hysteresis loop in the relative-pressure range of 0.6-1.0.<sup>237,238</sup> The specific surface areas and average pore diameters of the synthesized  $\text{TiO}_2$  were analyzed based on nitrogen adsorption and desorption measurements (Table 2.1). There is no remarkable change between pristine  $\text{TiO}_2$  and  $\text{TiO}_2$ -1, both of which have a BET surface area of around  $78.8 \text{ m}^2 \text{ g}^{-1}$ , while  $\text{TiO}_2$ -2 shows a remarkable decrease in surface area and only has a BET surface area of  $44.6 \text{ m}^2 \text{ g}^{-1}$ . Notably,  $\text{TiO}_2$ -3 shows a BET surface area of  $87.9 \text{ m}^2 \text{ g}^{-1}$  that is substantially higher than

that of the pristine TiO<sub>2</sub>. However, sample TiO<sub>2</sub>-4 again shows a significantly decreased surface area of 49.4 m<sup>2</sup> g<sup>-1</sup>. The pore size distribution was estimated by employing the BJH (Barret-Joyner-Halenda) method. TiO<sub>2</sub>-4 shows an average pore size of 97.8 Å that is significantly lower than those of other samples. It should be noted that the hierarchical structure could be beneficial for enhancing the surface area of a material, while the particle size and the pore volume are also key factors affecting the surface area. Both SEM images and calculations using Scherrer's equation based on XRD patterns suggest the TiO<sub>2</sub>-4 sample possesses the largest particle size compared with other samples, which might offset the effect from the hierarchical structure.

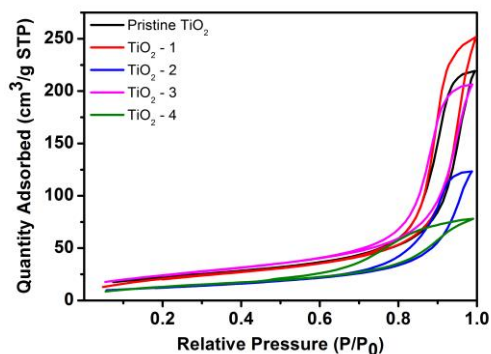


Fig. 2.5 N<sub>2</sub> adsorption-desorption isotherms for pristine TiO<sub>2</sub> and as-obtained TiO<sub>2</sub>.

Table 2.1 Surface properties of pristine TiO<sub>2</sub> and as-synthesized TiO<sub>2</sub>

Sample	BET Surface Area (m <sup>2</sup> /g)	Adsorption average pore width (Å)	Total pore volume (cm <sup>3</sup> /g)
Pristine TiO <sub>2</sub>	78.9	171.8	0.339
TiO <sub>2</sub> - 1	78.8	197.5	0.389
TiO <sub>2</sub> - 2	44.6	171.2	0.191
TiO <sub>2</sub> - 3	87.9	145.2	0.319
TiO <sub>2</sub> - 4	49.4	97.8	0.121

X-ray photoelectron spectroscopy (XPS) measurements were carried out to investigate the chemical states and electronic structure of  $Ti^{4+}$  in pristine  $TiO_2$ ,  $TiO_2$ -3, and  $TiO_2$ -4. As presented in Figure 2.6, the XPS signal of Ti 2p was recorded ranging from 454 to 465 eV for the pristine  $TiO_2$  and  $TiO_2$ -4. The Ti 2p<sub>3/2</sub> peak shifts from 457.2 eV of pristine  $TiO_2$  to 456.8 eV for  $TiO_2$ -4 accompanying with the negative shift of Ti 2p<sub>1/2</sub> peak from 463.2 eV to 462.4 eV, suggesting the partial reduction of  $TiO_2$  with the formation of  $Ti^{3+}$  on the surface of the as-prepared  $TiO_2$ -4. The existence of  $Ti^{3+}$  in the sample  $TiO_2$ -4 was also confirmed by the X-band Electron Paramagnetic Resonance (EPR) spectra, as shown in Fig. 2.6(d).<sup>239-241</sup> Based on the EPR results, it is found that  $TiO_2$ -4 shows a peak intensity of ca. 561, which is three times higher than that of the pristine  $TiO_2$  (160.4). Because the intensity signal of EPR evidences the number of unpaired electrons, it is reasonable to conclude that the amount of  $Ti^{3+}$  ions in the  $TiO_2$ -4 sample is much higher than that in the pristine  $TiO_2$ .<sup>242</sup> Also signals with g values in the range of 2.0 to 2.08 are belong to photogenerated holes that are trapped by the subsurface lattice oxygen. It is generally agreed that the holes are located at oxygen vacancies which react with the  $O^{2-}$  and  $OH^-$  to form  $O^{\cdot-}$  and  $OH^{\cdot-}$  radicals on the surface of catalysts for oxidative decomposition of organic materials. Based on the integrated area of the signals, a larger amount of  $O^{\cdot-}$  radicals present on the surface of  $Ti^{3+}$ -doped materials resulted in more effective photocatalysis.<sup>242</sup> It should be noted that the energy difference between XPS Ti2p 3/2 and Ti2p 1/2 peaks for the sample  $TiO_2$ -4 is ca. 5.55 eV; this value is slightly lower than that of the pristine  $TiO_2$  (ca. 6.0 eV).<sup>243-245</sup> The slight change in energy difference of the Ti2p peaks can be attributed to the formation of a mixed phase of rutile and anatase in the sample  $TiO_2$ -4.<sup>246</sup> In addition to  $Ti^{3+}$ , oxygen vacancies can also be possibly produced during the hydrothermal process.<sup>247,248</sup> Fig. 2.6b exhibits the O 1s XPS spectra of the pristine  $TiO_2$  and  $TiO_2$ -4. The Ti-O peak shifts from 528.6 eV for the pristine  $TiO_2$  to 528 eV for

the TiO<sub>2</sub>-4; in addition, a new peak located at 530 eV is attributed to Ti-OH, confirming the formation of the hydroxyl group on the TiO<sub>2</sub> surface after the hydrogen treatment.<sup>117,249</sup> We also observed the similar O 1s peak broadening and identical Ti 2p peaks in the as-prepared sample TiO<sub>2</sub>-3. Previous studies showed boron-doped TiO<sub>2</sub> exhibits improved visible light photocatalytic performance.<sup>250,251</sup> Generally, boron doping could be detected by the XPS survey at a binding energy of 192~193 eV. In this study, there is no B 1s peak (Fig. 2.6c) present in TiO<sub>2</sub>-4, which suggests B is not doped in the modified TiO<sub>2</sub>.

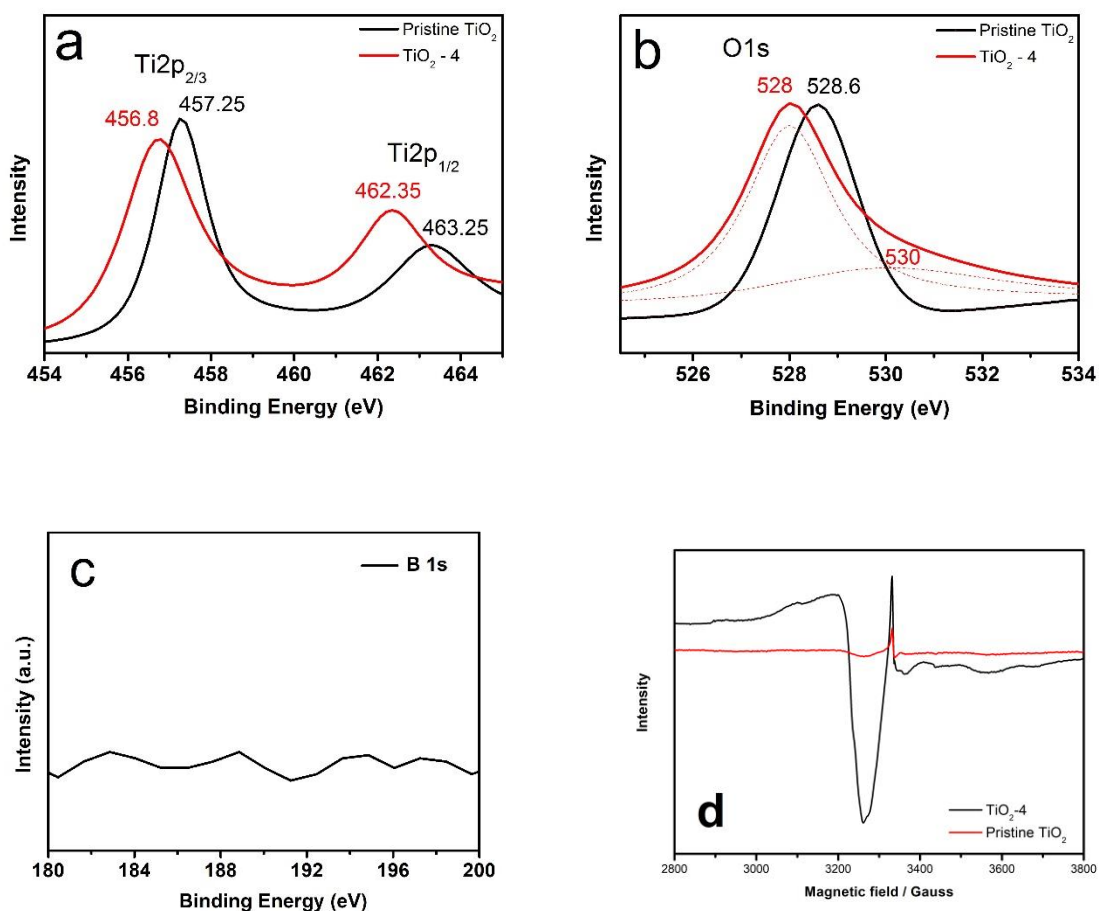


Fig. 2.6 X-ray photoelectron spectra (XPS) of (a) Ti2p and (b) O1s of pristine TiO<sub>2</sub> and TiO<sub>2</sub>-4; (c) B 1s of TiO<sub>2</sub>-4; (d) EPR spectra of the pristine TiO<sub>2</sub> and TiO<sub>2</sub>-4 at 100 K under N<sub>2</sub> atmosphere.

UV-visible diffuse reflectance spectra were obtained to investigate the light absorption characteristics of the series of TiO<sub>2</sub> samples. The absorption edges are measured to be 397.1 nm, 406.0 nm, 394.7 nm, 411.9 nm and 438.2 nm for pristine TiO<sub>2</sub>, TiO<sub>2</sub>-1, TiO<sub>2</sub>-2, TiO<sub>2</sub>-3 and TiO<sub>2</sub>-4 respectively. As is well known, the positive shift of the absorption spectra of the photocatalyst is in favor of enhancing photocatalytic performance. It should be noted the variation in the intensity of the spectra background could be attributed to the amount of TiO<sub>2</sub> samples used for testing or the particle size of the samples. Figure 2.7a shows diffuse reflectance spectra of pristine TiO<sub>2</sub> and as-prepared TiO<sub>2</sub>-4. It can be seen the absorption onset is around 397.1 nm for pristine TiO<sub>2</sub>, but this absorption extends into the visible region (438.2 nm) for TiO<sub>2</sub>-4, which can be attributed to the Ti<sup>3+</sup> doping, the crystallite size, and the phase structure of the samples. The redshift of absorption edge indicates a decrease in the band gap. The corresponding band gap energy value was obtained by plotting the Kubelka-Munk function against the photon energy, as shown in Figure 2.7b.<sup>252,253</sup> The band gap energy value of TiO<sub>2</sub>-4 is 3.1 eV, which is smaller than that of pristine TiO<sub>2</sub> (3.28 eV).

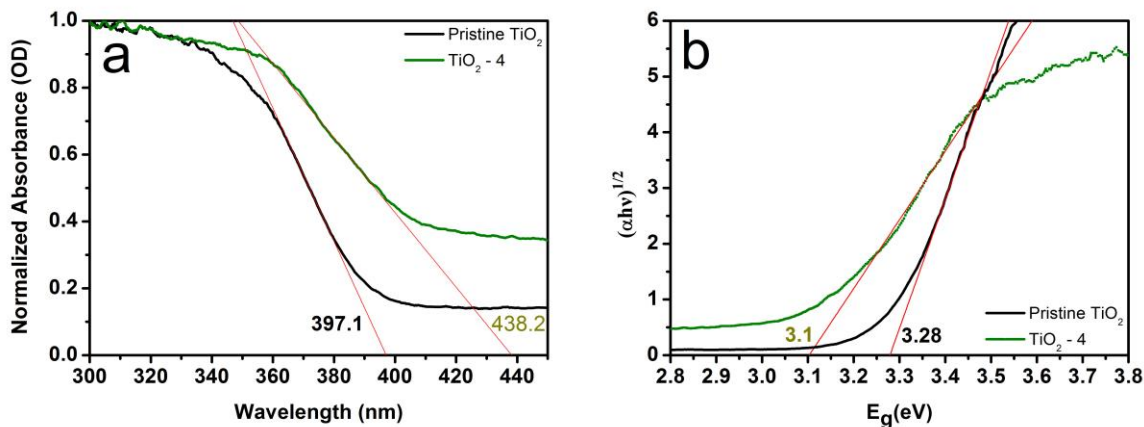


Fig. 2.7 (a) UV-visible diffuse reflectance spectra of pristine TiO<sub>2</sub> and TiO<sub>2</sub>-4. (b) Curve-fitting by using the Kubelka-Munk function method for the calculated absorbance against the photon energy for the pristine TiO<sub>2</sub> and TiO<sub>2</sub>-4.

Photocatalytic reactions for the degradation of methylene blue (MB) aqueous solution were performed to investigate the photocatalytic activity of the series of TiO<sub>2</sub> samples, as shown in Figure 2.8. All of the TiO<sub>2</sub> samples after the hydrothermal treatment showed an enhanced photodegradation rate for MB compared with the pristine TiO<sub>2</sub> under simulated sunlight irradiation (AM 1.5 G and 100 mW cm<sup>-2</sup>). The evolution of methylene blue solution, under 10 minutes' dark environment and 50 minutes' visible light irradiation, are shown in Figure 2.8b. Among the samples after hydrothermal reactions, the TiO<sub>2</sub>-4 catalyst showed the highest photocatalytic activity. After irradiation for 20 min, nearly 97.2% of MB was degraded by the sample TiO<sub>2</sub>-4. The TiO<sub>2</sub>-4 sample was far more efficient than any other samples TiO<sub>2</sub>-3, TiO<sub>2</sub>-2, TiO<sub>2</sub>-1, and pristine TiO<sub>2</sub> that present a degradation percentage of about 84.3%, 76.1%, 47.4%, and 23.5%, respectively. It should be noted that, in the dark environment, the TiO<sub>2</sub>-4, despite a relatively lower BET surface area, shows a significantly improved adsorption capability compared with pristine TiO<sub>2</sub>, indicating the Ti<sup>3+</sup> on the surface of TiO<sub>2</sub>-4 may also play a key role in promoting the capability to adsorb the organic dye, thereby leading to an outstanding photocatalytic activity.<sup>254</sup> The reusability of Ti<sup>3+</sup>-doped TiO<sub>2</sub> has been examined for selected samples. Compared with the TiO<sub>2</sub>-4 sample, the recycled TiO<sub>2</sub>-4 took 30 more minutes to achieve nearly 90% of MB degradation as shown in Figure 2.8c and 2.8d. After 60 min of visible light irradiation, nearly 96.7% of MB is degraded by reduced TiO<sub>2</sub>-2. However, only 27% of MB is degraded by recycled TiO<sub>2</sub>-2. It could be found that the photocatalytic activity of recycled TiO<sub>2</sub>-4 is much better than recycled TiO<sub>2</sub>-2.

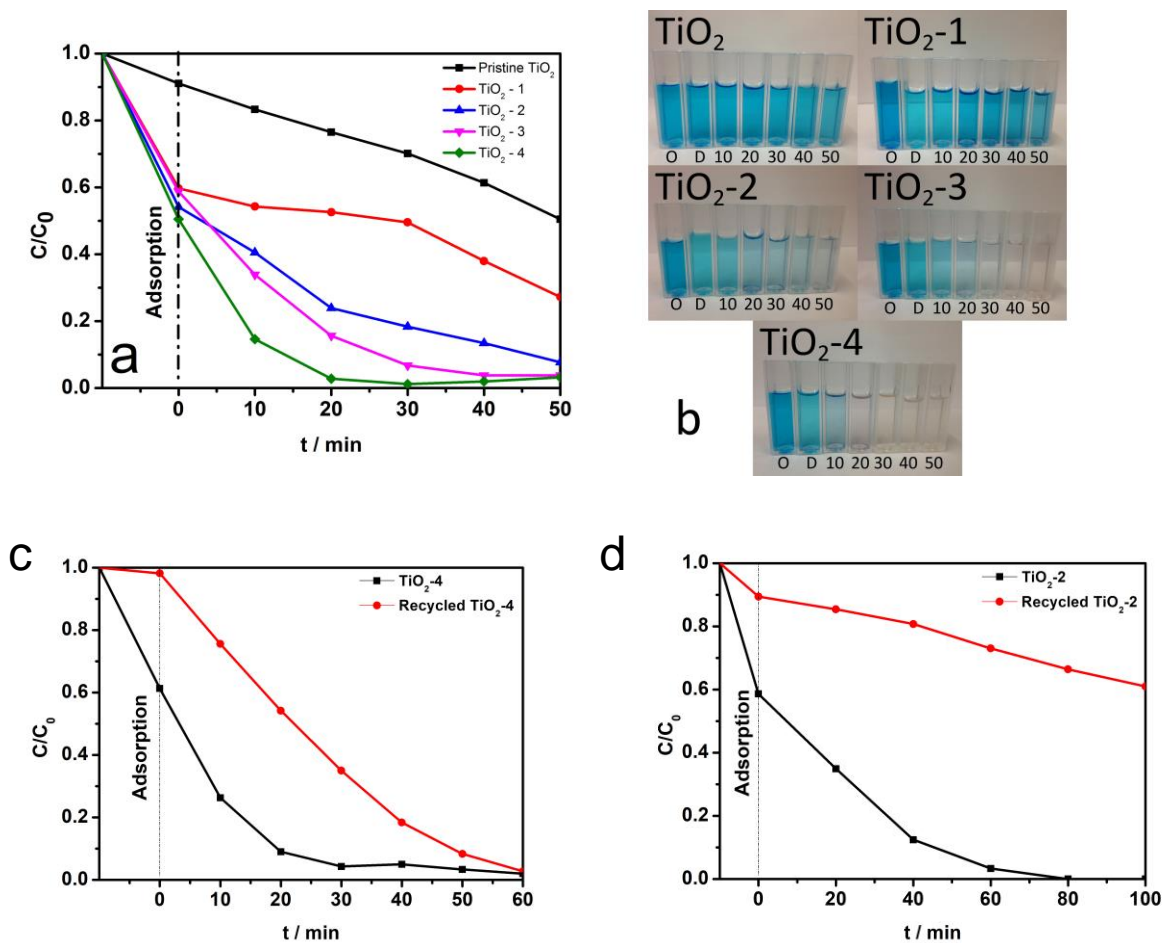
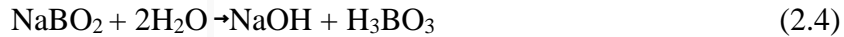
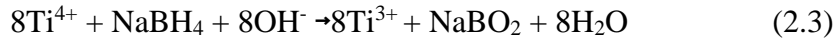
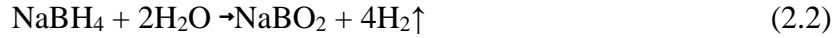


Fig. 2.8 (a) Photocatalytic degradation rate of methylene blue vs. irradiation time using pristine TiO<sub>2</sub> and as-synthesized TiO<sub>2</sub> samples. (b) The evolution of photodegradation of methylene blue solution under visible-light irradiation. (O: Original methylene blue aqueous solution; D: Dark environment; 10~50: 10~50 minutes' visible light irradiation). The photocatalytic degradation rate of methylene blue vs. irradiation time using (c) recycled TiO<sub>2</sub>-4 and (d) recycled TiO<sub>2</sub>-2.

Our work has demonstrated an improved approach to realize a controllable synthesis of Ti<sup>3+</sup>-doped TiO<sub>2</sub> by hydrothermal method using sodium borohydride (NaBH<sub>4</sub>) as a reductant. In comparison with the method reported previously, the as-prepared Ti<sup>3+</sup>-doped TiO<sub>2</sub> could be synthesized using a facile and convenient hydrothermal method. During the hydrothermal process, NaBH<sub>4</sub> can act as

a reductant directly or hydrolyze to release the reductive H<sub>2</sub> (Reaction 2.2). In such a reducing atmosphere, the reduction of Ti<sup>4+</sup> is facilitated by atomic hydrogen with the generation of Ti<sup>3+</sup> on the TiO<sub>2</sub> surface (Eq. 2.3).



With the increasing amount of NaBH<sub>4</sub> applied in the hydrothermal treatment, more hydrogen was released from the NaBH<sub>4</sub> hydrolytic process to generate a higher pressure at a mild temperature. Therefore, the TiO<sub>2</sub>-4 sample could have the highest defect concentration. In addition, the high concentration of NaBH<sub>4</sub> not only induces a higher pressure due to the generation of H<sub>2</sub> but also results in stronger alkali environment that originates from further hydrolysis of NaBO<sub>2</sub> (Reaction 2.4). Under such a condition, part of anatase TiO<sub>2</sub> transformed into rutile TiO<sub>2</sub> with the evolution of nanoparticles into hierarchical structures. According to the XPS results, Ti 2p peaks of the TiO<sub>2</sub> shift to a lower binding energy, confirming the presence of Ti<sup>3+</sup> decorating on the surface of as-obtained TiO<sub>2</sub>-4. In addition, oxygen vacancies are also produced during the hydrothermal process which can trap photo-excited electrons together with the additional formation of Ti<sup>3+</sup>. Thus, it is reasonable that the TiO<sub>2</sub>-4 sample possesses the highest photocatalytic activity since the hierarchical structure can multiply UV light absorption which results in a high efficiency of light-harvesting. Moreover, given the fact that P25 TiO<sub>2</sub> with mixed phases of rutile and anatase possess a higher catalytic activity than pure phase rutile and anatase TiO<sub>2</sub> and TiO<sub>2</sub>-4 exhibited the highest photocatalytic degradation efficiency of methylene blue despite the fact that the BET surface area of TiO<sub>2</sub>-4 is smaller than those of the pristine TiO<sub>2</sub> and TiO<sub>2</sub>-3, it is reasonable to deduce that the

hierarchical structure, the mixed phase (rutile and anatase), and the  $\text{Ti}^{3+}$  defects in the  $\text{TiO}_2$ -4 may synergistically contribute to enhancing the catalytic activity. It should be noted that the band gap of  $\text{TiO}_2$ -4 based on the Kubelka-Munk function is 3.1 eV, which is slightly smaller than that of pristine  $\text{TiO}_2$  (3.28 eV), confirming that adding  $\text{NaBH}_4$  as a reductant causes the absorption edge of  $\text{TiO}_2$  to shift to a lower energy region. Therefore, this study may offer a simple and low-cost route to functionalize the  $\text{TiO}_2$  and enhance its visible light absorption ability with a narrowed band gap, thereby leading to an improved photocatalytic activity.

## 2.4 Summary and conclusions

In summary, a set of  $\text{Ti}^{3+}$ -doped  $\text{TiO}_2$  samples with controllable photocatalytic properties were designed and prepared using a hydrothermal method *via* tuning the amount of  $\text{NaBH}_4$ . The as-developed method showed a well-controlled manner in tuning the surface properties of  $\text{TiO}_2$ , as evidenced by color changes from white, light yellow, light grey, to dark grey upon adjusting the amount of  $\text{NaBH}_4$ . In addition, we firstly reported that with a high concentration of  $\text{NaBH}_4$  applied in the hydrothermal reaction, a high pressure and strong alkali environment were introduced to facilitate the conversion of anatase  $\text{TiO}_2$  into rutile  $\text{TiO}_2$  with the evolution of nanoparticles into hierarchical structures. More importantly, it is demonstrated that the as-developed  $\text{Ti}^{3+}$ -doped  $\text{TiO}_2$  with a mixed phase and nanostructure can potentially lower the recombination rate of electron-hole pairs due to the presence of  $\text{Ti}^{3+}$  and oxygen vacancies that are able to trap photo-excited electrons on the surface. Furthermore, with the absorption edge of  $\text{TiO}_2$  shifting to the visible-light region by adding  $\text{NaBH}_4$  as a reductant, the synthesized  $\text{TiO}_2$  is expected to exhibit a higher photocatalytic activity and efficiency.



# CHAPTER 3 METALLIC $\text{CoS}_2$ NANOWIRES FOR SUPERCAPACITORS

## 3.1 Introduction

Among the TMD materials, vertically-aligned  $\text{CoS}_2$  NWs have a variety of advantages for supercapacitor applications. Metallic  $\text{CoS}_2$  NWs synthesized directly on the current collector with a good electrical connection enable efficient charge transfer between the active  $\text{CoS}_2$  materials and the current collector. In addition, the open spaces between the vertical NWs lead to a large accessible surface area and afford rapid mass transport. Moreover, the robust  $\text{CoS}_2$  NW structure results in high stability of the active materials during long-term operation. This chapter introduces the vertically-aligned metallic  $\text{CoS}_2$  NWs for supercapacitor applications, which expands the opportunities for transition metal sulfide-based nanostructures in emerging energy storage applications.

## 3.2 Experimental methods

### 3.2.1 Material synthesis

Vertically-aligned metallic  $\text{CoS}_2$  NWs were prepared by a two-step synthesis procedure reported in our previous study<sup>217</sup>. In the first step, vertically-aligned cobalt hydroxide carbonate hydrate ( $\text{Co}(\text{OH})(\text{CO}_3)_{0.5} \cdot x\text{H}_2\text{O}$ ; “CHCH”) NWs were synthesized directly on carbon cloth or graphite disc substrates by a hydrothermal method. In this step, the substrate was affixed to a glass support using carbon tape and suspended in the reaction mixture to prevent solid precipitates from accumulating on the surface. In the second step, the as-prepared CHCH NWs on the carbon cloth

or graphite substrate were thermally sulfidized to  $\text{CoS}_2$  using elemental sulfur powder as the sulfur precursor. The as-synthesized  $\text{CoS}_2$  NWs were evaluated on both carbon cloth and graphite disc current collector substrates in a three-electrode system for supercapacitors. The material synthesis process was carried out through collaboration with Dr. Shun Mao from the University of Wisconsin-Milwaukee and Mr. Matthew S. Faber from the University of Wisconsin-Madison.

### **3.2.2 Material characterization**

A Hitachi S-4800 scanning electron microscope (SEM) equipped with an energy-dispersive spectroscopy (EDS) analyzer was used for structural and elemental characterization of the prepared samples. Raman spectroscopy was conducted with a Renishaw Raman microscope (Bruker RFS 100/S spectrometer).

### **3.2.3 Supercapacitor measurements**

For the supercapacitor measurements, the  $\text{CoS}_2$  NW-based supercapacitors were evaluated in a three-electrode system. The as-synthesized  $\text{CoS}_2$  NWs on carbon cloth or graphite disc substrates were directly used for the capacitor test (i.e., without a binder) in a 6 M  $\text{KOH}(aq)$  electrolyte solution. The electrochemical performance of the supercapacitors was tested using cyclic voltammetry, galvanostatic charge/discharge, and electrochemical impedance spectroscopy techniques on a CHI 600 electrochemical workstation under ambient conditions.

### **3.2.4 Capacitor performance**

The specific capacitances of the  $\text{CoS}_2$  NWs were calculated from the cyclic voltammetry (CV) and galvanostatic charge/discharge results. From the CV test, the mass-specific capacitance of  $\text{CoS}_2$

NWs on a carbon cloth or graphite disc substrate ( $C_{cv}$ , unit: F/g) was calculated by the following equation:

$$C_{cv} = \frac{1}{m\nu\Delta V} \int I(V)dV, \quad (4.1)$$

where  $m$  is the mass of the single electrode (unit: g),  $\nu$  is the potential scan rate (unit: V/s),  $I(V)$  is the measured current (unit: A), and  $\Delta V$  is the potential range (unit: V).

From the galvanostatic charge/discharge test, the mass-specific capacitance of CoS<sub>2</sub> NWs on a carbon cloth or graphite disc substrate ( $C_g$ , unit: F/g) was calculated by the following equation:

$$C_g = \frac{2i\Delta t}{m\Delta U}, \quad (4.2)$$

where  $i$  is the discharge current (unit: A),  $\Delta t$  is the discharge time (unit: s), and  $\Delta U$  is the voltage drop upon discharging (unit: V).

The area specific capacitance of CoS<sub>2</sub> NWs on a carbon cloth or graphite disc substrate ( $C_a$ , unit: F/cm<sup>2</sup>) was calculated by the following equation:

$$C_a = \frac{2i\Delta t}{a\Delta U}, \quad (4.3)$$

where  $a$  is the surface area of the carbon cloth/graphite disc substrate (unit: cm<sup>2</sup>).

The energy density ( $E$ , unit: Wh/kg) and power density ( $P$ , unit: W/kg) of the capacitor were calculated by the following equations, respectively:

$$E = \frac{1}{8} C_g \Delta U^2, \quad (4.4)$$

$$P = \frac{E}{\Delta t}. \quad (4.5)$$

### 3.3 Results and discussion

The synthesis procedure used in this study yields high-quality, vertically-aligned CoS<sub>2</sub> NWs in large quantities on both carbon cloth and graphite disc substrates, as shown in the SEM images of

Fig. 3.1 The CoS<sub>2</sub> NWs typically exhibit a conical shape and textured surface, with an average diameter of approximately 100-200 nm. The CoS<sub>2</sub> NWs generally grow into dense, radial sea urchin-like structures with NW lengths around 5 μm (cf. Fig. 3.1e). These structures are particularly advantageous in supercapacitor applications since the open spaces between the vertical CoS<sub>2</sub> NWs lead to a large accessible surface area of the active materials and afford easy and quick channels for mass (ion and electrolyte) transport. As shown in Fig. 3.1, the CoS<sub>2</sub> NW morphologies are similar on both substrate types, and the NWs uniformly cover the entire substrate surface.

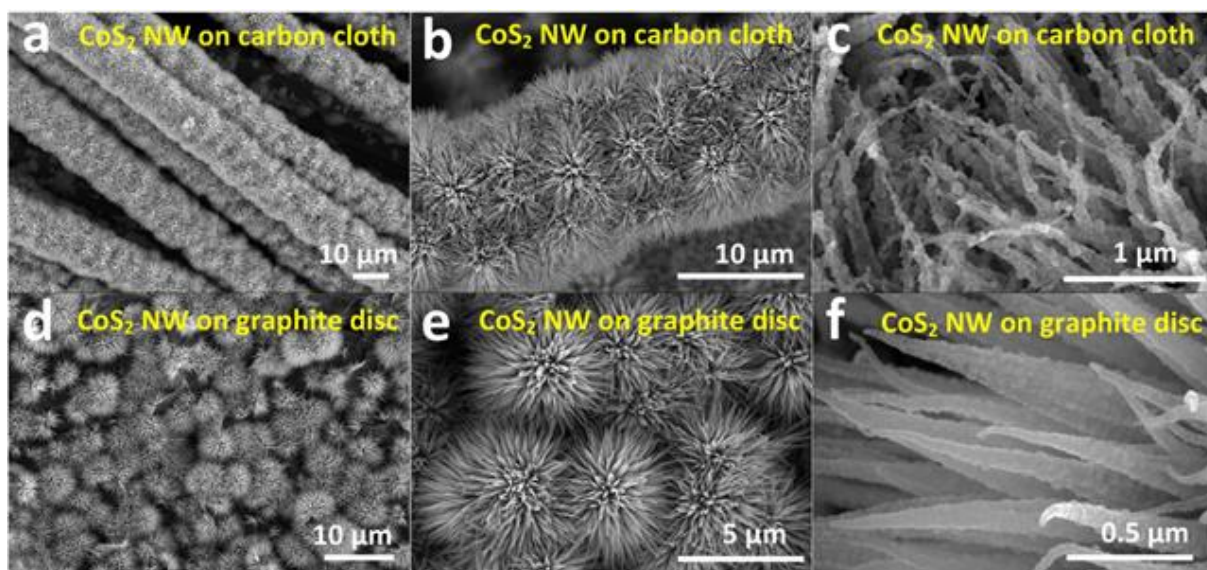


Fig. 3.1 SEM images of CoS<sub>2</sub> NWs on (a-c) carbon cloth and (d-f) graphite disc substrates.

To investigate the elemental composition of the CoS<sub>2</sub> NWs, EDS elemental mappings of the as-prepared materials were collected (Fig. 3.2). Cobalt and sulfur are clearly identified in the mapping data of the CoS<sub>2</sub> NWs, and the cobalt and sulfur signals correspond accordingly, suggesting that the NWs are indeed composed of cobalt and sulfur. Formation of the cobalt pyrite phase was confirmed by the Raman peak located at 393 cm<sup>-1</sup> (Fig. 3.3), which is the primary Raman peak of

CoS<sub>2</sub> (inset of Fig. 3.3) <sup>213</sup>. At the same time, the strong D and G bands of graphitic carbon appear at 1,348 and 1,584 cm<sup>-1</sup> in the Raman spectrum, respectively, due to the graphite disc substrate <sup>204</sup>. To investigate the capacitor performance of the CoS<sub>2</sub> NW electrodes, the carbon cloth and graphite disc substrates coated with CoS<sub>2</sub> NWs were evaluated in a three-electrode system using 6 M KOH(aq) as the electrolyte.

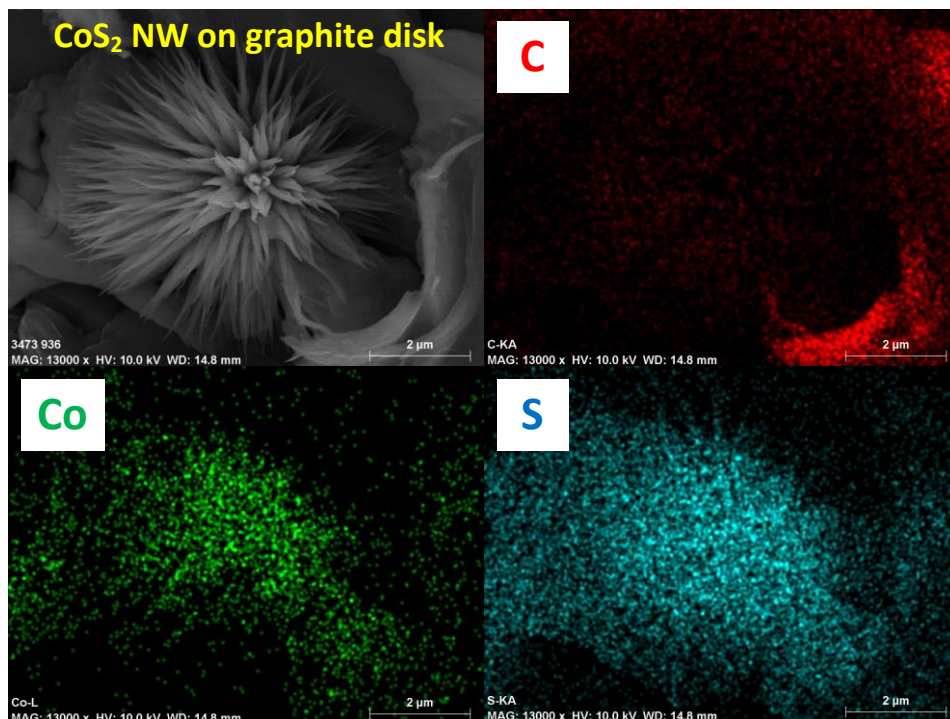


Fig. 3.2 SEM image and EDS elemental mappings of the CoS<sub>2</sub> NWs on graphite disc substrate. The cobalt and sulfur signals match well with each other and with the nanowire structure shown in the SEM image. The carbon signal results from the graphite substrate.

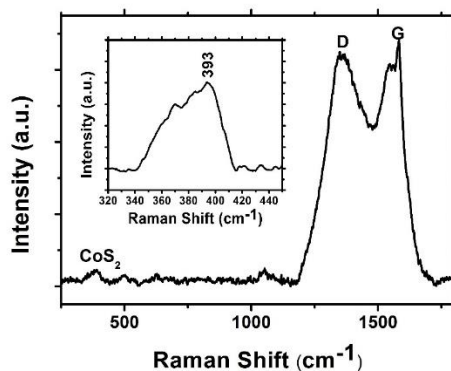


Fig. 3.3 Raman spectrum of the CoS<sub>2</sub> NWs on graphite disc substrate. The inset highlights the Raman spectrum in the range of 320-450 cm<sup>-1</sup>.

Figure 3.4a shows the cyclic voltammetry (CV) characterization of the CoS<sub>2</sub> NWs on a carbon cloth substrate with various scan rates from 10 to 100 mV/s. In order to study the effect of a blank carbon cloth for capacitance, the CV curve of a blank carbon cloth electrode at 0.01 V/s is shown in Fig. 3.5. All cyclic voltammograms exhibit a common shape suggestive of typical pseudocapacitive characteristics<sup>206</sup>. In the electrochemically reversible electron transfer process, the main reactions involve the Co<sup>2+</sup>/Co<sup>3+</sup> redox couple, possibly mediated by the OH<sup>-</sup> ions in the alkaline electrolyte<sup>203,211</sup>. The oxidation and reduction peaks are not significant at high scan rates (0.05 and 0.1 V/s) but are more evident at lower scan rates (0.01 V/s). It should be noted that the current resulting from the bare carbon cloth substrate is very low (Fig. 3.4a) compared with those bearing the CoS<sub>2</sub> NW active materials. Hence, the observed capacitance is mainly attributed to the CoS<sub>2</sub> NWs<sup>205</sup>. The specific capacitance of CoS<sub>2</sub> NWs on the carbon cloth substrate was calculated based on the scan rates and reaction currents in the CV traces. As shown in Fig. 3.4b, the CoS<sub>2</sub> NWs on the carbon cloth show a specific capacitance of 174.1 F/g (0.206 F/cm<sup>2</sup>) at 10 mV/s, which decreased to 83.7 F/g (51.9% decrease) when the scan rate increased to 100 mV/s. Galvanostatic charge-discharge curves of the CoS<sub>2</sub> NWs on the carbon cloth at different current densities in the

potential window of 0-0.4 V are shown in Fig. 3.4c. All of the curves are symmetrical in shape during the charge-discharge process, presenting advantageous supercapacitive behaviors<sup>208</sup>. As expected, when the current increases, the discharge time decreases. Based on the discharge times from Fig. 3.4c, a set of specific capacitances against various current densities were calculated (Fig. 3.4d). The specific capacitances of CoS<sub>2</sub> NWs on the carbon cloth substrate are 362, 355, 255 and 170 F/g (0.43, 0.42, 0.3 and 0.2 F/cm<sup>2</sup>) at current densities of 0.5, 1, 5 and 10 A/g, respectively. The good performance of the vertically-aligned CoS<sub>2</sub> NWs as an electrode material for supercapacitors is likely attributable to the open structure of the active materials, which accelerates the infiltration of the electrolyte and also provides a more active surface for faster redox reactions.

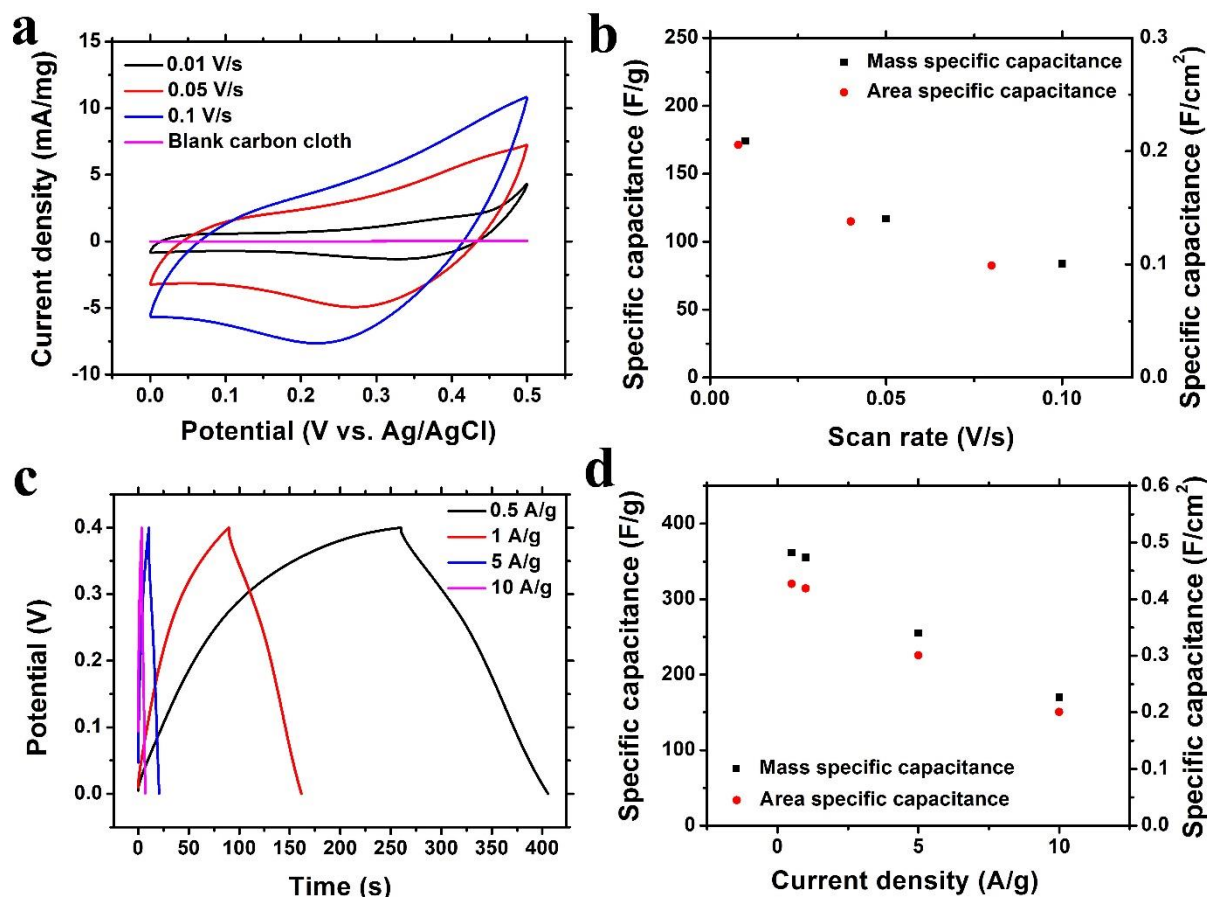


Fig. 3.4 Capacitive performance of the CoS<sub>2</sub> NWs on the carbon cloth substrate with an active material loading of 1.18 mg/cm<sup>2</sup> based on geometric area. (6 M KOH(aq) electrolyte.) (a) Cyclic voltammograms of the CoS<sub>2</sub> NWs on carbon cloth substrate at different scan rates from 10 to 100 mV/s. (b) Specific capacitance versus potential scan rate for the CoS<sub>2</sub> NWs on carbon cloth substrate. (c) Galvanostatic charge/discharge curves of the CoS<sub>2</sub> NWs on the carbon cloth substrate at different mass specific currents. (d) Specific capacitance versus discharge mass specific current for the CoS<sub>2</sub> NWs on the carbon cloth substrate. Mass and area-specific capacitances were calculated using the total mass of the CoS<sub>2</sub> NWs and geometric area of the carbon cloth substrate, respectively.

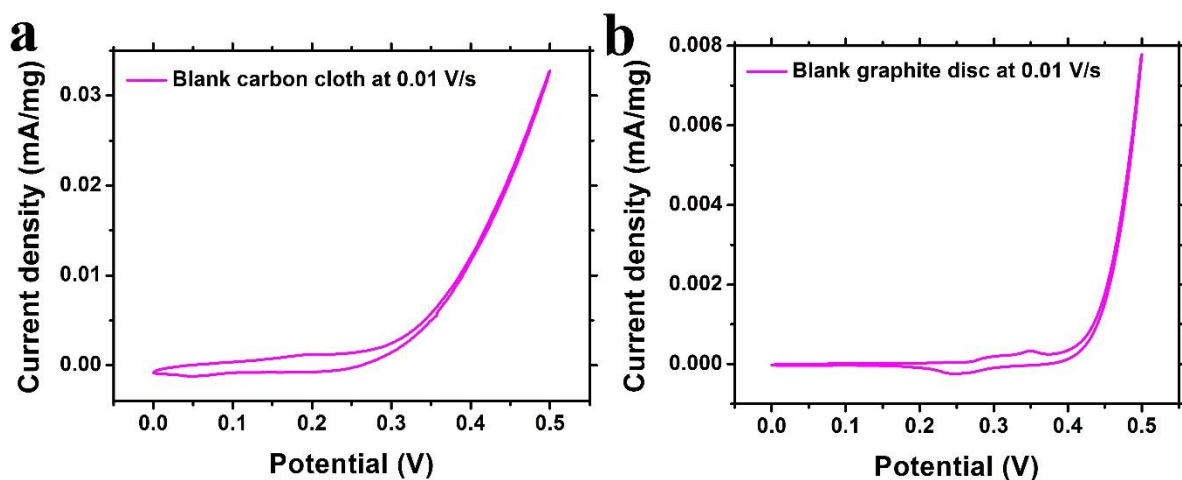


Fig. 3.5 CV curves at 0.01 V/s for CoS<sub>2</sub> NWs on (a) blank carbon cloth substrate and (b) blank graphite disc substrate.

The electrochemical capacitive properties of the CoS<sub>2</sub> NWs on the graphite disc substrate were also characterized by CV and galvanostatic charge-discharge tests. As shown in Fig. 3.6a, the shape of the CV curves recorded in the potential range of 0 to 0.5 V shows more significant pseudocapacitive characteristics (i.e., oxidation and reduction peaks) of the CoS<sub>2</sub> NWs, and the peak locations match with those from a previous study on hollow-sphere CoS<sub>2</sub> supercapacitors<sup>203</sup>. The CV curve of a blank graphite disc electrode at 0.01 V/s are shown in Fig. 3.7 The specific capacitance of the CoS<sub>2</sub> NWs on the graphite disc was calculated as 828, 377 and 275 F/g (1.236, 0.562 and 0.411 F/cm<sup>2</sup>) at scan rates of 10, 50 and 100 mV/s, respectively (Fig. 3.6b). Similar to the carbon cloth substrate, the reaction currents from a bare graphite disc are very small (Fig. 3.6a), indicating that the observed currents are mainly attributable to the CoS<sub>2</sub> NWs. The capacitance values of CoS<sub>2</sub> NWs on graphite disc are higher than those previously reported CoS<sub>x</sub>-based materials. For example, the specific capacitance of CoS<sub>2</sub> NWs on graphite disc (828.2 F/g, 10 mV/s) is higher than that of Co<sub>3</sub>S<sub>4</sub> hollow nanospheres (519.2 F/g)<sup>205</sup>, CoS<sub>2</sub>/graphene

nanocomposites (217 F/g)<sup>204</sup>, and CoS<sub>2</sub> nanoparticles (93 F/g)<sup>204</sup>. It is worth noting that the specific mass capacitance of the CoS<sub>2</sub> NWs on graphite disc is higher than that of the CoS<sub>2</sub> NWs on carbon cloth at the same scan rate, possibly due to the different CoS<sub>2</sub> NW loadings and packing densities on the substrates. To further assess the potential application of CoS<sub>2</sub> NWs on a graphite disc substrate as a supercapacitor electrode, galvanostatic charge-discharge measurements were carried out at various current densities ranging from 1 to 10 A/g (Fig. 3.6c). The specific capacitances of the CoS<sub>2</sub> NWs on graphite disc substrate were calculated based on the discharge mass specific current and the discharge time, and the results are plotted in Fig. 3.6d. As expected, the CoS<sub>2</sub> NWs on the graphite disc electrode exhibit a high pseudocapacitance of 322, 245, 188 and 131 F/g (0.48, 0.37, 0.28 and 0.20 F/cm<sup>2</sup>) at current densities of 0.5, 1, 5 and 10 A/g, respectively, consistent with measurements using carbon cloth electrodes.

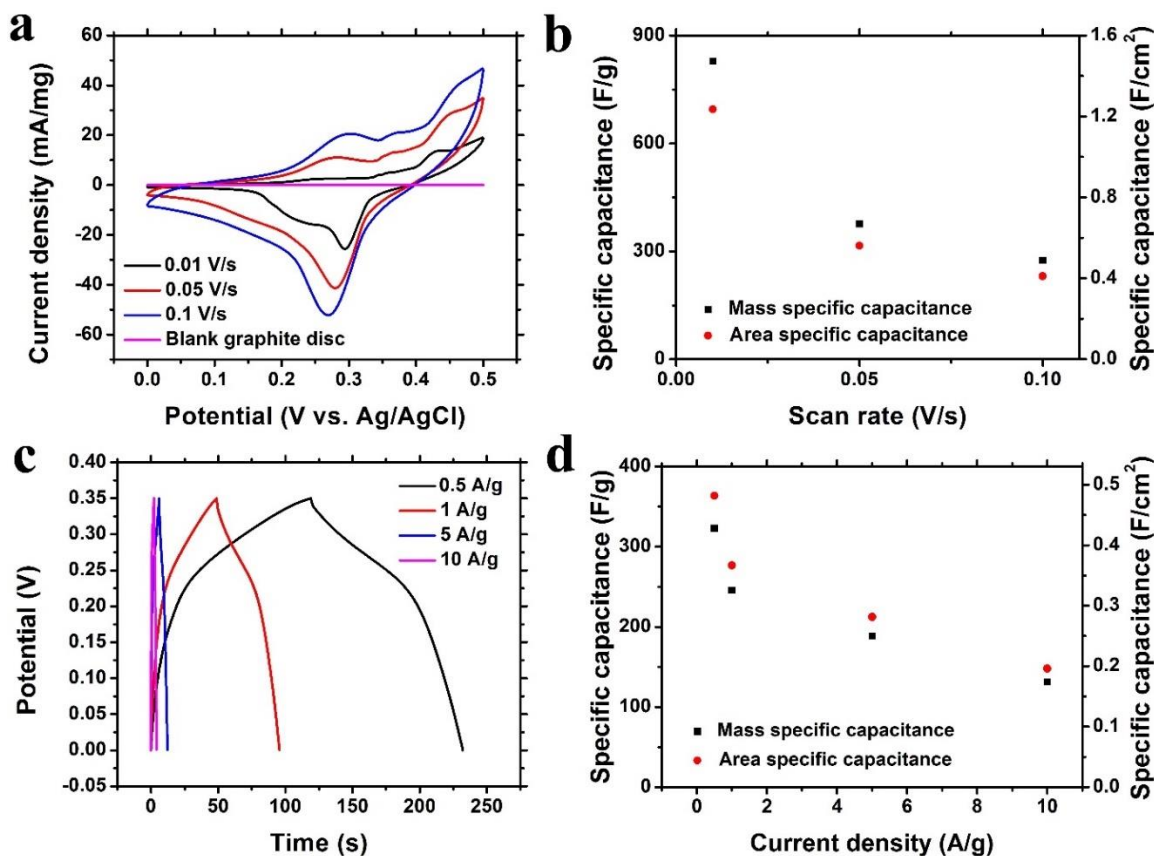


Fig. 3.6 Capacitive performance of the CoS<sub>2</sub> NWs on the graphite disc substrate with an active material loading of 1.49 mg/cm<sup>2</sup> based on geometric area. (6 M KOH(aq) electrolyte.) (a) Cyclic voltammograms of the CoS<sub>2</sub> NWs on graphite disc substrate at different scan rates from 10 to 100 mV/s. (b) Specific capacitance versus potential scan rate for the CoS<sub>2</sub> NWs on graphite disc substrate. (c) Galvanostatic charge/discharge curves of the CoS<sub>2</sub> NWs on graphite disc substrate under different mass specific currents. (d) Specific capacitance versus discharge mass specific current for the CoS<sub>2</sub> NWs on graphite disc substrate. Mass and area-specific capacitances were calculated using the mass of CoS<sub>2</sub> NWs and geometric area of the graphite disc substrate, respectively.

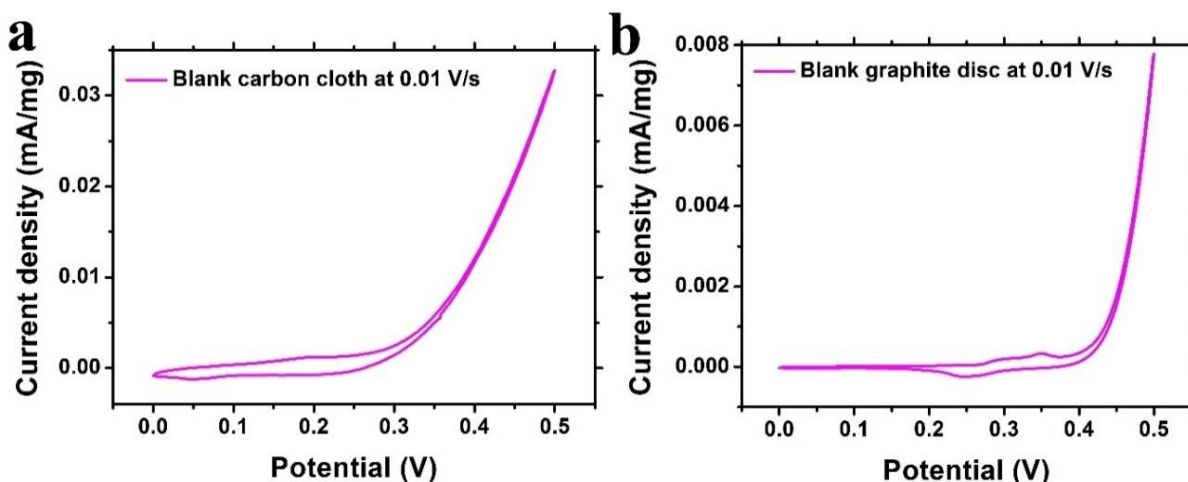


Fig. 3.7 CV curves at 0.01 V/s for CoS<sub>2</sub> NWs on (a) blank carbon cloth substrate and (b) blank graphite disc substrate.

To understand the dielectric and transport properties of the electrodes, electrochemical impedance spectroscopy (EIS) was conducted for the CoS<sub>2</sub> NWs electrodes on both substrate types. Fig. 3.8 shows the Nyquist plots for CoS<sub>2</sub> NWs in the frequency range from 0.03 Hz to 82,500 Hz measured at the equilibrium open circuit potential (0 V) with a 5 mV amplitude. The Nyquist plot of the CoS<sub>2</sub> NWs on both substrates shows a negligible semicircle in the high-frequency region and a straight line in the low-frequency region, characteristic of capacitive behavior and representative of ion diffusion in the electrode<sup>255</sup>. It is well known that a negligible semicircle for the electrode suggests frequency-dependent ion diffusion resistance towards the electrode surface, further indicating the relatively fast diffusion of ions or low interfacial charge-transfer resistance, resulting from the excellent electrical conductivity of active materials. Furthermore, the nearly vertical line indicates that the electrode is close to an ideal capacitor. The equivalent series resistance (ESR) of the supercapacitor can be estimated according to the X-intercept of the Nyquist plots (insets of Figs. 3.8a and 3.8b). The CoS<sub>2</sub> NWs on the carbon cloth and graphite disc substrates possess very

small ESR values (1.15  $\Omega$  for carbon cloth and 1.30  $\Omega$  for graphite disc), owing to the metallic conductivity of the CoS<sub>2</sub> NWs and the direct electrical contact to the current collector.

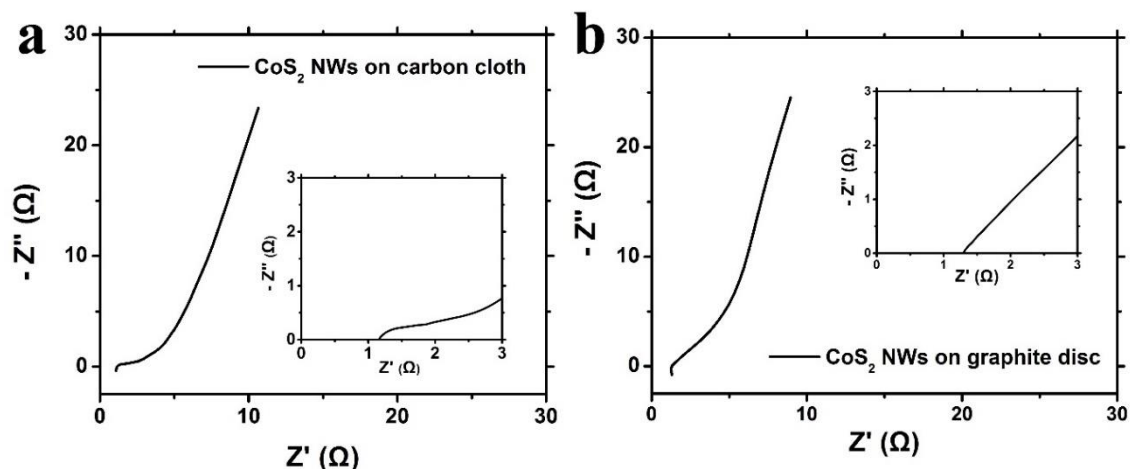


Fig. 3.8 Nyquist plots of the CoS<sub>2</sub> NWs (a) on carbon cloth and (b) graphite disc substrate. The inset spectra highlight the data at a high frequency.

The cycling performance of CoS<sub>2</sub> NWs on carbon cloth and graphite disc substrates (Fig. 3.9a) was examined by charge-discharge testing at a mass-specific current of 5 A/g. Remarkably, only ~2.5% of the capacitance fades for CoS<sub>2</sub> NWs on carbon cloth and no capacitance is lost for CoS<sub>2</sub> NWs on graphite disc after 4,250 cycles, representing excellent cycling stability. The small capacitance increase or fluctuations might originate from “active site activation” of the CoS<sub>2</sub> NWs during the charge-discharge process<sup>203</sup>. Importantly, this cycling performance of CoS<sub>2</sub> NWs is outstanding among CoS<sub>x</sub>-based supercapacitors. In general, transition metal sulfide-based pseudocapacitors suffer from instability during long-term operation due to non-reversible redox reactions or activity loss during the charge/discharge process. Additionally, some metal sulfides have relatively low stability in aqueous electrolyte solutions. A review of the previous studies on CoS<sub>x</sub>-based supercapacitors shows that typical cycling performance includes: 91.4% retention

after 2,000 cycles for  $\text{Co}_9\text{S}_8$  nanotubes<sup>206</sup>, 91% retention after 500 cycles for carbon nanotube/CoS composites<sup>256</sup>, 90.4% retention after 1,000 cycles for  $\text{Co}_3\text{S}_4$ /reduced graphene oxide composite<sup>205</sup>, 90.1% retention after 2,000 cycles for  $\text{CoS}_2$  hollow spheres<sup>203</sup>, and 81.2% retention for CoS NWs after 500 cycles<sup>207</sup>. This comparison clearly shows that the  $\text{CoS}_2$  NWs exhibit superior long-term stability as compared to previously reported  $\text{CoS}_x$ -based electrodes. This is likely due to the direct synthesis of the  $\text{CoS}_2$  NWs on the current collectors and the unique metallic properties of the  $\text{CoS}_2$  NWs. The Ragone plots are shown in Fig. 3.9b further demonstrate the good rate performance of the  $\text{CoS}_2$  NWs with high energy and power densities. The  $\text{CoS}_2$  NWs show an energy density of 7.2 Wh/kg at a power density of 0.18 kW/kg and a high power density of 3.6 kW/kg at an energy density of 3.4 Wh/kg. Compared with the  $\text{CoS}_2$  NWs on carbon cloth, the  $\text{CoS}_2$  NWs on graphite disc substrate shows an energy density of 5.0 Wh/kg at a power density of 0.16 kW/kg and 2.0 Wh/kg at a power density of 3.2 kW/kg. It is well known that charge-discharge voltage range has a significant impact on the energy density of supercapacitors. In this study, the relatively low energy density is likely due to the small potential range used in the charge/discharge test, which is limited by the alkaline aqueous electrolyte and possible oxygen evolution reactions at high potentials. By using organic solvents, larger potential ranges could be utilized, which can possibly lead to higher energy densities.

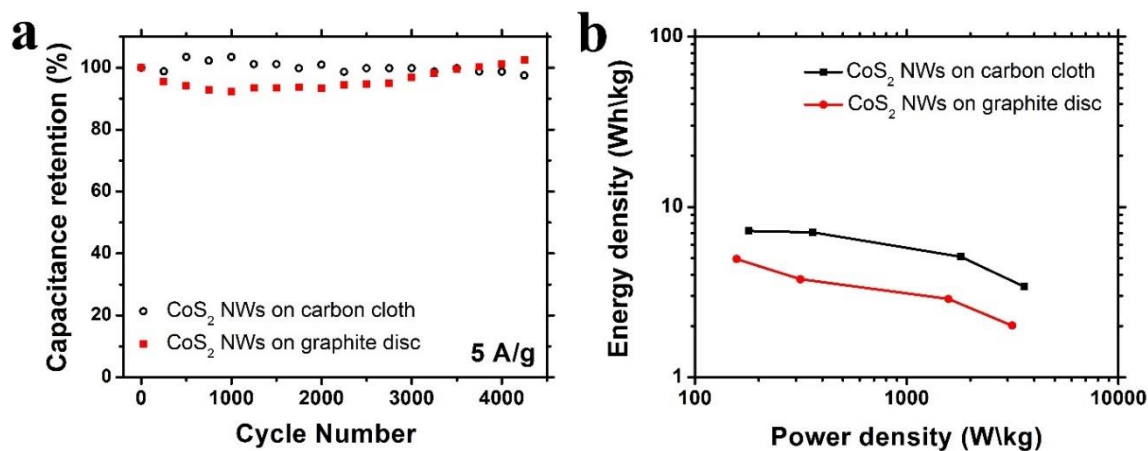


Fig. 3.9 (a) Cycling stability of the CoS<sub>2</sub> NWs on both substrates tested at a mass-specific current of 5 A/g. (b) Ragone charts of the CoS<sub>2</sub> NWs on carbon cloth and graphite disc substrates.

### 3.4 Summary and conclusions

To summarize, vertically-aligned metallic CoS<sub>2</sub> NWs synthesized directly on carbon cloth or graphite disc current collectors exhibit promising performance in supercapacitors, among the best reported for CoS<sub>x</sub>-based active materials. The open CoS<sub>2</sub> NW structure leads to a large accessible surface area and resists aggregation of the active material, resulting in a high specific capacitance. Notably, because the CoS<sub>2</sub> NWs were synthesized directly on the current collecting electrodes, the supercapacitors show excellent cycling stability. The as-reported metallic CoS<sub>2</sub> NWs represent a novel transition metal sulfide-based active nanomaterial for supercapacitors. Moreover, with their unique structures and outstanding properties, metallic CoS<sub>2</sub> NWs could be attractive for many other energy device applications, *e.g.*, batteries and fuel cells.

# CHAPTER 4 CRUMPLED GRAPHENE/TUNGSTEN DISULFIDE/TUNGSTEN TRIOXIDE TERNARY NANOHYBRIDS FOR ELECTROCATALYSIS

## 4.1 Introduction

Transition metal oxides and dichalcogenides are promising candidates for platinum-free electrocatalysts in renewable energy applications. In this chapter, we present an aerosol processing method for facile and green synthesis of reduced graphene oxide (rGO)/tungsten disulfide ( $\text{WS}_2$ )/tungsten trioxide ( $\text{WO}_3$ ) ternary nanohybrids in order to combine the benefits of TMOs and TMDs. The crumpled graphene/ $\text{WS}_2$ / $\text{WO}_3$  (CGTH) catalyst shows a superior electrocatalytic activity in the HER. This chapter introduces synthesis and characterization of CGTH, together with a mechanistic understanding of its electrocatalytic properties.

## 4.2 Experimental methods

### 4.2.1 Material synthesis

The crumpled graphene/ $\text{WS}_2$ / $\text{WO}_3$  (CGTH) was fabricated through a one-step aerosolization of GO suspension (ACS Materials, 1 mg/ml) mixed with  $(\text{NH}_4)_2\text{WS}_4$  (Alfa Aesar, 10 mg/ml). GO sheets provide active sites for the adsorption of precursor ions and nanocrystal growth. A brief (5 min) sonication was conducted on the mixed suspension for a better dispersion and ion adsorption. The as-prepared suspension was then aerosolized by an ultrasonic nebulizer (2.4 MHz). The aerosolized mist was carried by an inert gas (Argon, 1 L/min) and passed through a tube furnace preheated at 800 °C. The capillary force generated by the rapid evaporation of the solvent leads to

the shrinkage of aerosol droplets and the compression of GO sheets.  $(\text{NH}_4)_2\text{WS}_4$  in the aerosol droplets was thermally decomposed to  $\text{WS}_2$  nanocrystals (Equation 4.1), while the nanocrystals were encapsulated by thermally-reduced GO sheets.  $\text{WS}_2$  can react with water vapor under high temperature (Equation 4.2), so the surface of the encapsulated nanocrystals is covered by  $\text{WO}_3$ .<sup>257</sup> The as-produced hybrid materials were collected by a Teflon filter at the exhaust of the tube furnace for further analysis.



For the first control group, C1,  $(\text{NH}_4)_2\text{WS}_4$  solution (10 mg/ml) was aerosolized to fabricate nanocrystals without GO. For the second control group C2, the mixture of GO and  $(\text{NH}_4)_2\text{WS}_4$  was dried under vacuum and then heated at 800 °C without the aerosolization step. For the third control group, C3,  $(\text{NH}_4)_6\text{H}_2\text{W}_{12}\text{O}_4$  instead of  $(\text{NH}_4)_2\text{WS}_4$  was used as the precursor and cone-bulized with GO to fabricate crumpled graphene/ $\text{WO}_3$  hybrids. The materials synthesis process collaborated with Yantao Chen from the University of Wisconsin-Milwaukee.

#### 4.2.2 Material characterization

A Hitachi S-4800 scanning electron microscope (SEM) equipped with an energy-dispersive spectroscopy (EDS) analyzer was used for structural and elemental characterization of the prepared samples. An FEI Talos F200X S/TEM was used for HAADF STEM imaging and elemental mapping. Raman spectroscopy was conducted with a Renishaw Raman microscope (Bruker RFS 100/S spectrometer). X-ray photoelectron spectroscopy (XPS) spectra were obtained using an HP5950A ESCA spectrometer with monochromatic Al  $K\alpha$  radiation as the X-ray source and the C1s peak at 285 eV as an internal standard. The specific surface area was

obtained using ASAP2020 (Micromeritics, U.S.A) Brunauer-Emmett-Teller (BET) nitrogen adsorption-desorption. The N<sub>2</sub> adsorption-desorption measurements were carried out at 77 K using a Quantachrome Autosorb gas-sorption system. The samples were degassed at 300 °C for 2 hours before the measurements. The specific surface area of CGTH is calculated by Brunauer-Emmett-Teller (BET) method.

#### **4.2.3 Electrochemical measurements**

For the electrochemical measurements, all the samples were evaluated in a three-electrode system. The electrochemical performance of the CGTH and control groups were tested using Linear Sweep Voltammetry and Cyclic Voltammetry techniques on a CHI 600 electrochemical workstation under ambient conditions. A platinum wire (CHI115) was used as the counter electrode. The electrolyte used for all HER experiments was 0.5 M H<sub>2</sub>SO<sub>4</sub> saturated with Ar. Same mass/density of the active materials was loaded on the working electrode. For the sample preparation, 3 mg of catalyst and 30 µl of 5 wt.% Nafion solution were dispersed in 270 µl DI water by 15 min of sonication to form a homogeneous ink. Then 5 µl of the catalyst ink (containing 50 µg of catalyst) was loaded onto a glassy carbon electrode of 3 mm in diameter (loading ~ 0.707 mg/cm<sup>2</sup>). All potentials were measured against an Ag/AgCl reference electrode (1.0 M KCl, Sigma) and converted to the RHE reference scale using  $E \text{ (vs RHE)} = E \text{ (vs Ag/AgCl)} + 0.198 \text{ V} + 0.0591 \text{ V} \cdot \text{pH}$ .

#### **4.2.4 Reversible hydrogen electrode (RHE) calibration**

For the electrochemical measurements, Ag/AgCl electrode was used as the reference electrode. It was calibrated with respect to reversible hydrogen electrode. The calibration was performed in

the high purity H<sub>2</sub> saturated electrolyte with a Pt wire as the working electrode. Cyclic voltammetry tests were run at a scan rate of 60 mV·s<sup>-1</sup>, and the first potential at which the current crossed zero was taken to be the thermodynamic potential for the hydrogen electrode reactions which shown in Fig 4.1. In 0.5 M H<sub>2</sub>SO<sub>4</sub>, E (vs RHE) = E (Ag/AgCl) + 0.198 V. All the potentials reported in this manuscript were against RHE.

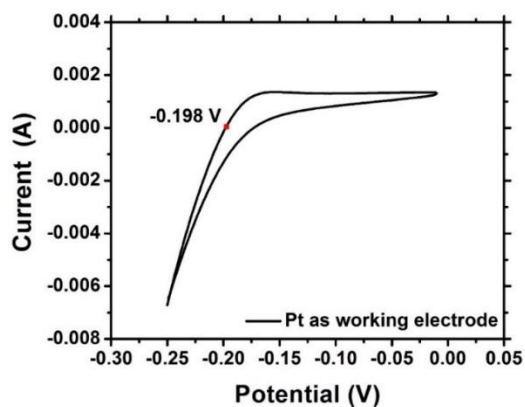


Fig. 4.1 Calibration of the reference electrode against the RHE.

### 4.3 Results and discussion

Figure 4.2 shows the experimental setup for fabricating the CGTH. GO suspension and ammonium tetrathiotungstate ((NH<sub>4</sub>)<sub>2</sub>WS<sub>4</sub>) were mixed first and then nebulized into a preheated tube furnace. GO sheets provided active sites for the adsorption of precursor ions and nanocrystals growth. The details for material synthesis can be found in Experimental Section. SEM analysis was conducted to study the structure and morphology of the CGTH. The SEM image in The SEM image in Fig. 4.3A shows that the CGTH has a size distribution from 200 to 800 nm with a 3D crumpled structure and the nanocrystals were decorated on the reduced GO (rGO) sheets. Another SEM image (Fig. 4.3B) with a higher magnification shows that the nanocrystals have a rod-like shape and the rGO sheets work as a frame/substrate for loading nanocrystals. CGTH had a smoother surface than empty crumpled graphene balls,<sup>156</sup> which can be attributed to the filling of the nanocrystals. The

swollen structure of the CGTH also indicates the ultra-high loading ratio (mass ratio of rGO:tungsten  $\sim$  1:4). Three groups of control experiments were carried out to demonstrate the unique structure and outstanding HER catalytic performance of CGTH. For the first control group (C1), the liquid suspension without GO was aerosolized under the same condition. The product showed a spherical structure due to the absence of GO as shown in Figure 4.5. In the second control group (C2), the same suspension was used as fabricating the CGTH (1 mg/ml GO with 10 mg/ml  $(\text{NH}_4)_2\text{WS}_4$ ). The suspension was directly dried under vacuum and then annealed at 800 °C for 1 hour without the aerosolization step. The as-produced material contains irregularly distributed rGO flakes and nanowires, as shown in Figure 4.5B. Regarding the third control group (C3), ammonium metatungstate ( $(\text{NH}_4)_6\text{H}_2\text{W}_{12}\text{O}_4$ ) instead of  $(\text{NH}_4)_2\text{WS}_4$  was used as the precursor and coneulized with GO to fabricate crumpled graphene/ $\text{WO}_3$  hybrids. The product of C3 has similar morphology with CGTH (see Figure 4.5C). C1 and C2 samples demonstrated that the aerosol synthesis of CGTH hybrids can achieve better material uniformity and electrical contact, which plays an important role in catalysis performance.<sup>151,258</sup> The performance of C3 sample will be compared with CGTH to demonstrate the function of  $\text{WS}_2$  in the ternary catalyst.

TEM was conducted to better understand the internal structure of CGTH. The rod-like shape of the encapsulated nanocrystals is confirmed by the TEM image in Fig. 4.3C. The precursor for fabricating the CGTH,  $(\text{NH}_4)_2\text{WS}_4$ , is decomposed into  $\text{WS}_2$  under high temperature, while  $\text{WS}_2$  is chemically unstable in the presence of water vapor at high temperature and can be partially oxidized by water to form  $\text{WO}_3$ .<sup>257</sup> The coexistence of  $\text{WS}_2$  and  $\text{WO}_3$  was further confirmed by the selected area electron diffraction (SAED) in Fig. 4.3D and the HRTEM image in Fig. 4.3E. Several obscure rings in Fig. 4.3D could be detected, which is due to the poor crystallinity of

CGTH. According to Xu et al.'s<sup>259</sup> and Wang et al.'s<sup>260</sup> studies, the possible reason for the poor crystallinity of CGTH is because the growth of crystalline WS<sub>2</sub> phase is restricted by the WO<sub>3</sub> phase. It was revealed that the measured d spacing of WS<sub>2</sub> in the nanorods is 0.617 nm, which matches well with the (002) lattice plane of WS<sub>2</sub> (0.616 nm). The measured lattice spacing of WO<sub>3</sub> in the nanorods is 0.378 nm, which is in agreement with the (020) lattice plane of WO<sub>3</sub> (0.377 nm). EDS elemental mapping analysis was also carried out for the CGTH to reveal the distribution of the W, C, O, S elements (Fig. 4.4). In Fig. 4.4, tungsten, carbon and oxygen elements are distributed uniformly on the nanohybrids, indicating the WS<sub>2</sub>/WO<sub>3</sub> nanorods are decorated uniformly on the crumpled graphene. In order to study the accurate distribution of elements on the WS<sub>2</sub>/WO<sub>3</sub> nanorod, the high angle annular dark field (HAADF) STEM imaging was conducted on the WS<sub>2</sub>/WO<sub>3</sub> nanorod with EDS elemental mapping scanning along the green arrow, as shown in Fig. 4.3F and 4.3G. The results indicate that the oxygen element has a higher intensity around the edge of the nanorod, while the sulfur element has a higher intensity near the center of the nanorod. In other words, there is a quasi core-shell structure between WS<sub>2</sub> and WO<sub>3</sub>. Most of WS<sub>2</sub> located at the center of the nanorod, while most of WO<sub>3</sub> located near the edge of the nanorod. The elemental mapping results show that sulfur is distributed on the CGTH and could be doped into the graphene basal plane via the formation of the C-S bond which has two trace peaks located at 164.2 eV and 165.4 eV<sup>261,262</sup>. There is no peak present in the XPS spectra at 164-165 eV, indicating the possibility of S-doping in CGTH is slim.

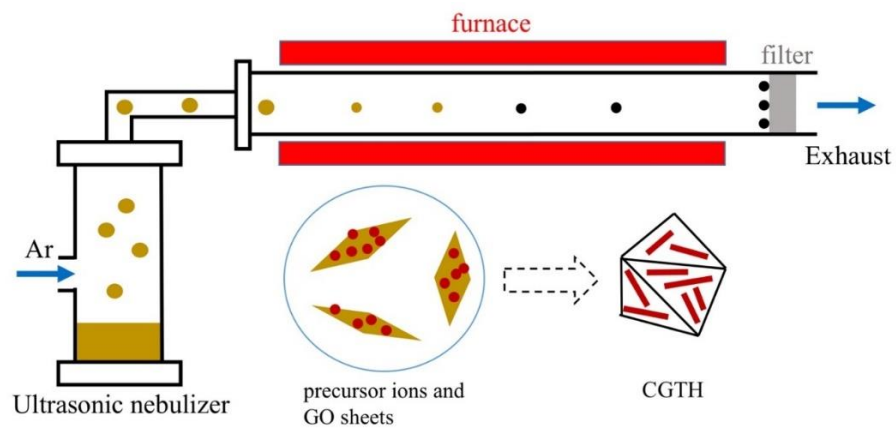


Fig. 4.2 Experimental setup for fabricating the CGTH hybrid materials. Aerosol droplets containing GO and precursor ions were carried by Ar and passed through the heated tube furnace. GO was thermally reduced and precursor ions adsorbed on GO sheets were converted into  $WS_2/WO_3$  nanocrystals.

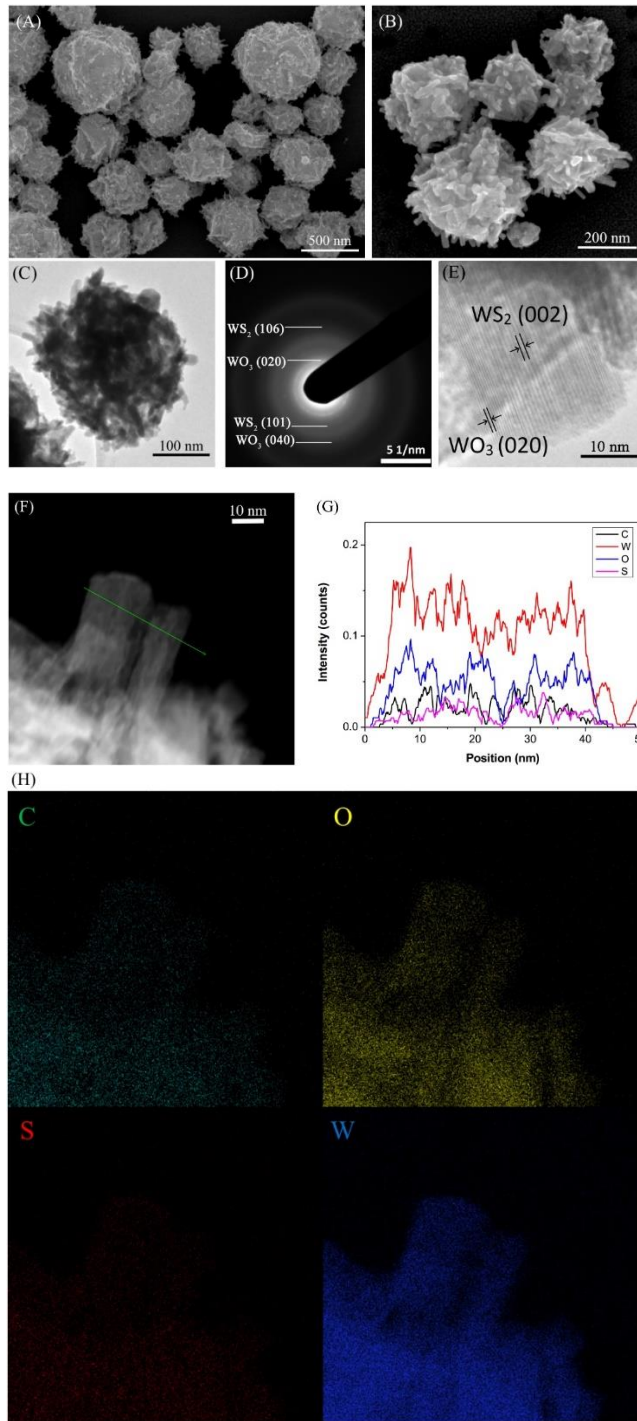


Fig. 4.3 Electron microscopy characterization of the CGTH. (A-B) SEM images of the as-produced CGTH with different magnifications. The CGTH has a 3D crumpled structure with filler materials. (C) TEM image of the CGTH confirms the rod-like shape of the encapsulated

nanomaterial and indicates the internal structure. (D) SAED pattern of the CGTH shows the lattice parameters of the encapsulated nanomaterial. (E) HRTEM image shows two distinct lattice spacings of  $WS_2$  and  $WO_3$ . The nanorod contains  $WS_2$  and  $WO_3$ . (F) HAADF STEM imaging of nanorods. (G) Elemental mapping along the green arrow in (F). (H) Elemental distribution of C, O, S, and W in (F).

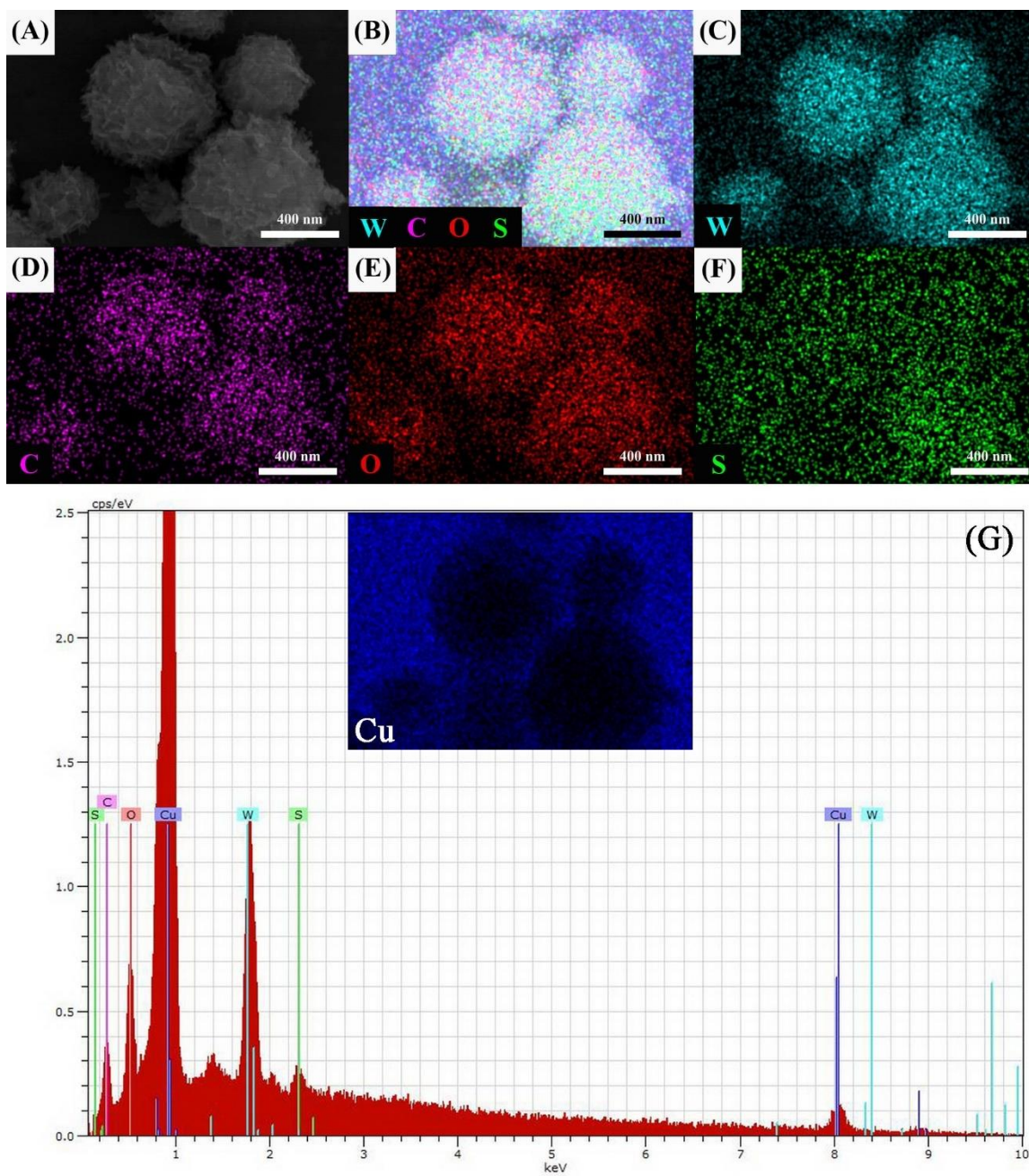


Fig. 4.4 (A) SEM image, (B-F) EDS elemental mappings of the CGTH and (G) EDAX spectrum of the CGTH with copper foil background.

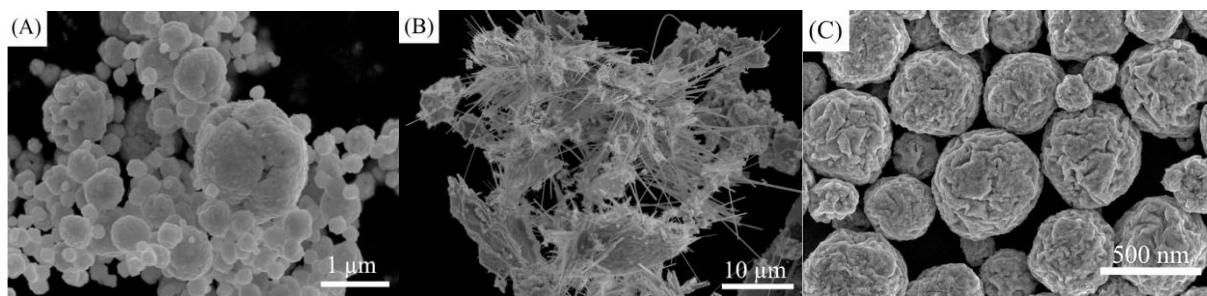


Fig 4.5 SEM images of the control groups. (A) The suspension was aerosolized without GO (C1). (B) The suspension containing GO and precursor was dried and annealed without the aerosolization step (C2). (C) GO was nebulized with  $(\text{NH}_4)_6\text{H}_2\text{W}_{12}\text{O}_4$  to fabricate the crumpled graphene/ $\text{WO}_3$  hybrids (C3).

XRD analysis was carried out to study the crystal structure of CGTH. In Fig. 4.6A, all the star marked peaks match well with the standard hexagonal  $\text{WS}_2$  diffraction peaks, and all the other diffraction peaks marked by a triangle are indexed to  $\text{WO}_3$ . The strongest  $\text{WS}_2$  peak at  $14^\circ$ , corresponding to (002), matches well with the HRTEM results. The relatively low intensity of (002) plane for  $\text{WS}_2$  reveals that only a few  $\text{WS}_2$  layers could be detected from the surface of CGTH and a compact  $\text{WO}_3$  layer formed during the synthesis process.<sup>163,263</sup> The strongest  $\text{WO}_3$  peak at  $23.4^\circ$ , corresponding to (020), matches well with the SAED results. The XRD patterns of the control groups were also collected to determine the crystal structure of the materials prepared with different approaches (Fig. 4.7). The C1 sample shows strong peaks corresponding to lattice planes of  $\text{WO}_3$  and smaller peaks of  $\text{WS}_2$ , which means without introducing the GO in the aerosolization process, most of the products were  $\text{WO}_3$  rather than  $\text{WS}_2$ . The crystallographic structure of C2 showed similar results with CGTH. Only the  $\text{WO}_3$  peaks can be observed for the material of C3, indicating the absence of  $\text{WS}_2$  by replacing the precursor during fabrication. Raman spectroscopy was conducted to further study the structure of the ternary catalysts. As shown in Fig.

4.6B, Raman peaks appear at 350.9 and 416.7  $\text{cm}^{-1}$ , corresponding to  $E_{2g}$  and  $A_{1g}$  vibration modes of  $\text{WS}_2$ , respectively, which are the primary Raman peaks of  $\text{WS}_2$  (inset of Figure 4.6B).<sup>264,265</sup> It can be seen that  $\text{WO}_3$  nanorods show two regions at 200-400 and 600-900  $\text{cm}^{-1}$ . The Raman peak observed at lower wavenumbers around 265  $\text{cm}^{-1}$  corresponds to the W-O-W bending modes of bridging oxide ions. The peak at 702  $\text{cm}^{-1}$  could be assigned to W-O-W vibration and the peak at 809  $\text{cm}^{-1}$  is attributed to crystalline  $\text{WO}_3$  stretching vibration mode of bridging oxygen of W-O-W.<sup>266,267</sup> In Fig. 4.6B, the relatively broad bands at 950  $\text{cm}^{-1}$  can be attributed to  $\text{W}6^{+}=\text{O}$  stretching mode of terminal oxygen atoms, which could be located at the surface of the nanorods.<sup>268</sup> The formation of monoclinic phase of  $\text{WO}_3$  could be confirmed by higher wavenumber peaks. As displayed on the right-hand side of the spectrum, the characteristic D and G bands of carbon materials were found at around 1,330 and 1,605  $\text{cm}^{-1}$ , respectively. Generally, the D band is referred to as the disorder or defect band which originates from a hybridized vibrational mode related to the edges of graphene; while the G band is the result of the first-order scattering of the  $E_{2g}$  mode of  $\text{sp}^2$  carbon domains. The higher intensity of D band for the CGTH ( $I_D/I_G=1.30$ ) indicates a large number of defects or edges, which is a characteristic for the 3D crumpled graphene structures.<sup>269,270</sup>

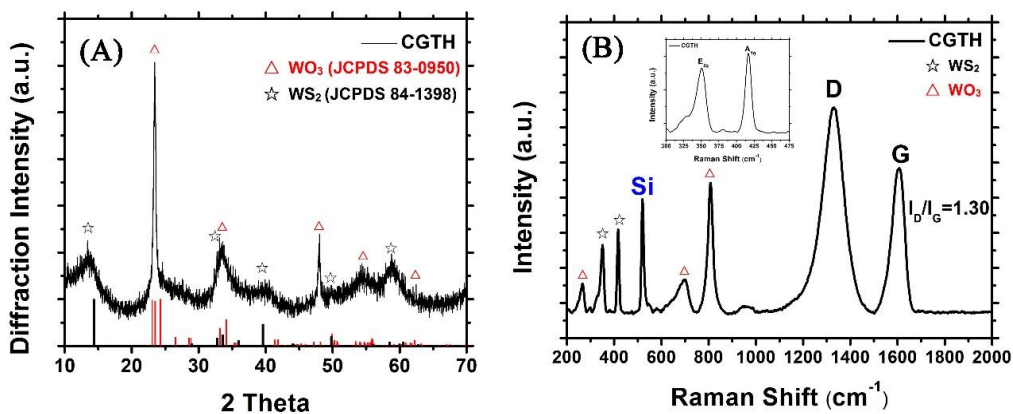


Fig. 4.6 (A) Representative XRD pattern and (B) Raman spectra of the CGTH. The inset highlights the Raman spectrum in the range of 320-450  $\text{cm}^{-1}$ .

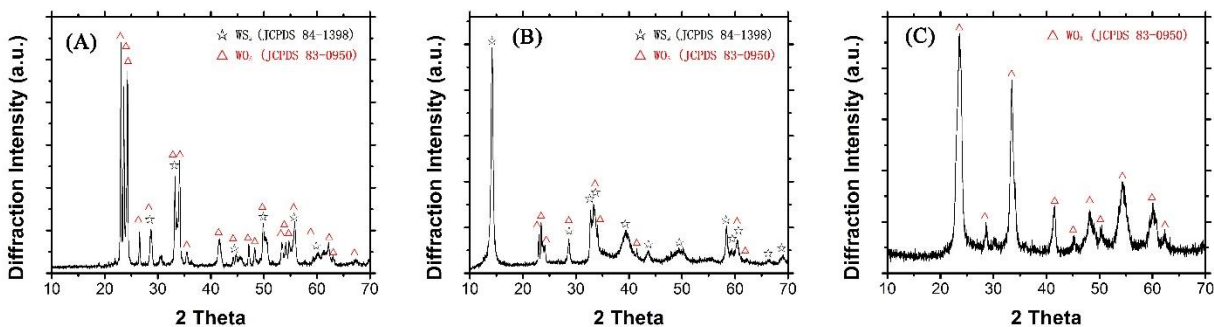


Fig. 4.7 Representative XRD pattern of the (A) C1, (B) C2, (C) C3.

XPS analysis was carried out to investigate the chemical states and surface chemical compositions of CGTH (Fig. 4.8). The XPS spectra of W4f, S2p, and O1s and the simulation results of their decomposition peaks are presented in Fig. 4.9A-C, respectively. For the W4f spectra, the peaks appear at 35.5 and 37.6 eV correspond to the W4f<sub>7/2</sub> levels of tungsten atoms for W<sup>6+</sup>-states of oxide and hydroxide.<sup>271,272</sup> It could be observed that the components of the 1T phase in the W4f spectrum appear at the binding energy of 32 eV, which is about 1 eV lower than that of the bulk WS<sub>2</sub> 2H phase.<sup>272,273</sup> Compared with the trigonal prismatic transition metal atom coordination of the 2H phase WS<sub>2</sub>, the metal atom coordination for 1T-WS<sub>2</sub> is octahedral.<sup>274</sup> Except for the structural differences, CGTH represents significantly different electronic properties depending on the evolutionary polymorph structures.<sup>275</sup> The 2H phase suggests semiconducting properties while the 1T phase indicates a metallic characteristic with a significantly enhanced conductivity, which has been reported to be an efficient hydrogen evolution catalyst.<sup>273-276</sup> Fig. 4.9B shows the S2p signals of the CGTH, where the S2p<sub>1/2</sub> located at 163.1 eV and S2p<sub>3/2</sub> located at 161.8 eV are attributed to WS<sub>2</sub>.<sup>271,277</sup> The O1s spectra of the CGTH shown in Figure 4.9C is the superposition of three peaks located at 530.2, 532.1 and 533.2 eV. The intensity at 530.2 eV is associated with the O<sup>2-</sup> ions, which is derived from the compact WO<sub>3</sub> layer. The O1s peak at 533.2 eV points to

the loosely bound oxygen mainly from H<sub>2</sub>O molecules on the surface of WO<sub>3</sub>. The peak located at 532.1 eV can be attributed to O<sup>2-</sup> in the oxygen-deficient regions with the matrix of WO<sub>3</sub>.<sup>278</sup> Considering that the OH<sup>-</sup> groups are bonded to the metal cations to maintain the charge balance in the oxygen-deficient surface region, the intensity of OH<sup>-</sup> groups is closely related to the oxygen vacancy density. To investigate the surface area and porous structure of CGTH, nitrogen adsorption-desorption isotherm curves were measured and identified as type IV, as shown in Fig. 4.8B. CGTH has a specific surface area of ~ 18 m<sup>2</sup>/g, with adsorption average pore width ~129.3 Å.

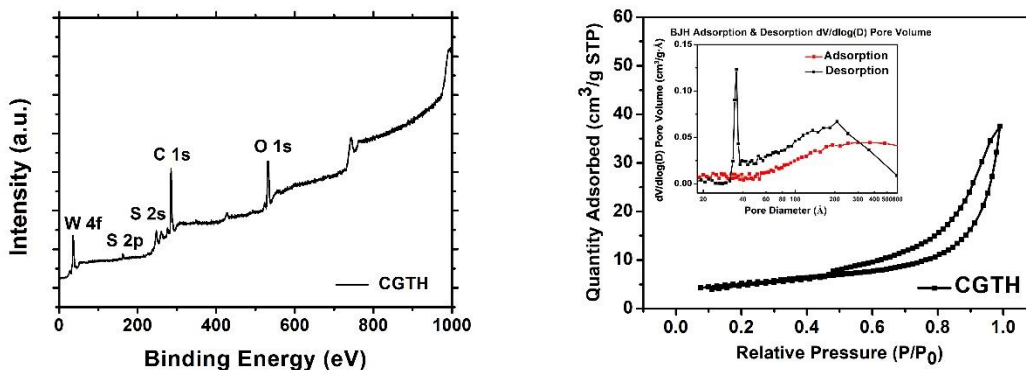


Fig. 4.8 (A) XPS spectrum of CGTH; (B) N<sub>2</sub> adsorption-desorption isotherms and BJH pore size distribution for CGTH.

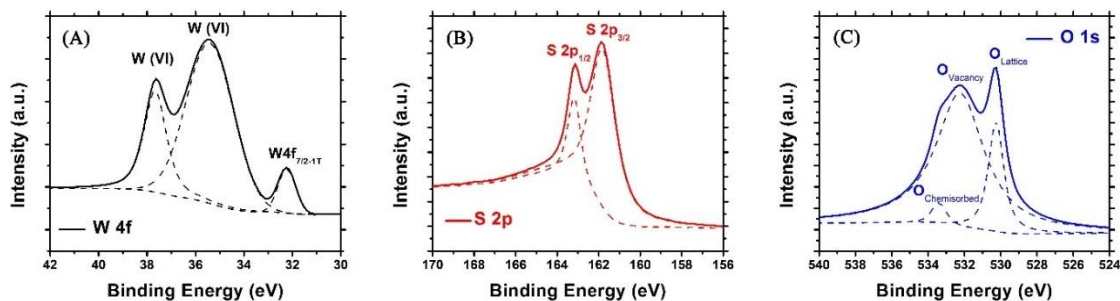


Fig. 4.9 XPS spectrum of (A) W4f, (B) S2p and (C) O1s of CGTH. The peaks in the O1s region located at 530.2, 532.1, 533.2 eV are assigned to lattice oxygen, oxygen vacancy and chemisorbed H<sub>2</sub>O, respectively.

The electrocatalytic HER activities of CGTH nanohybrids along with control groups were characterized by depositing these materials on a glassy carbon electrode and testing in a 0.5 M H<sub>2</sub>SO<sub>4</sub> solution using a three-electrode setup (see Experimental Methods section for details of reversible hydrogen electrode/RHE calibration). As a reference, a commercial Pt/C catalyst was used for comparison, which exhibited the highest catalytic performance (with a nearly 0 V onset potential). The polarization curve (i-V plot) recorded with CGTH hybrid on glassy carbon electrodes showed a small onset potential ( $\eta$ ) of 96 mV for the HER (Fig. 4.10A), which is comparable to that of Pt and implies low energy consumption in the catalytic process. In sharp contrast, C1, C2, C3 or glassy carbon alone exhibited limited HER activity with the onset potential of 400 mV for C1, 330 mV for C2, 468 mV for C3 and 520 mV for glassy carbon, respectively. The potential value at a fixed current density of 10 mA cm<sup>-2</sup> is usually used to compare the catalytic activity in HER. Based on the Linear Sweep Voltammetry (LSV) results shown in Fig. 4.10A, the potentials at a current density of 10 mA cm<sup>-2</sup> are 113 mV for CGTH, 475 mV for C1, 440 mV for C2, and 481 mV for C3, which suggest that the CGTH possesses a higher catalytic activity compared with the control groups. The value is very encouraging so far compared with the recently reported value (229 mV) for vertically-oriented WS<sub>2</sub> nanosheet sensitized by graphene.<sup>279</sup> There are three steps involved for HER in acidic medium: Volmer [Equation (4.3)], Heyrovsky [Equation (4.4)] and Tafel [Equation (4.5)] reactions.<sup>280</sup> H<sub>ads</sub> stands for the adsorbed hydrogen.



Tafel slope is an inherent property of catalysts, which depends on the rate determining step (RDS). The Tafel slope for Volmer, Heyrovsky and Tafel reactions at room temperature is calculated as 120, 40 and 30 mV/dec.<sup>280</sup> In order to investigate the HER kinetics of CGTH, the linear portions of the Tafel plots (Figure 4.10B) were fit to the Tafel equation ( $\eta = b \log j + a$ , where  $j$  is the current density and  $b$  is the Tafel slope),<sup>279</sup> yielding Tafel slopes of 28, 37, 78, 99 and 135 mV/decade for Pt/C, CGTH, C1, C2, and C3, respectively. The surface of Pt has a very high adsorbed hydrogen coverage ( $\theta_H \approx 1$ ) and is well known to proceed through the Volmer-Tafel mechanism (Equation 4.3 and 4.5). Meanwhile, the Tafel slope of CGTH is 37 mV/dec, suggesting the RDS for CGTH is Volmer-Heyrovsky mechanism. The observed small Tafel slope exhibited by CGTH can be attributed to the intimate contact between crumpled rGO and nanorods that results in a highly conductive system for facile electron transfer. For the control groups (C1-C3), the large Tafel slopes (78-135 mV/dec) indicate the sluggish HER kinetics and the corresponding RDS is Heyrovsky or Volmer reaction. The CGTH has a significantly faster HER kinetics, especially on the desorption step (Heyrovsky reaction). The HER performance especially the Tafel slope of C3 (crumpled rGO with the pure phase of  $\text{WO}_3$ ) is way below that of CGTH, which indicates that  $\text{WS}_2$  functioned as a catalyst. Yang et al.<sup>281</sup> proposed a “spillover” mechanism for HER electrocatalysis of  $\text{WO}_3$  and  $\text{WS}_2$  hybrid materials. This synergistic catalytic mechanism can be used to explain the outstanding performance of CGTH. The protons are first intercalated in the  $\text{WO}_3$  lattice and then spill over to the exposed active sites of  $\text{WS}_2$ .

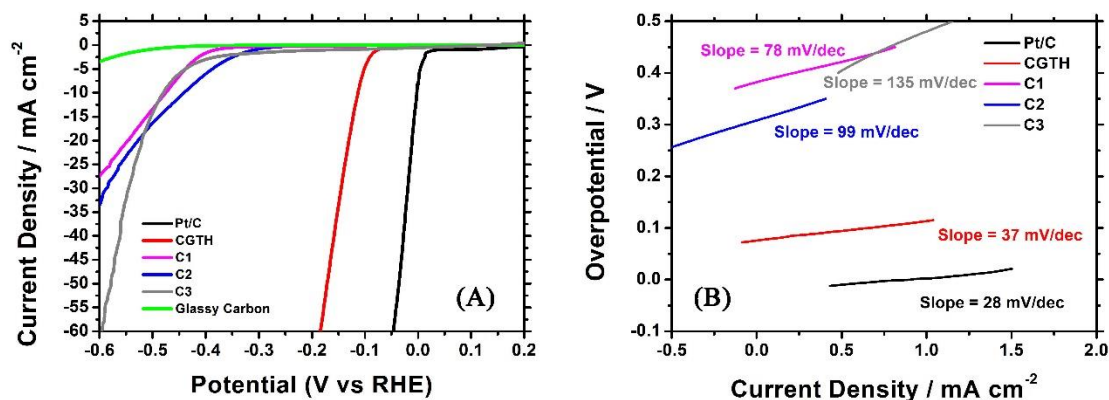


Fig. 4.10 Electrochemical measurements for the CGTH and control groups in H<sub>2</sub>SO<sub>4</sub> (0.5 M).

(A) Polarization curves obtained with several catalysts as indicated and (B) corresponding Tafel plots recorded on glassy carbon electrodes. The current density is normalized to the area (mA/cm<sup>2</sup>).

To further understand the electrochemical behavior under HER operating conditions, electrochemical impedance spectroscopy (EIS) tests were carried out for the CGTH and control groups, as shown in Fig. 4.11A. The semicircles could be observed in the plots, which are attributed to the charge transfer resistance ( $R_{ct}$ ) of protons that were reduced at the electrode-electrolyte interface. The CGTH showed a charge transfer resistance ( $R_{ct}$ ) of around 48.5  $\Omega$ , which is much smaller than those of the control groups. In addition,  $R_s$  can be estimated by the x-intercept of the Nyquist plots. The CGTH possess a low  $R_s$  value (9.7  $\Omega$ ), illustrating that the introduction of rGO to WS<sub>2</sub>/WO<sub>3</sub> nanorods could improve the electrical contact at the interface of electrolyte/electrode and decrease parasitic Ohmic losses.

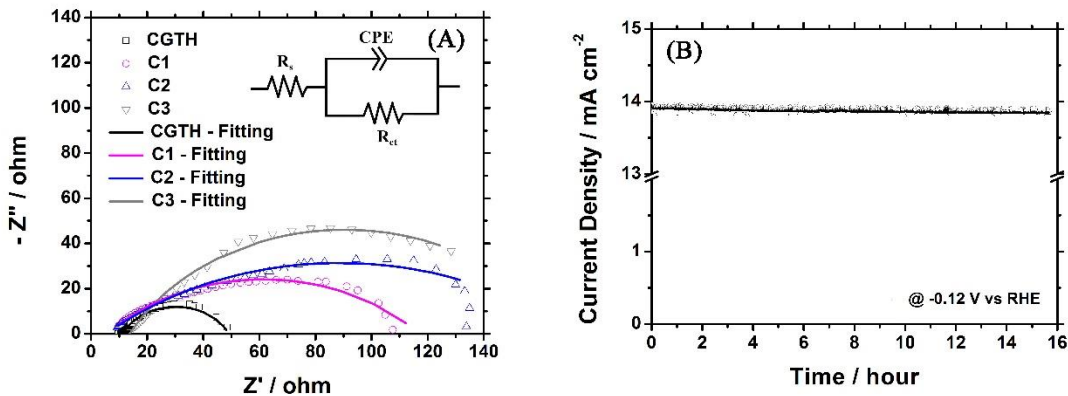


Fig. 4.11 (A) Nyquist plots of the CGTH, control group C1, C2 and C3 with the imaginary part versus the real part of the impedance. The data were collected under around HER overpotential  $\sim 500$  mV. (B) The I-t test results of the CGTH kept at  $-120$  mV versus RHE in an Ar-saturated  $0.5$  M  $\text{H}_2\text{SO}_4$  solution.

The stability of catalyst for long-term operation is also critical for the practical applications of the catalysts. In this study, CGTH was operated at a constant voltage of  $-120$  mV versus RHE in a  $0.5$  M  $\text{H}_2\text{SO}_4$  for more than 15 hours to investigate the catalyst durability for HER (Fig. 4.11B). The current retention results show that the CGTH catalyst retained 99.7% of the catalytic current after 15 hours, which is very encouraging for the long-term operation of the catalyst in HER. After the 15 hours' stability test, the remaining CGTH on the working electrode was collected for Raman spectroscopy. After comparing the Raman spectrum for the collected CGTH with the original CGTH, there is no peak position shift (Fig. 4.12), but we observed that the peak intensity for  $\text{WS}_2$  diminished after 15 hours' operation. It is highly possible that small part of the  $\text{WS}_2$  exposed to the electrolyte was converted to  $\text{WO}_3$  during the test. To further investigate the degradation of CGTH after long-term electrocatalysis, elemental analysis by XPS was performed on the catalyst collected on the working electrode after 15 hours' continuous operation. As shown in Table 4.1,

we can only observe negligible changes in the atomic percentage of CGTH, indicating the elemental composition is almost unchanged. One of the reasons why the CGTH can retain its structural integrity in the electrolyte for long-term operation is possibly due to the  $\text{WO}_3$  that partially covered the  $\text{WS}_2$ , which can resist the corrosion in an acidic environment.<sup>282</sup> The slight decay in the current density is due to the blocking of the active sites on the catalyst by the gradual accumulation of evolved hydrogen bubbles.

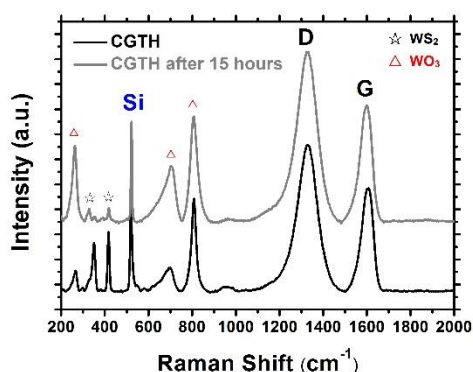


Fig. 4.12 Raman spectra of CGTH before and after 15 hours' test.

Table 4.1 The atomic percentage of elements in the CGTH before and after the long-term cycling performance

	C [%]	O [%]	S [%]	W [%]
CGTH	64.8	29.2	2.0	4.0
CGTH after 15 hours	66.6	31.0	1.2	1.2

The electrochemical double layer capacitance ( $C_{dl}$ ) of CGTH was measured ( $\sim 0.64 \text{ mF/cm}^2$ ) to estimate the electrochemically active surface area (ECSA,  $\sim 10.7 \text{ cm}^2_{\text{ECSA}}$ ), as shown in Fig. 4.13.

In order to avoid the faradaic processes, the potential range between 0.50 to 0.60 V vs RHE was chosen to record the capacitive currents. We performed cyclic voltammetry by sweeping between the above potential range for 5 times at 6 different scan rates (60, 80, 100, 120, 140, 160 mV s<sup>-1</sup>). The current density variation of anode and cathode ( $\Delta j = j_a - j_c$ ) at 0.55 V (vs RHE) was plotted against the scan rate. The electrochemical double layer capacitances ( $C_{dl}$ ) were estimated by fitting the  $\Delta j$ -potential plots. ECSA is calculated by the following equation:

$$A_{ECSA} = \frac{\text{specific capacitance}}{60 \mu\text{F cm}^{-2} \text{ per cm}^2_{ECSA}}$$

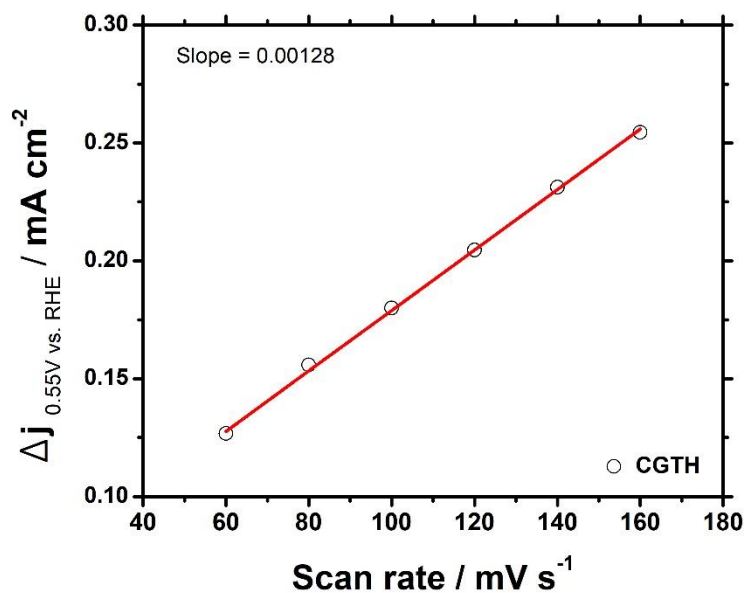


Fig. 4.13 The differences in current density ( $\Delta j = j_a - j_c$ ) at the overpotential of 0.55 V (vs. RHE) are plotted against scan rate and linearly fitted to estimate  $C_{dl}$ .

The performance of CGTH and previously reported electrocatalysts in HER are listed in Table 4.2 for comparison. As shown in Table 4.2, it is clearly seen that the CGTH has the smallest Tafel slope (37 mV/dec), which is superior to those of MoS<sub>2</sub>/WS<sub>2</sub>-based electrocatalysts (41-70 mV/dec)

reported so far. For the overpotential (corresponding current density 10 mA/cm<sup>2</sup>), the CGTH has the smallest value (113 mV vs. RHE). Meanwhile, the stability of CGTH is also outstanding among the MoS<sub>2</sub>/WS<sub>2</sub>-based electrocatalysts due to its ternary structure. The excellent HER activity of CGTH can be attributed to its unique structure. WS<sub>2</sub> is the HER active component in the CGTH, which is demonstrated by the small onset potential of 96 mV compared to sample C3 (without WS<sub>2</sub>, 468 mV). The partial coverage of WO<sub>3</sub> can prevent the corrosion and improve the stability. Typically, TMD nanosheets were grown on the surface of two-dimensional rGO<sup>151,163</sup>, while the drawback was that the charge transfer was limited to two dimensions. Compared with the previously reported works on TMD/rGO-based electrocatalysts, CGTH has the advantage of a 3D conductive network constructed by crumpled rGO for an even more efficient charge transfer, which is evidenced by the small R<sub>ct</sub> value of 48.5 Ω compared with sample C1 (without rGO, 107.6 Ω). Previous studies of TMDs/rGO give the credit to strong chemical and electronic coupling between the rGO and TMDs with an abundance of accessible edges that works as active sites in HER electrocatalysis. This study further verifies this theory and clearly demonstrates that crumpled rGO/WS<sub>2</sub>/WO<sub>3</sub> ternary structure could serve as an even more efficient electrocatalyst for HER. With the excellent electrocatalytic activity, stability, and corrosion-resistance, the CGTH could be a promising HER catalyst to replace the precious Pt catalyst for various applications such as water splitting.

Table 4.2 Comparison of HER catalytic activity for MoS<sub>2</sub>/WS<sub>2</sub>-based electrocatalysts.

Catalyst	Onset Potential (V vs. RHE, mV)	Potential at 10 mA/cm <sup>2</sup> (V vs. RHE, mV)	Tafel slope (mV/dec)	Stability	Reference
CGTH	96	113	37	retained 99.7% of the electrocatalytic current after 15 hours	This work
Metallic MoS <sub>2</sub> nanosheets		187	43	<15% decay in the electrocatalytic current density after 1000 cycles	Lukowski, et al. <sup>283</sup>
Mesoporous MoS <sub>2</sub>	150-200		50		Kibsgaard, et al. <sup>284</sup>
MoS <sub>2</sub> NPs on graphene	100		41	negligible activity loss after 1000 cycles	Li, et al. <sup>285</sup>
Ultrathin WS <sub>2</sub> nanoflakes	100		48	increase of overpotential < 10 mV after 10000 cycles	Cheng, et al. <sup>146</sup>
Metallic WS <sub>2</sub> nanosheets		142	70	slow decline in catalytic activity	Lukowski, et al. <sup>214</sup>
WS <sub>2</sub> nanodots	90		51	slight activity loss after 1000 cycles	Zhao, et al. <sup>161</sup>
MoP	77	153	66	no obvious activity decay after 2000 cycles	Yang, et al. <sup>286</sup>
CoNi nanoalloy encapsulated by graphene spheres	almost zero	142	105	fairly stable for 1000 cycles	Deng, et al. <sup>287</sup>
Nitrogen and sulfur co-doped nanoporous graphene	130	280	80.5	10% current decay after 7 days	Ito, et al. <sup>288</sup>

#### 4.4 Summary and conclusions

In summary, 3D crumpled rGO/WS<sub>2</sub>/WO<sub>3</sub> hybrids were fabricated through aerosolizing a mixture of GO suspension and precursors. The as-produced material has a stable ternary structure in aqueous electrolyte and a high accessible surface area, which is beneficial for rapid mass transfer of ions. As a demonstration, the crumpled graphene/WS<sub>2</sub>/WO<sub>3</sub> (CGTH) catalyst showed a superior electrocatalytic activity in the hydrogen evolution reaction (HER), with a Tafel slope of 37 mV/dec and an onset potential of 96 mV. Compared with reported MoS<sub>2</sub>/WS<sub>2</sub>-based electrocatalysts, this hybrid material shows one of the highest catalytic activities in HER, which is attributed to the synergistic effect of different factors, including crumpled open structure, facile charge transfer, and abundant catalytic active sites. The environmentally-friendly synthesis and outstanding performance suggest a great potential of CGTH for noble metal-free electrocatalysts in water splitting.

# CHAPTER 5 MOLYBDENUM DISULFIDE QUANTUM DOTS FOR LITHIUM-ION AND POTASSIUM-ION BATTERIES

## 5.1 Introduction

Lithium-ion batteries (LIBs) have become the vital energy storage devices due to the requirements of high energy density and long cycling life, particularly for portable devices. However, the commercial graphite anode for LIBs could not fulfill the urgent need of increasing energy and power densities due to its limited theoretical capacity. To improve the specific capacity of LIBs and relieve volume expansion of electrodes, TMD materials especially MoS<sub>2</sub> QDs have been considered a promising anode material for LIBs owing to their higher theoretical capacity and better rate capability compared with the commercial graphite anode. This chapter describes the preparation and application of exfoliated mesoporous MoS<sub>2</sub> QDs-graphite composite anodes. The MoS<sub>2</sub> QDs can be located in the void spaces between graphite particles, thereby preventing the graphite particles from losing electrical contact with the current collector and enhancing the cycling stability of MoS<sub>2</sub>/graphite composite anodes. Furthermore, MoS<sub>2</sub> QDs can also be promising anode material for potassium-ion batteries (PIBs).

## 5.2 Experimental methods

### 5.2.1 Material synthesis

**Synthesis of large surface area hard template SBA-15.** 6.67 g of Poly(ethylene glycol)-block-poly(propylene glycol)-block-poly(ethylene glycol) triblock copolymer (P123: EO20PO70EO20 purchased from Sigma-Aldrich) was dissolved in a mixture of 33.3 mL 12M Hydrochloric acid

(HCl) and 216.7 mL DI H<sub>2</sub>O at 38°C. Then 13.87 g of Tetraethyl orthosilicate (TEOS: Si(OC<sub>2</sub>H<sub>5</sub>)<sub>4</sub> purchased from Sigma-Aldrich) was poured into the solution with vigorous stirring, and the mixture was kept at the same temperature for 24 hrs. Next, the above mixture was heated up to 100 °C for 48 hrs for hydrothermal treatment in a 100 mL Teflon lined hydrothermal reactor. Finally, the white solids were recovered by filtration and calcinated at 550 °C for 4 hrs in the air to remove the P123 surfactant.

**Synthesis of mesoporous MoS<sub>2</sub> (M-MoS<sub>2</sub>).** 0.5 g of Phosphomolybdic acid (PMA: H<sub>3</sub>PMO<sub>12</sub>O<sub>40</sub> purchased from Sigma-Aldrich) was mixed with 0.5 g of SBA-15 and 10 mL of ethanol under stirring in an open crucible at room temperature. After the ethanol evaporated after about 8 hrs, the obtained powder was loaded on a quartz boat and put in the middle of a quartz tube furnace. Another two quartz boats that loaded with 4 g of sulfur powder were also placed in the tube furnace in the upstream direction just by the side of the PMA@SBA-15 boat. Then the furnace was heated to 600 °C at a rate of 2 °C/min under a hydrogen gas flow (100 mL min<sup>-1</sup>). After keeping in this temperature for 6 hrs, the furnace was cooled down to room temperature. The H<sub>2</sub>S in the off-gas was absorbed by 2 M sodium hydroxide (NaOH) aqueous solution. Then MoS<sub>2</sub>@SBA-15 composite was treated with 4% Hydrofluoric acid (HF) aqueous solution for 2 hrs to remove the silica template. Finally, M-MoS<sub>2</sub> was obtained after the filtration and drying process.

**Synthesis of exfoliated MoS<sub>2</sub> QDs (MQDs).** Lithium intercalation was achieved by immersing 5 mg of M-MoS<sub>2</sub> powder in 5 mL of 1.6 M butyllithium solution in hexane (purchased from Sigma-Aldrich) for 72 hrs in a flask filled with argon gas. Then Li<sub>x</sub>MoS<sub>2</sub> was retrieved by washing with hexane and dialysis process to remove excess lithium and organic residues. The exfoliation was achieved by adding Li<sub>x</sub>MoS<sub>2</sub> into DI water and sonicated in an ultrasonic bath continuously for 4 hrs. Next, the dispersion was sonicated with a sonic tip for another 4 hrs. The bath temperature

during sonication was kept below 277 K by keeping the sample in an ice water bath. The top two-thirds of the dispersion was centrifuged at 10,000 rpm for 15 min three times to obtain MQDs.

### **5.2.2 Material characterization**

A Hitachi S-4800 scanning electron microscope (SEM) and Hitachi H-9000NAR transmission electron microscope (TEM) were used for structural and elemental characterization of the as-prepared samples. The X-ray powder diffraction (XRD) analyses were conducted on a Bruker D8 Discover X-ray diffractometer equipped with a scintillation counter and Cu k-alpha radiation (0.15418 nm) reflection mode. Raman spectroscopy was conducted with a Renishaw Raman microscope (Bruker RFS 100/S spectrometer) with an excitation wavelength of 1,064 nm at an input power of 1 mW. The specific surface area was obtained using ASAP2020 (Micromeritics, U.S.A) Brunauer-Emmett-Teller (BET) nitrogen adsorption-desorption. The N<sub>2</sub> adsorption-desorption measurements were carried out at 77 K using a Quantachrome Autosorb gas-sorption system. The thickness measurement was conducted by Atomic-force microscopy (AFM) from Agilent Technologies. The fluorescence spectra for MQDs was examined by the PerkinElmer LS 55 Fluorescence spectrometer.

### **5.2.3 Preparation of electrodes and coin cells**

The charge/discharge performance was characterized by using 2032-type coin cells that were assembled in an argon-filled glove box, with oxygen and moisture content below 1 ppm. Electrodes of LIBs were prepared by mixing the as-prepared mesoporous MoS<sub>2</sub> and graphite (denote as M-MoS<sub>2</sub>-G) as the active material with a weight ratio of 30:70 for the electrodes and the same ratio was used for preparing exfoliated MoS<sub>2</sub> QDs (denote as MQDs-G) electrodes. The

active material, sodium carboxymethyl cellulose, and carbon black as a conductor were mixed with a weight ratio of 80:10:10 to form a slurry. The resulting slurries were coated onto a Cu foil disks current collector with 12- $\mu\text{m}$  in thickness and 1.1 cm in diameter. After drying and pressing, the Cu foil disks with typical electrode material loadings of ca.  $1 \text{ mg cm}^{-2}$ . Then, 1 M  $\text{LiPF}_6$  dissolved in ethylene carbonate/ethyl methyl carbonate (40:60, v/v) with additives of fluoroethylene carbonate (5 wt. %) and vinylene carbonate (1 wt. %) was employed as an electrolyte. Compare to LIBs, only MQDs (denote as MQDs-PIBs) was used as active material for PIBs. And 0.6 M  $\text{KPF}_6$  dissolved in ethylene carbonate/propylene carbonate (50:50, v/v) without any additives was employed as an electrolyte.

#### **5.2.4 Electrochemistry measurements**

The coin cells were tested on a LAND battery tester with a cut-off voltage range between 0.1 and 3.0 V. The lithiation behavior was defined as “charge” because the  $\text{MoS}_2$  is an anode material for LIBs. Note that the 1 C capacities for graphite and  $\text{MoS}_2$  are different; for the fair comparison of the capacity, the C-rates for charging and discharging their batteries are the same while the 1 C current densities are different. The 1 C rate for graphite and  $\text{MoS}_2$  were defined as 372 and 670 mA/g, respectively. In contrast, the 1 C rate for M- $\text{MoS}_2$ -G and MQDs-G was 460 mA/g because the contents of graphite and  $\text{MoS}_2$  were 70wt.% and 30wt.%, respectively.

### **5.3 Results and discussion**

The mesoporous  $\text{MoS}_2$  (denote as M- $\text{MoS}_2$ ) was synthesized through a hard-template method with SBA-15 silica as a sacrificial template. Next, the  $\text{MoS}_2$  quantum dots (denoted as MQDs) were prepared by using chemically exfoliating as-synthesized mesoporous  $\text{MoS}_2$ . Morphology of as-

prepared M-MoS<sub>2</sub> and MQDs were characterized by SEM and TEM. Fig. 5.1a and Fig. 5.1b show that the M-MoS<sub>2</sub> is composed of irregular agglomerates with the particle size ranging from several hundred nm to several  $\mu\text{m}$ . The enlarged TEM image (Fig. 5.1c) shows an example of M-MoS<sub>2</sub> agglomerates with a dimension of  $\sim 500$  nm due to the employment of the rodlike morphologies of SBA-15 templates (Fig. 5.1h) in the synthesis process. Furthermore, the HRTEM analysis reveals that the surface of the architecture is composed of MoS<sub>2</sub> sheets with 4-10 layers as shown in Fig. 5.1c. The interplanar distance is 0.615 nm and agrees with the d-spacing between (002) planes of MoS<sub>2</sub>, which is similar to that of the reported MoS<sub>2</sub>.<sup>289,290</sup> In addition, as demonstrated in Fig. 5.1e, SAED pattern was used to identify the crystallographic phase of the synthesized M-MoS<sub>2</sub>. Fig. 5.1f and Fig. 5.1g show high-resolution TEM images of the synthesized MQDs, from which the lattice fringes can be clearly seen. The interplanar spacing in a representative crystallite is 0.223 nm, which is close to that of MoS<sub>2</sub> (103) planes.

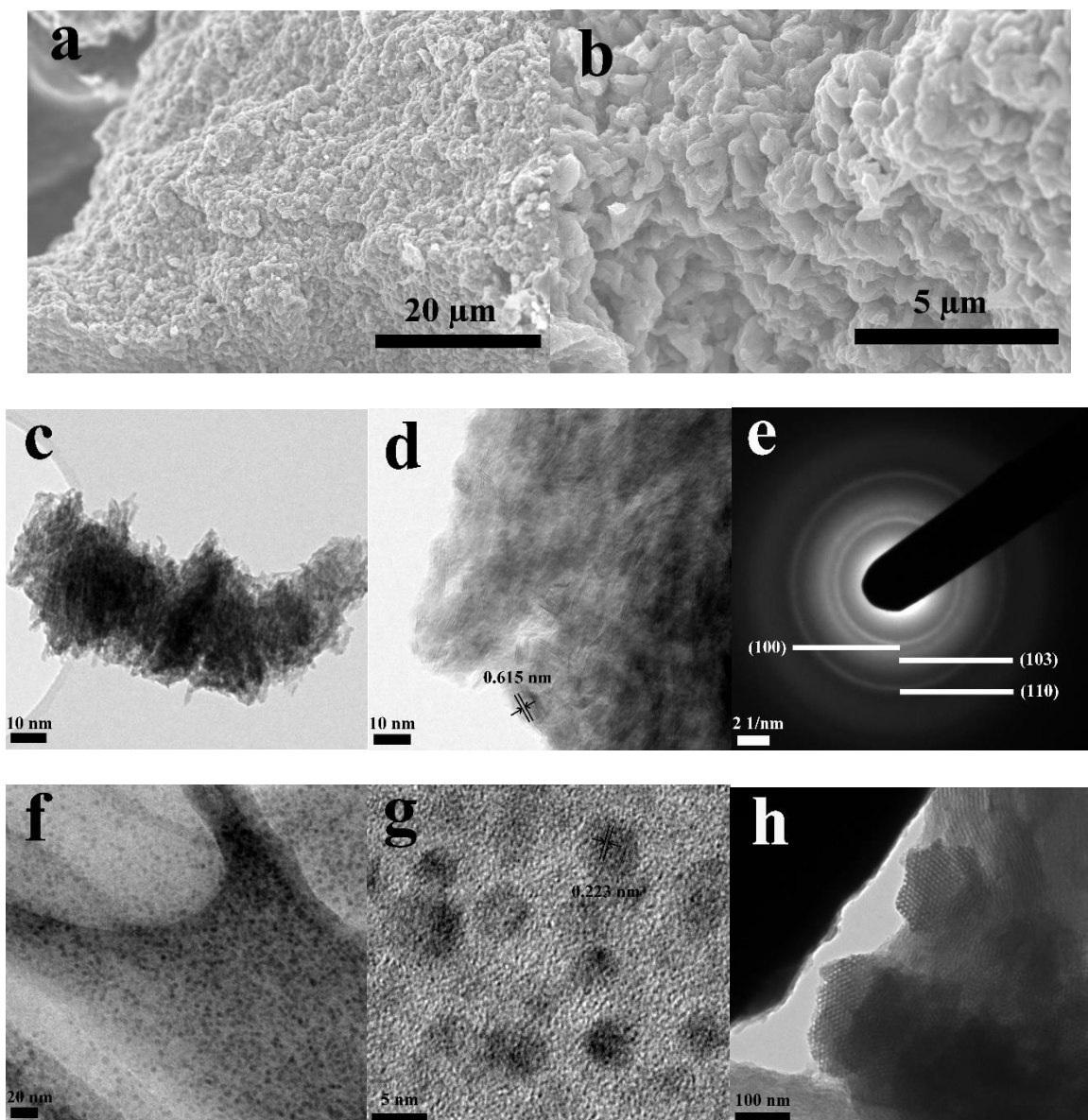


Fig. 5.1 a, b) SEM images c, d) TEM images and e) SAED pattern of synthesized M-MoS<sub>2</sub>; f, g) TEM images of synthesized MQDs and h) TEM image of hard template SBA-15.

XRD analysis was carried out to study the crystal structure of as-prepared M-MoS<sub>2</sub> and MQDs. In Fig. 5.2a, a set of diffraction peaks appear at 14.36°, 33.04°, 39.24° and 58.92° for M-MoS<sub>2</sub>; these four peaks can be well indexed to the characteristic peaks of (002), (100), (103) and (110) crystal planes of 2H phase MoS<sub>2</sub> (JCPDS card no. 65-0160), which matches well with the SAED

results.<sup>290</sup> As for the synthesized MQDs, the signal of the (002) plane is broadened with the disappearance of most of the other peaks after ultrasonication, indicating the highly-exfoliated nature of the quantum dots.<sup>291</sup> It is well known that the peak position corresponds to the d-spacing of crystals. Theoretically, there would be no signal or peak in the XRD pattern if all the materials are monolayer and have no interaction with each other.<sup>292</sup> It should be noted that there is one broad peak at (004) planes for MQDs, which likely results from the partial re-stacking of quantum dots during the drying process since the peak is absent from the M-MoS<sub>2</sub> pattern.<sup>293</sup> As shown in Fig. 5.2b, Raman peaks of M-MoS<sub>2</sub> appear at 376.02, 402.89, and 448.96 cm<sup>-1</sup>, corresponding to E<sub>2g</sub>, A<sub>1g</sub>, and C vibration modes of MoS<sub>2</sub>, respectively.<sup>292</sup> After the exfoliation process, the intensity of the MQDs peaks are stronger than those of M-MoS<sub>2</sub>. Generally, since interlayer van der Waals force decreases with the decreasing number of layers, atomic vibration becomes more strenuous in MoS<sub>2</sub>, and thus both E<sup>1</sup><sub>2g</sub> peak and A<sub>1g</sub> peak are expected to red-shift. However, on the contrary, the frequency of A<sub>1g</sub> peak increased from 402.89 to 403.85 cm<sup>-1</sup> (blue-shift), reflecting the dominant influence of stacking induced structure changes or long-range Coulombic interlayer interactions.<sup>294</sup> Fig. 5.2c-f show nitrogen gas adsorption and desorption isotherms and the corresponding pore size distributions of M-MoS<sub>2</sub> and SBA-15, respectively. Both samples can be classified as typical type-IV isotherm with a clear adsorption-desorption hysteresis loop, which is the characteristic of mesoporous materials with large pores and uniform cylindrical channels.<sup>295</sup> The specific surface areas, adsorption average pore widths and total pore volumes of the SBA-15, M-MoS<sub>2</sub> and intermediate products were analyzed based on nitrogen adsorption and desorption measurements as shown in Table 5.1. From the table, the surface area and adsorption average pore width of synthesized template SBA-15 are 685.8 m<sup>2</sup>/g and 58.3 Å, respectively. After PMA was mixed with SBA-15 in the synthesis process, the specific surface area of the mixture decreased to 314.5 m<sup>2</sup>/g but the pore

width remained unchanged. Subsequently, the results show the surface area of MoS<sub>2</sub>@SBA-15 remained unchanged but the pore width decreased from 59.2 Å to 55.6 Å. Finally, the M-MoS<sub>2</sub> with a specific surface area of 92.9 m<sup>2</sup>/g and pore width of 49.8 Å was obtained after HF solution treatment to remove the silica template. The M-MoS<sub>2</sub> showed similar isotherm patterns and pore size distributions compared with the SBA-15, indicating that the mesoporous structure was still maintained after the template removal treatment.<sup>296</sup>

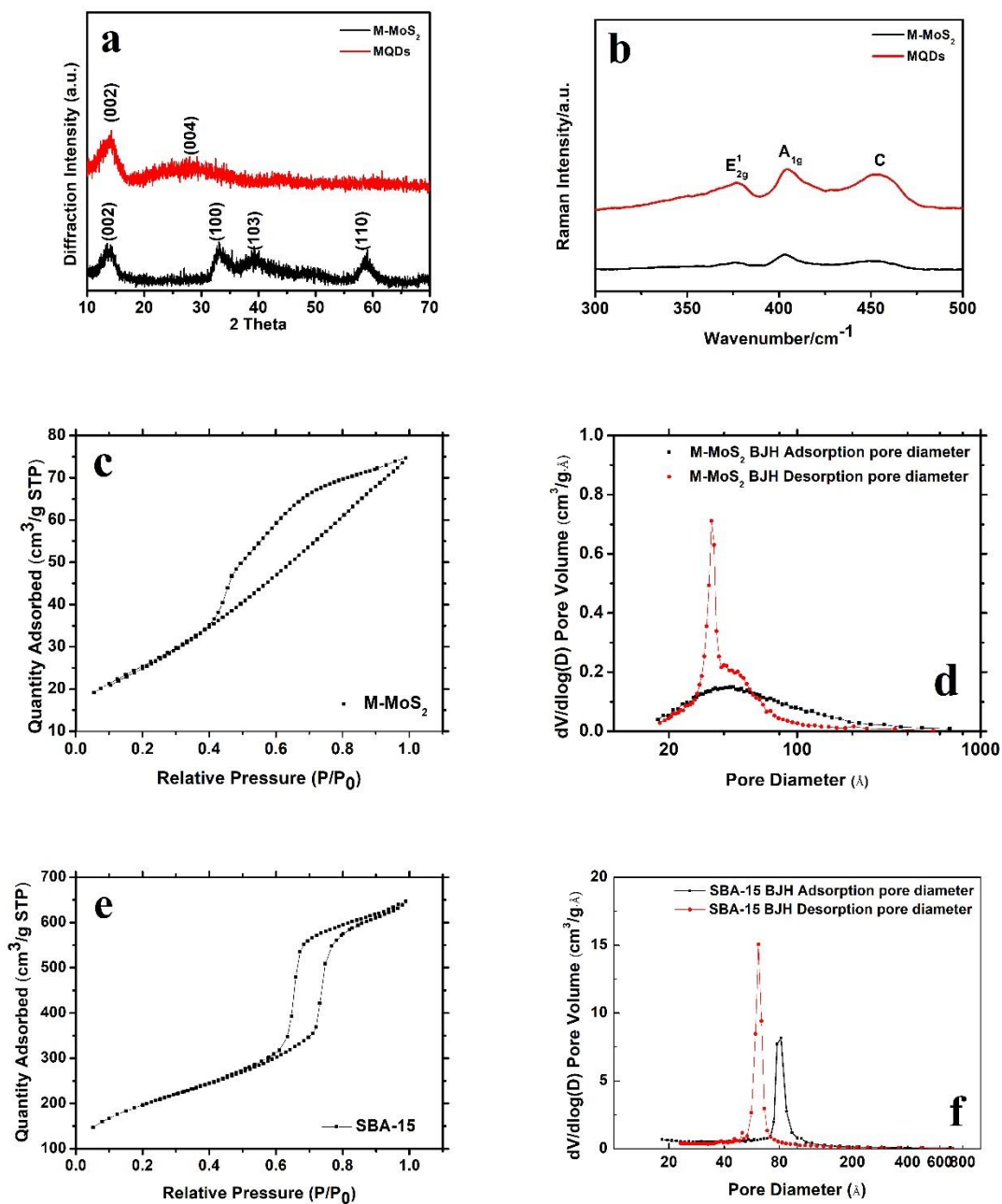


Fig. 5.2 a) Representative XRD pattern and b) Raman spectra of the M-MoS<sub>2</sub> and MQDs. c) N<sub>2</sub> adsorption-desorption isotherms d) Pore size distribution of M-MoS<sub>2</sub>. e) N<sub>2</sub> adsorption-desorption isotherms and f) Pore size distribution of SBA-15.

Table 5.1 Surface properties of M-MoS<sub>2</sub>, SBA-15, and the intermediate products

Sample	BET Surface Area (m <sup>2</sup> /g)	Adsorption average pore width (Å)	Total pore volume (cm <sup>3</sup> /g)
<b>SBA-15</b>	685.8	58.3	1.00
<b>SBA-15 w/ PMA</b>	314.5	59.2	0.47
<b>MoS<sub>2</sub>@SBA-15</b>	314.8	55.6	0.44
<b>M-MoS<sub>2</sub></b>	92.9	49.8	0.12

AFM measurements were carried out to further investigate the morphology and thickness of the as-prepared MQDs. The results show the thickness ranged from 0.8-5.8 nm (Fig. 5.3a) and the average height was ~1.7 nm, which is close to the height of monolayer MoS<sub>2</sub> (0.8-1.0 nm), indicating the presence of monolayers in the solvent, as well as few-layer materials. The optical properties of MQDs were investigated by photoluminescence (PL) spectroscopy at room temperature. Generally, bulk MoS<sub>2</sub> has an indirect band gap of 1.2 eV that does not exhibit PL properties; however, as the thickness of this material reduces to that of the monolayer, electronic properties change drastically, resulting in a direct band-gap semiconductor with a band gap of 1.9 eV.<sup>297,298</sup> As shown in Fig. 5.3b, as-prepared MQDs exhibited a weak emission with the peak maximum at 480 nm under an excitation wavelength of 323 nm. In semiconductors, it is well known that light absorption generally leads to an electron being excited from the valence to the conduction band, leaving behind a hole. An exciton (fluorescence emission) forms when the electron and the hole bind to each other. In other words, when this exciton (electron-hole pair) recombines, the exciton's energy can be emitted as light.<sup>299</sup> The weak fluorescence intensity indicating the recombination of photo-induced electrons-holes is efficiently suppressed by the existence of MQDs.<sup>300</sup>

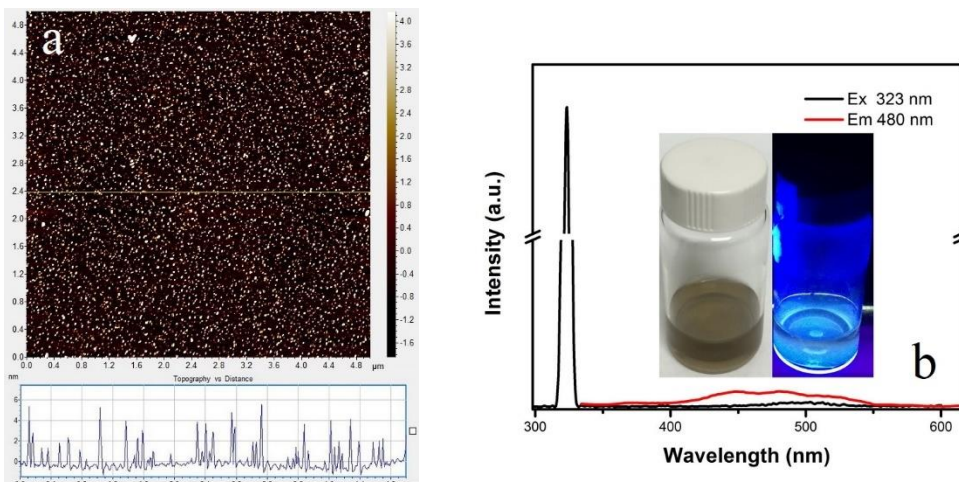
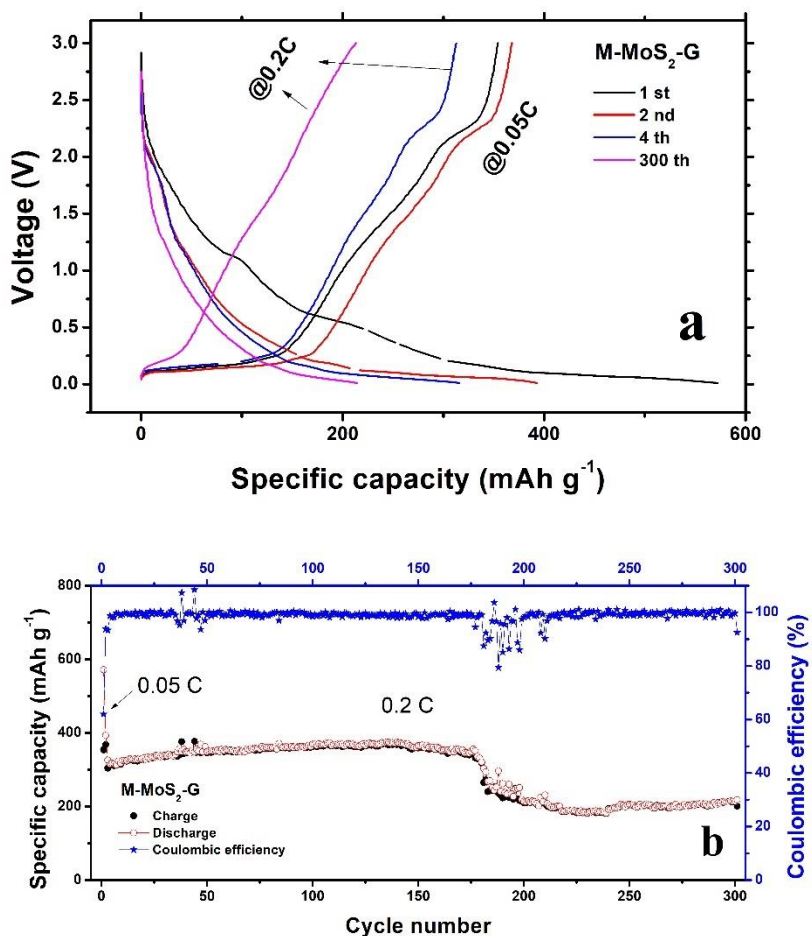


Fig. 5.3 a) AFM thickness measurement with height distribution for MQDs and b) excitation and emission PL spectra of MQDs. Inset images show the photographs of MQDs in room light (left) and under a UV light source (right) emitting 365 nm light.

The charge/discharge (lithiation/delithiation) performance of the M-MoS<sub>2</sub>-G and MQDs-G LIBs was tested using coin cells. During the test, an upper cutoff voltage of 3.0 V was used to investigate the full energy of the anode. As shown in Fig. 5.4a and 5.4b, the initial discharge (delithiation) capacity is 572 mAh g<sup>-1</sup> with an initial Coulombic efficiency of 62% at 0.05 C rate for M-MoS<sub>2</sub>-G. After activation at 0.05 C for two cycles, the cell was cycled at 0.2 C, exhibiting a stable capacity of approximately 363 mAh g<sup>-1</sup> for 100 cycles. As for the MQDs-G, the initial discharge (delithiation) capacity is 714 mAh g<sup>-1</sup> with an initial Coulombic efficiency of 64.2% at a current density of 0.05 C. After activation at 0.05 C for two cycles, the cell was cycled at 0.2 C, exhibiting a stable capacity of approximately 448.3 mAh g<sup>-1</sup> for 100 cycles. The capacity decrease during the initial several cycles might be related to the fact that as-prepared materials need time for activation at a higher current density. To evaluate the long-term cyclic performance, both electrodes were cycled at 0.2 C; MQDs-G showed a reversible capacity of approximately 449.8 mAh g<sup>-1</sup> and no

capacity degradation was observed after 300 cycles (Fig. 5.4e). In comparison, nearly 30% of capacity loss was observed for M-MoS<sub>2</sub>-G after 300 cycles. It is very clear to see that the cyclic performance of MQDs-G is much better than that of M-MoS<sub>2</sub>-G, especially after 175 cycles. In the MQDs-G structure, the MQDs can be located in the void spaces between the graphite particles, thus preventing the expansion phenomenon of active materials and graphite particles from losing contact with the current collector. MQDs-G composites demonstrated a good charge/discharge character and the capacity still maintained at 449.8 mAh g<sup>-1</sup> after 300 charge/discharge cycles at a current density of 0.5 C. In contrast, the M-MoS<sub>2</sub>-G electrodes only retained 214 mAh g<sup>-1</sup> after 300 charge/discharge cycles.



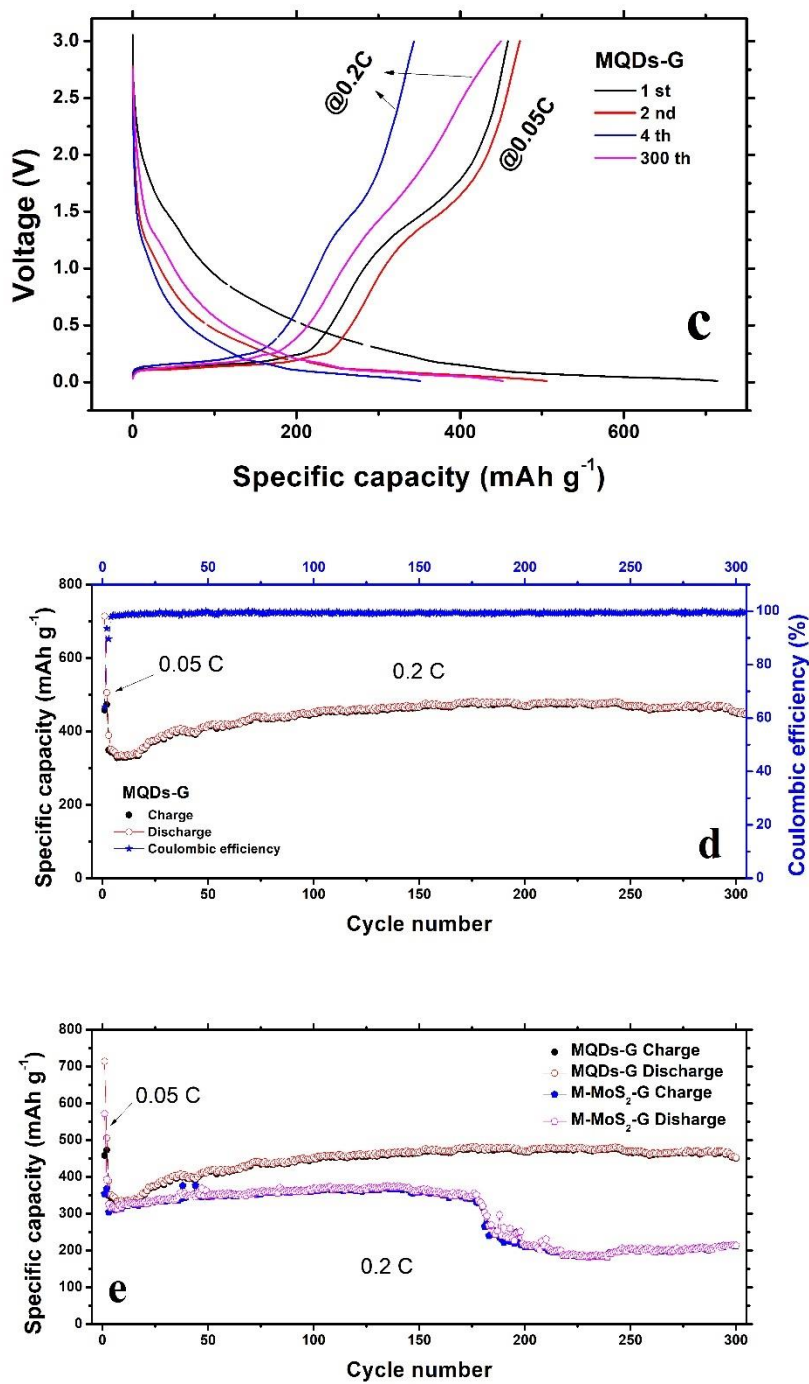
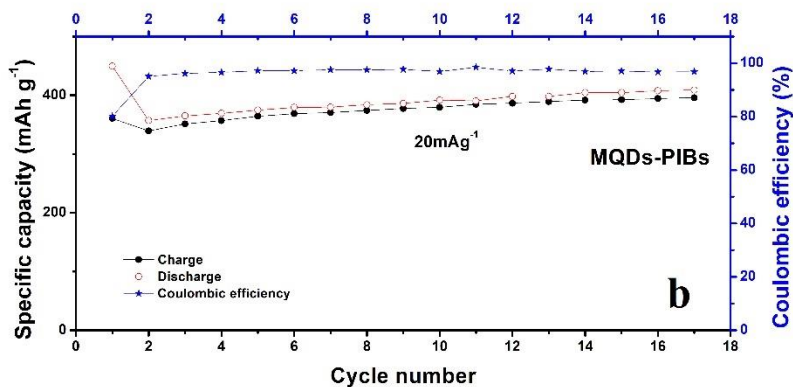
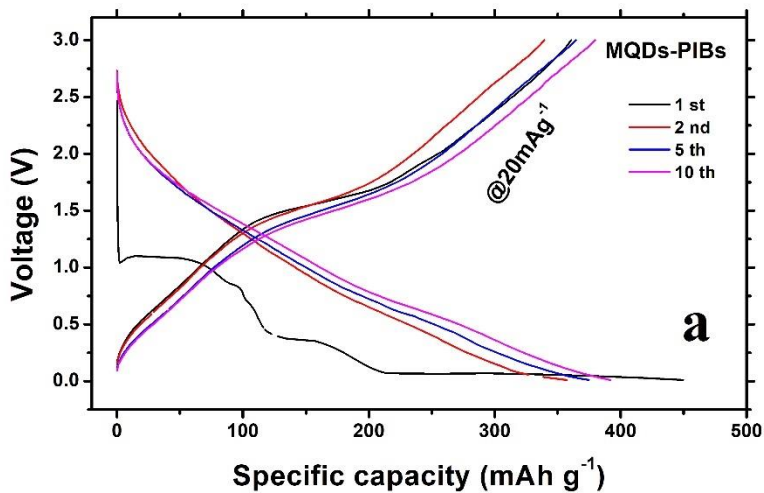


Fig. 5.4 LIBs cyclic performance and Coulombic efficiency of a, b) M-MoS<sub>2</sub>-G electrodes. c, d) MQDs-G electrodes. e) A comparison of long-term cyclic performance between the two electrodes.

The charge/discharge (potassiation/depotassiation) performance of the MQDs as anodes for PIBs was tested also using coin cells. During the test, an upper cutoff voltage of 3.0 V was used to investigate the full energy of the anode. As shown in Fig. 5.5a and 5.5b, the initial discharge (depotassiation) capacity was 361 mAh g<sup>-1</sup> with an initial Coulombic efficiency of 80.2% at 20 mA g<sup>-1</sup> for MQDs. The cell was cycled at 20 mA g<sup>-1</sup> and exhibited a stable capacity of approximately 409 mAh g<sup>-1</sup> for 17 cycles. The rate capability of the MQDs-PIBs is shown in Fig. 5.5c. The MQDs-PIBs delivered 366, 315.4, 300.3, 282.6, 257.4, and 195.5 mAh g<sup>-1</sup> at current densities of 20, 40, 100, 200, 400, and 1,000 mA h g<sup>-1</sup>, respectively, suggesting the good rate capability for the MQDs in PIBs.



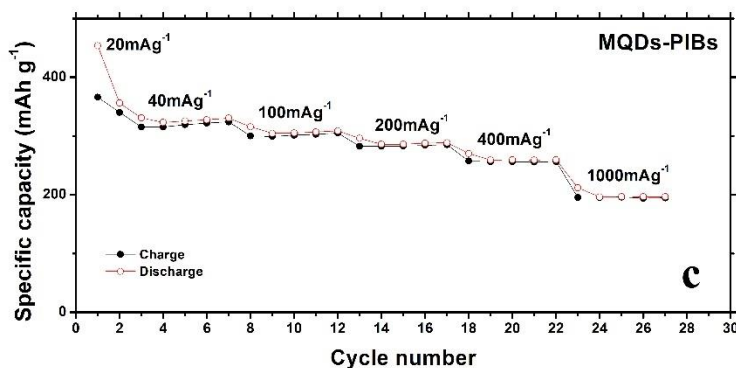


Fig. 5.5 Electrochemical performance of MQDs electrodes for PIBs. a, b) cyclic performance and Coulombic efficiency of MQDs electrodes at 20 mA g<sup>-1</sup>. c) rate capability of MQDs electrodes.

#### 5.4 Summary and conclusions

Exfoliated mesoporous MoS<sub>2</sub> QDs-graphite composites have been produced for LIB anodes, in which MoS<sub>2</sub> QDs can be located in the void spaces between graphite particles, thereby preventing the graphite particles from losing contact with the current collector and enhancing the cycling stability of MoS<sub>2</sub>/graphite composite anodes. The composite anode samples were characterized by XRD, Raman spectra, SEM, HRTEM, BET, AFM, PL and electrochemical testing. The results showed MQDs were uniformly exfoliated with an average thickness of ~1.7 nm. The optimized MQDs-G composites displayed good charge/discharge characteristics and the capacity maintained at 449.8 mAh g<sup>-1</sup> after 300 charge/discharge cycles at a current density of 0.5 C, whereas the M-MoS<sub>2</sub>-G electrodes only retained 214 mAh g<sup>-1</sup> after 300 charge/discharge cycles. MoS<sub>2</sub> QDs were demonstrated for PIB anodes, which exhibited a stable capacity of approximately 409 mAh g<sup>-1</sup> for 17 cycles.

# CHAPTER 6 EXFOLIATED MOLYBDENUM DISULFIDE WITH METAL ORGANIC FRAMEWORK FOR PHOTOCATALYTIC HYDROGEN EVOLUTION

## 6.1 Introduction

Metal-organic frameworks (MOFs) consist of metal ions and organic bridging ligands with unique properties due to their tunable pore size, high pore volume, high specific surface area, and highly ordered crystalline porous networks. However, its application for photocatalysis is limited because it lacks the ability to absorb visible light. Therefore, by combining MOFs with a visible-light-active photocatalyst, such as encapsulating TMDs into MOFs to form core-shell structures, it not only offers combined properties but may also lead to synergistic functionalities. Much research attention has been focused on applying MOFs especially the Zeolitic Imidazolate Framework (ZIF-8) structure to carbon capture, sensing, drug delivery, batteries, selective catalysis; however, their application as photocatalysts to address environmental issues and the energy crisis has not been thoroughly reported. This chapter describes the synthesis, characterization, and application of exfoliated MoS<sub>2</sub>@ZIF-8 for visible light enhanced photocatalytic hydrogen evolution.

## 6.2 Experimental methods

### 6.2.1 Material synthesis

**Synthesis of exfoliated MoS<sub>2</sub> (EM).** 100 mg of MoS<sub>2</sub> bulk powder (purchased from Sigma-Aldrich) was first immersed in 100 mL of methanol (purchased from Sigma-Aldrich). Then exfoliation was achieved by sonicating the dispersion in an ultrasonic bath continuously for 1 hr

and then probe-sonicated for another 1 hr. The bath temperature during sonication was kept below 277 K by keeping the sample in an ice water bath. The top two-thirds of the exfoliated MoS<sub>2</sub> were collected for further experiments.

**Synthesis of MoS<sub>2</sub>@ZIF8 (MZ).** Zinc nitrate hexahydrate (Zn(NO<sub>3</sub>)<sub>2</sub>·6H<sub>2</sub>O), 2.47 mmol) was first added to the exfoliated MoS<sub>2</sub> methanolic solution (25 mL). Next, the resulting solution was added to 25 mL of 2-methylimidazole (19.85 mmol) and kept at room temperature stirring for 12 hrs. Last, the dispersion was centrifuged at 10,000 rpm for 5 min three times and vacuum dried to obtain MZ.

### 6.2.2 Material characterization

A Hitachi S-4800 scanning electron microscope (SEM) was used for structural and elemental characterization of the as-prepared samples. The X-ray powder diffraction (XRD) analyses were conducted on a Bruker D8 Discover X-ray diffractometer equipped with a scintillation counter and Cu k-alpha radiation (0.15418 nm) reflection mode. Raman spectroscopy was conducted with a Renishaw Raman microscope (Bruker RFS 100/S spectrometer) with an excitation wavelength of 1,064 nm at an input power of 1 mW. X-ray photoelectron spectroscopy (XPS) spectra were obtained using a Perkin Elmer PHI 5440 ESCA System with monochromatic Al K $\alpha$  radiation as the X-ray source and the C1s peak at 285 eV as an internal standard. The specific surface area was obtained using ASAP2020 (Micromeritics, U.S.A) Brunauer-Emmett-Teller (BET) nitrogen adsorption-desorption. The N<sub>2</sub> adsorption-desorption measurements were carried out at 77 K using a Quantachrome Autosorb gas-sorption system. The samples were degassed at 200 °C for 2 hours before the measurements. The specific surface area of samples is calculated by the Brunauer-Emmett-Teller (BET) method.

### 6.2.3 Photocatalytic hydrogen production measurements

The schematic of the photocatalytic reaction system is illustrated in Fig. 6.1. Compressed N<sub>2</sub> was used as the carrier gas for examining the performance of H<sub>2</sub> production. The carrier gas regulated by two mass flow controllers passed through a bubbler containing de-ionized water to generate a water vapor mixture. Estimated from the saturation vapor pressure-temperature profile, the volume fraction of H<sub>2</sub>O in the gas mixture at 20 °C was calculated to be 2.2%, which balanced with the carrier gas. The gas mixture was then introduced into a photoreactor. 25 mg powder catalysts were dispersed on a glass fiber filter and placed in the middle of the tube reactor. A Xe lamp (AM 1.5 G and 100 mW cm<sup>-2</sup>) with an incident direction normal to the surface of the sample was used as the photo-excitation source. Before the illumination, the reactor was purged with the carrier gas at a flow rate of 200 ml/min for 1 hr. and then at 2 ml/min for 1 hr. During the illumination, the carrier gas flow rate was maintained at 2 ml/min and the sample of effluent gas was taken every 15 min by an automated valve for gas chromatography (GC, Agilent 7890A). The GC in this study was equipped with a thermal conductivity detector (TCD).

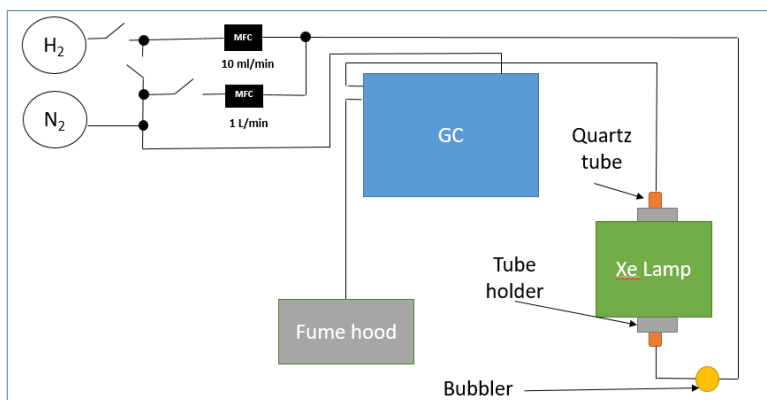


Fig. 6.1 The schematic of the photocatalytic reaction system.

### 6.3 Results and discussion

The exfoliated MoS<sub>2</sub>@ZIF-8 (denoted as MZ) was synthesized by a two-step method. First, the exfoliated MoS<sub>2</sub> (denoted as EM) was achieved by sonicating the MoS<sub>2</sub>/methanol dispersion in an ultrasonic bath. Next, the EM was added in the process of preparing ZIF-8 to obtain MZ. Morphology of as-prepared MZ was characterized by SEM and EDS analyses. Fig. 6.2a and 6.2 b show that the MZ is composed of irregular agglomerates with the particle size ranging from 10 to 30 μm. Fig. 6.2c and 6.2d are the EDS elemental mapping results of MZ for Zn, C, N, Mo and S elements. The Zn, C, N elements are well dispersed in MZ particles and Mo, S elements are clearly encapsulated in the ZIF-8 shell.<sup>136</sup> From the elemental distribution results of O element, it can be seen that ZnO rarely exists in the MZ without further calcination process.

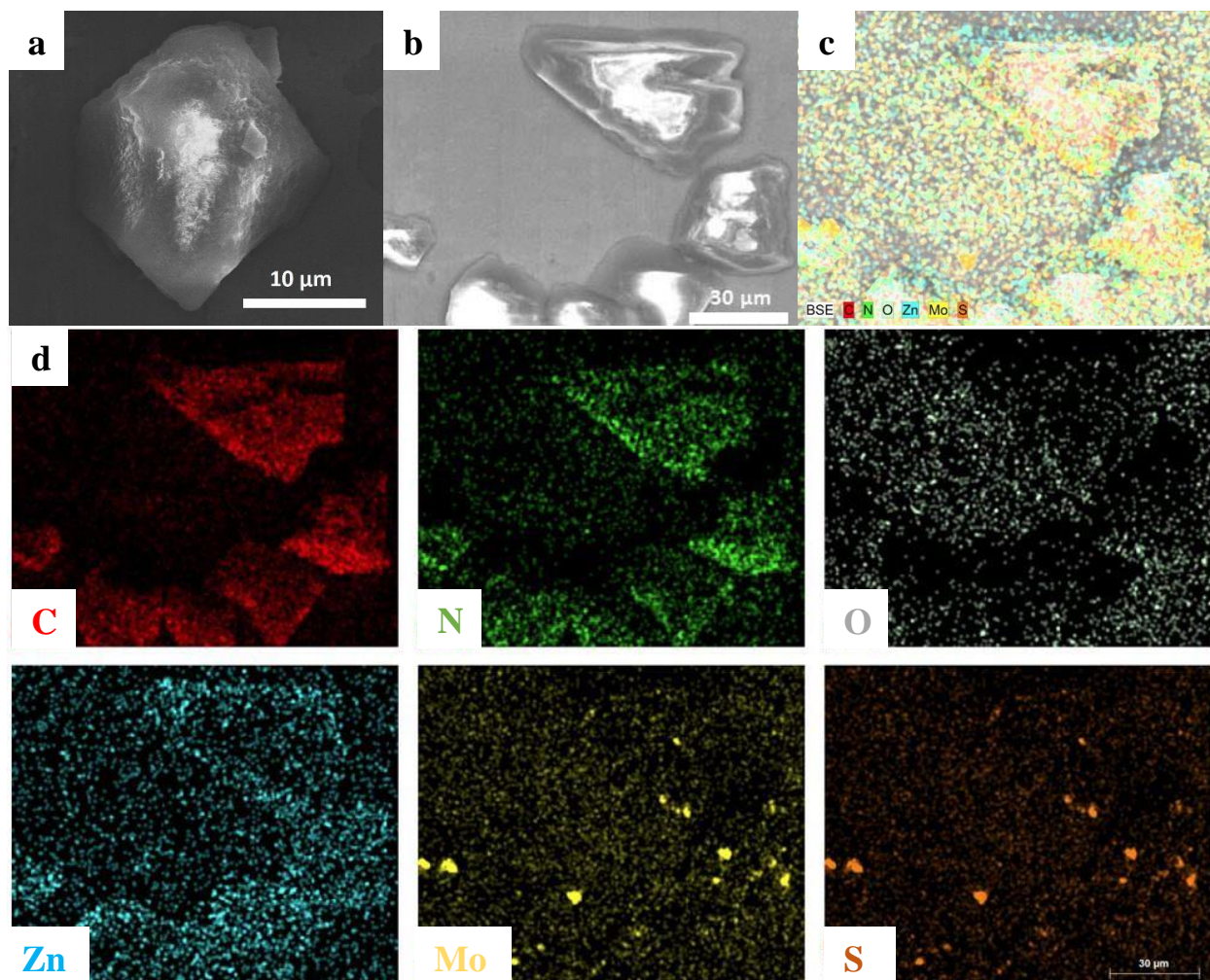


Fig. 6.2 a-b) SEM images, c-d) EDS elemental mappings of the MZ with a copper foil background.

XRD analysis was carried out to study the crystal structure of MZ, EM, and ZIF-8 as a comparison. In Fig. 6.3a, all the peaks in the XRD pattern of MZ can be attributed to ZIF-8 and MoS<sub>2</sub>. The diffraction peaks ( $2\theta$ ) at 14.4°, 32.7°, 33.5°, 35.8°, 39.5°, 44.1°, 49.7°, and 58.3° correspond to the (002), (100), (101), (102), (103), (006), (105), and (110) crystal planes of 2H-MoS<sub>2</sub> (PDF#37-1742), respectively.<sup>301</sup> The diffraction peaks ( $2\theta$ ) at 10.4°, 12.7°, 14.7°, 16.4°, and 18.1° correspond to the (011), (002), (112), (022), (013), and (222) crystal planes of ZIF-8, respectively.<sup>302</sup> Fig. 6.3b

and 6.3c show the nitrogen gas adsorption and desorption isotherms of the MZ and ZIF-8, respectively. The BET surface area of ZIF-8 is as high as 1,313.8 m<sup>2</sup>/g while the BET surface area of MZ reduces to 955.3 m<sup>2</sup>/g, but similarities were observed in the surface pore characteristics of the as-synthesized samples. Both curves of the prepared samples can be classified as Type I isotherm characteristics that reveal their microporous nature. However, the behavior of the isotherms for values of P/P<sub>0</sub> larger than 0.85 changes to Type IV, which suggests the existence of large pores due to intra-aggregate voids.<sup>303</sup> The specific surface areas and average pore diameters of the as-prepared materials were analyzed based on nitrogen adsorption and desorption measurements (Table 6.1). XPS analysis was carried out to investigate the chemical states and surface chemical compositions of MZ (Fig. 6.3). The XPS spectra of N 1s, O1s, Zn 2p, and the simulation results of their decomposition peaks are presented in Fig. 6.3d-f, respectively. For the N 1s spectra, the peak appear at 398.8 eV corresponds to the sp<sup>2</sup>-hybridized nitrogen (C=N-C) group.<sup>304</sup> The N 1s and C 1s peaks could be attributed to the presence of ZIF-8 that was synthesized by 2-methylimidazole.<sup>305</sup> The Zn 2p<sub>1/2</sub> and Zn 2p<sub>3/2</sub> peaks (Fig. 6.3f) at binding energies of 1,045.5 and 1,022.1 eV are in good agreement with of Zn<sup>2+</sup>, which means that the Zn element mainly exists in the Zn<sup>2+</sup> state. The main peak in the O 1s region at 530.3 eV is assigned to carbonates (Fig. 6.3f).<sup>306</sup>

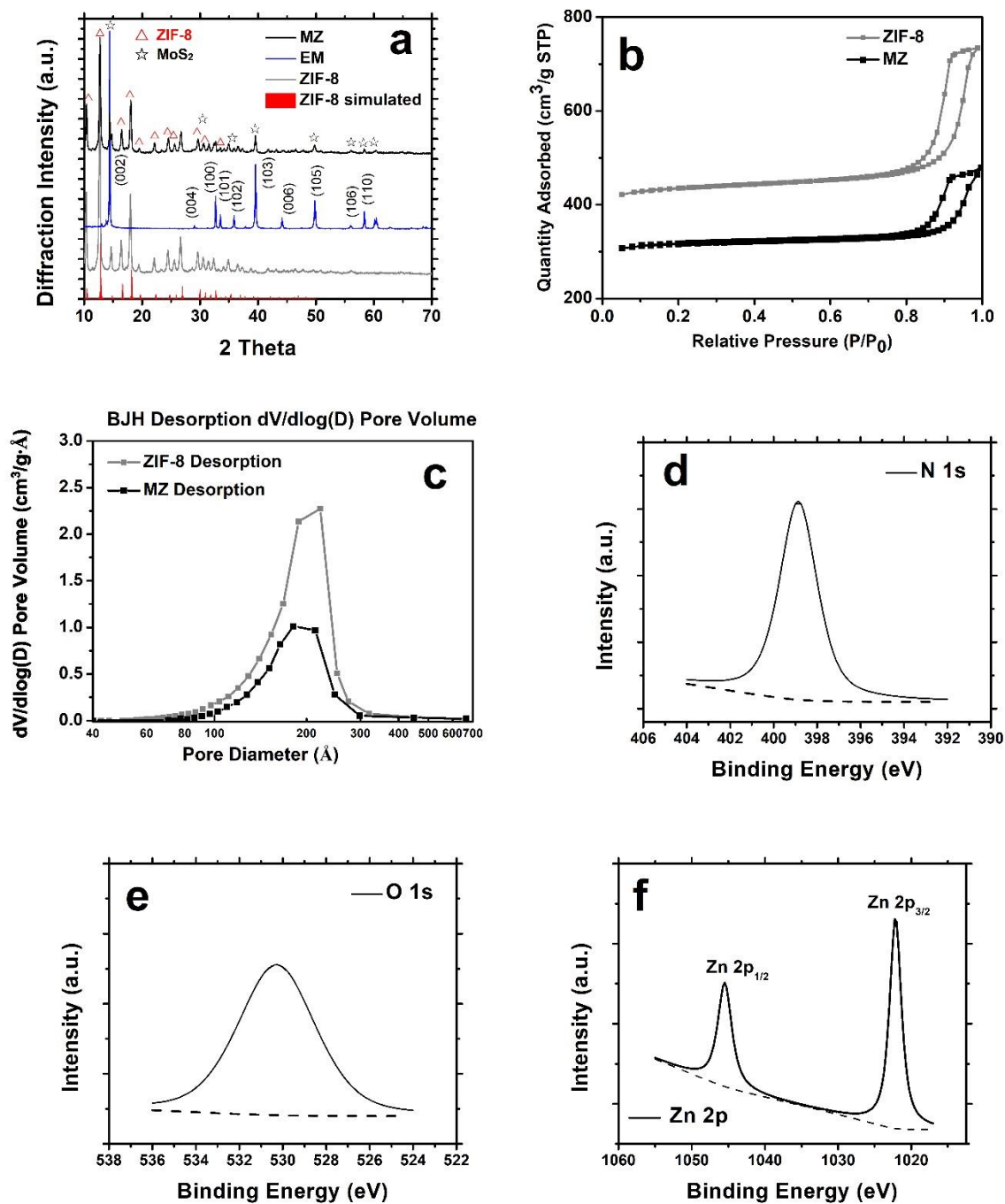


Fig. 6.3 a) Representative XRD patterns of the as-prepared samples; b) N<sub>2</sub> adsorption-desorption isotherms and c) Pore size distribution of MZ and ZIF-8; XPS spectrum of d) N1s, e) O1s and f) Zn 2p of MZ.

Table 6.1 Surface properties of ZIF-8 and as-synthesized MZ

Sample	BET Surface	BJH desorption average	Total pore volume (cm <sup>3</sup> /g)
	Area (m <sup>2</sup> /g)	pore diameter (Å)	
ZIF-8	1,313.8	139.0	1.14
MZ	955.3	127.2	0.74

Generally, bulk MoS<sub>2</sub> (band gap of 1.2 eV) is unsuitable for photocatalytic applications due to its insufficient reduction and oxidation ability for the activation of the photocatalytic reaction as shown in Fig. 6.4a. Nonetheless, exfoliated MoS<sub>2</sub> exhibits a direct band gap of 1.89~3.96 eV resulting from quantum confinement. In Huang *et al.*'s work, monolayer MQDs were prepared via a hydrothermal method and exhibit a 3.96 eV of direct band gap compared with monolayer MoS<sub>2</sub> NSs (1.89 eV).<sup>307</sup> By using scanning tunnelling microscopy (STM), another study reported CVD-prepared single-layer MoS<sub>2</sub> possesses a band gap of 2.40 eV.<sup>308</sup> Based on the self-consistent GW<sub>0</sub> (scGW<sub>0</sub>) calculations, Shi *et al.* predicted that the quasiparticle (QP) band structures of monolayer MoS<sub>2</sub> exhibit a direct band gap energy of 2.80 eV.<sup>309</sup> This offers the exfoliated MoS<sub>2</sub> with appropriate band positions to retain good visible-light absorption ability. As a result, the exfoliated MoS<sub>2</sub> is considered to be a promising candidate for photocatalytic applications. The optical absorption of ZIF-8, EM and MZ was investigated by UV-Vis absorption spectra (Fig. 6.4). The absorption edge for ZIF-8 (Fig. 6.4a) at ~250 nm without significant absorption in the visible light region suggests a band gap of 5.15 eV. The absorption edge of EM (Fig. 6.4b) is at ~390 nm showing limited visible light absorption ability with the band gap of 2.84 eV. However, for EM (band gap of 3.41 eV), the absorption edge appears at ~ 415 nm (Fig. 6.4c), which indicates EM is active in the visible light region. The possible mechanism is illustrated in Fig. 6.4d. The photocatalytic activity of MZ was investigated by monitoring visible light photocatalytic hydrogen evolution with a Xe lamp irradiation (AM 1.5 G and 100 mW cm<sup>-2</sup>). The hydrogen evolution rate

for the reported ZIF-8 is  $0.01 \mu\text{mol h}^{-1}\text{g}^{-1}$  and no activity is shown for bulk  $\text{MoS}_2$ . As shown in Fig. 6.4e, with the coexistence of EM, MZ gives an improved average hydrogen evolution rate of  $29.9 \mu\text{mol h}^{-1}\text{g}^{-1}$ .

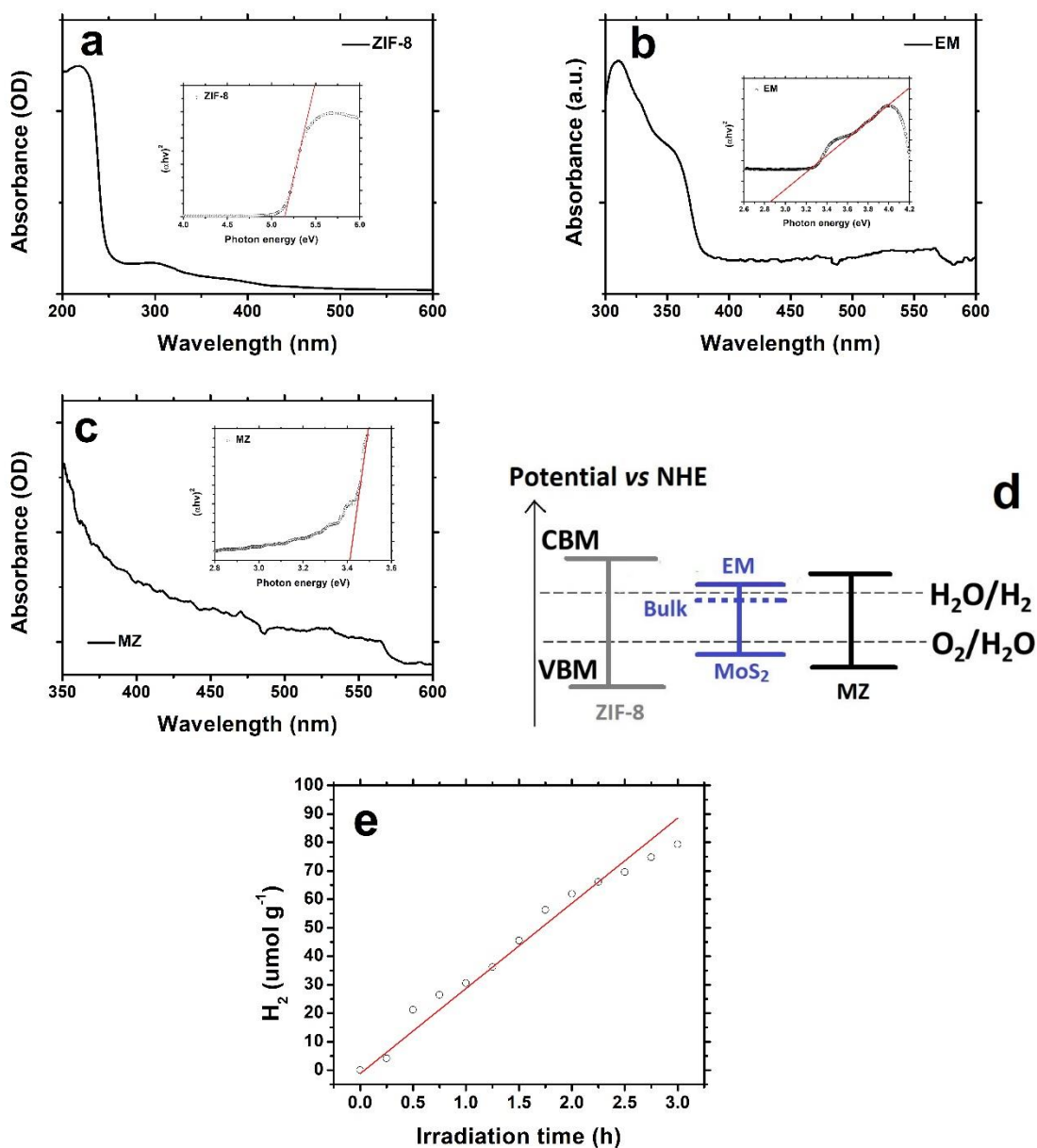


Fig. 6.4 UV-vis absorption spectra and Tauc's plot (inset) for band gap energy determination of (a) ZIF-8, (b) EM, and (c) MZ; d) Schematic illustration of the energy band structure of the as-prepared samples; e) Photocatalytic hydrogen production rate collected for MZ.

## 6.4 Summary and conclusions

In summary, a facile and effective method was demonstrated to synthesize exfoliated MoS<sub>2</sub>@ZIF-8 hybrids with improved photocatalytic activity in hydrogen production. Encapsulating exfoliated MoS<sub>2</sub> into ZIF-8 could maintain the desired porous structural characteristics of MOFs and large specific surface area (955.3 m<sup>2</sup>/g for MZ) that are critical for photocatalysis. The obtained hybrid photocatalyst exhibits enhanced absorption (~ 415 nm) in visible light range compared with pure ZIF-8 (~ 250 nm). As a result, as-prepared MoS<sub>2</sub>@ZIF-8 hybrids possess more desirable band gap structure (3.41 eV) than ZIF-8 (5.15 eV), which leads to an enhanced efficiency for photocatalysis. In comparison with the pristine ZIF-8, the MZ exhibits substantially higher photocatalytic activity for hydrogen production at 29.9 μmol h<sup>-1</sup>g<sup>-1</sup> under visible-light irradiation. The improved photocatalytic performance can be attributed to the larger specific surface area, suitable band structure and improved visible light-harvesting ability as a result of the hybrid structure.

## CHAPTER 7 SUMMARY AND FUTURE WORK

### 7.1 Summary

In summary, TMOs and TMDs are promising materials in various applications due to their unique structures and properties. In particular,  $\text{TiO}_2$  as one of the TMOs has multiple advantages in photocatalysis applications, such as structural stability, abundance, environmental-friendliness, and low-cost. However, the photocatalytic performance of  $\text{TiO}_2$  is limited since its relatively wide band gap makes it less efficient for harvesting solar energy. Modifying  $\text{TiO}_2$  with a suitable dopant not only changes the mechanism and kinetics under UV irradiation but also introduces more visible-light activity that is absent with pure  $\text{TiO}_2$ . The resulting  $\text{Ti}^{3+}$ -doped  $\text{TiO}_2$  with tunable photocatalytic properties synthesized using a hydrothermal method with varying amounts of reductant was proven to enhance visible light absorption, narrowing the band gap and improving the photocatalytic activity.

Cobalt sulfide-based nanostructures as one of the TMDs are ideal materials for supercapacitor electrodes due to their high specific surface area, conductivity, and redox active structures. Nevertheless,  $\text{CoS}_x$  materials still suffer from relatively low specific capacitances, degradation of performance over long cycling duration, and tedious synthesis and assembly methods. Vertically-aligned metallic  $\text{CoS}_2$  NWs were synthesized directly on carbon cloth or graphite disc current collectors with an open structure, which leads to a large accessible surface area and resists aggregation of the active material. Vertically-aligned metallic  $\text{CoS}_2$  NWs exhibited promising performance in supercapacitors, which is among the best reported for  $\text{CoS}_x$ -based active materials.

Both TMOs and TMDs are promising candidates for platinum-free electrocatalysts in renewable energy applications. In order to combine the advantages of TMOs and TMDs, an aerosol processing method was developed for the facile and green synthesis of reduced graphene oxide (rGO)/tungsten disulfide ( $WS_2$ )/tungsten trioxide ( $WO_3$ ) ternary nano hybrids. The resulting hybrid catalysts show one of the highest catalytic activities in HER compared with reported  $MoS_2/WS_2$ -based electrocatalysts. The environmentally-friendly synthesis and outstanding performance suggest a great potential of TMO and TMD hybrids for noble metal-free electrocatalysts in water splitting.

TMDs QDs have emerged as promising candidates for renewable energy applications due to their unique structure and optoelectronic properties. An exfoliated mesoporous  $MoS_2$  QDs-graphite composite structure was prepared as a promising anode material for LIBs/PIBs owing to its higher theoretical capacity and better rate capability compared with the commercial graphite anode. In the composite structure,  $MoS_2$  QDs can be located in the void spaces between graphite particles, thereby improving the specific capacity of LIBs/PIBs and relieving volume expansion of nanoparticles to meet the urgent need of reliable energy storage applications.

MOFs especially ZIF-8 have received great attention in energy storage, catalysis and sensing due to their high specific surface area, large pore volume, and excellent chemical stability. But its application as photocatalysts has not been adequately studied. Exfoliated  $MoS_2$  exhibits a suitable band gap resulting from quantum confinement, which makes it a promising candidate for photocatalytic applications compared with the bulk  $MoS_2$ . Encapsulating exfoliated  $MoS_2$  into ZIF-8 can lead to a promising visible light active photocatalyst for the application of hydrogen

production due to the larger specific surface area, suitable band structure and improved light-harvesting ability as a result of the hybrid structure.

## **7.2 Future work**

Previous studies have demonstrated the promising performance of TMOs, TMDs and their hybrids in energy conversion and storage applications. To better understand the mechanism of the MoS<sub>2</sub> QDs for applications in PIBs, further characterization and analysis for MoS<sub>2</sub> QDs and their improved electrochemical performance are warranted; Exfoliated MoS<sub>2</sub>@ZIF-8 hybrids for photocatalytic hydrogen production still need further understanding and exploration. Therefore, future studies can be summarized into the following two tasks.

### **7.2.1 MQDs for potassium-ion batteries**

To further explore the electrochemical properties of MQDs as the active material for PIBs. The cyclic voltammetry (CV) of the as-prepared anode should be measured on an electrochemical station using a three-electrode cell, with the MQDs as the working electrode, a potassium disk as the counter electrode, and a potassium ring as the reference electrode. Finally, Electrochemical impedance spectroscopy (EIS) needs to be performed between 10,000-0.1 Hz with an amplitude of 10 mV to examine the intrinsic electrochemical properties of MQDs-PIBs.

### **7.2.2 Photocatalytic hydrogen evolution studies**

To improve the photocatalytic hydrogen production by exfoliated MoS<sub>2</sub>@ZIF-8 hybrids, both materials aspect and the testing system aspect could be enhanced through the future work. For the materials aspect, ZnO is proved to accelerate the photocatalytic efficiency in the ZIF system but

only trace amount of ZnO can be found now without further annealing process. Thus, the annealing temperature and environment need to be explored. For example, the previous study showed that the structure and morphology of ZIF-8 were maintained when the calcination temperature was less than 500 °C. However, ZIF-8 began to decompose and the ZnO@C was formed when the temperature reached 600°C.<sup>310</sup> And another study showed that Ag<sup>+</sup> can break coordinative bonds and create a hydroxyl-rich environment to transform Zn<sup>2+</sup> into ZnO to narrow the band gap and slow its electron-hole pair recombination.<sup>311</sup> Besides, WS<sub>2</sub> NSs are anticipated to be active photocatalysts with a low rate of recombination and narrow bandgap either under the visible or under NIR irradiation. Therefore, WS<sub>2</sub>@ZIF-8 holds interesting potential for the application of photocatalytic hydrogen evolution.<sup>312</sup> For the testing system of the photocatalytic hydrogen evolution, most of the photocatalysis was conducted in the liquid interface, which means many sacrificial agents could be chosen such as TEOA, glycerol, Na<sub>2</sub>SO<sub>3</sub>, and H<sub>2</sub>C<sub>2</sub>O<sub>4</sub>.<sup>313-315</sup> On the contrary, limited choice of sacrificial agents is available for the gas interface system such as methanol. Furthermore, the liquid interface system is more favorable because potential electrochemical measurements for the photocatalysis are easier to realize.

## REFERENCES

1. Yuan, C. Z., Wu, H. B., Xie, Y. & Lou, X. W. Mixed Transition-Metal Oxides: Design, Synthesis, and Energy-Related Applications. *Angew. Chem. Int. Ed.* **53**, 1488-1504 (2014).
2. Chen, X. & McDonald, A. R. Functionalization of Two-Dimensional Transition-Metal Dichalcogenides. *Adv. Mater.* **28**, 5738-5746 (2016).
3. Choi, W. *et al.* Recent development of two-dimensional transition metal dichalcogenides and their applications. *Mater. Today* **20**, 116-130 (2017).
4. Dong, R. & Kuljanishvili, I. Review Article: Progress in fabrication of transition metal dichalcogenides heterostructure systems. *J. Vac. Sci. Technol. B* **35** (2017).
5. Tran, P. D. *et al.* Coordination polymer structure and revisited hydrogen evolution catalytic mechanism for amorphous molybdenum sulfide. *Nat. Mater.* **15**, 640-+ (2016).
6. Norskov, J. K. *et al.* Trends in the exchange current for hydrogen evolution. *J. Electrochem. Soc.* **152**, J23-J26 (2005).
7. Tsai, C., Chan, K. R., Norskov, J. K. & Abild-Pedersen, F. Theoretical insights into the hydrogen evolution activity of layered transition metal dichalcogenides. *Surf. Sci.* **640**, 133-140 (2015).
8. He, C. Y. & Tao, J. Z. Three-dimensional hollow porous Co<sub>6</sub>Mo<sub>6</sub>C nanoframe as an highly active and durable electrocatalyst for water splitting. *J. Catal.* **347**, 63-71 (2017).
9. Marschall, R. & Wang, L. Z. Non-metal doping of transition metal oxides for visible-light photocatalysis. *Catal. Today* **225**, 111-135 (2014).
10. Ola, O. & Maroto-Valer, M. M. Review of material design and reactor engineering on TiO<sub>2</sub> photocatalysis for CO<sub>2</sub> reduction. *J Photoch Photobio C* **24**, 16-42 (2015).
11. Chen, H. S. *et al.* Progress in electrical energy storage system: A critical review. *Prog. Nat. Sci.* **19**, 291-312 (2009).
12. Li, R. Y. *et al.* Significantly enhanced electrochemical performance of lithium titanate anode for lithium ion battery by the hybrid of nitrogen and sulfur co-doped graphene quantum dots. *Electrochim. Acta* **178**, 303-311 (2015).
13. Choudhary, N. *et al.* High-Performance One-Body Core/Shell Nanowire Supercapacitor Enabled by Conformal Growth of Capacitive 2D WS<sub>2</sub> Layers. *ACS Nano* **10**, 10726-10735 (2016).

14. Luo, X., Wang, J. H., Dooner, M. & Clarke, J. Overview of current development in electrical energy storage technologies and the application potential in power system operation. *Appl. Energ.* **137**, 511-536 (2015).
15. Hong, W. T. *et al.* Toward the rational design of non-precious transition metal oxides for oxygen electrocatalysis. *Energ. Environ. Sci.* **8**, 1404-1427 (2015).
16. Liu, C. F., Neale, Z. G. & Cao, G. Z. Understanding electrochemical potentials of cathode materials in rechargeable batteries. *Mater. Today* **19**, 109-123 (2016).
17. Yoo, H. D., Markevich, E., Salitra, G., Sharon, D. & Aurbach, D. On the challenge of developing advanced technologies for electrochemical energy storage and conversion. *Mater. Today* **17**, 110-121 (2014).
18. Acerce, M., Voiry, D. & Chhowalla, M. Metallic 1T phase MoS<sub>2</sub> nanosheets as supercapacitor electrode materials. *Nat. Nanotechnol.* **10**, 313-318 (2015).
19. Chhowalla, M., Liu, Z. F. & Zhang, H. Two-dimensional transition metal dichalcogenide (TMD) nanosheets. *Chem. Soc. Rev.* **44**, 2584-2586 (2015).
20. Choi, S. H., Ko, Y. N., Lee, J. K. & Kang, Y. C. 3D MoS<sub>2</sub>-Graphene Microspheres Consisting of Multiple Nanospheres with Superior Sodium Ion Storage Properties. *Adv. Funct. Mater.* **25**, 1780-1788 (2015).
21. Duan, X. D., Wang, C., Pan, A. L., Yu, R. Q. & Duan, X. F. Two-dimensional transition metal dichalcogenides as atomically thin semiconductors: opportunities and challenges. *Chem. Soc. Rev.* **44**, 8859-8876 (2015).
22. Ji, Q. Q. *et al.* Morphological Engineering of CVD-Grown Transition Metal Dichalcogenides for Efficient Electrochemical Hydrogen Evolution. *Adv. Mater.* **28**, 6207-6212 (2016).
23. Krishnamoorthy, K., Pazhamalai, P., Veerasubramani, G. K. & Kim, S. J. Mechanically delaminated few layered MoS<sub>2</sub> nanosheets based high performance wire type solid-state symmetric supercapacitors. *J. Power Sources* **321**, 112-119 (2016).
24. Ping, J. F., Fan, Z. X., Sindoro, M., Ying, Y. B. & Zhang, H. Recent Advances in Sensing Applications of Two-Dimensional Transition Metal Dichalcogenide Nanosheets and Their Composites. *Adv. Funct. Mater.* **27** (2017).
25. Kang, M. *et al.* Universal Mechanism of Band-Gap Engineering in Transition-Metal Dichalcogenides. *Nano Lett.* **17**, 1610-1615 (2017).
26. Kumar, A. & Ahluwalia, P. K. Tunable dielectric response of transition metals dichalcogenides MX<sub>2</sub> (M=Mo, W; X=S, Se, Te): Effect of quantum confinement. *Physica. B, Condensed matter.* **407**, 4627-4634 (2012).

27. El-Kady, M. F. *et al.* Engineering three-dimensional hybrid supercapacitors and microsupercapacitors for high-performance integrated energy storage. *Proc. Natl. Acad. Sci. U.S.A.* **112**, 4233-4238 (2015).
28. Liu, H. L. *et al.* Optical properties of monolayer transition metal dichalcogenides probed by spectroscopic ellipsometry. *Appl. Phys. Lett.* **105** (2014).
29. Huang, Z. F. *et al.* Tungsten Oxides for Photocatalysis, Electrochemistry, and Phototherapy. *Adv. Mater.* **27**, 5309-5327 (2015).
30. Wei, W. *et al.* Transition metal oxide hierarchical nanotubes for energy applications. *Nanotechnology* **27** (2016).
31. Gerling, L. G., Mahato, S., Voz, C., Alcubilla, R. & Puigdollers, J. Characterization of Transition Metal Oxide/Silicon Heterojunctions for Solar Cell Applications. *Appl. Sci.* **5**, 695-705 (2015).
32. Lai, X. Y. *et al.* General Synthesis and Gas-Sensing Properties of Multiple-Shell Metal Oxide Hollow Microspheres. *Angew. Chem. Int. Ed.* **50**, 2738-2741 (2011).
33. Chen, P. C., Shen, G. Z., Shi, Y., Chen, H. T. & Zhou, C. W. Preparation and Characterization of Flexible Asymmetric Supercapacitors Based on Transition-Metal-Oxide Nanowire/Single-Walled Carbon Nanotube Hybrid Thin-Film Electrodes. *Acs Nano* **4**, 4403-4411 (2010).
34. Guo, T., Yao, M. S., Lin, Y. H. & Nan, C. W. A comprehensive review on synthesis methods for transition-metal oxide nanostructures. *Crystengcomm* **17**, 3551-3585 (2015).
35. Lany, S. Semiconducting transition metal oxides. *J. Phys. Condens. Matter* **27** (2015).
36. Li, C., Li, J. C., Lian, J. S. & Jiang, Q. Improving Levine model for dielectric constants of transition metal compounds. *J. Appl. Phys.* **106** (2009).
37. Lin, C. W., Posadas, A., Choi, M. & Demkov, A. A. Optical properties of transition metal oxide quantum wells. *J. Appl. Phys.* **117** (2015).
38. Choi, W. S. *et al.* Wide bandgap tunability in complex transition metal oxides by site-specific substitution. *Nat. Commun.* **3** (2012).
39. Rao, C. N. R. Transition-Metal Oxides. *Annu. Rev. Phys. Chem.* **40**, 291-326 (1989).
40. Yamanaka, S., Kanki, T., Kawai, T. & Tanaka, H. Enhancement of Spin Polarization in a Transition Metal Oxide Ferromagnetic Nanodot Diode. *Nano Lett.* **11**, 343-347 (2011).
41. Leong, C. C., Pan, H. & Ho, S. K. Two-dimensional transition-metal oxide monolayers as cathode materials for Li and Na ion batteries. *Phys. Chem. Chem. Phys.* **18**, 7527-7534 (2016).

42. Seo, J. W., Jun, Y. W., Ko, S. J. & Cheon, J. In situ one-pot synthesis of 1-dimensional transition metal oxide nanocrystals. *J. Phys. Chem. B* **109**, 5389-5391 (2005).
43. Li, F. *et al.* MoS<sub>2</sub> quantum dot decorated RGO: a designed electrocatalyst with high active site density for the hydrogen evolution reaction. *J. Mater. Chem. A* **3**, 21772-21778 (2015).
44. Sun, Z. Q. *et al.* Generalized self-assembly of scalable two-dimensional transition metal oxide nanosheets. *Nat. Commun.* **5** (2014).
45. Niu, D. *et al.* Elementary reaction schemes for physical and chemical vapor deposition of transition metal oxides on silicon for high-k gate dielectric applications. *J. Appl. Phys.* **91**, 6173-6180 (2002).
46. Xu, Z. H. *et al.* The compositional, structural, and magnetic properties of a Fe<sub>3</sub>O<sub>4</sub>/Ga<sub>2</sub>O<sub>3</sub>/GaN spin injecting hetero-structure grown by metal-organic chemical vapor deposition. *Appl. Surf. Sci.* **388**, 141-147 (2016).
47. Lamb, D. A. & Irvine, S. J. C. A temperature dependant crystal orientation transition of cadmium oxide films deposited by metal organic chemical vapour deposition. *J. Cryst. Growth* **332**, 17-20 (2011).
48. Kwon, J. M. *et al.* Facile hydrothermal synthesis of cubic spinel AB<sub>2</sub>O<sub>4</sub> type MnFe<sub>2</sub>O<sub>4</sub> nanocrystallites and their electrochemical performance. *Appl. Surf. Sci.* **413**, 83-91 (2017).
49. Nakata, K. & Fujishima, A. TiO<sub>2</sub> photocatalysis: Design and applications. *J Photoch Photobio C* **13**, 169-189 (2012).
50. Liu, B. *et al.* Ligand-Assisted Co-Assembly Approach toward Mesoporous Hybrid Catalysts of Transition-Metal Oxides and Noble Metals: Photochemical Water Splitting. *Angew Chem Int Edit* **54**, 9061-9065 (2015).
51. Gupta, S. & Tripathi, M. A review of TiO<sub>2</sub> nanoparticles. *Chin. Sci. Bull.* **56**, 1639-1657 (2011).
52. Jiang, W. Y. *et al.* Integration of Multiple Plasmonic and Co-Catalyst Nanostructures on TiO<sub>2</sub> Nanosheets for Visible-Near-Infrared Photocatalytic Hydrogen Evolution. *Small* **12**, 1640-1648 (2016).
53. Kment, S. *et al.* Photoelectrochemical properties of hierarchical nanocomposite structure: Carbon nanofibers/TiO<sub>2</sub>/ZnO thin films. *Catal. Today* **161**, 8-14 (2011).
54. Pal, A., Jana, A., Bhattacharya, S. & Datta, J. SPR effect of AgNPs decorated TiO<sub>2</sub> in DSSC using TPMPi in the electrolyte: Approach towards low light trapping. *Electrochim. Acta* **243**, 33-43 (2017).
55. Pang, Y. L. & Abdullah, A. Z. Fe<sup>3+</sup> doped TiO<sub>2</sub> nanotubes for combined adsorption-sonocatalytic degradation of real textile wastewater. *Appl. Catal., B* **129**, 473-481 (2013).

56. Gao, M. M., Zhu, L. L., Ong, W. L., Wang, J. & Ho, G. W. Structural design of TiO<sub>2</sub>-based photocatalyst for H<sub>2</sub> production and degradation applications. *Catal. Sci. Tech.* **5**, 4703-4726 (2015).
57. Hashimoto, K., Irie, H. & Fujishima, A. TiO<sub>2</sub> photocatalysis: A historical overview and future prospects. *Jpn. J. Appl. Phys. I* **44**, 8269-8285 (2005).
58. Buonsanti, R. *et al.* Hyperbranched Anatase TiO<sub>2</sub> Nanocrystals: Nonaqueous Synthesis, Growth Mechanism, and Exploitation in Dye-Sensitized Solar Cells. *J. Am. Chem. Soc.* **133**, 19216-19239 (2011).
59. Hardin, B. E. *et al.* Energy and Hole Transfer between Dyes Attached to Titania in Cosensitized Dye-Sensitized Solar Cells. *J. Am. Chem. Soc.* **133**, 10662-10667 (2011).
60. Song, W. X., Wang, H., Liu, G. C., Peng, M. & Zou, D. C. Improving the photovoltaic performance and flexibility of fiber-shaped dye-sensitized solar cells with atomic layer deposition. *Nano Energy* **19**, 1-7 (2016).
61. Meng, Q. Q., Wang, J. G., Xie, Q., Dong, H. Q. & Li, X. N. Water splitting on TiO<sub>2</sub> nanotube arrays. *Catal. Today* **165**, 145-149 (2011).
62. Wang, D. *et al.* Photoelectrochemical Water Splitting with Rutile TiO<sub>2</sub> Nanowires Array: Synergistic Effect of Hydrogen Treatment and Surface Modification with Anatase Nanoparticles. *Electrochim. Acta* **130**, 290-295 (2014).
63. Li, L. D. *et al.* Sub-10 nm rutile titanium dioxide nanoparticles for efficient visible-light-driven photocatalytic hydrogen production. *Nat. Commun.* **6** (2015).
64. Zhang, Y. Z. *et al.* Photoelectrocatalytic degradation of recalcitrant organic pollutants using TiO<sub>2</sub> film electrodes: An overview. *Chemosphere* **88**, 145-154 (2012).
65. Yang, X. F. *et al.* Fabrication of P25/Ag<sub>3</sub>PO<sub>4</sub>/graphene oxide heterostructures for enhanced solar photocatalytic degradation of organic pollutants and bacteria. *Appl. Catal., B* **166**, 231-240 (2015).
66. Xiong, Z. G. *et al.* Synthesis of mesoporous anatase TiO<sub>2</sub> with a combined template method and photocatalysis. *Crystengcomm* **12**, 3455-3457 (2010).
67. Elhajj, J. *et al.* Electrochemical Fabrication of TiO<sub>2</sub>-Au Nanocomposites. *J. Electrochem. Soc.* **157**, D5-D9 (2010).
68. Cui, L. *et al.* Facile microwave-assisted hydrothermal synthesis of TiO<sub>2</sub> nanotubes. *Mater. Lett.* **75**, 175-178 (2012).
69. Bai, H., Liu, Z. & Sun, D. D. The design of a hierarchical photocatalyst inspired by natural forest and its usage on hydrogen generation. *Int. J. Hydrogen Energy* **37**, 13998-14008 (2012).

70. Ng, J., Pan, J. H. & Sun, D. D. Hierarchical assembly of anatase nanowhiskers and evaluation of their photocatalytic efficiency in comparison to various one-dimensional TiO<sub>2</sub> nanostructures. *J. Mater. Chem.* **21**, 11844-11853 (2011).
71. Xu, Y. F. *et al.* CdS/CdSe co-sensitized TiO<sub>2</sub> nanowire-coated hollow Spheres exceeding 6% photovoltaic performance. *Nano Energy* **11**, 621-630 (2015).
72. Xi, G. C. *et al.* Synthesis of Multiple-Shell WO<sub>3</sub> Hollow Spheres by a Binary Carbonaceous Template Route and Their Applications in Visible-Light Photocatalysis. *Chem. Eur. J.* **18**, 13949-13953 (2012).
73. Ciftiyurek, E., Sabolsky, K. & Sabolsky, E. M. Molybdenum and tungsten oxide based gas sensors for high temperature detection of environmentally hazardous sulfur species. *Sens. Actuator B-Chem.* **237**, 262-274 (2016).
74. Yoon, S. *et al.* Development of a high-performance anode for lithium ion batteries using novel ordered mesoporous tungsten oxide materials with high electrical conductivity. *Phys. Chem. Chem. Phys.* **13**, 11060-11066 (2011).
75. Jin, J., Yu, J. G., Guo, D. P., Cui, C. & Ho, W. K. A Hierarchical Z-Scheme CdS-WO<sub>3</sub> Photocatalyst with Enhanced CO<sub>2</sub> Reduction Activity. *Small* **11**, 5262-5271 (2015).
76. Wu, R., Zhang, J. F., Shi, Y. M., Liu, D. & Zhang, B. Metallic WO<sub>2</sub>-Carbon Mesoporous Nanowires as Highly Efficient Electrocatalysts for Hydrogen Evolution Reaction. *J. Am. Chem. Soc.* **137**, 6983-6986 (2015).
77. Tedstone, A. A., Lewis, D. J. & O'Brien, P. Synthesis, Properties, and Applications of Transition Metal-Doped Layered Transition Metal Dichalcogenides. *Chem. Mater.* **28**, 1965-1974 (2016).
78. Ouyang, B., Mi, Z. T. & Song, J. Bandgap Transition of 2H Transition Metal Dichalcogenides: Predictive Tuning via Inherent Interface Coupling and Strain. *J. Phys. Chem. C* **120**, 8927-8935 (2016).
79. Lin, Z. *et al.* Defect engineering of two-dimensional transition metal dichalcogenides. *2D Mater.* **3** (2016).
80. Sun, Y. J., Wang, D. & Shuai, Z. G. Indirect-to-Direct Band Gap Crossover in Few-Layer Transition Metal Dichalcogenides: A Theoretical Prediction. *J. Phys. Chem. C* **120**, 21866-21870 (2016).
81. Ma, Y. D., Kou, L. Z., Li, X., Dai, Y. & Heine, T. Two-dimensional transition metal dichalcogenides with a hexagonal lattice: Room-temperature quantum spin Hall insulators. *Phys. Rev. B* **93** (2016).
82. Bissett, M. A., Worrall, S. D., Kinloch, I. A. & Dryfe, R. A. W. Comparison of Two-Dimensional Transition Metal Dichalcogenides for Electrochemical Supercapacitors. *Electrochim. Acta* **201**, 30-37 (2016).

83. Zhang, X. *et al.* Phonon and Raman scattering of two-dimensional transition metal dichalcogenides from monolayer, multilayer to bulk material. *Chem. Soc. Rev.* **44**, 2757-2785 (2015).
84. Sun, G. Z. *et al.* Fabrication of Ultralong Hybrid Microfibers from Nanosheets of Reduced Graphene Oxide and Transition-Metal Dichalcogenides and their Application as Supercapacitors. *Angew. Chem. Int. Ed.* **53**, 12576-12580 (2014).
85. Schmidt, H., Giustiniano, F. & Eda, G. Electronic transport properties of transition metal dichalcogenide field-effect devices: surface and interface effects. *Chem. Soc. Rev.* **44**, 7715-7736 (2015).
86. Wang, Y. L. *et al.* Monolayer PtSe<sub>2</sub>, a New Semiconducting Transition-Metal-Dichalcogenide, Epitaxially Grown by Direct Selenization of Pt. *Nano Lett.* **15**, 4013-4018 (2015).
87. Johari, P. & Shenoy, V. B. Tuning the Electronic Properties of Semiconducting Transition Metal Dichalcogenides by Applying Mechanical Strains. *Acs Nano* **6**, 5449-5456 (2012).
88. Fan, X. B. *et al.* Controlled Exfoliation of MoS<sub>2</sub> Crystals into Trilayer Nanosheets. *J. Am. Chem. Soc.* **138**, 5143-5149 (2016).
89. Eng, A. Y. S., Ambrosi, A., Sofer, Z., Simek, P. & Pumera, M. Electrochemistry of Transition Metal Dichalcogenides: Strong Dependence on the Metal-to-Chalcogen Composition and Exfoliation Method. *Acs Nano* **8**, 12185-12198 (2014).
90. Li, Y. *et al.* Metal to semiconductor transition in metallic transition metal dichalcogenides. *J. Appl. Phys.* **114** (2013).
91. Voiry, D., Mohite, A. & Chhowalla, M. Phase engineering of transition metal dichalcogenides. *Chem. Soc. Rev.* **44**, 2702-2712 (2015).
92. Du, Y. C., Neal, A. T., Zhou, H. & Ye, P. D. Transport studies in 2D transition metal dichalcogenides and black phosphorus. *J. Phys. Condens. Matter* **28** (2016).
93. Chia, X. Y., Ambrosi, A., Lazar, P., Sofer, Z. & Pumera, M. Electrocatalysis of layered Group 5 metallic transition metal dichalcogenides (MX<sub>2</sub>, M = V, Nb, and Ta; X = S, Se, and Te). *J. Mater. Chem. A* **4**, 14241-14253 (2016).
94. Wu, J. Z., Dai, J., Shao, Y. B., Cao, M. Q. & Wu, X. H. Carbon dot-assisted hydrothermal synthesis of flower-like MoS<sub>2</sub> nanospheres constructed by few-layered multiphase MoS<sub>2</sub> nanosheets for supercapacitors. *RSC Adv.* **6**, 77999-78007 (2016).
95. Sun, T. H. *et al.* Oxygen-incorporated MoS<sub>2</sub> microspheres with tunable interiors as novel electrode materials for supercapacitors. *J. Power Sources* **352**, 135-142 (2017).
96. Yu, J. H. *et al.* ESR signal of superoxide radical anion adsorbed on TiO<sub>2</sub> generated at room temperature. *J. Phys. Chem. B* **108**, 2781-2783 (2004).

97. Usubharatana, P., McMartin, D., Veawab, A. & Tontiwachwuthikul, P. Photocatalytic process for CO<sub>2</sub> emission reduction from industrial flue gas streams. *Ind. Eng. Chem. Res.* **45**, 2558-2568 (2006).
98. Nakata, K. & Fujishima, A. TiO<sub>2</sub> photocatalysis: Design and applications. *J. Photochem. Photobiol. C-Photochem. Rev.* **13**, 169-189 (2012).
99. Nakata, K., Ochiai, T., Murakami, T. & Fujishima, A. Photoenergy conversion with TiO<sub>2</sub> photocatalysis: New materials and recent applications. *Electrochim. Acta* **84**, 103-111 (2012).
100. Augugliaro, V. *et al.* Overview on oxidation mechanisms of organic compounds by TiO<sub>2</sub> in heterogeneous photocatalysis. *J. Photochem. Photobiol. C-Photochem. Rev.* **13**, 224-245 (2012).
101. Mohamed, H. H. & Bahnemann, D. W. The role of electron transfer in photocatalysis: Fact and fictions. *Appl. Catal., B* **128**, 91-104 (2012).
102. Di Paola, A., Garcia-Lopez, E., Marci, G. & Palmisano, L. A survey of photocatalytic materials for environmental remediation. *J. Hazard. Mater.* **211**, 3-29 (2012).
103. Fujishima, A., Zhang, X. T. & Tryk, D. A. TiO<sub>2</sub> photocatalysis and related surface phenomena. *Surf. Sci. Rep.* **63**, 515-582 (2008).
104. Park, H., Park, Y., Kim, W. & Choi, W. Surface modification of TiO<sub>2</sub> photocatalyst for environmental applications. *J. Photochem. Photobiol. C-Photochem. Rev.* **15**, 1-20 (2013).
105. Kamat, P. V. & Meisel, D. Nanoparticles in advanced oxidation processes. *Curr. Opin. Colloid Interface Sci.* **7**, 282-287 (2002).
106. Gupta, N. & Pal, B. Photocatalytic activity of transition metal and metal ions impregnated TiO<sub>2</sub> nanostructures for iodide oxidation to iodine formation. *J. Mol. Catal. A: Chem.* **371**, 48-55 (2013).
107. Liu, S.-H. *et al.* Theoretical Study of N749 Dyes Anchoring on the (TiO<sub>2</sub>)<sub>(28)</sub> Surface in DSSCs and Their Electronic Absorption Properties. *J. Phys. Chem. C* **116**, 16338-16345 (2012).
108. Ziolk, M. *et al.* A photo-induced electron transfer study of an organic dye anchored on the surfaces of TiO<sub>2</sub> nanotubes and nanoparticles. *Phys. Chem. Chem. Phys.* **13**, 4032-4044 (2011).
109. Wang, J. G., Zhang, P., Li, X., Zhu, J. & Li, H. X. Synchronical pollutant degradation and H<sub>2</sub> production on a Ti<sup>3+</sup>-doped TiO<sub>2</sub> visible photocatalyst with dominant (001) facets. *Appl Catal B-Environ* **134**, 198-204 (2013).

110. Wang, W., Lu, C. H., Ni, Y. R., Peng, F. P. & Xu, Z. Z. Enhanced performance of {0 0 1} facets dominated mesoporous TiO<sub>2</sub> photocatalyst composed of high-reactive nanocrystals and mesoporous spheres. *Appl. Surf. Sci.* **265**, 438-442 (2013).
111. Fan, L. M., Yu, C., Yang, J., Duan, J. B. & Qiu, J. S. Preparation of ruthenium-loaded CNT-TiO<sub>2</sub> nanohybrids and their catalytic performance for the selective oxidation of benzyl alcohol. *New Carbon Mater* **28**, 289-294 (2013).
112. Williams, G., Seger, B. & Kamat, P. V. TiO<sub>2</sub>-graphene nanocomposites. UV-assisted photocatalytic reduction of graphene oxide. *Acs Nano* **2**, 1487-1491 (2008).
113. Zhang, Y., Tang, Z.-R., Fu, X. & Xu, Y.-J. TiO<sub>2</sub>-Graphene Nanocomposites for Gas-Phase Photocatalytic Degradation of Volatile Aromatic Pollutant: Is TiO<sub>2</sub>-Graphene Truly Different from Other TiO<sub>2</sub>-Carbon Composite Materials? *Acs Nano* **4**, 7303-7314 (2010).
114. Chen, X., Liu, L., Yu, P. Y. & Mao, S. S. Increasing solar absorption for photocatalysis with black hydrogenated titanium dioxide nanocrystals. *Science* **331**, 746-750 (2011).
115. Hamdy, M. S., Amrollahi, R. & Mul, G. Surface Ti<sup>3+</sup>-Containing (blue) Titania: A Unique Photocatalyst with High Activity and Selectivity in Visible Light-Stimulated Selective Oxidation. *Acs Catalysis* **2**, 2641-2647 (2012).
116. Ng, J., Wang, X. & Sun, D. D. One-pot hydrothermal synthesis of a hierarchical nanofungus-like anatase TiO<sub>2</sub> thin film for photocatalytic oxidation of bisphenol A. *Appl Catal B-Environ* **110**, 260-272 (2011).
117. Wang, G. *et al.* Hydrogen-treated TiO<sub>2</sub> nanowire arrays for photoelectrochemical water splitting. *Nano Lett.* **11**, 3026-3033 (2011).
118. Zhang, J., Xiao, X. & Nan, J. Hydrothermal-hydrolysis synthesis and photocatalytic properties of nano-TiO<sub>2</sub> with an adjustable crystalline structure. *J. Hazard. Mater.* **176**, 617-622 (2010).
119. Golabiewska, A., Zielinska-Jurek, A. & Zaleska, A. Characterization of TiO<sub>2</sub> Modified with Bimetallic Ag/Au Nanoparticles Obtained in Microemulsion System. *J. Adv. Oxid. Technol.* **15**, 71-77 (2012).
120. Huang, H., Ye, X., Huang, H., Zhang, L. & Leung, D. Y. C. Mechanistic study on formaldehyde removal over Pd/TiO<sub>2</sub> catalysts: Oxygen transfer and role of water vapor. *Chem. Eng. J.* **230**, 73-79 (2013).
121. Kojima, Y. *et al.* Hydrogen generation using sodium borohydride solution and metal catalyst coated on metal oxide. *Int. J. Hydrog. Energy* **27**, 1029-1034 (2002).
122. Lee, Y., Kim, Y., Jeong, H. & Kang, M. Hydrogen production from the photocatalytic hydrolysis of sodium borohydride in the presence of In-, Sn-, and Sb-TiO<sub>(2)s</sub>. *J. Ind. Eng. Chem.* **14**, 655-660 (2008).

123. Lu, Y.-C., Chen, M.-S. & Chen, Y.-W. Hydrogen generation by sodium borohydride hydrolysis on nanosized CoB catalysts supported on TiO<sub>2</sub>, Al<sub>2</sub>O<sub>3</sub> and CeO<sub>2</sub>. *Int. J. Hydrog. Energy* **37**, 4254-4258 (2012).
124. Mingyang Xing, W. F., Muhammad Nasir, Yunfei Ma, Jinlong Zhang, Masakazu Anpo. Self-doped Ti<sup>3+</sup>-enhanced TiO<sub>2</sub> nanoparticles with a high-performance photocatalysis. *J. Catal.* **297**, 236-243 (2013).
125. Zuo, F. *et al.* Active Facets on Titanium(III)-Doped TiO<sub>2</sub>: An Effective Strategy to Improve the Visible-Light Photocatalytic Activity. *Angew Chem Int Edit* **51**, 6223-6226 (2012).
126. Gao, P., Li, A., Sun, D. D. & Ng, W. J. Effects of various TiO<sub>2</sub> nanostructures and graphene oxide on photocatalytic activity of TiO<sub>2</sub>. *J. Hazard. Mater.* **279**, 96-104 (2014).
127. LI, H. Y., Yu, H. W., Sun, L., Zhai, J. L. & Han, X. R. A self-assembled 3D Pt/TiO<sub>2</sub> architecture for high-performance photocatalytic hydrogen production. *Nanoscale* **7** (2015).
128. Sun, Z. Q. *et al.* Rational Design of 3D Dendritic TiO<sub>2</sub> Nanostructures with Favorable Architectures. *J. Am. Chem. Soc.* **133**, 19314-19317 (2011).
129. Chaubey, R., Sahu, S., James, O. O. & Maity, S. A review on development of industrial processes and emerging techniques for production of hydrogen from renewable and sustainable sources. *Renew. Sust. Energ. Rev.* **23**, 443-462 (2013).
130. Clarizia, L., Russo, D., Di Somma, I., Andreozzi, R. & Marotta, R. Hydrogen Generation through Solar Photocatalytic Processes: A Review of the Configuration and the Properties of Effective Metal-Based Semiconductor Nanomaterials. *Energies* **10** (2017).
131. Hisatomi, T., Kubota, J. & Domen, K. Recent advances in semiconductors for photocatalytic and photoelectrochemical water splitting. *Chem. Soc. Rev.* **43**, 7520-7535 (2014).
132. Kudo, A. & Miseki, Y. Heterogeneous photocatalyst materials for water splitting. *Chem. Soc. Rev.* **38**, 253-278 (2009).
133. Suzuki, T., Watanabe, H., Oaki, Y. & Imai, H. Tuning of photocatalytic reduction by conduction band engineering of semiconductor quantum dots with experimental evaluation of the band edge potential. *Chem. Commun.* **52**, 6185-6188 (2016).
134. Wu, M., Ye, H. L., Zhao, F. Q. & Zeng, B. Z. High-Quality Metal-Organic Framework ZIF-8 Membrane Supported on Electrodeposited ZnO/2-methylimidazole Nanocomposite: Efficient Adsorbent for the Enrichment of Acidic Drugs. *Sci. Rep.* **7** (2017).
135. Gong, X., Wang, Y. J. & Kuang, T. R. ZIF-8-Based Membranes for Carbon Dioxide Capture and Separation. *ACS Sustain. Chem. Eng.* **5**, 11204-11214 (2017).

136. Zeng, M. *et al.* Core-shell CdS@ZIF-8 structures for improved selectivity in photocatalytic H<sub>2</sub> generation from formic acid. *Nano Res.* **9**, 2729-2734 (2016).
137. Khaselev, O. & Turner, J. A. A monolithic photovoltaic-photoelectrochemical device for hydrogen production via water splitting. *Science* **280**, 425-427 (1998).
138. Zou, Z., Ye, J., Sayama, K. & Arakawa, H. Direct splitting of water under visible light irradiation with an oxide semiconductor photocatalyst. *Nature* **414**, 625-627 (2001).
139. Wang, X. *et al.* A metal-free polymeric photocatalyst for hydrogen production from water under visible light. *Nat. Mater.* **8**, 76-80 (2009).
140. Popczun, E. J. *et al.* Nanostructured Nickel Phosphide as an Electrocatalyst for the Hydrogen Evolution Reaction. *J. Am. Chem. Soc.* **135**, 9267-9270 (2013).
141. Chhowalla, M. *et al.* The chemistry of two-dimensional layered transition metal dichalcogenide nanosheets. *Nat. Chem.* **5**, 263-275 (2013).
142. Hinnemann, B. *et al.* Biomimetic hydrogen evolution: MoS<sub>2</sub> nanoparticles as catalyst for hydrogen evolution. *J. Am. Chem. Soc.* **127**, 5308-5309 (2005).
143. Kibsgaard, J., Chen, Z., Reinecke, B. N. & Jaramillo, T. F. Engineering the surface structure of MoS<sub>2</sub> to preferentially expose active edge sites for electrocatalysis. *Nat. Mater.* **11**, 963-969 (2012).
144. Greeley, J., Jaramillo, T. F., Bonde, J., Chorkendorff, I. B. & Norskov, J. K. Computational high-throughput screening of electrocatalytic materials for hydrogen evolution. *Nat. Mater.* **5**, 909-913 (2006).
145. Voiry, D. *et al.* Enhanced catalytic activity in strained chemically exfoliated WS<sub>2</sub> nanosheets for hydrogen evolution. *Nat. Mater.* **12**, 850-855 (2013).
146. Cheng, L. *et al.* Ultrathin WS<sub>2</sub> nanoflakes as a high-performance electrocatalyst for the hydrogen evolution reaction. *Angew. Chem. Int. Ed. Engl.* **53**, 7860-7863 (2014).
147. He, Z. & Que, W. Molybdenum disulfide nanomaterials: Structures, properties, synthesis and recent progress on hydrogen evolution reaction. *Appl. Mater. Today* **3**, 23-56 (2016).
148. Zhu, Y. *et al.* Graphene and graphene oxide: synthesis, properties, and applications. *Adv. Mater.* **22**, 3906-3924 (2010).
149. Yoo, E. *et al.* Enhanced electrocatalytic activity of Pt subnanoclusters on graphene nanosheet surface. *Nano Lett.* **9**, 2255-2259 (2009).
150. Mao, S., Pu, H. H. & Chen, J. H. Graphene oxide and its reduction: modeling and experimental progress. *RSC Adv.* **2**, 2643-2662 (2012).

151. Li, Y. *et al.* MoS<sub>2</sub> nanoparticles grown on graphene: an advanced catalyst for the hydrogen evolution reaction. *J. Am. Chem. Soc.* **133**, 7296-7299 (2011).
152. Smith, A. J. *et al.* Molybdenum Sulfide Supported on Crumpled Graphene Balls for Electrocatalytic Hydrogen Production. *Adv. Energy Mater.* **4** (2014).
153. Chen, Y. *et al.* Aerosol synthesis of cargo-filled graphene nanosacks. *Nano Lett.* **12**, 1996-2002 (2012).
154. Chen, Y. *et al.* Encapsulation of particle ensembles in graphene nanosacks as a new route to multifunctional materials. *ACS Nano* **7**, 3744-3753 (2013).
155. Luo, J. *et al.* Crumpled Graphene-Encapsulated Si Nanoparticles for Lithium Ion Battery Anodes. *J. Phys. Chem. Lett.* **3**, 1824-1829 (2012).
156. Mao, S. *et al.* A general approach to one-pot fabrication of crumpled graphene-based nanohybrids for energy applications. *ACS Nano* **6**, 7505-7513 (2012).
157. Wang, Z. *et al.* Crumpled graphene nanoreactors. *Nanoscale* **7**, 10267-10278 (2015).
158. Carraro, F. *et al.* Fast One-Pot Synthesis of MoS<sub>2</sub>/Crumpled Graphene p-n Nanonjunctions for Enhanced Photoelectrochemical Hydrogen Production. *ACS Appl. Mater. Interfaces* **7**, 25685-25692 (2015).
159. Lukowski, M. A. *et al.* Highly active hydrogen evolution catalysis from metallic WS<sub>2</sub> nanosheets. *Energy Environ. Sci.* **7**, 2608-2613 (2014).
160. Xu, S., Li, D. & Wu, P. One-Pot, Facile, and Versatile Synthesis of Monolayer MoS<sub>2</sub>/WS<sub>2</sub> Quantum Dots as Bioimaging Probes and Efficient Electrocatalysts for Hydrogen Evolution Reaction. *Adv. Funct. Mater.* **25**, 1127-1136 (2015).
161. Zhao, X., Ma, X., Sun, J., Li, D. & Yang, X. Enhanced Catalytic Activities of Surfactant-Assisted Exfoliated WS<sub>2</sub> Nanodots for Hydrogen Evolution. *ACS Nano* **10**, 2159-2166 (2016).
162. Ratha, S. & Rout, C. S. Supercapacitor electrodes based on layered tungsten disulfide-reduced graphene oxide hybrids synthesized by a facile hydrothermal method. *ACS Appl. Mater. Interfaces* **5**, 11427-11433 (2013).
163. Yang, J. *et al.* Two-Dimensional Hybrid Nanosheets of Tungsten Disulfide and Reduced Graphene Oxide as Catalysts for Enhanced Hydrogen Evolution. *Angew. Chem. Int. Ed. Engl.* **52**, 13751-13754 (2013).
164. Duan, J. J., Chen, S., Chambers, B. A., Andersson, G. G. & Qiao, S. Z. 3D WS<sub>2</sub> Nanolayers@Heteroatom-Doped Graphene Films as Hydrogen Evolution Catalyst Electrodes. *Adv. Mater.* **27**, 4234-4241 (2015).

165. Chen, T. Y. *et al.* Comparative study on MoS<sub>2</sub> and WS<sub>2</sub> for electrocatalytic water splitting. *Int. J. Hydrog. Energy* **38**, 12302-12309 (2013).
166. Cao, X., Yin, Z. & Zhang, H. Three-dimensional graphene materials: preparation, structures and application in supercapacitors. *Energy & Environmental Science* **7**, 1850-1865 (2014).
167. Mao, S., Lu, G. & Chen, J. Three-dimensional graphene-based composites for energy applications. *Nanoscale* **7**, 6924-6943 (2015).
168. Snook, G. A., Kao, P. & Best, A. S. Conducting-polymer-based supercapacitor devices and electrodes. *J. Power Sources* **196**, 1-12 (2011).
169. Zhang, L. L. & Zhao, X. S. Carbon-based materials as supercapacitor electrodes. *Chem. Soc. Rev.* **38**, 2520-2531 (2009).
170. Simon, P. & Gogotsi, Y. Materials for electrochemical capacitors. *Nature Materials* **7**, 845-854 (2008).
171. Wang, G., Zhang, L. & Zhang, J. A review of electrode materials for electrochemical supercapacitors. *Chem. Soc. Rev.* **41**, 797-828 (2012).
172. Miller, J. R. & Simon, P. Materials science - Electrochemical capacitors for energy management. *Science* **321**, 651-652 (2008).
173. Wu, Z.-S. *et al.* Anchoring Hydrrous RuO<sub>2</sub> on Graphene Sheets for High-Performance Electrochemical Capacitors. *Adv. Funct. Mater.* **20**, 3595-3602 (2010).
174. Zhang, J., Jiang, J., Li, H. & Zhao, X. S. A high-performance asymmetric supercapacitor fabricated with graphene-based electrodes. *Energy & Environmental Science* **4**, 4009-4015 (2011).
175. Chen, S., Zhu, J., Wu, X., Han, Q. & Wang, X. Graphene Oxide-MnO<sub>2</sub> Nanocomposites for Supercapacitors. *ACS Nano* **4**, 2822-2830 (2010).
176. Wei, W., Cui, X., Chen, W. & Ivey, D. G. Manganese oxide-based materials as electrochemical supercapacitor electrodes. *Chem. Soc. Rev.* **40**, 1697-1721 (2011).
177. Cheng, Y., Lu, S., Zhang, H., Varanasi, C. V. & Liu, J. Synergistic Effects from Graphene and Carbon Nanotubes Enable Flexible and Robust Electrodes for High-Performance Supercapacitors. *Nano Lett.* **12**, 4206-4211 (2012).
178. Han, Z. J., Seo, D. H., Yick, S., Chen, J. H. & Ostrikov, K. MnOx/carbon nanotube/reduced graphene oxide nanohybrids as high-performance supercapacitor electrodes. *NPG Asia Materials* **6** (2014).

179. Chen, S., Duan, J., Jaroniec, M. & Qiao, S. Z. Hierarchically porous graphene-based hybrid electrodes with excellent electrochemical performance. *Journal of Materials Chemistry A* **1**, 9409-9413 (2013).
180. Yang, Y. *et al.* Hydrothermally Formed Three-Dimensional Nanoporous Ni(OH)<sub>2</sub> Thin-Film Supercapacitors. *ACS Nano* **8**, 9622-9628 (2014).
181. Yu, M. *et al.* Scalable self-growth of Ni@NiO core-shell electrode with ultrahigh capacitance and super-long cyclic stability for supercapacitors. *NPG Asia Materials* **6** (2014).
182. Dong, X.-C. *et al.* 3D Graphene-Cobalt Oxide Electrode for High-Performance Supercapacitor and Enzymeless Glucose Detection. *ACS Nano* **6**, 3206-3213 (2012).
183. Liu, J. *et al.* Co<sub>3</sub>O<sub>4</sub> Nanowire@MnO<sub>2</sub> Ultrathin Nanosheet Core/Shell Arrays: A New Class of High-Performance Pseudocapacitive Materials. *Adv. Mater.* **23**, 2076-2081 (2011).
184. Xia, X. *et al.* High-Quality Metal Oxide Core/Shell Nanowire Arrays on Conductive Substrates for Electrochemical Energy Storage. *ACS Nano* **6**, 5531-5538 (2012).
185. Liu, Y. *et al.* Hierarchical SnO<sub>2</sub> Nanostructures Made of Intermingled Ultrathin Nanosheets for Environmental Remediation, Smart Gas Sensor, and Supercapacitor Applications. *Acs Appl Mater Inter* **6**, 2174-2184 (2014).
186. Rakhi, R. B., Chen, W., Cha, D. & Alshareef, H. N. High performance supercapacitors using metal oxide anchored graphene nanosheet electrodes. *J. Mater. Chem.* **21**, 16197-16204 (2011).
187. Davies, A. *et al.* Graphene-Based Flexible Supercapacitors: Pulse-Electropolymerization of Polypyrrole on Free-Standing Graphene Films. *Journal of Physical Chemistry C* **115**, 17612-17620 (2011).
188. Wang, D.-W. *et al.* Fabrication of Graphene/Polyaniline Composite Paper via In Situ Anodic Electropolymerization for High-Performance Flexible Electrode. *ACS Nano* **3**, 1745-1752 (2009).
189. Cao, L. *et al.* Direct Laser-Patterned Micro-Supercapacitors from Paintable MoS<sub>2</sub> Films. *Small* **9**, 2905-2910 (2013).
190. Feng, J. *et al.* Metallic Few-Layered VS<sub>2</sub> Ultrathin Nanosheets: High Two-Dimensional Conductivity for In-Plane Supercapacitors. *J. Am. Chem. Soc.* **133**, 17832-17838 (2011).
191. Lin, T.-W., Dai, C.-S. & Hung, K.-C. High Energy Density Asymmetric Supercapacitor Based on NiOOH/Ni<sub>3</sub>S<sub>2</sub>/3D Graphene and Fe<sub>3</sub>O<sub>4</sub>/Graphene Composite Electrodes. *Scientific Reports* **4**, 7274 (2014).

192. Ratha, S. & Rout, C. S. Supercapacitor Electrodes Based on Layered Tungsten Disulfide-Reduced Graphene Oxide Hybrids Synthesized by a Facile Hydrothermal Method. *Acs Appl Mater Inter* **5**, 11427-11433 (2013).
193. Winchester, A. *et al.* Electrochemical Characterization of Liquid Phase Exfoliated Two-Dimensional Layers of Molybdenum Disulfide. *Acs Appl Mater Inter* **6**, 2125-2130 (2014).
194. Yang, J., Duan, X., Qin, Q. & Zheng, W. Solvothermal synthesis of hierarchical flower-like beta-NiS with excellent electrochemical performance for supercapacitors. *Journal of Materials Chemistry A* **1**, 7880-7884 (2013).
195. Gu, X. *et al.* A Solution-Processed Hole Extraction Layer Made from Ultrathin MoS<sub>2</sub> Nanosheets for Efficient Organic Solar Cells. *Advanced Energy Materials* **3**, 1262-1268 (2013).
196. Rhee, J. H., Chung, C.-C. & Diao, E. W.-G. A perspective of mesoscopic solar cells based on metal chalcogenide quantum dots and organometal-halide perovskites. *NPG Asia Materials* **5** (2013).
197. Yun, J.-M. *et al.* Exfoliated and Partially Oxidized MoS<sub>2</sub> Nanosheets by One-Pot Reaction for Efficient and Stable Organic Solar Cells. *Small* **10**, 2319-2324 (2014).
198. Chang, K. & Chen, W. L-Cysteine-Assisted Synthesis of Layered MoS<sub>2</sub>/Graphene Composites with Excellent Electrochemical Performances for Lithium Ion Batteries. *ACS Nano* **5**, 4720-4728 (2011).
199. Chen, Y., Song, B., Tang, X., Lu, L. & Xue, J. Ultrasmall Fe<sub>3</sub>O<sub>4</sub> Nanoparticle/MoS<sub>2</sub> Nanosheet Composites with Superior Performances for Lithium Ion Batteries. *Small* **10**, 1536-1543 (2014).
200. Kong, D. *et al.* Synthesis of MoS<sub>2</sub> and MoSe<sub>2</sub> Films with Vertically Aligned Layers. *Nano Lett.* **13**, 1341-1347 (2013).
201. Mao, S. *et al.* Perpendicularly Oriented MoSe<sub>2</sub>/Graphene Nanosheets as Advanced Electrocatalysts for Hydrogen Evolution. *Small* **11**, 414-419 (2015).
202. Faber, M. S. & Jin, S. Earth-abundant inorganic electrocatalysts and their nanostructures for energy conversion applications. *Energy Environ. Sci.* **7**, 3519-3542 (2014).
203. Peng, S. *et al.* MS<sub>2</sub> (M = Co and Ni) Hollow Spheres with Tunable Interiors for High-Performance Supercapacitors and Photovoltaics. *Adv. Funct. Mater.* **24**, 2155-2162 (2014).
204. Wang, B. *et al.* Solvothermal synthesis of CoS<sub>2</sub>-graphene nanocomposite material for high-performance supercapacitors. *J. Mater. Chem.* **22**, 15750-15756 (2012).

205. Wang, Q. *et al.* Co<sub>3</sub>S<sub>4</sub> hollow nanospheres grown on graphene as advanced electrode materials for supercapacitors. *J. Mater. Chem.* **22**, 21387-21391 (2012).
206. Pu, J., Wang, Z., Wu, K., Yu, N. & Sheng, E. Co<sub>9</sub>S<sub>8</sub> nanotube arrays supported on nickel foam for high-performance supercapacitors. *PCCP* **16**, 785-791 (2014).
207. Bao, S.-J., Li, C. M., Guo, C.-X. & Qiao, Y. Biomolecule-assisted synthesis of cobalt sulfide nanowires for application in supercapacitors. *J. Power Sources* **180**, 676-681 (2008).
208. Lin, J.-Y. & Chou, S.-W. Cathodic deposition of interlaced nanosheet-like cobalt sulfide films for high-performance supercapacitors. *Rsc Adv* **3**, 2043-2048 (2013).
209. Yang, Z., Chen, C.-Y. & Chang, H.-T. Supercapacitors incorporating hollow cobalt sulfide hexagonal nanosheets. *J. Power Sources* **196**, 7874-7877 (2011).
210. Wang, Q. *et al.* Facile synthesis and superior supercapacitor performances of three-dimensional cobalt sulfide hierarchitectures. *Crystengcomm* **13**, 6960-6963 (2011).
211. Zhang, L., Wu, H. B. & Lou, X. W. Unusual CoS<sub>2</sub> ellipsoids with anisotropic tube-like cavities and their application in supercapacitors. *Chem. Commun.* **48**, 6912-6914 (2012).
212. Ding, Q. *et al.* Efficient Photoelectrochemical Hydrogen Generation Using Heterostructures of Si and Chemically Exfoliated Metallic MoS<sub>2</sub>. *J. Am. Chem. Soc.* **136**, 8504-8507 (2014).
213. Faber, M. S., Lukowski, M. A., Ding, Q., Kaiser, N. S. & Jin, S. Earth-Abundant Metal Pyrites (FeS<sub>2</sub>, CoS<sub>2</sub>, NiS<sub>2</sub>, and Their Alloys) for Highly Efficient Hydrogen Evolution and Polysulfide Reduction Electrocatalysis. *Journal Of Physical Chemistry C* **118**, 21347-21356 (2014).
214. Lukowski, M. A. *et al.* Highly active hydrogen evolution catalysis from metallic WS<sub>2</sub> nanosheets. *Energy Environ. Sci.* **7**, 2608-2613 (2014).
215. Faber, M. S., Park, K., Caban-Acevedo, M., Santra, P. K. & Jin, S. Earth-Abundant Cobalt Pyrite (CoS<sub>2</sub>) Thin Film on Glass as a Robust, High-Performance Counter Electrode for Quantum Dot-Sensitized Solar Cells. *J. Phys. Chem. Lett.* **4**, 1843-1849 (2013).
216. Faber, M. S. *et al.* High-Performance Electrocatalysis Using Metallic Cobalt Pyrite (CoS<sub>2</sub>) Micro- and Nanostructures. *J. Am. Chem. Soc.* **136**, 10053-10061 (2014).
217. Faber, M. S. *et al.* High-Performance Electrocatalysis Using Metallic Cobalt Pyrite (CoS<sub>2</sub>) Micro- and Nanostructures. *J. Am. Chem. Soc.* **136**, 10053-10061 (2014).
218. Xu, Z. W. *et al.* MoO<sub>2</sub>@MoS<sub>2</sub> Nanoarchitectures for High-Loading Advanced Lithium-Ion Battery Anodes. *Part. Part. Syst. Charact.* **34** (2017).

219. Xie, K. Y. *et al.* Superior Potassium Ion Storage via Vertical MoS<sub>2</sub> "Nano-Rose" with Expanded Interlayers on Graphene. *Small* **13** (2017).
220. An, Y. L. *et al.* A titanium-based metal-organic framework as an ultralong cycle-life anode for PIBs. *Chem. Commun.* **53**, 8360-8363 (2017).
221. Grigoriev, V. A., Cheng, D., Hill, C. L. & Weinstock, I. A. Role of alkali metal cation size in the energy and rate of electron transfer to solvent-separated 1 : 1 [(M<sup>+</sup>)(Acceptor)] (M<sup>+</sup> = Li<sup>+</sup>, Na<sup>+</sup>, K<sup>+</sup>) ion pairs. *J. Am. Chem. Soc.* **123**, 5292-5307 (2001).
222. Zhao, J., Zou, X. X., Zhu, Y. J., Xu, Y. H. & Wang, C. S. Electrochemical Intercalation of Potassium into Graphite. *Adv. Funct. Mater.* **26**, 8103-8110 (2016).
223. Ren, X. D., Zhao, Q., McCulloch, W. D. & Wu, Y. Y. MoS<sub>2</sub> as a long-life host material for potassium ion intercalation. *Nano Res.* **10**, 1313-1321 (2017).
224. Fu, H. B., Lin, J., Zhang, L. W. & Zhu, Y. F. Photocatalytic activities of a novel ZnWO<sub>4</sub> catalyst prepared by a hydrothermal process. *Appl Catal a-Gen* **306**, 58-67 (2006).
225. Huang Yi, S. Y., Wu jihuai, Huang Miaoliang. Synthesis and characterization of flower-like Bi<sub>2</sub>WO<sub>6</sub> and its photocatalytic activity. *J. Func. Marter.* **41**, 52-56 (2010).
226. Choi, H. C., Jung, Y. M. & Kim, S. B. Size effects in the Raman spectra of TiO<sub>2</sub> nanoparticles. *Vib. Spectrosc* **37**, 33-38 (2005).
227. Xue, X. *et al.* Raman Investigation of Nanosized TiO<sub>2</sub>: Effect of Crystallite Size and Quantum Confinement. *J. Phys. Chem. C* **116**, 8792-8797 (2012).
228. Mao, L., Wang, Y., Zhong, Y., Ning, J. & Hu, Y. Microwave-assisted deposition of metal sulfide/oxide nanocrystals onto a 3D hierarchical flower-like TiO<sub>2</sub> nanostructure with improved photocatalytic activity. *J. Mater. Chem. A* **1**, 8101-8104 (2013).
229. Tian, G. *et al.* Facile solvothermal synthesis of hierarchical flower-like Bi<sub>2</sub>MoO<sub>6</sub> hollow spheres as high performance visible-light driven photocatalysts. *J. Mater. Chem.* **21**, 887-892 (2011).
230. Li, H. *et al.* Mesoporous Titania Spheres with Tunable Chamber Structure and Enhanced Photocatalytic Activity. *J. Am. Chem. Soc.* **129**, 8406-8407 (2007).
231. Zhang, L. & Yu, J. C. A sonochemical approach to hierarchical porous titania spheres with enhanced photocatalytic activity. *Chem. Commun.*, 2078-2079 (2003).
232. Li, L. *et al.* Synthesis of anatase TiO<sub>2</sub> nanowires by modifying TiO<sub>2</sub> nanoparticles using the microwave heating method. *Appl. Surf. Sci.* **257**, 8006-8012 (2011).
233. Rather, S. U. *et al.* Hydrogen storage of nanostructured TiO<sub>2</sub>-impregnated carbon nanotubes. *Int. J. Hydrog. Energy* **34**, 961-966 (2009).

234. Das, S. K., Bhunia, M. K. & Bhaumik, A. Self-assembled TiO<sub>2</sub> nanoparticles: mesoporosity, optical and catalytic properties. *Dalton Trans.* **39**, 4382-4390 (2010).
235. Zhang, Q. Y., Li, Y., Ackerman, E. A., Gajdardziska-Josifovska, M. & Li, H. L. Visible light responsive iodine-doped TiO<sub>2</sub> for photocatalytic reduction of CO<sub>2</sub> to fuels. *Appl Catal a-Gen* **400**, 195-202 (2011).
236. Babu, V. J., Nair, A. S., Peining, Z. & Ramakrishna, S. Synthesis and characterization of rice grains like Nitrogen-doped TiO<sub>2</sub> nanostructures by electrospinning–photocatalysis. *Mater. Lett.* **65**, 3064-3068 (2011).
237. Ma, Y., Ji, G., Ding, B. & Lee, J. Y. Facile solvothermal synthesis of anatase TiO<sub>2</sub> microspheres with adjustable mesoporosity for the reversible storage of lithium ions. *J. Mater. Chem.* **22**, 24380-24385 (2012).
238. Jitputti, J., Pavasupree, S., Suzuki, Y. & Yoshikawa, S. Synthesis and photocatalytic activity for water-splitting reaction of nanocrystalline mesoporous titania prepared by hydrothermal method. *J. Solid State Chem.* **180**, 1743-1749 (2007).
239. Giannakas, A. E., Seristatidou, E., Deligiannakis, Y. & Konstantinou, I. Photocatalytic activity of N-doped and N-F co-doped TiO<sub>2</sub> and reduction of chromium(VI) in aqueous solution: An EPR study. *Appl Catal B-Environ* **132**, 460-468 (2013).
240. Xiong, L. B., Li, J. L., Yang, B. & Yu, Y. Ti<sup>3+</sup> in the Surface of Titanium Dioxide: Generation, Properties and Photocatalytic Application. *J Nanomater.* 1-13 (2012).
241. Zheng, W. C., Zhou, Q., Wu, X. X. & Mei, Y. Theoretical investigations of the EPR parameters of Ti<sup>3+</sup> in beryl crystal. *Z Naturforsch A* **61**, 286-288 (2006).
242. Yang, G. D., Jiang, Z., Shi, H. H., Xiao, T. C. & Yan, Z. F. Preparation of highly visible-light active N-doped TiO<sub>2</sub> photocatalyst. *J. Mater. Chem.* **20**, 5301-5309 (2010).
243. Castro, C. A. *et al.* Photocatalytic production of O-1(2) and (OH)-O-center dot mediated by silver oxidation during the photoinactivation of Escherichia coli with TiO<sub>2</sub>. *J. Hazard. Mater.* **211**, 172-181 (2012).
244. Jou, J. L., Lei, C. M., Xu, Y. W. & Yeh, W. C. V. The Higher Energy Components in Ti2p Xps Spectrum of Ga Doped Barium Titanate. *Chinese J Phys* **50**, 926-931 (2012).
245. Parra, E. R., Arango, P. J. A. & Palacio, V. J. B. XPS STRUCTURE ANALYSIS OF TiN/TiC BILAYERS PRODUCED BY PULSED VACUUM ARC DISCHARGE. *Dyna-Colombia* **77**, 64-74 (2010).
246. Laidani, N. *et al.* Intrinsic defects and their influence on the chemical and optical properties of TiO<sub>2-x</sub> films. *J Phys D Appl Phys* **43**, 1-11 (2010).
247. Wang, M. *et al.* Improved photovoltaic performance of dye-sensitized solar cells by Sb-doped TiO<sub>2</sub> photoanode. *Electrochim. Acta* **77**, 54-59 (2012).

248. Xing, M., Zhang, J., Chen, F. & Tian, B. An economic method to prepare vacuum activated photocatalysts with high photo-activities and photosensitivities. *Chem. Commun.* **47**, 4947-4949 (2011).
249. McCafferty, E. & Wightman, J. P. Determination of the concentration of surface hydroxyl groups on metal oxide films by a quantitative XPS method. *Surf. Interface Anal.* **26**, 549-564 (1998).
250. Li, L. *et al.* A direct synthesis of B-doped TiO<sub>2</sub> and its photocatalytic performance on degradation of RhB. *Appl. Surf. Sci.* **265**, 36-40 (2013).
251. Chen, D., Yang, D., Wang, Q. & Jiang, Z. Y. Effects of boron doping on photocatalytic activity and microstructure of titanium dioxide nanoparticles. *Ind. Eng. Chem. Res.* **45**, 4110-4116 (2006).
252. Khan, S. U., Al-Shahry, M. & Ingler, W. B., Jr. Efficient photochemical water splitting by a chemically modified n-TiO<sub>2</sub>. *Science* **297**, 2243-2245 (2002).
253. Murphy, A. B. Band-gap determination from diffuse reflectance measurements of semiconductor films, and application to photoelectrochemical water-splitting. *Sol. Energy Mater. Sol. Cells* **91**, 1326-1337 (2007).
254. Wang, W. *et al.* Enhanced visible-light photoactivity of {001} facets dominated TiO<sub>2</sub> nanosheets with even distributed bulk oxygen vacancy and Ti<sup>3+</sup>. *Catal. Commun.* **22**, 19-23 (2012).
255. Mao, S. *et al.* Hierarchical Nanohybrids with Porous CNT-Networks Decorated Crumpled Graphene Balls for Supercapacitors. *ACS Appl. Mater. Interfaces* **6**, 9881-9889 (2014).
256. Chen, C.-Y., Shih, Z.-Y., Yang, Z. & Chang, H.-T. Carbon nanotubes/cobalt sulfide composites as potential high-rate and high-efficiency supercapacitors. *J. Power Sources* **215**, 43-47 (2012).
257. Li, Y. H. *et al.* Novel route to WO<sub>x</sub> nanorods and WS<sub>2</sub> nanotubes from WS<sub>2</sub> inorganic fullerenes. *J. Phys. Chem. B* **110**, 18191-18195 (2006).
258. Lukowski, M. A. *et al.* Enhanced hydrogen evolution catalysis from chemically exfoliated metallic MoS<sub>2</sub> nanosheets. *J. Am. Chem. Soc.* **135**, 10274-10277 (2013).
259. Xu, S. S. *et al.* Morphology evolution of Ag alloyed WS<sub>2</sub> films and the significantly enhanced mechanical and tribological properties. *Surf. Coat. Technol.* **238**, 197-206 (2014).
260. Wang, S. Q. *et al.* Synthesis and Characterization of Cobalt-Doped WS<sub>2</sub> Nanorods for Lithium Battery Applications. *Nanoscale Res. Lett.* **5**, 1301-1306 (2010).

261. Huang, Y. X. *et al.* Sulfurized activated carbon for high energy density supercapacitors. *Journal of Power Sources* **252**, 90-97 (2014).
262. Zhou, Y. C. *et al.* Sulfur and nitrogen self-doped carbon nanosheets derived from peanut root nodules as high-efficiency non-metal electrocatalyst for hydrogen evolution reaction. *Nano Energy* **16**, 357-366 (2015).
263. Whitby, R. L. D. *et al.* WS<sub>2</sub> layer formation on multi-walled carbon nanotubes. *Appl. Phys. A* **76**, 527-532 (2003).
264. Berkdemir, A. *et al.* Identification of individual and few layers of WS<sub>2</sub> using Raman Spectroscopy. *Sci. Rep.* **3** (2013).
265. Terrones, H. *et al.* New First Order Raman-active Modes in Few Layered Transition Metal Dichalcogenides. *Sci. Rep.* **4** (2014).
266. Vernardou, D. *et al.* Electrochemical and photocatalytic properties of WO<sub>3</sub> coatings grown at low temperatures. *J. Mater. Chem.* **21**, 513-517 (2011).
267. Verma, M., Chandra, R. & Gupta, V. K. Synthesis of magnetron sputtered WO<sub>3</sub> nanoparticles-degradation of 2-chloroethyl ethyl sulfide and dimethyl methyl phosphonate. *J. Colloid Interface Sci.* **453**, 60-68 (2015).
268. Poongodi, S. *et al.* Synthesis of hierarchical WO<sub>3</sub> nanostructured thin films with enhanced electrochromic performance for switchable smart windows. *Rsc Adv* **5**, 96416-96427 (2015).
269. Dresselhaus, M. S., Jorio, A., Souza, A. G. & Saito, R. Defect characterization in graphene and carbon nanotubes using Raman spectroscopy. *Phil. Trans. R. Soc. A* **368**, 5355-5377 (2010).
270. Pimenta, M. A. *et al.* Studying disorder in graphite-based systems by Raman spectroscopy. *Phys. Chem. Chem. Phys.* **9**, 1276-1291 (2007).
271. Dartigeas, K., Gonbeau, D. & PfisterGuillouzo, G. Core and valence spectra of TaS<sub>2</sub> and WS<sub>2</sub> - Experimental and theoretical studies. *J. Chem. Soc. Faraday Trans.* **92**, 4561-4566 (1996).
272. Shpak, A. P., Korduban, A. M., Medvedskij, M. M. & Kandyba, V. O. XPS studies of active elements surface of gas sensors based on WO<sub>3-x</sub> nanoparticles. *J. Electron. Spectrosc. Relat. Phenom.* **156**, 172-175 (2007).
273. Mahler, B., Hoepfner, V., Liao, K. & Ozin, G. A. Colloidal Synthesis of 1T-WS<sub>2</sub> and 2H-WS<sub>2</sub> Nanosheets: Applications for Photocatalytic Hydrogen Evolution. *J. Am. Chem. Soc.* **136**, 14121-14127 (2014).

274. Ambrosi, A., Sofer, Z. & Pumera, M. 2H  $\rightarrow$  1T phase transition and hydrogen evolution activity of MoS<sub>2</sub>, MoSe<sub>2</sub>, WS<sub>2</sub> and WSe<sub>2</sub> strongly depends on the MX<sub>2</sub> composition. *Chem. Commun.* **51**, 8450-8453 (2015).
275. Mayorga-Martinez, C. C., Ambrosi, A., Eng, A. Y. S., Sofer, Z. & Pumera, M. Metallic 1T-WS<sub>2</sub> for Selective Impedimetric Vapor Sensing. *Adv. Funct. Mater.* **25**, 5611-5616 (2015).
276. Liu, Q. *et al.* Stable metallic 1T-WS<sub>2</sub> ultrathin nanosheets as a promising agent for near-infrared photothermal ablation cancer therapy. *Nano Res.* **8**, 3982-3991 (2015).
277. Spath, B. *et al.* X-ray photoelectron spectroscopy and tribology studies of annealed fullerene-like WS<sub>2</sub> nanoparticles. *Phys. Status Solidi B* **245**, 1779-1784 (2008).
278. Rahimnejad, S., He, J. H., Chen, W., Wu, K. & Xu, G. Q. Tuning the electronic and structural properties of WO<sub>3</sub> nanocrystals by varying transition metal tungstate precursors. *RSC Adv.* **4**, 62423-62429 (2014).
279. Shifa, T. A. *et al.* A vertical-oriented WS<sub>2</sub> nanosheet sensitized by graphene: an advanced electrocatalyst for hydrogen evolution reaction. *Nanoscale* **7**, 14760-14765 (2015).
280. Conway, B. E. & Tilak, B. V. Interfacial processes involving electrocatalytic evolution and oxidation of H<sub>2</sub>, and the role of chemisorbed H. *Electrochim. Acta* **47**, 3571-3594 (2002).
281. Yang, L. *et al.* Synergistic WO<sub>3</sub>·2H<sub>2</sub>O Nanoplates/WS<sub>2</sub> Hybrid Catalysts for High-Efficiency Hydrogen Evolution. *ACS Appl. Mater. Interfaces* **8**, 13966-13972 (2016).
282. Zhang, Z. H., Liu, J., Gu, J. J., Su, L. & Cheng, L. F. An overview of metal oxide materials as electrocatalysts and supports for polymer electrolyte fuel cells. *Energy Environ. Sci.* **7**, 2535-2558 (2014).
283. Lukowski, M. A. *et al.* Enhanced hydrogen evolution catalysis from chemically exfoliated metallic MoS<sub>2</sub> nanosheets. *J Am Chem Soc* **135**, 10274-10277 (2013).
284. Kibsgaard, J., Chen, Z., Reinecke, B. N. & Jaramillo, T. F. Engineering the surface structure of MoS<sub>2</sub> to preferentially expose active edge sites for electrocatalysis. *Nat Mater* **11**, 963-969 (2012).
285. Li, Y. G. *et al.* MoS<sub>2</sub> Nanoparticles Grown on Graphene: An Advanced Catalyst for the Hydrogen Evolution Reaction. *J Am Chem Soc* **133**, 7296-7299 (2011).
286. Yang, J. *et al.* Porous Molybdenum Phosphide Nano-Octahedrons Derived from Confined Phosphorization in UIO-66 for Efficient Hydrogen Evolution. *Angew. Chem. Int. Ed. Engl.* **55**, 12854-12858 (2016).

287. Deng, J., Ren, P. J., Deng, D. H. & Bao, X. H. Enhanced Electron Penetration through an Ultrathin Graphene Layer for Highly Efficient Catalysis of the Hydrogen Evolution Reaction. *Angew Chem Int Edit* **54**, 2100-2104 (2015).
288. Ito, Y., Cong, W., Fujita, T., Tang, Z. & Chen, M. High catalytic activity of nitrogen and sulfur co-doped nanoporous graphene in the hydrogen evolution reaction. *Angew. Chem. Int. Ed. Engl.* **54**, 2131-2136 (2015).
289. Wang, H. T. *et al.* Electrochemical tuning of vertically aligned MoS<sub>2</sub> nanofilms and its application in improving hydrogen evolution reaction. *Proc. Natl. Acad. Sci. U.S.A.* **110**, 19701-19706 (2013).
290. Wang, D. Z. *et al.* Phase engineering of a multiphasic 1T/2H MoS<sub>2</sub> catalyst for highly efficient hydrogen evolution. *J. Mater. Chem. A* **5**, 2681-2688 (2017).
291. Carey, B. J. *et al.* Two solvent grinding sonication method for the synthesis of two-dimensional tungsten disulphide flakes. *Chem. Commun.* **51**, 3770-3773 (2015).
292. Cheng, P. F., Sun, K. & Hu, Y. H. Mechanically-induced reverse phase transformation of MoS<sub>2</sub> from stable 2H to metastable 1T and its memristive behavior. *RSC Adv.* **6**, 65691-65697 (2016).
293. Vullum, P. E. *et al.* Quantitative strain analysis of InAs/GaAs quantum dot materials. *Sci. Rep.* **7** (2017).
294. Luo, X., Zhao, Y. Y., Zhang, J., Xiong, Q. H. & Quek, S. Y. Anomalous frequency trends in MoS<sub>2</sub> thin films attributed to surface effects. *Phys. Rev. B* **88** (2013).
295. Aliyan, H., Fazaeli, R. & Jalilian, R. Fe<sub>3</sub>O<sub>4</sub>@mesoporous SBA-15: A magnetically recoverable catalyst for photodegradation of malachite green. *Appl. Surf. Sci.* **276**, 147-153 (2013).
296. Qiu, S. B. *et al.* Simply packaging Ni nanoparticles inside SBA-15 channels by co-impregnation for dry reforming of methane. *RSC Adv.* **7**, 24551-24560 (2017).
297. Lu, C. P., Li, G. H., Mao, J. H., Wang, L. M. & Andrei, E. Y. Bandgap, Mid-Gap States, and Gating Effects in MoS<sub>2</sub>. *Nano Lett.* **14**, 4628-4633 (2014).
298. Shen, W. C., Chen, R. S. & Huang, Y. S. Photoconductivities in MoS<sub>2</sub> Nanoflake Photoconductors. *Nanoscale Res. Lett.* **11** (2016).
299. Fan, Q. J. *et al.* Superior nanoporous graphitic carbon nitride photocatalyst coupled with CdS quantum dots for photodegradation of RhB. *Catal. Today* **264**, 250-256 (2016).
300. Qin, J. Y. & Zeng, H. P. Photocatalysts fabricated by depositing plasmonic Ag nanoparticles on carbon quantum dots/graphitic carbon nitride for broad spectrum photocatalytic hydrogen generation. *Appl. Catal., B.* **209**, 161-173 (2017).

301. Gao, D. Q. *et al.* Ferromagnetism in freestanding MoS<sub>2</sub> nanosheets. *Nanoscale Res. Lett.* **8** (2013).
302. Yang, X. B., Qiu, L. Q. & Luo, X. T. ZIF-8 derived Ag-doped ZnO photocatalyst with enhanced photocatalytic activity. *RSC Adv.* **8**, 4890-4894 (2018).
303. Da Silva, J. D. F. *et al.* Adsorption in a Fixed-Bed Column and Stability of the Antibiotic Oxytetracycline Supported on Zn(II)-[2-Methylimidazolate] Frameworks in Aqueous Media. *Plos One* **10** (2015).
304. He, F. *et al.* ZIF-8 derived carbon (C-ZIF) as a bifunctional electron acceptor and HER cocatalyst for g-C<sub>3</sub>N<sub>4</sub>: construction of a metal-free, all carbon-based photocatalytic system for efficient hydrogen evolution. *J. Mater. Chem. A* **4**, 3822-3827 (2016).
305. Kong, R. M., Zhao, Y., Zheng, Y. Q. & Qu, F. L. Facile synthesis of ZnO/CdS@ZIF-8 core-shell nanocomposites and their applications in photocatalytic degradation of organic dyes. *RSC Adv.* **7**, 31365-31371 (2017).
306. He, L. *et al.* Fabrication of Au/ZnO nanoparticles derived from ZIF-8 with visible light photocatalytic hydrogen production and degradation dye activities. *Dalton Trans.* **43**, 16981-16985 (2014).
307. Huang, H. *et al.* Water-Soluble Monolayer Molybdenum Disulfide Quantum Dots with Upconversion Fluorescence. *Part. Part. Syst. Charact.* **32**, 72-79 (2015).
308. Huang, Y. L. *et al.* Bandgap tunability at single-layer molybdenum disulphide grain boundaries. *Nat. Commun.* **6** (2015).
309. Shi, H. L., Pan, H., Zhang, Y. W. & Yakobson, B. I. Quasiparticle band structures and optical properties of strained monolayer MoS<sub>2</sub> and WS<sub>2</sub>. *Phys. Rev. B* **87** (2013).
310. He, L. *et al.* ZIF-8 templated fabrication of rhombic dodecahedron-shaped ZnO@SiO<sub>2</sub>, ZIF-8@SiO<sub>2</sub> yolk-shell and SiO<sub>2</sub> hollow nanoparticles. *Crystengcomm* **16**, 6534-6537 (2014).
311. Jing, Y. Q. *et al.* A MOF-derived ZIF-8@Zn<sub>1-x</sub>Ni<sub>x</sub>O photocatalyst with enhanced photocatalytic activity. *RSC Adv.* **7**, 42030-42035 (2017).
312. Sang, Y. H. *et al.* From UV to Near-Infrared, WS<sub>2</sub> Nanosheet: A Novel Photocatalyst for Full Solar Light Spectrum Photodegradation. *Adv. Mater.* **27**, 363-369 (2015).
313. Wang, Y. *et al.* Hydrogen production with ultrahigh efficiency under visible light by graphene well-wrapped UiO-66-NH<sub>2</sub> octahedrons. *J. Mater. Chem. A* **5**, 20136-20140 (2017).
314. Slamet, Ratnawati, Gunlazuardi, J. & Dewi, E. L. Enhanced photocatalytic activity of Pt deposited on titania nanotube arrays for the hydrogen production with glycerol as a sacrificial agent. *Int. J. Hydrog. Energy* **42**, 24014-24025 (2017).

315. Hsieh, S. H. *et al.* Synthesis of Pt Doped Bi<sub>2</sub>O<sub>3</sub>/RuO<sub>2</sub> Photocatalysts for Hydrogen Production from Water Splitting Using Visible Light. *J. Nanosci. Nanotechnol* **12**, 5930-5936 (2012).

# CURRICULUM VITAE

**Ren Ren**

**Place of birth: China**

## 1. Education:

Ph.D., Mechanical Engineering May 2018

University of Wisconsin-Milwaukee, Milwaukee, Wisconsin, USA.

Research Advisor: Dr. Junhong Chen

Title of thesis: Synthesis and Characterization of Transition Metal Oxide and Dichalcogenide Nanomaterials for Energy and Environmental Applications

Master of Engineering, Materials Science and Engineering July 2010

Beijing University of Technology, Beijing, CHINA.

Research Advisor: Dr. Fu Guo

Title of thesis: Study on the Microstructure and Mechanical Properties of Vacuum Brazed Titanium Alloy using Ti-Zr-Ni-Cu Amorphous Solder.

Bachelor of Engineering, Materials Science and Engineering July 2007

Beijing University of Technology, Beijing, CHINA.

Research Advisor: Dr. Fu Guo

Title of thesis: The Study of DMA in the Measurement of Dynamic Mechanical Properties of Lead-free Solder Joints.

## 2. Experience:

**Research Assistant at UW-Milwaukee for Nanotechnology for Sustainable Energy and Environment Lab (2013 ~ 2018)**

**Energy conversion:** Developed a facile route for the controllable synthesis of modified Ti<sup>3+</sup>-doped TiO<sub>2</sub> with tunable photocatalytic properties by using a hydrothermal method for removing

organic/inorganic contaminants such as water purification. Focused on developing novel nanostructured transition metal dichalcogenides and oxides as next-generation electrocatalysts for clean and renewable energy applications.

**Energy storage:** Synthesized vertically-aligned metallic CoS<sub>2</sub> nanowires directly on carbon cloth or graphite disc current collectors which exhibit promising performance and excellent cycling stability in supercapacitors, among the best reported for CoS<sub>x</sub>-based active materials. Working on developing next-generation lithium-ion/potassium-ion batteries with the unique structures to address the volume expansion of anode materials in the synthesis process.

**Sensors:** Part of a collaboration team developing a highly sensitive, low-cost sensor that can be easily modified to detect lead and other heavy metal ions in drinking water. Focused on using atomic layer deposition (ALD), atomic force microscopy (AFM) and ellipsometry for the surface modification and measurement.

#### **Teaching Assistant and Lab Manager at UW-Milwaukee (2013 ~ 2017)**

Teaching assistant and lab manager for the course “MAT. 330: Materials and Processes in Manufacturing” and “ME. 438: Mechanical Engineering Experimentation”.

#### **Industry: Research & Development Scientist at GRIKIN Advanced Materials Co., Ltd. (2011 ~ 2012)**

The main job focused on designing, developing the new target materials, bonding technologies and Non-destructive testing. Main bonding method contains solder bond, e-beam weld, diffusion bond and mechanical assembly. Use USIP40 C-Scan ultrasonic non-destructive testing detects the sputtering target, backing plate, and finished products.

#### **Research Assistant at Beijing University of Technology for Materials Processing Engineering Lab (2007 ~ 2010)**

Study of amorphous solder alloys used in astronavigation/navigation facility. A special emphasis of the study is on the solderability, reliability/failure issues as well as microstructural characterization and analysis of vacuum brazing Titanium Alloy.

### 3. Skills:

**Materials Characterization:** Transmission electron microscopy (TEM); Scanning electron microscopy (SEM); Energy Dispersive X-ray (EDX); X-ray powder diffraction (XRD); Raman/FTIR; Photoluminescence (PL); Brunauer-Emmett-Teller (BET); Dynamic mechanical analysis (DMA); Differential scanning calorimetry (DSC); Thermogravimetric analysis (TGA); Ultraviolet-visible spectroscopy (UV-Vis); Ellipsometry; Atomic force microscopy (AFM), Gas Chromatography (GC).

**Materials Preparation Method:** Hydrothermal; Templated-assistant; Vacuum Deposition and Vaporization; Chemical Vapor Deposition (CVD); Wet chemical; Aerosolization, Metal-Organic Frameworks (MOF) technology.

**Welding:** Preparation of amorphous brazing filler metals and lead-free solder; Brazing; Manual fusion welding. (electrode/wire); Electron Beam Welding (EBW); Stress/Strain measurement; Creep testing and data extraction/analysis technique.

**Programming:** LabVIEW, Matlab; Modeling: ANSYS; CAD: SolidWorks, AutoCAD, 3D max.

**Certifications:** ANSYS Mechanical Analyst - Level 1 (Issued by ANSYS-CHINA); Chinese SolidWorks Accredited Engineer (Issued by SolidWorks Corporation)

### 4. Honors:

Distinguished Dissertation Fellowship; Graduate Student Travel Award. 2017~2018 (Sponsored by UW-Milwaukee)

Chancellor Award. 2018, 2015 (Sponsored by ME, UWM)

Research Excellence Award. 2008~2009 (Sponsored by MSE)

Academic and Scientific Award for Graduate Students. 2007~2008 (Sponsored by BJUT)

Excellent Thesis Prize. 2007 (Sponsored by MSE)

Excellent Student Cadre & Scholarship. 2003~2004, 2004~2005, 2005~2006, 2007~2008 (Sponsored by BJUT)

A prestigious member of the 2008 Beijing Olympic games volunteer team for the Beach Volleyball Competition. 2008

## 5. Publications:

1. **Y. T. Chen,<sup>+</sup> R. Ren,<sup>+</sup>** Zhenhai Wen, Suqin Ci, Jingbo Chang, Shun Mao and Junhong Chen. Superior electrocatalysis for hydrogen evolution with crumpled graphene/tungsten disulfide/tungsten trioxide ternary nanohybrids. [+] These authors contributed equally to this work. **Nano Energy**, 47 (2018) 66-73.
2. **R. Ren**, M. S. Faber, R. Dzedzic, Z. H. Wen, S. Jin, S. Mao and J. H. Chen. Metallic CoS<sub>2</sub> nanowire electrodes for high cycling performance supercapacitors. **Nanotechnology**, 2015, 26, 494001.
3. **R. Ren**, Z. H. Wen, S. M. Cui, Y. Hou, X.R. Guo, and J. H. Chen. Controllable synthesis and tunable photocatalytic properties of Ti<sup>3+</sup>-doped TiO<sub>2</sub>. **Sci. Rep.** 2015, 5, 10714.
4. **R. Ren**, F. Guo, Y. Y. Cui and Z. D. Xia. Study on the microstructure and mechanical properties of vacuum brazing titanium alloy using Ti-Zr-Cu-Ni amorphous filler metal. **Mater. Sci. Technol.** 2009, 17, Sup. 1.
5. Y. T. Chen, **R. Ren**, H. H. Pu, X. R. Guo, J. B. Chang, G. H. Zhou, S. Mao, M. Kron, J. H. Chen. Field-effect transistor biosensors for rapid detection of Ebola antigen. **Sci. Rep.** 2017, 7, 10974.
6. Y. T. Chen, **R. Ren**, H. H. Pu, J. B. Chang, S. Mao, J. H. Chen. Field-effect transistor biosensors with two-dimensional black phosphorus nanosheets. **Biosens. Bioelectron.** 2016.03.0592.
7. X. R. Guo, H. Yang, **R. Ren** and J. H. Chen. Temperature-dependent crystallization of MoS<sub>2</sub> nanoflakes on graphene nanosheets for electrocatalysis. **Nanoscale Res. Lett.**, 2017 12 (1), 479.
8. S. M. Cui, X. R. Guo, **R. Ren**, G. H. Zhou and J. H. Chen. Decoration of vertical graphene with aerosol nanoparticles for gas sensing. **J. Phys. D: Appl. Phys.** 48, 2015, 314008.
9. X. K. Huang, X. Y. Sui, H. Yang, **R. Ren**, Y. P. Wu, X.R. Guo, and J. H. Chen. Hf-free synthesis of Si/C yolk/shell anodes for lithium-ion batteries. **J. Mater. Chem. A** 2018, 6, 2593-2599.
10. W. M. Xiao, Y. W. Shi, G. C. Xu, and **R. Ren**. Effect of rare earth on mechanical creep-fatigue property of SnAgCu solder joint. **J. Alloys Compd.**, 2009; 478.

11. Y. P. Wu, X. K. Huang, L. Huang, X. R. Guo; **R. Ren**, D. Liu, D. Y. Qu and J. H. Chen. Self-healing liquid metal and Si composite as a high-performance anode for lithium-ion batteries. **ACS Appl. Energy Mater.** 2018,02
12. G. Wang, M. Yue, J. Zhang, W. Liu, **R. Ren** and C. Liu. Research on the mechanical properties of spark plasma sintering NdFeB sintered magnets. **Powder. Metall. Technol.**, 2006, 24, 4, 259-262.
13. S. Mao, H. H. Pu, J. B. Chang, X. Y. Sui, G. H. Zhou, **R. Ren**, Y. T. Chen and J. H. Chen. Ultrasensitive detection of orthophosphate ions with reduced graphene oxide/ferritin field-effect transistor sensors. **Environ. Sci.: Nano** 2017, 4 (4), 856-863.
14. S. Q. Ci, S. Mao, Y. Hou, S. M. Cui, H. Kim, **R. Ren**, Z. H. Wen and J. H. Chen. Rational design of mesoporous NiFe-alloy-based hybrids for oxygen conversion electrocatalysis. **J. Mater. Chem. A**, 2015, 3, 7986-7993.
15. G. H. Zhou, J. B. Chang, H. H. Pu, K.Y. Shi, S. Mao, X.Y. Sui, **R. Ren**, S. M. Cui and J. H. Chen. Ultrasensitive Mercury Ion Detection Using DNA-functionalized Molybdenum Disulfide Nanosheet/Gold Nanoparticle Hybrid Field-Effect Transistor Device. **ACS Sens.**, 2016, 1 (3), pp 295–302.
16. Maity, X. Y. Sui, C. R. Tarman, H. H. Pu, J. B. Chang, G. H. Zhou, **R. Ren**, S. Mao and J. H. Chen. Pulse-Driven Capacitive Lead Ion Detection with Reduced Graphene Oxide Field-Effect Transistor Integrated with an Analyzing Device for Rapid Water Quality Monitoring. **ACS Sens.**, 2017, 2 (11), pp 1653–1661.
17. Y. P. Wu, L. Huang, X. K. Huang, X. R. Guo, D. Liu, D. Zheng, X. L. Zhang, **R. Ren**, D. Y. Qu and J. H. Chen. A room-temperature liquid metal-based self-healing anode for lithium-ion batteries with an ultra-long cycle life. **Energy Environ. Sci.**, 2017, 10 (8), 1854-1861.